2019

Sprinkler systems for the protection of buildings from wildfire

Alan Green
University of Wollongong

SPRINKLER SYSTEMS FOR THE PROTECTION OF BUILDINGS FROM WILDFIRE

A thesis submitted in fulfilment of the requirements for the award of the degree

DOCTOR OF PHILOSOPHY

from

UNIVERSITY OF WOLLONGONG

by

ALAN GREEN

SUSTAINABLE BUILDINGS RESEARCH CENTRE,

FACULTY OF ENGINEERING AND INFORMATION SCIENCES

July 2019

Acknowledgements

I would like to thank my partner Monique, family and friends for supporting me and tolerating my preoccupation over the past four years. Thanks also to my supervisors, Paul Cooper, Ross Bradstock and Trent Penman, who have been a great source of guidance throughout the process. This research has been conducted with the support of an Australian Government Research Training Program Scholarship.

Abstract

Wildfires pose a significant hazard in many residential areas around the world. Minimisation of the risk to human lives and property requires a multi-faceted approach, involving fuel reduction, fire suppression, and engineering measures to improve the resistance of buildings to the effects of intense radiant heat, burning embers and flame contact.

Measures that are recommended to improve the wildfire resistance of buildings typically focus on building materials and design features, as well as fuel sources close to the building. Wildfire sprinkler systems are often promoted as an optional, additional risk-mitigation measure. Typically, such systems are designed to spray water on building external surfaces, surround the building with airborne droplets, and/or wet nearby fuel sources during wildfires.

Very little rigorous scientific investigation has previously been conducted into the performance of wildfire sprinkler systems, and consequently little consensus has been reached as to the mechanisms by which water sprays mitigate the impacts of wildfire on buildings, or the degree of protection that can be achieved. Furthermore, the effects of strong, hot, dry winds (which typically occur during wildfires) on wildfire sprinkler performance do not appear to have previously been quantified. The lack of reliable quantitative evidence has prevented wildfire sprinkler systems from being fully incorporated into risk-mitigation activities, other than as an optional/additional measure of unknown effectiveness. A series of experiments and simulations were designed and conducted in the present study to form a foundation for such evidence.

Six water sprays, generated by ‘butterfly’, ‘impact’, hollow-cone, flat-fan and deflector-plate sprinklers, were experimentally characterised, using a single-camera high-speed videography technique. Video analysis software was developed and applied to measure the size, velocity and location of individual droplets within the video footage. A new technique to separate overlapping images of non-spherical droplets was developed and found to outperform several existing methods. Data, describing in the order of 100,000 droplets in each spray, were corrected for

statistical bias and converted into continuous co-distributions of droplet diameter, velocity and mass flux, resolved in time and space.

Experiments were also conducted outdoors to generate fundamental test cases, for the validation of simulations involving wind–spray interaction around bluff bodies in the atmospheric boundary layer. Individual sprinklers were operated in the vicinity of an isolated 2.4 m cube in an open field. Water deposition was measured on the cube surfaces and ground using custom-built collection gauges, and detailed wind characteristics were measured at a nearby 10-m-tall mast.

An extensive investigation was undertaken into the performance of computational fluid dynamics (CFD) methods in simulations of spray dispersion around buildings in wind, using the commercial code ANSYS Fluent 14.5. Test cases from the above-mentioned experiments were replicated in steady Reynolds-averaged Navier-Stokes (RANS) simulations with Lagrangian particle tracking. Several hundred such simulations were conducted, to evaluate different approaches to the definition of droplet sources and the modelling of turbulence. It was discovered that even some transient sprays, such as those produced by 'butterfly' sprinklers, could be simulated reasonably accurately using steady RANS-based methods, with the majority of time-averaged deposition fluxes agreeing with experimental results to within ±15%. However, some local deposition fluxes did differ from the experimental values by more than 50%, especially those on the cube top surface. Comparison of different CFD methodologies revealed that: i) one and two-way coupled simulations produced very similar results, as did simulations conducted using the RNG k-ε and realisable k-ε turbulence models; ii) turbulent dispersion models needed to be implemented in order to obtain results that agreed with experiments; iii) at least 1,000 spatially unique source points and 10 or more distinct size classes needed to be used to represent each sprinkler; iv) small changes in the initial location of droplets caused large differences in CFD results, if droplet initial velocities were not modified accordingly; and v) disagreement between CFD and experimental results in the present study did not appear to be caused by large-scale 'inactive' turbulence.

The CFD methodology that was developed was then applied to evaluate the performance of nine typical wildfire sprinkler configurations in three sets of weather conditions (including air

temperature, humidity and wind speed). The simulations revealed that if wildfire sprinklers are not positioned appropriately more than half of the water ejected from the sprinkler nozzles can be blown downwind of the building, and/or evaporated while airborne. Sprinklers located close to the target surfaces and aimed directly towards them were the least prone to such losses.

Results from the CFD simulations were post-processed to estimate: i) the heat flux that could be removed by water deposited on the building, and ii) the radiant heat flux that could be attenuated by airborne droplets. Sprinklers that sprayed water directly onto the top section of the wall (e.g. from under the building eaves) were effective at removing a 30 kW m^{-2} heat flux from all, or most, of the wall height, while sprinklers that emitted droplets away from the building from near the roof perimeter removed less than half this heat flux. The airborne droplets projected around the building by five of the nine sprinkler configurations were able to attenuate 6–26% of incident radiant heat. Wind-drift and evaporation were found to influence sprinkler system effectiveness strongly, e.g. the attenuation of radiative heat fluxes varied by more than 39% between the weather scenarios investigated, due to differences in the ambient air temperature, humidity and wind speed.

The evidence presented in this thesis indicates that wildfire sprinkler systems can provide significant protection to buildings during wildfires, if designed appropriately. Results also indicate that the effects of wind need to be taken into account in order to obtain accurate assessments of wildfire sprinkler performance. Moreover, the tools and techniques that have been developed in the present project are a relatively simple means by which to quantify the performance of such sprinklers in the hot, windy conditions that occur during wildfires. With further development, and application to a larger set of sprinkler configurations, these tools and techniques could be used to form the rigorous quantitative evidence base that is required to guide the design of effective wildfire sprinkler systems, and to facilitate the use of sprinklers as a worthwhile and quantifiable wildfire risk mitigation measure.

Contents

List of Figures

List of Tables

Nomenclature

α	Exponent in 'power-law' atmospheric boundary layer velocity, k and ε profile functions
β	Parameter used in the canopy-flow velocity, k and ε profile functions
γ_k	Blending parameter, used in the canopy-flow k and ε profile functions
γ_{LNRR}	Distribution parameter used in the hybrid log-normal/Rosin Rammler diameter distribution function
γ_{RR}	Distribution parameter used in the Rosin Rammler diameter distribution function
γ_u	Blending parameter, used in the canopy-flow velocity and ε profile functions
δ	Spray source radius reduction factor
δ_k	Blending parameter, used in the canopy-flow k and ε profile functions
δ_u	Blending parameter, used in the canopy-flow velocity and ε profile functions
δ_{ULLN}	Function of the distribution parameter, σ_{ULLN}, used in the upper-limit log-normal diameter distribution function
δ_t	Time period separating the two video frames [s]
ε	Turbulence dissipation rate [m^2 s^{-3}]
ζ	Azimuthal angle [°]
η	Elevation angle (above horizontal) [°]
θ	Mean wind angle [°]
λ	Wavelength of electromagnetic radiation [m]
Λ_i	Integral length scale of turbulence in dimension i [m]
μ_{LN}	Size parameter used in the log-normal diameter distribution function [m]
ξ_i	Liquid mass per unit frontal area of a 'curtain' of airborne droplets, at height i [L m^{-2}]
ρ_a	Air density [kg m^{-3}]
ρ_d	Droplet density [kg m^{-3}]
σ_d	Standard deviation of Gaussian kernel used to calculate local mean diameter [°]
σ_i	RMS velocity fluctuations in direction i [m s^{-1}]
σ_{LN}	Distribution parameter used in the log-normal diameter distribution function [m]
σ_{q^*}	Standard deviation of simulated dimensionless water deposition flux
σ_s	Standard deviation of Gaussian kernel used to calculate local mean speed [°]
σ_{ULLN}	Distribution parameter used in the upper-limit log-normal diameter distribution function [m]
τ_i	Eulerian integral timescale of turbulence [s]
ϕ_i	Correction factor, used to weight data measured from droplet i
Φ	Dispersed-phase volume fraction in a multiphase flow
ω	Turbulence specific dissipation rate [s^{-1}]
a	Ratio of d_{max} to d_{ULLN}, used in the upper-limit log-normal diameter distribution function
B	Spectral radiance of a hot body [W sr^{-1} m^{-3}]
c	Speed of light in air [m s^{-1}]
C_μ	Constant from the k-ε model
C_0	Fixed 'cost', used in the droplet tracking procedure

C_d	Drag coefficient
C_{dia}	'Cost' associated with droplet diameters, used in the droplet tracking procedure
C_{fee}	'Joining fee', used in the droplet tracking procedure
C_{foc}	'Cost' associated with droplet image focus, used in the droplet tracking procedure
C_{loc}	'Cost' associated with droplet image locations, used in the droplet tracking procedure
C_p	Specific heat capacity of water [kJ kg^{-1} K^{-1}]
d	Droplet equivalent spherical diameter [m]
d_{10}	Arithmetic mean diameter [m]
d_{30}	Volume mean diameter [m]
d_{31}	Volume-length mean diameter [m]
d_{32}	Sauter mean diameter [m]
$\grave{d}_{32}$	Local Sauter mean diameter [m]
d_i	Equivalent spherical diameter of droplet i [m]
d_{max}	Maximum diameter, set in the upper-limit log-normal diameter distribution [m]
d_{RR}	Size parameter used in Rosin Rammler diameter distribution function [m]
d_{ULLN}	Size parameter used in upper-limit log-normal diameter distribution function [m]
d_{v50}	Volume median diameter [m]
f_a	Factor between 0 and 1, used to estimate droplet initial velocities
f_q	Factor used to convert flame spectral radiance into a heat flux that would be incident on a building [sr]
f_{FR}	Video framerate [s^{-1}]
f_{LN}	Log-normal diameter distribution function [m^{-1}]
f_{ULLN}	Upper-limit log-normal diameter distribution function [m^{-1}]
F	Fixed joining fee, used in the droplet tracking procedure
F_{RR}	Rosin Rammler diameter distribution function
h	Planck constant
h_e	Latent heat of vaporisation of water [kJ kg^{-1}]
H	Building height [m]
I_i	Turbulence intensity in direction i
k	Turbulence kinetic energy [m^2 s^{-2}]
k_B	Boltzmann constant [J K^{-1}]
k_{ref}	Turbulence kinetic energy at the reference height, z_{ref} [m^2 s^{-2}]
m_d	Droplet mass [kg]
$\dot{m}_e$	Mass of vaporising water per unit time and wall width, between two heights [kg s^{-1} m^{-1}]
$\dot{m}_i$	Liquid film mass flow rate per unit wall width, at height i [kg s^{-1} m^{-1}]
$\dot{m}_s$	Water deposition rate per unit wall width, between two heights [kg s^{-1} m^{-1}]
n	Number of droplets measured in a spray
n_i	Number of video frames spanned by the track associated with droplet image i
n_d	Number of distinct droplet size classes simulated

n_{di}	Number of video frames in which droplet i was within the field of view
n_{min}	Minimum number of video frames with which tracks would be included in the measurement
n_p	Number of video frames separating the start of each sample
n_f	Number of frames included in each sample
n_s	Number of spatially unique droplet source points used to represent each sprinkler
Oh	Ohnesorge number
p_i	Measured properties of droplet image i
P_i	Probability that a droplet i would appear in enough video frames to be measured
P_t	Time-series length [s]
$q"$	Radiant heat flux [kW m^{-2}]
q^*	Dimensionless water deposition flux
q_*	Dimensionless spectral radiative flux transmitted through a spray
$q"_{abs}$	Radiant heat flux absorbed by spray 'curtain' [kW m^{-2}]
$q"_{tr}$	Radiant heat flux transmitted through spray 'curtain' [kW m^{-2}]
q_w	Water deposition flux [L s^{-1} m^{-2}]
Q_w	Sprinkler flow rate [L s^{-1}]
r_m	Distance from sprinkler at which spray had been measured and characterised
r_s	Spray source radius set in CFD simulation
$R_{i,z}$	Temporal autocorrelation of velocity fluctuations in the i^{th} coordinate direction, at height z
Re_d	Droplet Reynolds number
RH	Relative humidity [%]
s	Time difference, used in the autocorrelation of a time-series [s]
S_{ch}	Volume-weighted mean droplet speed [m s^{-1}]
$\grave{S}_{ch}$	Local volume-weighted mean droplet speed [m s^{-1}]
St	Stokes' number
S_i	Speed of droplet i [m s^{-1}]
t_e	Integral time-scale of turbulence
T	Dry-bulb air temperature [K]
T_{dia}	Threshold parameter associated with droplet diameters, used in the droplet tracking procedure
T_f	Radiation source (e.g. flame) temperature [K]
T_{foc}	Threshold parameter associated with droplet image focus, used in the droplet tracking procedure
T_i	Temperature of liquid film at height i [K]
T_{loc}	Threshold parameter associated with droplet image locations, used in the droplet tracking procedure
T_s	Mean temperature of water deposited between two heights [K]
T_{WB}	Wet-bulb air temperature [K]
u	Wind velocity in the x direction [m s^{-1}]
u_a	Air velocity surrounding droplet, in the direction of the droplet motion [m s^{-1}]

u_e	Initial estimate of droplet velocity component in the x direction, used in the droplet tracking procedure [m s^{-1}]
u_d	Droplet velocity [m s^{-1}]
u_{d1}	Estimated droplet initial velocity [m s^{-1}]
u_{dm}	Measured droplet velocity [m s^{-1}]
u_i	Velocity component of droplet i in the x direction [m s^{-1}]
$u_{m,min}$	Minimum droplet velocity that was measured in the region of spray surrounding the droplet of interest [m s^{-1}]
u_{ref}	Mean streamwise wind velocity at the reference height, z_{ref} [m s^{-1}]
U	Wind velocity in the mean streamwise direction [m s^{-1}]
v	Wind velocity in the y direction [m s^{-1}]
v_e	Initial estimate of droplet velocity component in the y direction [m s^{-1}]
v_i	Velocity component of droplet i in the y direction [m s^{-1}]
V	Wind velocity in the mean lateral direction [m s^{-1}]
w	Wind velocity in the z direction [m s^{-1}]
w_*	Dimensionless spectrum of radiation absorbed by a spray
w_{FOV}	Width of the camera field of view on the focal plane [m]
W	Wind velocity in the vertical direction [m s^{-1}]
W_i	Factor for the correction of bias in data from axisymmetric sprays
W_{dia}	Weighting parameter associated with droplet diameter, used in the droplet tracking procedure
W_{foc}	Weighting parameter associated with droplet image focus, used in the droplet tracking procedure
W_{loc}	Weighting parameter associated with droplet location, used in the droplet tracking procedure
We	Weber number
x	Spatial Cartesian dimension
y	Spatial Cartesian dimension
z	Spatial Cartesian dimension
z_c	Canopy height, used to calculate canopy-flow velocity, k and ε profile functions
z_g	Atmospheric boundary layer depth
z_{ref}	Reference height, used in atmospheric boundary layer and canopy-flow profile functions

Glossary

ABL	Atmospheric boundary layer
CFD	Computational fluid dynamics
CRW	Continuous random walk
CSIRO	Commonwealth Scientific and Industrial Research Organisation
DES	Detached-eddy simulation
DF	Drought factor
DRW	Discrete random walk
FFDI	Forest fire danger index
LES	Large-eddy simulation
PSF	Point-spread function
RANS	Reynolds-averaged Navier Stokes
RMS	Root mean square
RNG	Renormalisation group
RSM	Reynolds stress model
WEEDS	Wind-enabled ember dousing system

Chapter 1

Introduction

This thesis documents a research project that was focused on sprinkler systems for the protection of buildings from wildfire. The work covered a wide range of topics and activities including in-depth investigations into high-speed videography, image analysis, atmospheric fluid dynamics, multiphase flows and computational fluid dynamics. This chapter outlines the motivations for the research, the overarching methodology that was adopted and the contents of the subsequent chapters.

1.1 Background

The destruction of buildings by wildfires is an issue faced in many regions around the world (Blanchi *et al.* 2010; Caton *et al.* 2016; Mell *et al.* 2010; Viegas *et al.* 2003). The number of buildings destroyed each year is increasing and is predicted to continue to increase into the future (Bowman *et al.* 2017; Moritz *et al.* 2014; Syphard *et al.* 2013). This trend is generally attributed to changes in climate and continued urban expansion into forested areas, amongst other factors (Caton *et al.* 2016; IPCC 2014; Krawchuk *et al.* 2009; Lucas *et al.* 2007; Mell *et al.* 2010). Improved building resistance to wildfire has consistently been identified by researchers as an important aspect of the multi-faceted approach that is required to most effectively mitigate this increasing risk (Bradstock *et al.* 2012; Calkin *et al.* 2014; Cohen 1999, 2000; Mell *et al.* 2010; Moritz *et al.* 2014; Pellegrino, Bryner & Johnsson 2013; Penman *et al.* 2017).

Improvements to the wildfire resistance of a building not only help in averting the significant financial and sentimental losses inherent in the destruction of a home, but they can also provide a safer place of refuge for those who choose to 'stay and defend' their property or are unexpectedly unable to escape the fire (Blanchi *et al.* 2014; Cova *et al.* 2009; Haynes *et al.* 2010; Paveglio, Carroll & Jakes 2008). Measures that are taken to reduce the vulnerability of a building to wildfire can also benefit other nearby structures by eliminating the building as a fuel source (Blanchi & Leonard 2005; Butry & Donovan 2008; Calkin *et al.* 2014; Maranghides & Mell 2011; Mell *et al.* 2010).

Wildfires affect buildings through three primary mechanisms: i) ember attack (i.e. the transport of solid, burning materials from the fire to the building by wind), ii) radiant heat transfer, and iii) direct flame contact (Blanchi, Leonard & Leicester 2006; Caton *et al.* 2016; Leonard, Blanchi & Bowditch 2004; Ramsay, McArthur & Dowling 1987; Standards Australia 2009). In addition to these primary mechanisms, the strong winds that often coincide with wildfires can cause significant structural damage to buildings (Blanchi *et al.* 2011; Blanchi *et al.* 2010; McRae *et al.* 2013; Weber & Dold 2006). It should be noted that these mechanisms do not operate in isolation, for example wind or the uneven heating of glazing elements can create and/or damage openings in the building, through which embers can enter and ignite the building from within (Blanchi, Leonard & Leicester 2006).

Previous research has provided many insights into how buildings can be made less vulnerable to wildfire (Blanchi & Leonard 2005; Blanchi, Leonard & Leicester 2006; Bowditch *et al.* 2006; Caton *et al.* 2016; Cohen 1995, 2004; Hakes *et al.* 2016; Leonard, Blanchi & Bowditch 2004; Macindoe 2006; Macindoe & Leonard 2009; Macindoe, Mikaelsson & Leonard 2008; Manzello *et al.* 2005; Manzello *et al.* 2010; Manzello, Park & Cleary 2009; Manzello *et al.* 2011; Manzello & Suzuki 2012; Manzello, Suzuki & Hayashi 2012; Mell *et al.* 2010; Ramsay 1985; Ramsay, McArthur & Dowling 1996; Ramsay, McArthur & Dowling 1987; Watson *et al.* 2010). New buildings must comply with design standards in some regions, and many agencies provide guidance on how to improve the wildfire resistance of existing buildings. It is typically advised

that a ‘defensible space’ be established around the building (i.e. an area with significantly reduced fuel load). Measures that are often recommended to ‘harden’ the building itself include: covering of any vents or other gaps that would allow embers to enter; use of non-combustible building materials in exposed locations (especially at the base of walls, window sills and doors, where embers can accumulate); and protection of exposed glazing elements with non-combustible screens or shutters. The installation of sprinklers, on or around buildings, is also often cited as an effective method to mitigate the impacts of wildfire (CFS 2011; FEMA 2008; FPAA 2000; GTVFD 2007; Hakes *et al.* 2016; Potter & Leonard 2010). Such systems are predominantly presented as an optional measure, which can be taken in addition to, rather than as an alternative to, the ‘passive’ measures outlined above. The literature indicates that such spray systems have been used since at least 1984 (FPAA 2000) and there are currently many commercial entities offering wildfire sprinkler systems in Australia and the USA.

Very little research focussed on wildfire sprinkler systems appears to have been published, despite calls for scientific investigation into various aspects their operation (FPAA 2000; Potter & Leonard 2010). Consequently, technical guidance that is currently available to assist in the design of such systems, e.g. Standards Australia (2012), CFS (2011), FEMA (2008) and GTVFD (2007), is largely based on a combination of anecdotal evidence (FPAA 2000; Johnson, Downing & Nelson 2008; Mitchell 2006), knowledge from other, related fields (e.g. indoor fire sprinklers) and engineering judgement. Much of the guidance that is given is arguably inconsistent, and does not provide the detailed information required to tailor a wildfire sprinkler system to the needs of a specific building, or to accurately predict the capabilities of a given system.

1.1 Aims and Objectives

The primary aim of the present work was to progress towards a more complete and rigorous understanding of wildfire sprinkler system operation in windy conditions. The author also aimed to identify and communicate gaps in the understanding of such systems to the wider scientific community, since it was not an active field of research at the time of writing.

Key research questions addressed in the work include the following.

- What gaps exist in the scientific understanding of wildfire sprinkler systems?
- What are the characteristics of sprays currently recommended for use in wildfire sprinklers?
- Can simulation techniques, such as computational fluid dynamics (CFD) accurately simulate wildfire sprinkler system operation in windy conditions?
- How do typical wildfire sprinkler systems compare, in terms of the dispersion of water in windy conditions?

To address these questions, a series of objectives were set for the research.

1. Conduct an extensive literature review of:
    a. previous scientific investigations into wildfire sprinkler systems; and
    b. current technical guidance on the design of wildfire sprinkler systems.
2. Measure and characterise the sprays generated by several sprinklers that are used in wildfire sprinkler systems. This objective involved:
    a. a literature review into relevant experimental methods;
    b. measurement of six sprays; and
    c. analysis and presentation of detailed spray characteristics.
3. Conduct experiments to provide validation data for simulations of sprinkler operation and water deposition around buildings, in windy conditions.
4. Compare the performance of various CFD methods in simulations of wildfire sprinkler systems, using validation data from item 4, above. This objective involved:
    a. a literature review into CFD techniques relevant to the simulation of wildfire sprinkler systems; and
    b. a simulation study, comparing the performance of various CFD methods using the commercial code ANSYS Fluent 14.5.
5. Quantify the effects of wind and evaporation on various wildfire sprinkler systems that are described in the literature.

1.2 Thesis Structure

This thesis is comprised of seven chapters. Chapters 2–6 each outline a distinct body of work, involving one of the five objectives described above (see Figure 1.1). Each chapter draws on findings from the previous chapters.

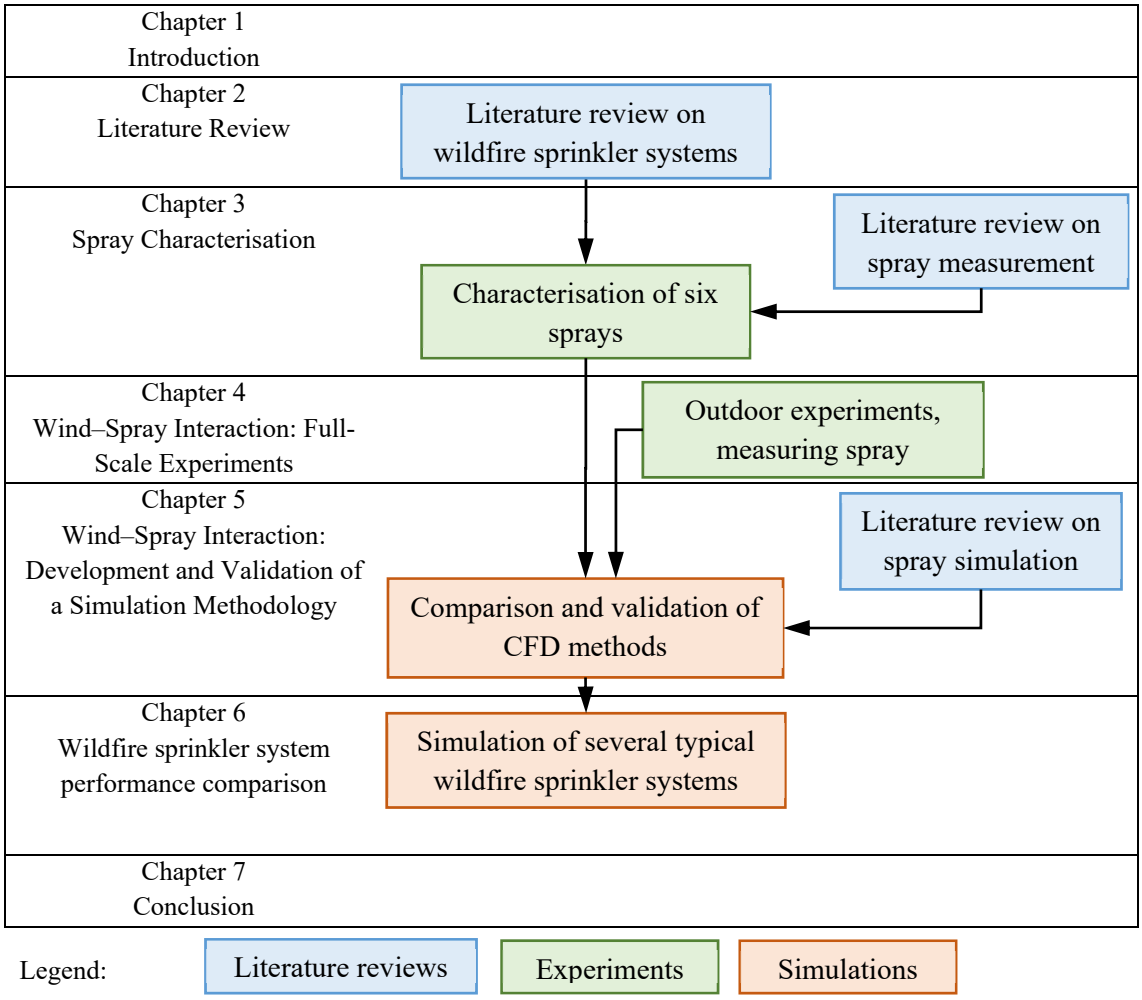

FIGURE 1.1: Schematic outline of the thesis structure.

1.3 List of Publications Associated with the Thesis

Green, A., Cooper, P., Penman, T. & Bradstock, R. (2016). Characterisation of water sprays using high-speed videography. Proceedings of the 20th Australasian Fluid Mechanics Conference (pp. 1-4). Melbourne, Australia: Australasian Fluid Mechanics Society.

Chapter 2

Literature Review

As explained in Chapter 1, measures to improve the resistance of buildings to wildfire are needed, to protect people and property from the significant and growing hazard posed by wildfires. This chapter summarises a review of literature related to wildfire sprinkler systems. Such sprinklers are often suggested as an additional protective measure to owners of wildfire-prone buildings, however very few scientific investigations appear to have been conducted into their performance. For background on the hazard posed by wildfires, the mechanisms by which they affect buildings, and typical measures taken to mitigate these effects, the reader is directed to section 1.1 of this thesis. Wildfire sprinkler systems reported in the literature have been described in sections 2.1–2.3, and in sections 2.4–2.6 a brief analysis has been presented of existing evidence related to three aspects of their operation: 1) the influence of sprays in mitigating the effects of wildfire; 2) the dispersion of sprayed droplets to the exterior of buildings and/or surrounding surfaces; and 3) the supply of water which is to be sprayed.

2.1 Wildfire Sprinkler Types

At the time of writing, only one peer-reviewed publication appeared to exist which focused specifically on wildfire sprinkler systems (Mitchell 2006). However, two technical reports had been published which described the 'state-of-the-art' in wildfire sprinkler system design (FPAA

2000; Potter & Leonard 2010), and several sources of technical guidance for system designers had also described the type of sprinklers that should be used and how they should be configured around buildings (CFS 2011; FEMA 2008; GTVFD 2007; Standards Australia 2012).

Sprinklers primarily designed for garden irrigation have often been recommended, although purpose-built wildfire sprinklers were commercially available at the time of writing. 'Butterfly' and 'Impact' irrigation sprinklers (see Figure 2.1) have been recommended in several design guides (CFS 2011; FPAA 2000; GTVFD 2007; Johnson, Downing & Nelson 2008). However, such sprinklers do not meet the requirements outlined in Australian Standard AS 5414-2012, which specifies that wildfire sprinklers should contain no moving parts, to reduce the probability of malfunction (Standards Australia 2012). Mitchell (2006) proposed a design that featured hollow-cone sprinklers, and 'small-bore misting nozzles' were documented in several of the sprinkler systems surveyed by the Fire Protection Association Australia (FPAA 2000). However, such sprinklers do not comply with recommendations made by others, that wildfire sprinklers should produce large droplets (CFS 2011; FEMA 2008; GTVFD 2007; Potter & Leonard 2010).

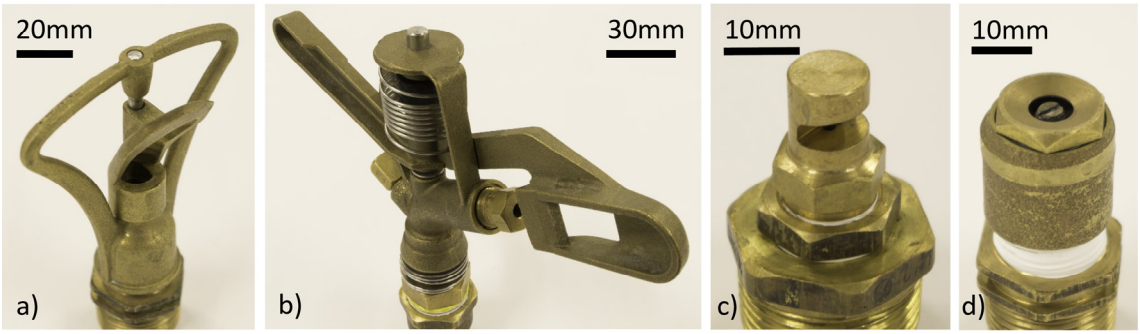

FIGURE 2.1: Examples of sprinklers used to protect buildings from wildfires: a) a 'butterfly' sprinkler; b) an 'impact' sprinkler; c) a small-bore misting nozzle designed to produce a 180° 'flat-fan' spray; and d) a 'hollow cone' sprinkler similar to those recommended by Mitchell (2006).

2.2 Wildfire Sprinkler System Configurations

The configuration of sprinklers around the building to be protected has varied widely among systems reported in the literature. Sprinklers have been located on building roofs, under eaves, near vulnerable building elements (e.g. doors and windows), and in areas surrounding buildings (see Figure 2.2 and Table 2.1). It is typically recommended that the spacing of sprinklers be such

that there is some overlap of their sprays, to ensure complete coverage of key surfaces (FPAA 2000; Standards Australia 2012), and a degree of 'overspray' is also often prescribed (CFS 2011; Potter & Leonard 2010; Standards Australia 2012), which is a recommendation that the sprays impinge on the ground surrounding a building as well as on the building itself.

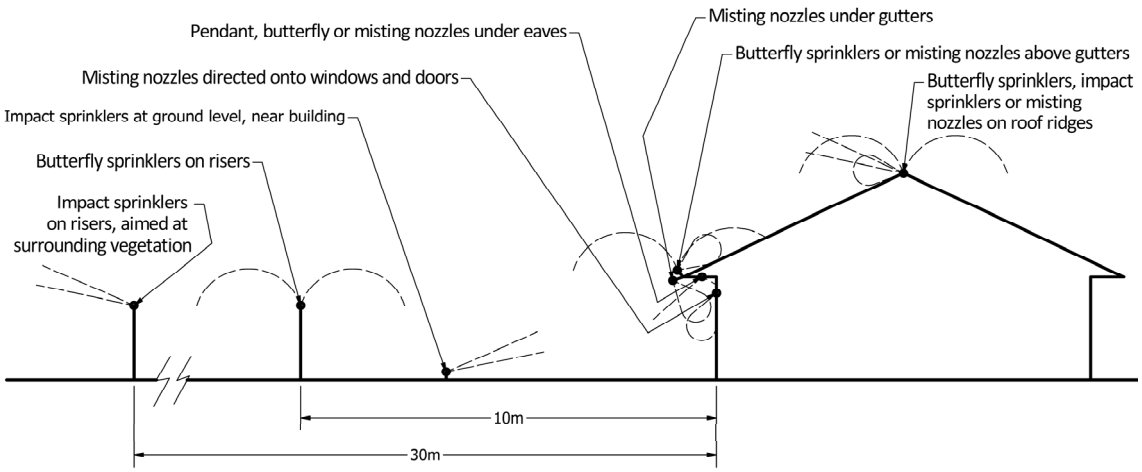

FIGURE 2.2: A selection of the various sprinkler configurations that have been recommended for wildfire sprinkler systems, shown on the cross-section of a building.

The most comprehensive account of existing wildfire sprinkler system designs appears to be that of the Fire Protection Association Australia (FPAA 2000). Thirteen systems were evaluated and six distinct types were identified, as described below.

1. Small-bore misting nozzles positioned to spray over vulnerable building features, e.g. roof penetrations, gutters, door and window openings, etc.
2. Misting nozzles as in 1, but with the addition of sprinklers designed for higher volume flow-rates, such as 'butterfly' sprinklers, located around the perimeter of the roof.
3. Misting nozzles and high-flow sprinklers as in 2, except the high-flow sprinklers are located on metal upstands, in a ring surrounding the building at a distance of 4–5 m, rather than on the roof.
4. Misting nozzles and high-flow sprinklers as in 3, except the ring of high-flow sprinklers is located approximately 10m from the building and an additional ring of 'impact' sprinklers surrounds the building at a distance of approximately 30 m.

5. An automatically activated indoor sprinkler system, identical to those conventionally used to defend against structural fires except that the sprinklers are also installed in outdoor areas such as verandas and awnings, and 'upright' sprinklers are installed on the roof ridges.
6. Garden sprinklers of the 'butterfly' or 'impact' type installed near the building, to serve the dual purpose of garden watering and wetting the building walls during wildfires.

In addition to the documentation of system 5, above, several sources of technical guidance have also promoted the use of conventional indoor fire sprinklers to aid in the protection of buildings from wildfire (FEMA 2008; FPAA 2000; Potter & Leonard 2010; Standards Australia 2012).

TABLE 2.1: Summary of documented wildfire sprinkler systems. The symbols 'X' and 'O' denote properties of the system that are presented as necessary and optional, respectively. References: 1 – FPAA (2000); 2 – Standards Australia (2012); 3 – Mitchell (2006); 4 – GTVFD (2007); 5 – Johnson et al. (2008); 6 – CFS (2011); 7 – FEMA (2008).

Sprinkler Type	**Sprinkler Location**	**Systems Recommended in Technical Guidance**									**Systems from a Survey conducted in Australia, 2000**										
Misting nozzles	On roof	X	X											X	X	X	X	X			X
Misting nozzles	Directed at windows and doors	X	X		O*									X	X	X	X	X			
Misting nozzles	Directed inwards from gutters																				
Butterfly sprinklers	Roof ridges																				
Butterfly sprinklers	Near gutters	O						O			X			X							
Butterfly sprinklers	Under eaves				O*																
Butterfly sprinklers	On risers, 4–5 m from building								O			O				X					
Butterfly sprinklers	On risers, 10 m from building		X	O													X	X			
Butterfly sprinklers	At property perimeter																			X	
Impact sprinklers	On roof ridges																				
Impact sprinklers	On risers, 30 m from building		O	O					O				X					X			
Impact sprinklers	'At ground level'						X	X				O									X
Hollow-cone sprinklers	Directed outwards from gutters					X															
'Modified' upright sprinklers	Roof ridges			X															X		
Upright or pendant sprinklers	Near gutters				O*			O													
Pendant sprinklers	Under eaves				O*																
'Rotating' sprinklers	Near gutters and barge boards				O*																
'Large-droplet' nozzles	Directed at windows and doors				O*																
Indoor sprinkler system	Indoors and extended to verandahs, etc.			X	O					X									X		
	Reference:	1	1	1	2	3	4	5	6	6	7	1	1	1	1	1	1	1	1	1	1

* It is not clear exactly what type of sprinkler is recommended.

All of the wildfire sprinkler systems that were reviewed were designed to spray water. A number of publications suggested that the water supplied to sprinklers can be dosed with foam or gel-forming agents, to increase its 'dwell time' on surfaces (FEMA 2008; FPAA 2000; Standards Australia 2012). However, no further guidance was provided on the selection of such products, or their implementation in a sprinkler system.

2.3 Operational Timing of Sprinkler Systems During Wildfire Events

The commencement and duration of wildfire sprinkler operation during wildfire events should be chosen to provide sufficient protection to prevent building ignition, yet minimise water usage. The passage of the main front of a wildfire past a building can occur in a relatively short period of time; fine fuels (< 6 mm) can burn for as little as 30 or 40 s (Butler *et al.* 2004; Wotton *et al.* 2012), while larger wildland fuels typically undergo flaming combustion for several minutes (Albini *et al.* 1995; CFS 2011). However, ember attack and spot-fires can endanger buildings for much longer periods of time prior-to and after the passage of a wildfire front (Blanchi, Leonard & Maughan 2004; Leonard, Blanchi & Bowditch 2004; Mell *et al.* 2010; Ramsay, McArthur & Dowling 1987).

The minimum total operational duration of various wildfire sprinkler systems has been suggested to be 30 min (Standards Australia 2012), 60 min (FPAA 2000), 90 min (FPAA 2000), 2 h (CFS 2011), 3 h (Mitchell 2006), 6 h (Potter & Leonard 2010) and 18 h (GTVFD 2007). Recommendations have been made that systems operate for at least 10 min (Potter & Leonard 2010), or 15 min (FPAA 2000), prior to the passage of wildfire, to saturate potential fuels. A fact-sheet distributed by the South Australian Country Fire Service (CFS 2011) recommends that sprinklers be operated overnight prior to wildfires, if possible. Suggestions have also been made that sprinkler systems should be operated at full capacity for a short period (typically 0.5–2 h) and a lower level of protection should be provided outside of this period, by intermittent sprinkler operation (Potter & Leonard 2010; Standards Australia 2012), operation of a reduced number of sprinklers (Standards Australia 2012) or manual intervention by people defending the building

(FPAA 2000); in order for, it has been suggested, limited water resources to be used more effectively.

It is likely that there will be an element of uncertainty in the potential temporal profiles of radiant heat, ember attack and flame contact incident on buildings during wildfires. Moreover, factors that vary between different buildings, such as the magnitude of the local wildfire hazard, building construction details, and the availability of water, are likely to cause variation in the 'ideal' timing and duration of wildfire sprinkler operation. Progress towards a situation where the effectiveness of wildfire sprinklers can be predicted would allow such factors to be taken into account in the design of systems.

2.4 System Influence

Conclusive evidence of the effectiveness of wildfire sprinkler systems does not appear to exist, but several accounts do indicate that sprinkler systems may have prevented the destruction of buildings during previous wildfires. Johnson, Downing and Nelson (2008) documented building losses during the 2007 Ham Lake Fire in Minnesota, USA, where 56 threatened residential buildings had sprinkler systems installed. Nine of the systems failed to operate, but only 2% of buildings with functional systems were destroyed, as compared to 67% of buildings without sprinkler protection. Mitchell (2006) conducted a survey of a single building fitted with a sprinkler system, after it had survived the 2003 Cedar Fire in Southern California, USA. Conclusions could not be drawn as to the effects of the sprinkler system in that case, but the building did appear to have withstood some ember attack. The FPAA report (FPAA 2000) also cites anecdotal evidence that wildfire sprinkler systems can be effective.

The mechanisms by which wildfire sprinkler systems mitigate the effects of ember attack, radiant heat and direct flame contact have also not been clearly established. Some guidelines are accompanied by caveats, specifying that the systems discussed are primarily designed to address ember attack (Mitchell 2006; Potter & Leonard 2010) or ember attack with the addition of a limited level of radiant heat flux (CFS 2011; FPAA 2000; Standards Australia 2012). However,

there does not appear to be a consensus on how such protection is achieved. Seven mechanisms have been suggested in the literature that was reviewed, as follows.

1. The intensity of ember attack and radiant heat incident on the building is reduced by wetting surrounding fuels, e.g. vegetation (GTVFD 2007; Mitchell 2006; Potter & Leonard 2010; Standards Australia 2012).
2. The cooling of exposed combustible surfaces on the building (FPAA 2000; Potter & Leonard 2010; Standards Australia 2012) or exposed glazing (Potter & Leonard 2010; Standards Australia 2012).
3. Radiant heat is attenuated by airborne droplets (CFS 2011; FPAA 2000).
4. Embers are prevented from entering the building by flooding of any gaps or cracks in the building envelope (Potter & Leonard 2010).
5. Airborne embers are extinguished when they collide with water droplets (Mitchell 2006).
6. A 'humid bubble' of air is established around the building (FPAA 2000; Mitchell 2006).
7. Sprays inside the building extinguish fires arising therein, e.g. due to ember ingress or radiant heat transmission through windows (FEMA 2008; FPAA 2000; Standards Australia 2012).

Such claims were typically not accompanied by any evidence/justification. However, some insight into the validity of each claim was obtained by reviewing literature from related fields, and this has been briefly summarised in the following sections.

2.4.1 Extinguishment of Spot-Fires and Accumulated Embers

The action of water as a fire suppressant is primarily through cooling of burning fuel, cooling of gases in the flame zone and volumetric displacement of oxygen by water vapour (Grant, Brenton & Drysdale 2000). Solid, non-metallic fuels have a tendency to 'burn back' (i.e. reignite after extinguishment) if not thoroughly cooled, so the cooling effects of water are much more important than those due to the displacement of oxygen in the extinguishment of such fuels. Therefore, it is likely that water sprays are able to extinguish spot-fires and accumulated embers near buildings,

by direct cooling of the fuels. However, it is not clear whether the water vapour produced by wildfire sprinklers would displace enough oxygen to influence such fires significantly, since the strong winds that often occur during wildfires are likely to advect water vapour away from buildings.

2.4.2 Evaporative Cooling of Unignited Fuels and Glazing

Water can also effectively prevent fire spread onto unburnt fuels, by acting as a 'heat sink' (Grant, Brenton & Drysdale 2000). Heat that is radiated or convected to wet surfaces from nearby fire is absorbed as the water rises in temperature, and removed in substantial quantities as it vaporises. Experimental studies, conducted by Glenn *et al.* (2012) and Urbas (2013), have investigated the protection of a number of building materials, garden plants and mulch from wildfire using water, foams and gels, with and without retardants. However, they focused on a scenario where the materials are pre-wetted only (i.e. they did not investigate the effectiveness of continuous or intermittent wetting). Results from these studies indicated that little benefit was offered by water or foam in this pre-wetting scenario, but some items coated with gel could withstand double the heat flux as compared to when untreated. The addition of starch to foams and gels was found to reduce the tendency of these coatings to 'slump' after application, and acted as a retardant by forming an insulating layer of char. Research on the continuous or intermittent application of water, foams and gels, to protect building elements from wildfire attack mechanisms, could not be found in open literature.

The absorption and removal of heat by water can also prevent glass from breaking when heated by fire. Several experimental studies have investigated the protection of glass windows by water sprays, in the context of structural fires (Beason 1986; Kim & Lougheed 1990; Kim, Taber & Lougheed 1998; Richardson & Oleszkiewicz 1987). Sprinklers have typically been shown to prevent tempered glass from breaking, when exposed to radiant heat flux up to at least 25 kW m^{-2}. Plate and laminated glazing tended to break prior to the activation of automatic sprinklers in experiments, so it is not clear whether a continuous spray, activated prior to exposure, could protect such windows. The risk of glass breakage due to thermal shock, when water is applied

after the glass has already risen sufficiently in temperature or when water is not applied to the entire glass surface, has also been identified. This evidence suggests that, when applied appropriately, the cooling effect of water sprays could prevent windows from breaking during wildfires.

The effectiveness of external water spray systems on fire trucks were tested in Australia between April 2002 and November 2003, by exposing full-scale truck cabins to simulated wildfire conditions produced using gas burners (Bowditch, Leonard & O'Brien 2004; Nichols *et al.* 2005). A rigorous matching of simulated radiant heat flux and flame temperature to measured values from wildfires is reported, but it does not appear as though strong winds were included in the simulated wildfire conditions. Detailed results from these experiments do not appear to be publicly available. However, Nichols *et al.* (2005) reported that 'well-designed spray systems' provided 'useful gains in firefighter safety at low to moderate fire burnover scenarios', and that 'an efficient spray system will consistently reduce glass surface heat load and the inside cabin temperature'. The importance of complete, even water coverage on windows was also highlighted in this work. Although quantitative evidence was not published, this previous research does provide anecdotal evidence that spray systems can cool glass surfaces significantly, even within the flame zone of a wildfire.

2.4.3 Attenuation of Radiant Heat

The capability of airborne water droplets to attenuate radiant heat has been well documented. Numerous studies have investigated this phenomenon in the context of indoor fire sprinklers (Boulet, Collin & Parent 2006; Chueng 2009; Coppalle, Nedelka & Bauer 1993; Dembele, Wen & Sacadura 2001; Murrell, Crowhurst & Rock 1995; Usui & Matsuyama 2014), and the use of fine, wide-angle sprays is an established method to reduce the radiant heat flux to firefighters (Rasbash 1962; Reischl 1979).

For a given mass of water, maximum attenuation is achieved by droplets with diameters approximately equal to the radiant heat wavelength—typically in the order of 1 μm (Coppalle,

Nedelka & Bauer 1993; Dembele, Wen & Sacadura 2001; Murrell, Crowhurst & Rock 1995). The portion of radiant heat attenuated by sprays also depends on the spray 'density' (i.e. liquid volume fraction) and depth, which dictate the total mass of airborne droplets per unit of spray frontal-area. Attenuation of 10%, 40% and 92% of incident radiation has been modelled for monodisperse sprays of 1 μm droplets, containing 0.5, 5 and 50 grams of liquid water per square-metre of spray frontal-area, respectively (Coppalle, Nedelka & Bauer 1993). (However, these should be considered as approximate values since the effects of droplet temperature and evaporation were not included in the calculations and several assumptions were made in regard to the emitting characteristics of the fire.) Reductions of this magnitude in the radiant heat flux incident on a building could substantially reduce the risk of ignition during a wildfire. However, sprays of such small (1 μm) droplets are likely to be unsuitable for the wildfire context, since the droplets would be very prone to being blown off-course by wind, thereby disrupting attempts to establish a 'curtain' of droplets between the fire and the building. Larger droplets can also attenuate substantial radiant heat, when distributed in sufficient quantities, but it is unclear whether such quantities would be practicable for wildfire sprinkler systems, given the limited water resources that are typically available. Additional research is required to determine whether radiant heat attenuation could be an effective mechanism of influence for wildfire sprinkler systems, given the various practical considerations relevant to such systems.

2.4.4 Extinguishment of Airborne Embers

It is likely that some droplets projected by wildfire sprinklers would collide with airborne embers during a wildfire. However, the nature of embers produced by wildfires, including their size, shape, velocity, composition and flux ahead of the fire front, are still poorly understood (Caton *et al.* 2016; Manzello 2014). Without such knowledge it is difficult to accurately predict the fraction of embers that could be intercepted by droplets in a given spray. Furthermore, the collision of individual embers with airborne water droplets appears to have not been investigated previously. Observations of related phenomena, such as droplet impact on heated plates (Liang & Mudawar 2017) and collision with other droplets (Frohn & Roth 2000; Orme 1997), indicate that this is

likely to be a complex interaction. Factors such as droplet size and velocity are likely to influence the processes that are involved (which could include, for example, film boiling, droplet bouncing or splashing), which will in-turn influence the propensity for ember extinguishment. Investigations into the nature of ember showers, and the collision of water droplets with these embers, would allow an assessment of whether this is a mechanism that significantly influences the effectiveness of wildfire sprinklers.

2.4.5 Indoor Sprinklers

Indoor sprinklers or hybrid indoor/outdoor sprinkler systems may use limited water resources to greater effect than purely outdoor systems, since the enclosed environment offered by the building would allow the use of the type of heat-sensitive activation mechanisms that are already in common use in indoor sprinkler systems (e.g. glass bulbs that break when the liquid inside exceeds a known temperature), thereby allowing the deployment of water only when and where it is required. Indoor sprinkler systems would also be functional in the event of a conventional structural fire, which contributes to their appeal in terms of risk reduction for a given financial investment.

Anecdotal evidence suggests that buildings often burn 'from the inside, out' during wildfires (Leonard & McArthur 1999); i.e. combustion of buildings in wildfires is often relatively minor until the interior ignites, at which point an indoor fire begins to predominate and eventually destroys the building. This behaviour could be attributed to the copious flammable materials present in common furnishings and the enclosed indoor space, which can allow hot combustion products to accumulate and reradiate heat to burning and unburnt fuels (Drysdale 2011). Such fires can arise in three ways: 1) an ember enters the building through an opening (e.g. an unprotected vent or broken window); 2) sufficient radiant heat is transmitted through windows to ignite items within the building; or 3) combustion of external building surfaces forms openings in the building, allowing fire to spread inside. Indoor sprinkler systems could suppress indoor fires in all three scenarios. However, in the third case, it is not clear whether the combustion of external building surfaces would continue, or whether the damage already incurred by the

building would be acceptable. Also, in all three cases, other protective measures may be preferable (e.g. covering vents and windows with screens, or installing external sprinklers), since they would not cause water damage inside the building. Issues related to the availability of water supplies and resistance of pipework, etc. to bushfire attack are also relevant to indoor systems, and have been discussed in more detail in Section 2.6.

New research is required to understand the effectiveness of indoor sprinklers at preventing damage to buildings during wildfire, in scenarios where fire 'burns through' the building envelope. With such knowledge, and the ability to quantify the effectiveness of external wildfire sprinkler systems, it would be possible to compare the performance of internal and external sprinklers.

2.5 Water Dispersion

Prediction of the performance of a sprinkler system in wildfire conditions is complicated by processes such as wind drift (i.e. the influence of wind on droplet trajectories), evaporation, splashing, runoff and absorption, which all influence the dispersion of water from sprays. In particular, wind drift is seen to influence wildfire sprinkler performance significantly (FEMA 2008; FPAA 2000; Mitchell 2006; Potter & Leonard 2010; Standards Australia 2012).

2.5.1 Wind Drift

Provisions to address the effects of wind on wildfire sprinkler sprays have generally not been documented in great detail. A number of sources recommend the use of sprinklers that produce large droplets to reduce wind drift (CFS 2011; FEMA 2008; GTVFD 2007; Potter & Leonard 2010) or the use of a 'run-down' method whereby water is sprayed over a relatively short range, directly onto an inclined surface, and gravity is relied upon to spread the water (FPAA 2000). However, suitable droplet sizes have not been quantified and the importance of droplet initial velocity does not appear to have been investigated.

A method to test the susceptibility of sprays to wind drift is presented in AS 5414-2012, which sets a limit on the acceptable deflection of each spray when it is installed on a building façade and

subjected to a constant 45 km h^{-1} (12.5 m s^{-1}) cross-wind (Standards Australia 2012). This wind speed is consistent with those measured at weather stations near major wildfires in Australia, but does not represent a 'worst case' wind speed for these events; winds of up to 70 km h^{-1} (19.4 m s^{-1}) have been recorded near wildfires (Blanchi *et al.* 2010). Performance tests of this nature can serve as a relatively simple means to address wind drift in wildfire sprinkler systems without obtaining a comprehensive understanding of the fluid dynamics that is involved. However, they do not accurately replicate the hot, dry, turbulent air flows that occur during wildfires, nor do they take into account factors such as the wind angle of incidence with the building or the building shape. Investigation into the importance of such factors could lead to more evidence-based recommendations and regulations, which may also take into account potential design optimisation, e.g. trade-offs between the propensity for wind drift and the capacity for radiant heat attenuation when considering droplet size.

The 'wind-enabled ember dousing system' (WEEDS) proposed by Mitchell (2006) is notable in that it manages the effects of wind in a novel way, and that some analysis of these effects has been reported. Rather than spraying water in a way that limits wind drift, this system directs a fine spray outwards from below the gutters of the building and relies on wind to blow the droplets back onto the structure. Results from a set of simulations were reported, demonstrating an acceptable dispersion of water on the windward side of a building, at wind speeds between 20 km h^{-1} and 60 km h^{-1} (5.6–16.7 m s^{-1}). However, these simulations were greatly simplified models of reality in that the wind was modelled as a uniform, laminar flow which was unaffected by the building, i.e. the air was able to effectively pass through the structure. It was claimed that this was a conservative assumption, which is not necessarily true given the acceleration of airflow that typically occurs around buildings in wind. While the thermo-physical principles underlying the WEEDS concept may have merit, further research is required to determine the performance of such systems in real wind and to compare this performance with that of other wildfire sprinkler system designs.

2.5.2 Evaporation

In-flight droplet evaporation is another process which could conceivably have a significant influence on the performance of wildfire sprinklers. Molle *et al.* (2012) experimentally and analytically investigated the evaporation of airborne water droplets (with a mean diameter of approximately 3.65 mm) generated by an impact sprinkler. They found that up to 10% of the total liquid volume could evaporate in that case. A significantly larger portion could be expected to evaporate from some wildfire sprinkler sprays, given the hot, dry, windy conditions that typically occur during wildfires and the widespread use of sprinklers that produce much smaller droplets than the impact sprinkler studied by Molle *et al.* (2012). Additional evaporation could then be expected to occur after the water impinges on a surface, where it may adhere or be transported further, as it continues to be exposed to a vapour-pressure deficit in the surrounding air. Depending on the mechanism by which a given system is intended to function, evaporation may be desirable (e.g. for the cooling of exposed building elements), however, it could lead to the waste of a substantial portion of the water that is available. This aspect of wildfire sprinkler system operation does not appear to have been previously investigated.

2.5.3 Post-Impact Transport of Water

The effects of splashing, bouncing, runoff, absorption and re-entrainment on the dispersion of water by wildfire sprinklers have also seen very little attention in the literature. Foam or gel-forming agents could provide a means to minimise unwanted runoff. As mentioned above, there have been some experimental investigations into the effectiveness of such agents when applied for a single, short period prior to exposure to wildfire attack (Glenn *et al.* 2012; Urbas 2013), but no studies relating to their continuous or intermittent application via sprinklers appear to have been published. Other considerations relating to the transport of water post-impact, such as the critical velocities and impingement angles beyond which droplets bounce or splash from surfaces rather than adhering to them, have been investigated extensively from a fundamental scientific perspective (Yarin 2006). However, there does not appear to currently be any published analysis of how these processes relate to the performance of wildfire sprinklers.

2.6 Water Supply Systems

The reliability of wildfire sprinkler systems is dependent on the systems by which water is supplied to the sprinklers. The relative complexity of sprinkler systems, compared to other wildfire protection measures, such as the establishment of defensible space or installation of non-combustible, well-sealed façades, renders them more prone to malfunction during wildfire events. This additional risk constitutes one of the major challenges to the integration of sprinkler systems into building regulations and technical guidance for the protection of buildings from wildfire. However, the susceptibility of water supply systems to failure is also relatively well understood. Knowledge from other water-handling applications can be applied to systems for wildfire protection, and observations during and after wildfires have shed light on the specific requirements of systems that are to withstand the impact of wildfire. As a result, much of the technical guidance available on wildfire sprinkler systems focuses on this aspect of their design. In particular, AS 5414-2012 (Standards Australia 2012) and a report by Potter and Leonard (2010) lay out explicit requirements for water sources, pumps and pipework that should be used.

2.6.1 Water Supply Requirements

Anecdotal evidence indicates that there are often substantial reductions in the water pressure available from public utilities networks and interruptions to the supply of grid electricity to buildings during wildfires (CFS 2011; FPAA 2000; Potter & Leonard 2010). So it is important for wildfire sprinkler systems to have an independent source of water and a means to supply it at a suitable pressure that does not rely on electricity from the grid. Technical guidance on the minimum permissible storage capacity for typical Australian systems varies from 16,000 L (FPAA 2000) to 36,000 L (Standards Australia 2012). In practice, the required volume depends on the size and intended functions of the system, which could be more accurately prescribed were the influence of water sprays on wildfire attack mechanisms better understood. There is an opportunity to recycle a portion of the water sprayed by wildfire sprinklers in cases where a rainwater collection system is present, however the potential contamination of collected rainwater

should be considered if, for example, pool water, dam water, retardant, foam or gel is to be used (Potter & Leonard 2010).

It is important that the pressure drop along pipes be taken into account during the selection of pumps and design of pipework, to ensure that every sprinkler in the system is provided with water at sufficient pressure (Standards Australia 2012). This aspect of wildfire sprinkler system design can be addressed using established engineering practices from other water-handling applications.

2.6.2 System Resilience

Water supply systems for wildfire sprinklers must also be designed to withstand the high temperatures and smoke that accompany wildfires. The CSIRO has experimentally investigated the ability of water tanks to withstand radiant heat and direct flame contact (Blanchi *et al.* 2007). Results indicated that tanks should be of a metal or concrete construction; although, polyethylene tanks can withstand a low intensity of wildfire attack if certain mitigating steps are taken, and buried tanks may also be suitable (Blanchi *et al.* 2007; Potter & Leonard 2010).

Post-fire surveys have also provided many insights into the resilience of sprinkler system components to wildfire attack (Blanchi & Leonard 2005; Blanchi, Leonard & Leicester 2006; Potter & Leonard 2010). It has been observed that exposed plastic pipework can fail during a wildfire, even when water is flowing inside. It is therefore advisable that all pipework used in wildfire sprinkler systems be of a metal construction, or be buried or otherwise protected.

The failure of pumps and generators is another risk. Many sources of technical guidance advocate the use of gravity-fed systems when practicable, and otherwise advise that any pumps and generators be appropriately located and shielded to avoid failure during the passage of a wildfire (FPAA 2000; Potter & Leonard 2010; Standards Australia 2012). However, none of these sources provide specific information to guide the protection of pumps and generators. Future research on this issue would allow the provision of more prescriptive guidance to system designers.

2.6.3 System Activation

The activation of wildfire sprinklers is usually achieved manually, on-site. This can be problematic in cases where the building occupants evacuate during a wildfire or are absent for other reasons, and can lead to systems either not being used at all or prematurely exhausting their supply of water. To overcome these issues, a number of methods to achieve automatic or remote activation have been proposed. These include the use of external smoke or heat sensors (Potter & Leonard 2010), pagers, radios and mobile telephones (CFS 2011; FEMA 2008; Mitchell 2006; Potter & Leonard 2010; Standards Australia 2012). Little information has been published on the appropriate implementation of such technologies in wildfire sprinkler systems. While it is likely to be relatively simple to test and confirm the correct operation of systems for remote manual activation, the design of effective automatic activation systems would be difficult for the layperson (who is not able to predict the likely distribution of smoke, heat, etc. during a wildfire and is not aware of the appropriate timing of system activation). Detailed guidance would be required to enable non-specialist building owners to design such systems but there does not appear to be any published research on which to base such guidance currently. Remote and automatic activation systems would also add to the complexity of wildfire sprinkler systems, thereby increasing the risk of system failure during wildfire events (if, for example, the local phone networks are interrupted or a heat sensor fails to operate correctly). New research on the implementation of such technologies in the context of a wildfire would assist system designers in the consideration of these trade-offs.

2.7 Conclusion

A review of published research related to wildfire sprinkler systems has revealed only one peer-reviewed publication and three technical reports that focused specifically on such systems. It was discovered that many aspects of wildfire sprinkler systems are poorly understood (see Figure 2.3). As a result, the guidance that is currently available to system designers is not consistent or complete, and generally lacks detail.

No conclusive evidence was found indicating the effectiveness of wildfire sprinkler systems, although anecdotal evidence and documented building losses from one wildfire in Minnesota, USA (Johnson, Downing & Nelson 2008), do suggest that such systems can reduce the probability of building destruction significantly. The mechanisms by which the effects of wildfire are mitigated by sprinklers have also not been clearly established. Published research from related fields indicates that the cooling of burning and unburnt fuels, and the cooling of glass windows, are likely to be important mechanisms, and that it appears plausible that 'curtains' of airborne droplets could significantly reduce the radiant heat flux incident on buildings. Further investigation is required to determine whether oxygen displacement, or the interception of airborne embers by droplets, can play a significant role in the function of wildfire sprinkler systems.

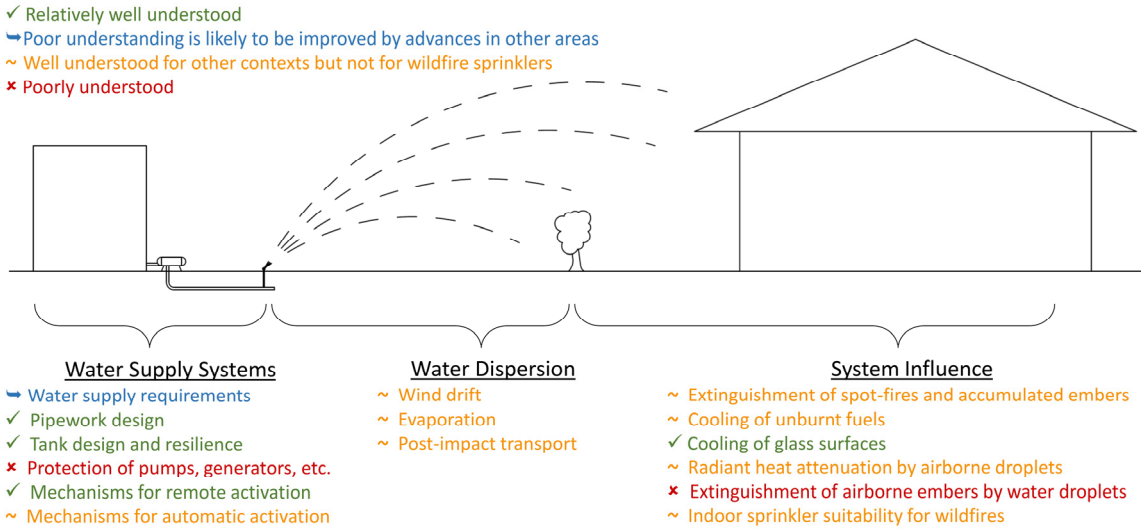

FIGURE 2.3: Schematic summary of the various aspects of wildfire sprinkler systems that have been analysed herein; colour-coding is used to indicate the current state of scientific knowledge relevant to each aspect.

It is likely that indoor sprinklers can assist in protecting buildings from wildfires, when ignited from within by embers or radiant heat, but their effectiveness in cases where the building exterior ignites and burns inwards does not appear to be known. The water damage caused by indoor sprinklers may be another important consideration in the comparison between indoor and outdoor sprinkler systems for wildfire protection. Technologies such as gels, foams and retardants have the potential to reduce the water resources required by wildfire sprinkler systems, and could also

improve their effectiveness. However, previous studies of such products have not included scenarios where they are applied continuously or intermittently, as they would be by a sprinkler system.

The dispersion of water from sprinklers in the hot, dry, windy conditions of a wildfire has also not been investigated in-depth. The effects of wind drift are likely to influence the system performance significantly, but they have not yet been quantified. The influence of evaporation, splashing, bouncing, runoff, etc. on wildfire sprinkler systems also appears to have not been investigated. New research on how different systems disperse water in the conditions of a wildfire would provide a much more rigorous evidence base than is currently available, for guidance on the selection and arrangement of sprinklers.

Requirements for the design of water supply systems for wildfire sprinklers are relatively well understood, since established practices from other water-handling applications can be applied, and a number of post-fire surveys and experimental campaigns have revealed which tanks and pipes can withstand the conditions of wildfires. However, methods for the protection of pumps and generators do not appear to have been clearly established. Mechanisms for automatic sprinkler activation (e.g. smoke or heat sensors) have been proposed. However, the added complexity of such mechanisms would increase the risk of system failure, and no evidence appears to exist to guide the effective implementation of these technologies to the wildfire context.

Wildfire sprinkler systems have the potential to prevent or extinguish building ignitions when the occupants are unable or unwilling to ‘stay and defend’ their property, or when they are absent for other reasons. The additional protection provided by these systems could also prevent the destruction of buildings that are serving as a place of refuge during wildfire, thereby saving human lives. An ability to quantify the effects of wildfire sprinkler systems would enable system designers to make better use of the available water and financial resources, and would allow residents to gain a more realistic understanding of the capabilities of such systems. Given the current forecasts for an increase in wildfire frequency and intensity, and the growing number of

buildings in wildfire-prone areas, wildfire sprinklers are certainly worthy of immediate attention from the scientific community.

Chapter 3

Spray Characterisation

This chapter describes an experimental investigation into the characteristics of six water sprays. Results from the study have been applied in Chapters 5 and 6, as inputs to CFD simulations. The focus of this chapter is to: 1) describe the combination of new and existing methods that were found to be useful in characterising the sprays; and 2) present detailed descriptions of each spray, which have been applied in subsequent chapters of this thesis, and could be useful in other, similar research.

3.1 Introduction and Literature Review

3.1.1 Spray Characterisation

Characterisation of liquid sprays is necessary for a wide range of engineering tasks. With appropriate information, interactions between sprays and their surroundings can be predicted, which can allow the design of highly effective spray systems. The details required for such work vary; from simple representations of droplet sizes, spray shape or droplet speeds, to highly detailed spatial and/or temporal distributions of droplet sizes and velocities.

Primary atomisation processes, by which sprays are formed from a bulk liquid, are extremely complex and still not completely understood (Faeth, Hsiang & Wu 1995; Tharakan *et al.* 2013). Instabilities in the liquid are formed primarily by aerodynamic interactions with the surrounding gas, surface tension forces and the liquid momentum (Ashgriz, Li & Sarchami 2011; Lin & Reitz

1998; Reitz & Bracco 1986). A dispersion of droplets is formed, which can interact effectively with the continuous gas phase through the transfer of momentum, energy and mass. Droplets formed by the primary breakup process can also become unstable and undergo secondary breakup further from the spray source (Hsiang & Faeth 1992; Jain *et al.* 2015). The balance of forces acting on the liquid throughout the atomisation process, and the eventual characteristics of the spray that is produced, are a product of the geometry of the atomisation device in use, the properties of the fluids involved and the operational conditions (e.g. liquid and gas temperatures and pressures).

For many practical applications, the complex mechanisms by which a spray is formed are of less interest than the eventual characteristics of the spray after formation. For example, simulations of sprays using computational fluid dynamics (CFD) often omit primary atomisation, and model the spray as a set of pre-formed discrete particles (e.g. Delele *et al.* (2007); Husted (2007); Meroney (2008); Montazeri, Blocken and Hensen (2015a); Nijdam *et al.* (2006); Sanjosé *et al.* (2011); Sidahmed, Taher and Brown (2005); Woo *et al.* (2008); Yoon, Kim and Hewson (2007)). Techniques do exist to explicitly simulate breakup processes using CFD (Gorokhovski & Herrmann 2008; Jiang *et al.* 2010; Tharakan *et al.* 2013), however, inclusion of the detailed physics of these processes, and resolution of the spatial scales involved, entails a significant computational cost and is often not required for the accurate simulation of the phenomena of interest.

Spray characteristics, suitable for input into CFD simulations and other similar applications, can either be predicted using analytical or empirical models, estimated using numerical simulations, or measured experimentally. Simulation of liquid atomisation, using techniques such as direct numerical simulation, can predict spray characteristics; although, as mentioned previously, the computational requirements of such simulations are extremely high. Analytical models for the breakup of various liquid sheets and jets have been implemented to reduce the computational cost of numerical simulations, and combined with stochastic and/or empirical models to form stand-alone models for the prediction of spray characteristics (Babinsky & Sojka 2002; Tharakan *et al.*

2013). However, such models and simulation techniques are of limited use outside of the cases for which they have been validated, due to the existence of distinct breakup regimes, and the myriad different fluids, operating conditions and device geometries in common use (Babinsky & Sojka 2002; Tharakan *et al.* 2013). Likewise, it has thus-far proven difficult to form empirical models that are applicable to atomisation devices, operational conditions or fluids other than those that have been measured. Therefore, physical measurements remain the most reliable source of detailed information on spray characteristics in many cases, even though they are generally limited in applicability to the specific cases that were measured. Bulk spray properties, such as the spray pattern and nozzle discharge coefficient, can be measured relatively easily and with a high degree of accuracy. More labour-intensive measurements can record the sizes and velocities of individual droplets, beyond the primary breakup region.

Previous experimental campaigns have focused on a limited selection of sprays, to cater for specific research needs. Experimental data has been published, in various degrees of detail, describing: twin-fluid and multi-hole fuel injectors, used in internal combustion engines (Batarseh, Roisman & Tropea 2010; Gupta & Agarwal 2016; Igual *et al.* 2015; Koo & Martin 1990; Mitroglou *et al.* 2006; Nouri & Whitelaw 2001; Pathania, Chakravarthy & Mehta 2016; Pitcher, Wigley & Saffman 1990); flat-fan, solid-cone and hollow-cone sprays, used for pesticide application (Dorr *et al.* 2013; Guler *et al.* 2007; Guler *et al.* 2012; Nuyttens *et al.* 2007; Sidahmed, Taher & Brown 2005; Vulgarakis Minov *et al.* 2016); impact sprinklers, used for irrigation (Bautista-Capetillo *et al.* 2014; Bautista-Capetillo *et al.* 2009; Molle *et al.* 2012; Salvador *et al.* 2009); misting nozzles, upright sprinklers and pendant sprinklers, designed for fire suppression (Everest & Atreya 2003; Ren, Baum & Marshall 2011; Santangelo 2010; Sheppard & Lueptow 2005; Widmann, Sheppard & Lueptow 2001; Yoon *et al.* 2011; You 1986; Zhou, D'Aniello & Yu 2014; Zhou, D'Aniello & Yu 2012); various aeroengine combustor sprays (Fdida *et al.* 2016; Jaegle *et al.* 2011; Sanjosé *et al.* 2011); a supersonic pressure swirl spray, for chemical processing (Marklund & Engstrom 2010); a containment spray for pressurised water reactors (Malet &

Parduba 2016); and a solid-cone spray, used for dust scrubbing (Kohnen *et al.* 2011). Nevertheless, a vast number of sprays have not been characterised with such rigor.

Wildfire sprinkler systems employ a wide variety of spray nozzles and sprinklers, as discussed in Chapter 2. Typically, sprinklers intended for garden irrigation, e.g. 'impact' or 'butterfly' sprinklers, are recommended for such systems (FPAA 2000; Johnson, Downing & Nelson 2008; Potter & Leonard 2010); although, traditional indoor fire sprinklers have also been recommended (FEMA 2008; FPAA 2000; Potter & Leonard 2010; Standards Australia 2012) and a number of purpose-built wildfire sprinklers are also currently available. Detailed measurements of droplet sizes and velocities produced by an impact sprinkler have been published by Bautista-Capetillo et al. (Bautista-Capetillo *et al.* 2014; Bautista-Capetillo *et al.* 2009; Salvador *et al.* 2009). However, these measurements were taken at ground level, to investigate the properties of droplets impacting on crops during irrigation, so they do not provide the droplet 'initial' conditions that could be used to predict the performance of the spray in other contexts. The flat-fan, hollow-cone and solid-cone pesticide sprays that have been characterised in detail do not match sprays mentioned specifically in documentation related to wildfire sprinkler systems. However, the flow rates associated with these sprays, as well as the operational conditions and working fluids used to create them, are similar to those relevant to such systems. Measured characteristics of indoor fire sprinkler sprays may be applied directly to indoor or outdoor spray systems designed for wildfires. Other spray types commonly used in wildfire sprinkler systems, such as 'butterfly' sprinklers, do not appear to have been characterised in detail.

3.1.2 Spray Measurement

A diverse range of experimental methods have been applied to spray characterisation (Bachalo 2000; Black, McQuay & Bonin 1996; Chigier 1991; Fansler & Parrish 2015; Tropea 2011). Optical techniques have been favoured in recent decades, for their ability to take non-intrusive, instantaneous measurements. Many optical techniques infer droplet sizes by comparing measured patterns of scattered laser light to those predicted by theory for spherical particles (e.g. phase Doppler interferometry); however, such models are not easily adapted to suit non-spherical

droplets (Frohn & Roth 2000; Tropea 2011). Image-based techniques (involving photography or videography) are typically better-suited to measure such droplets, and also provide some qualitative insight into the nature of sprays, in addition to the quantitative measurement.

True three-dimensional resolution is only achieved in image-based spray measurements that use holographic techniques, or multiple cameras to observe the spray from more than one angle (e.g. work by Meng *et al.* (2004) and Klinner and Willert (2012), respectively). Alternatively, a single camera can be used to take pseudo-planar measurements through a spray by illuminating a thin volume with a 'lateral' sheet of light (parallel to the plane of the camera sensor), or by applying a focal criterion during image post-processing to eliminate droplets that were outside of a known, narrow depth of field (DOF). A series of such measurements can resolve the spatial distribution of droplets, but not droplet extent or velocity components, in the dimension normal to the imaging plane. Droplet velocities parallel to the imaging plane can be estimated, or measured directly, using particle image velocimetry (PIV) or particle tracking velocimetry (PTV) techniques, respectively, while the method for droplet size estimation depends on how the spray is illuminated.

Determining the size of droplets from side-illuminated images is challenging. Fluorescent tracers have been widely adopted for this purpose; droplet volumes either being estimated directly from the intensity of laser-induced fluorescence (LIF), or from the ratio of LIF intensity to that of Mie-scattered light (Le Gal, Farrugia & Greenhalgh 1999). The latter approach, usually termed 'planar droplet sizing', minimises the influence of light attenuation by other droplets and non-uniformities in the intensity profile across the laser sheet, but is still sensitive to changes in dye concentration (due to evaporation for example), non-linear LIF response and multiple scattering (Fansler & Parrish 2015; Tropea 2011). By contrast, use of focal criteria to set a DOF, rather than the width of a lateral sheet of light, allows the use of incoherent back-illumination. Droplet sizes can be estimated relatively easily from the resulting images, based on the size of each droplet silhouette; although, some correction is required for size measurements from defocused images (Castanet *et al.* 2013; Fdida & Blaisot 2010; Lebrun, Touil & Özkul 1996; Malot & Blaisot 2000;

Ren *et al.* 1996). Back-lit spray imaging is also typically less expensive and labour-intensive than side-lit techniques, since it does not require a precisely aligned, coherent light-source.

Various focal criteria have been applied to back-lit spray images, removing defocused droplet images from analysis based on variables related to either: the contrast between the minimum and background grey-level intensities (Kim & Kim 1994; Koh, Kim & Lee 2001), or the grey-level gradient at the image boundary (Fantini, Tognotti & Tonazzini 1990; Hay, Liu & Hanratty 1998; Kashdan, Shrimpton & Whybrew 2003; Koh, Kim & Lee 2001; Lecuona *et al.* 2000; Legrand *et al.* 2014; Vulgarakis Minov *et al.* 2016). It has been well documented that fixed thresholds, applied to such variables, result in DOFs that decrease with decreasing droplet size (Fantini, Tognotti & Tonazzini 1990; Kashdan, Shrimpton & Whybrew 2003; Kim & Kim 1994; Koh, Kim & Lee 2001; Lecuona *et al.* 2000; Lee & Kim 2004). Previous studies have mitigated the resulting bias towards larger droplets by varying the focal criterion threshold as a function of droplet size (Fantini, Tognotti & Tonazzini 1990; Kim & Kim 1994; Lecuona *et al.* 2000; Vulgarakis Minov *et al.* 2016), or applying statistical corrections to the measurement data (Castanet *et al.* 2013; Kashdan, Shrimpton & Whybrew 2003). One notable approach, first proposed by Blaisot and Yon (2005) and developed further in subsequent publications (Blaisot 2012; Fdida & Blaisot 2010), avoids such bias altogether by imposing a threshold on the point-spread function (PSF) half-width—a measure of the image 'blurriness' that can be estimated using the image contrast and boundary gradient. In this way, one distinct volume can be defined, in which droplets of all sizes are measured.

The present study involved the detailed experimental characterisation of six sprays that are typical of those used in wildfire sprinkler systems. A back-lit high-speed videography technique was employed and the videos were analysed using a combination of established and new techniques. The sprays that were characterised exhibit a range of droplet shapes, sizes, velocities and spatiotemporal distributions, including periodic behaviour. Some relevant theoretical concepts are introduced in Section 3.2, the sprays that were investigated are described in Section 3.3, details of the experimental method are outlined in Section 3.4, and Section 3.5 contains detailed

descriptions of the spatiotemporal distributions of droplet sizes, speeds and volume flux within each spray.

3.2 Theoretical Concepts Relevant to Droplets and Sprays

Airborne droplets are acted on by drag, pressure, gravitational and surface tension forces. The combination of these forces and internal viscous forces can influence the droplet inertia, causing acceleration, deformation, and/or breakup of the droplet. Several dimensionless numbers have been developed to characterise these processes in a manner that is not dependent on fluid properties or scale. Some of the most relevant of these dimensionless parameters are introduced below. They have relevance to the sprays investigated in this chapter, and to the rest of this thesis, especially Chapter 5, in which different methods to model droplet trajectories are explored.

Three distinct drag regimes have been observed in liquid droplets (Ishii & Zuber 1979; Mashayek & Ashgriz 2011; Turton & Levenspiel 1986). The regime of a specific droplet can be determined using the droplet Reynolds number, given by:

$$Re_d = \frac{\rho_a u_{rel} d}{\mu_a} \tag{3.1}$$

where ρ_a and μ_a are the density and viscosity of the surrounding fluid (air, in the present case), respectively, u_{rel} is the relative velocity between the droplet and surrounding fluid, and d is the droplet diameter. When $Re_d \lesssim 1$, viscous forces dominate and Stokes' Law is a good approximation of the real drag forces. Under Stokes' regime the drag coefficient decreases linearly with increasing Re_d. In Newton's regime, delineated by $Re_d \gtrsim 10^3$, inertial forces dominate and the drag coefficient for spherical particles becomes virtually independent of Re_d. Between Stokes' and Newton's regimes, drag on spherical particles is influenced significantly by both viscous and inertial forces.

Deformation of liquid droplets can cause drag forces to increase substantially. Many experimental and numerical studies have investigated such effects (Guildenbecher, López-Rivera

& Sojka 2011; Hsiang & Faeth 1992, 1995; Jain *et al.* 2015; Mashayek & Ashgriz 2011; Stone 1994). Deformation and breakup of individual droplets can be correlated with the Weber number:

$$We = \frac{\rho_{\mathrm{a}} u_{rel}^2 d}{\sigma} \tag{3.2}$$

which represents the ratio of inertial forces (which destabilise the droplet) to surface tension forces (which stabilise the droplet), and the Ohnesorge number:

$$Oh = \frac{\mu_{\mathrm{d}}}{\sqrt{\rho_{\mathrm{d}} d \sigma}} \tag{3.3}$$

which represents the ratio of internal droplet viscous forces to surface tension forces. Here, d is the diameter of a sphere with equivalent volume to the deformed droplet, ρ_{d} and μ_{d} are the density and viscosity of the droplet liquid, respectively, and σ is the droplet surface tension coefficient. As We increases, droplets transition from having no significant deformation, to mild deformation, oscillatory deformation, and, eventually, breakup (Hsiang & Faeth 1992, 1995). The correlation between these phenomena and We is affected by viscous forces within the droplet when $Oh \gtrsim 0.1$. In the case of water droplets in air, when $d \gtrsim 1$ μm, significant droplet deformation arises when $We \gtrsim 1$ and droplet breakup occurs when $We \gtrsim 11 \pm 2$.

The Stokes' number, St, of a droplet represents the ratio of the droplet timescale to that of the continuous phase flow (Elghobashi 1994), e.g. the St most relevant to wildfire sprinklers could be the ratio of droplet timescales to the timescale of wind flow over the building. Lower Stokes' numbers indicate a tendency for droplets to follow continuous phase streamlines.

3.3 Sprays Investigated

Six sprays were investigated, each produced by sprinklers similar to those mentioned in technical guidance, or other literature, related to wildfire sprinkler systems (see Figure 3.1 and Table 3.1). Sprays produced by a 'butterfly' sprinkler (spray B), and the main and auxiliary nozzles of an 'impact' sprinkler (sprays IM and IA, respectively) represent two commonly available irrigation sprinklers that are often cited as being appropriate for use in wildfire sprinkler systems (CFS 2011; FPAA 2000; GTVFD 2007; Johnson, Downing & Nelson 2008). A hollow-cone spray

(spray HC) was investigated, which is very similar in design to those used in the 'wind-enabled ember dousing system' promoted by Mitchell (2006). Sprays produced by a flat-fan nozzle and deflector-plate sprinkler (sprays FF and DP, respectively) were also investigated. The flat-fan nozzle produced a fine, mist-like spray, similar to those recorded in a survey of wildfire sprinkler systems in a report by the Fire Protection Association Australia (FPAA 2000). The deflector-plate spray was of a similar design to 'upright' and 'pendant' sprinklers that are traditionally used in indoor fire-suppression systems, except that the deflector plate featured three concentric corrugations and did not have any 'tines' or 'prongs' at its edge. Fire-fighting is cited as a typical application for both spray FF and spray DP in literature from their respective manufacturers. Each of the six sprays was characterised at one supply pressure, within the range recommended by the device manufacturers (see Table 3.1). The devices were new at the time of measurement.

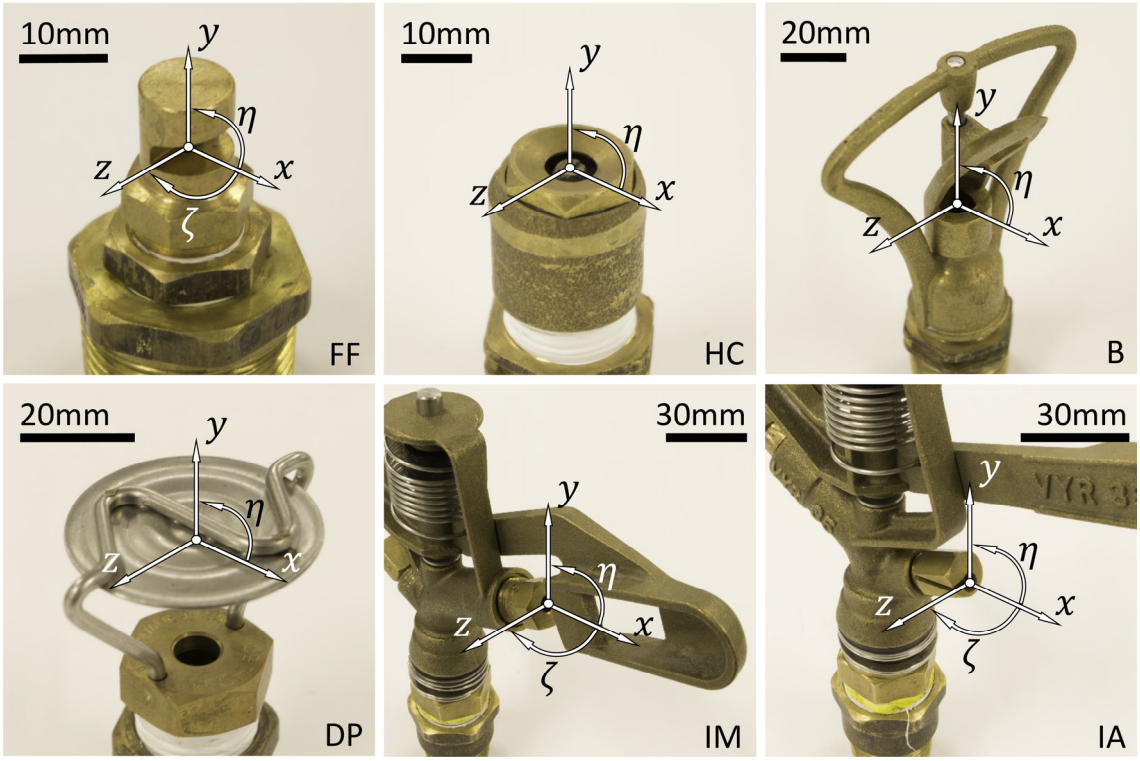

FIGURE 3.1: Photographs of the (FF) flat-fan spray nozzle; (HC) hollow-cone nozzle; (B) 'butterfly sprinkler'; (DP) deflector-plate sprinkler; (IM) 'impact sprinkler' main nozzle; and (IA) 'impact' sprinkler auxiliary nozzle. Both Cartesian coordinates (x, y and z) and spherical coordinates (elevation angle, η, and azimuthal angle, ζ) are defined, where applicable.

TABLE 3.1: Details of the sprinklers used to produce each spray and the operating pressures at which they were characterised.

Spray	Sprinkler model	Pressure [kPa]	Flow rate [L min^{-1}]
FF	Tecpro KHW-1390 180° deflector flat-fan nozzle	400	4.1
HC	½-inch Champion S9F hollow-cone nozzle	345	12.5
B	Holman ½-inch brass butterfly sprinkler	200	34
DP	Lechler 525.049 deflector-plate sprinkler	245	41.8
IA	Vyrsa VYR 35 ¾-inch 360° impact sprinkler auxiliary nozzle	250	5.4
IM	Vyrsa VYR 35 ¾-inch 360° impact sprinkler main nozzle	250	17.4

All six sprays were produced using single-fluid nozzles (i.e. the nozzles were not air-assisted), and each nozzle achieved atomisation by a different mechanism as summarised below.

- Spray FF was formed by a 1.8 mm diameter cylindrical liquid jet which was ejected onto an inclined surface, formed by a 'notch', machined into the sprinkler. The radially expanding, semi-circular liquid sheet, that was produced, atomised a short distance from the nozzle.
- Spray HC was formed by the atomisation of a continuous conical liquid sheet, formed by an annular orifice, the outer and inner diameters of which were 8 mm and 4.5 mm, respectively.
- The 'butterfly sprinkler' formed spray B by ejecting liquid through a 6.5 mm circular orifice onto an asymmetric, 'scooped' deflector, which was free to rotate about the y-axis. The deflector was driven in a negative rotation about this axis by the flow of water, producing a swirling stream of droplets.
- Spray DP was formed by an 8 mm diameter cylindrical liquid jet, which was ejected onto a deflector plate that featured three concentric corrugations. The radially expanding, circular liquid sheet formed by this process atomised a short distance from the deflector plate.
- The impact sprinkler main nozzle produced spray IM by emitting a 4.4 mm diameter cylindrical liquid jet onto a deflector paddle. The paddle was forced to rotate out of the

jet by the water flow, and then forced back towards the liquid jet by a spring. The result was a spray with two distinct modes, which it oscillated between periodically: an undisturbed cylindrical jet and a transient burst of sprays emitted through a wide range of ζ and η.

- The auxiliary nozzle on the same sprinkler produced spray IA by emitting a 2.4 mm diameter cylindrical jet into a short, 5 mm diameter cylindrical chamber. The chamber axis was orientated at a lower elevation angle, η, than the jet, was open on one end and had a 1.5 mm slot machined along one side. An uneven liquid sheet was emitted from the chamber, which atomised as it travelled away from the sprinkler. Both spray IM and spray IA had a relatively slow, incremental, negative rotation about the y-axis, driven by the deflector paddle, which imparted an impulse on the sprinkler head with every oscillation.

3.4 Method

The characterisation procedure was comprised of eight steps:

1. Videography of each spray;
2. Videography of isolated droplets and discs, for model calibration and verification;
3. Analysis of individual video frames, to locate and measure droplet images;
4. Tracking of droplets between video frames, to measure their velocities and ensure that each droplet was only measured once;
5. Implementation of the focal criterion;
6. Identification and removal of spurious results;
7. Correction for statistical bias in the results; and
8. Interpretation of the results.

A script was developed by the present author, for Matlab software (version R2016a), to undertake steps 3 to 7.

3.4.1 Videography

Each spray was operated individually within a 3 m × 1.8 m × 2.4 m (high) enclosure shown in Figures 3.2 and 3.3. The enclosure was used to contain water from the sprays, recirculate it to the supply pump and exclude light other than that which was introduced deliberately as back-lighting for spray characterisation. The sprinklers were supplied with clean water via an electric pump with a pressure regulator installed 2 m upstream of the nozzle. The water pressure directly downstream of the regulator was monitored using a Wika analogue pressure gauge and maintained within ±5% of the values reported in Table 3.1. The pressure drop between the pressure sensor and sprinkler was estimated to have contributed an additional error of less than 3%. The water flowrate through each sprinkler was measured using a Trimec TF015 positive-displacement flow meter, which was located upstream of the pressure regulator and gauge.

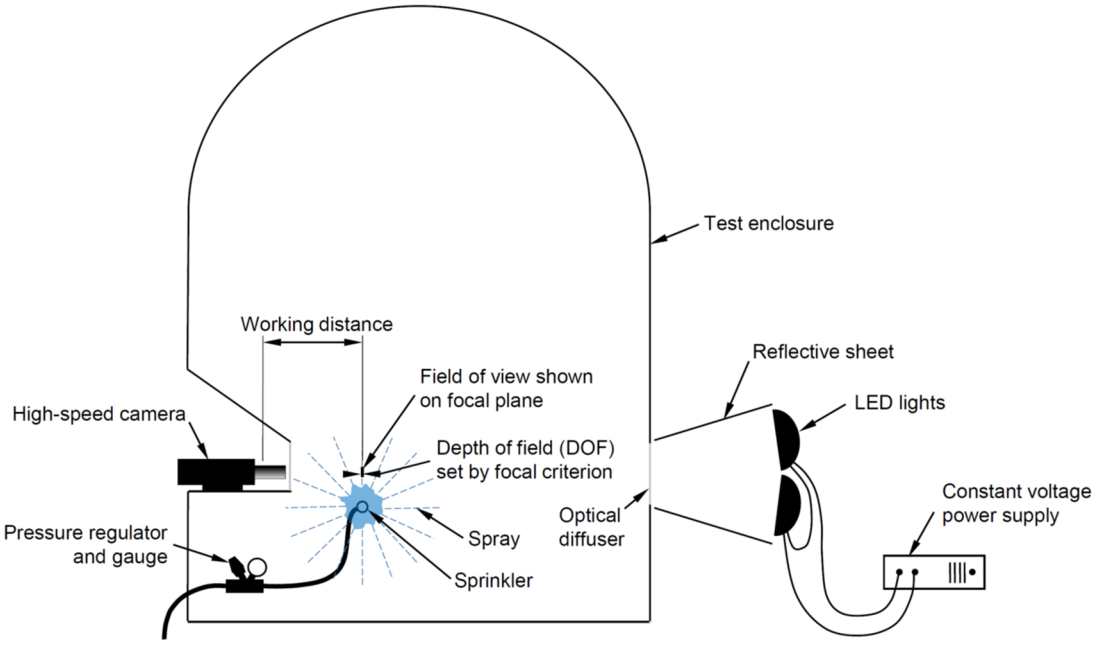

FIGURE 3.2: Cross-section of the experimental arrangement used for spray videography.

Back-illumination was provided to the sprays by four 185 W LED lights, which shone into the test enclosure through a diffuser. A constant d.c. voltage was supplied via a GW Instek GPR-6015HD linear power supply to the lights, to avoid flicker in the high-speed footage. The sprays were videoed through a window on the opposite wall of the enclosure, producing silhouette images of droplets within the sprays. A single Vision Research Phantom v611 high-speed camera

with colour sensor was used, fitted with a Tamron 90 mm f/2.8 macro lens. The lens aperture was fully opened, giving a focal ratio of f/2.8. Figure 3.2 depicts a cross-section of the experimental arrangement and Figure 3.3 shows a sprinkler being positioned the inside the test enclosure during its early development.

FIGURE 3.3: Photograph taken inside the test enclosure that was used for spray videography.

Camera settings, and the sprinkler location and orientation relative to the camera, were customised to suit each spray (see Table 3.2). Optimisation of these variables was an iterative process in many cases. Working distances (i.e. distances between the camera and focal plane) of either 122 mm or 247 mm were used, depending on the spatial scale required to resolve the smallest typical droplet size in the spray, and whether there was substantial visual interference caused by water impingement on the window through which the camera recorded videos of the sprays. The sprays were located and orientated such that the predominant droplet velocity within the DOF was parallel with the focal plane and light attenuation by highly defocused droplets was minimised. The framerate was set to the maximum value possible at full resolution (6,273 frames s^{-1} at 1280 × 800 pixels) for all sprays except spray FF for which a higher framerate was used to capture the fast droplets in this spray in a sufficient number of frames to allow reliable droplet tracking. Exposure lengths were set to produce images that were bright but not overexposed, and to avoid blurred images of fast droplets; hence, the optimum exposure time was dependant on the degree

of light attenuation by defocused droplets, the working distance and the fastest droplet velocity in a given spray.

TABLE 3.2: Test conditions set for each spray; sprays were produced using the flat-fan nozzle (FF), hollow-cone nozzle (HC), deflector-plate sprinkler (DP), butterfly sprinkler (B), impact sprinkler auxiliary nozzle (IA) and impact sprinkler main nozzle (IM).

	FF	**HC**	**B**	**DP**	**IA**	**IM**	
						Disrupted	**Undisrupted**
Working distance [mm]	122	122	247	247	247	247	247
Scale [pixels mm^{-1}]	50.53	50.53	22.42	22.42	22.42	22.42	22.42
Field of view (width; height) [mm]	13.9; 13.9	25.3; 15.8	57.1; 35.7	57.1; 35.7	57.1; 35.7	57.1; 35.7	57.1; 35.7
Framerate [frames s^{-1}]	11,104	6,273	6,273	6,273	6,273	6,273	6,273
Exposure length [μs]	4	7	7	5	4	5	6
Measurement distance from nozzle [mm]	100	326	533	221	536	300	6,000
Assumed axis of symmetry	xy-plane	y-axis	y-axis	y-axis	-	-	-
Number of regions videoed	160	23	24	22	74	12	20

Videos of several overlapping regions were recorded within each spray, such that a series of videos could be combined to produce a pseudo-planar measurement, through a 'slice' of the spray (see Figure 3.4). The processed regions were a fixed distance from each sprinkler (see Table 3.2), large enough to avoid unatomised sheets and ligaments of water. The number of videos required to characterise each spray depended on the measurement distance from the nozzle, the pattern of the spray, the camera field of view and whether any assumptions could be made as to the symmetry of the spray. The influence of the sprinkler frames on sprays DP and B, at azimuthal angles of 90° and 270°, was neglected. Thus, sprays HC, DP and B were assumed to be approximately axisymmetric about the y-axis—when time-averaged, in the case of spray B—which reduced the number of videos required to characterise these sprays significantly. A comparatively large number of measurements was required to resolve 3-dimensional variations in sprays FF and IA, even though the number of measurements required for spray FF was halved, due to the assumption that it was symmetric about the xy-plane.

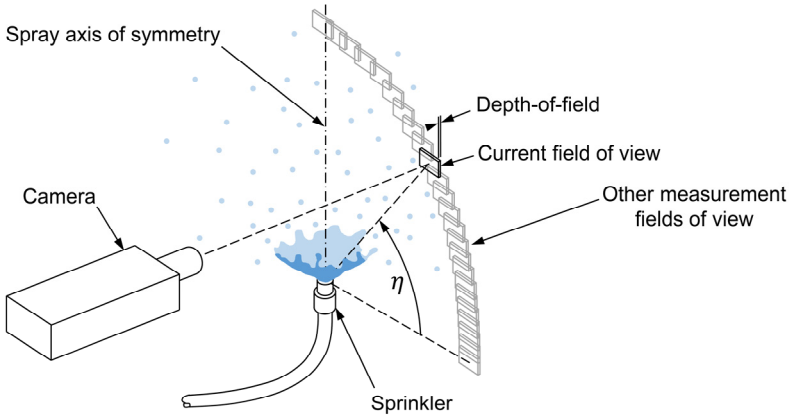

FIGURE 3.4: Schematic diagram showing how, by measuring a series of overlapping regions within a spray, droplets within a pseudo-planar region were measured.

Three aspects of spray IM rendered it particularly difficult to characterise: i) the complex temporal variations caused by the combined oscillation of the deflector paddle and gradual rotation of the entire sprinkler head; ii) the large range of η and ζ through which droplets were emitted from the deflector paddle, the resolution of which would have required videography in several hundred locations; and iii) the long range (from the sprinkler) over which primary breakup of the undisrupted jet occurred. The experimental method was adapted to address these issues.

The two distinct modes of spray IM, i.e. when the liquid jet was disrupted by the deflector paddle and when it was not, were characterised separately. Videography of the spray in both these modes was conducted with the sprinkler head restrained, to prevent rotation; the frequency with which the unrestrained sprinkler head rotated was measured in a separate experiment, using a stopwatch. Resolution of spatial variations in the disrupted spray would have required a prohibitively large number of videos; instead, twelve regions within the spray were videoed, to provide a sample of droplets rather than a full spatial characterisation.

Observations of the undisrupted jet gave some insight into the mechanisms of primary and secondary breakup that produced spray IM (see Figure 3.5). Significant perturbations grew on the (initially cylindrical) jet within 0.25 m of the sprinkler, and continued to grow until the jet separated into discrete droplets and ligaments at approximately 1 m from the nozzle. This primary breakup mechanism is consistent with what has been defined as the 'first wind-induced regime' (Lin & Reitz 1998; Reitz & Bracco 1986; Reitz & Bracco 1982), and is driven by shear between

the liquid jet and surrounding gas. Secondary breakup was also evident in the undisrupted jet; in particular, numerous examples of 'bag breakup' (Faeth, Hsiang & Wu 1995; Guildenbecher, López-Rivera & Sojka 2011; Hsiang & Faeth 1995; Jain *et al.* 2015) were observed 2–5 m from the sprinkler.

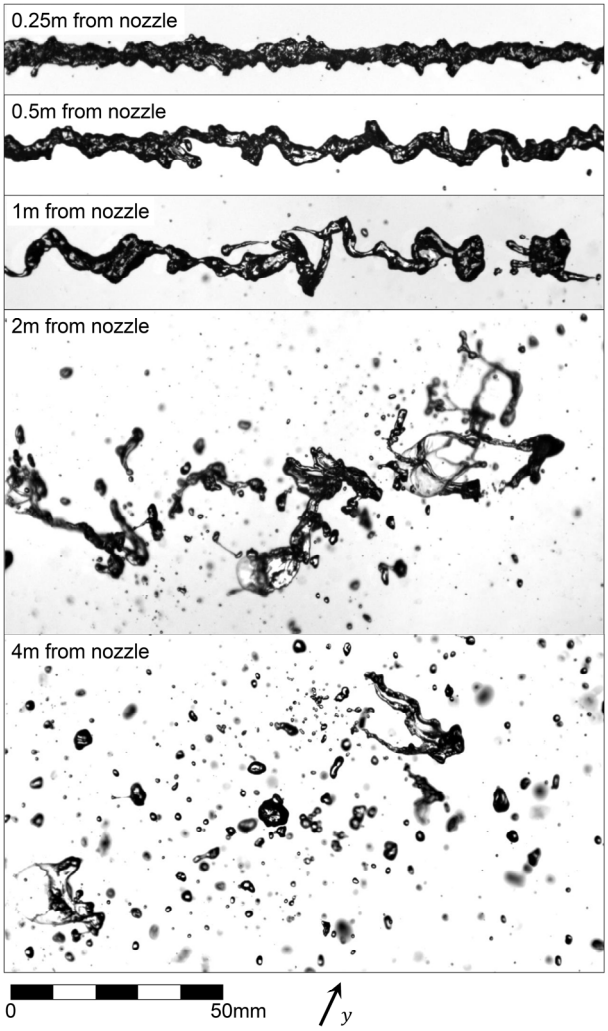

FIGURE 3.5: Breakup of the liquid jet ejected from the impact sprinkler main nozzle (spray IM), when undisrupted, viewed at various distances from the nozzle; each image has been rotated, such that the liquid flow is from left to right. Primary breakup is in the first wind-induced regime and bag-breakup of some larger droplets is evident further downstream. Numerous ligaments and unstable droplets are visible as far as 4 m from the spray nozzle, which complicated the characterisation of this spray.

Consequently, measurements of spray IM (when undisrupted) within ~6 m of the sprinkler contained many liquid sheets and ligaments, which were not well-suited to the video analysis script, and did not represent the eventual, fully-atomised character of the spray. However, spray characteristics measured several metres from the sprinkler were more prone to influence from

ambient conditions than those measured closer to the source. For these reasons, spray IM was not characterised definitively at one distance from the sprinkler; instead, the spray was measured through a vertical plane, 6m from the sprinkler, to provide data that could be used to validate simulations of the spray in still air, and the angle, diameter and flowrate of the liquid jet, as it left the sprinkler nozzle, were recorded. The sprinkler was tilted forwards during videography of the undisrupted jet, such that $(\eta, \zeta) = (15°, 0°)$ was horizontal, to place the spray within the field of view.

3.4.2 Calibration and Verification of the Video Analysis Procedure

Videos were recorded of opaque discs and individual droplets, of known diameter. The droplets and discs were positioned at a range of known distances in front of and behind the focal plane, and this process was repeated at each of the two working distances. Images from the video footage were used to verify and calibrate the image analysis script, and to define variables for the focal criterion.

The opaque discs came etched on a glass slide, designed for the calibration of imaging systems, and ranged in diameter from 0.15 mm to 3.5 mm. Droplets were generated using a piezoelectric-actuated drop-on-demand generator and three 'dropper' nozzles, which were a blunt 36-gauge hypodermic needle and the nozzles from the drip chambers of two intravenous administration sets. Droplet volumes were determined by dividing the liquid flow rate (set using a syringe pump) by the rate at which droplets were produced.

The drop-on-demand generator and each of the three dropper nozzles were fed with water, resulting in droplets with four different diameters: 47 μm, 1.58 mm, 3.17 mm and 4.57 mm. Droplets were also generated from a mixture of methanol and water (in a volume ratio of 80% methanol to 20% water) using the hypodermic needle. This mixture has a similar refractive index to water (Herráez & Belda 2006) but a significantly lower surface tension (Vazquez, Alvarez & Navaza 1995). Droplets separate from dropper nozzles when the weight of the accumulating droplet overcomes the restraining surface-tension forces holding it to the nozzle (Frohn & Roth

2000). Thus, the methanol/water mixture theoretically produces smaller droplets than pure water. In this study, it reliably formed droplets 1.27 mm in diameter.

3.4.3 Image Analysis

Frames from videos of the sprays, and calibration droplets and discs, were analysed individually. The method adopted for this analysis was modelled closely on that of Blaisot et al. (Blaisot 2012; Blaisot & Yon 2005; Fdida & Blaisot 2010; Malot & Blaisot 2000), with some new techniques, developed to suit the large, often non-spherical droplets in this study. Rather than analysing every frame from the spray videos, regularly spaced samples were analysed, each containing an equal number of sequential frames. Droplets were measured with relatively fewer image analysis and droplet tracking iterations with this approach, since each new sample introduced an entirely new set of droplets, whereas analysis of a continuous sequence of frames would have accumulated new measurements gradually, at the rate that new droplets entered the field of view.

The image intensity of the frame under analysis was first normalised and converted to grey-scale. Image normalisation involved the division of the frame by a 'background' image—the average of 20 video frames of the back-illumination, with no spray in view. Droplet images were located within each frame using a grey-level intensity threshold of 0.3, and by convoluting the image with three inverted 'Mexican hat' (i.e. Laplacian of Gaussian) wavelet functions, each with a different width. The union of regions identified by these methods formed a collection of regions (or 'blobs'), which corresponded with regions in the frame that were dark or had a grey-level intensity profile that was highly concave. Blobs that touched the border of the frame or were comprised of less than 3 pixels were disregarded, to avoid any incomplete droplet images or noise from being included in the measurement.

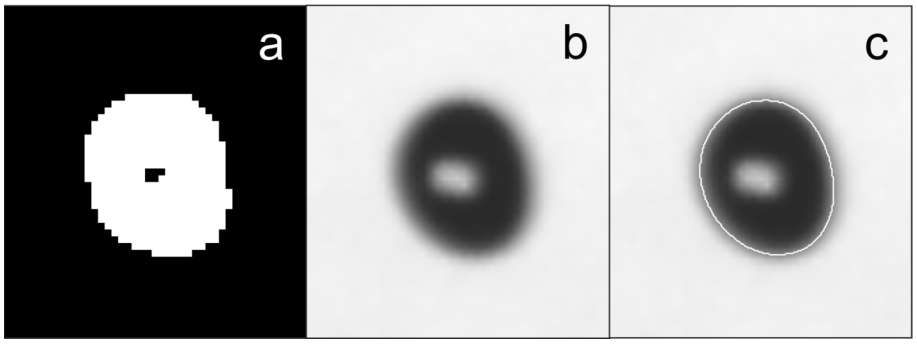

FIGURE 3.6: Preliminary treatment of a 'blob', corresponding to a droplet image. Steps included: (a) segregation of a region surrounding the blob; (b) sub-pixel interpolation of the corresponding droplet image; and (c) definition of the droplet image boundary as the contour of 0.5 relative level.

Droplet images, corresponding to the remaining blobs were then analysed individually (see Figure 3.6). A bilinear sub-pixel interpolation was performed on a region encompassing the droplet image, to improve the precision with which the droplet boundary could be defined. Regions corresponding to other blobs, near the image under analysis, were masked, to prevent them from influencing the analysis. The droplet image local contrast was calculated using the method reported by Fdida and Blaisot (2010), and the boundary of the droplet was defined as the contour of 0.5 relative level (i.e. the line along which the grey-level intensity was half-way between the background and minimum intensities in the droplet image).

Some droplet images overlapped, such that the boundary of 0.5 relative level erroneously combined their outlines. Methods that had previously been used to automatically detect and separate overlapping droplet images, such as watershed algorithms (Castanet *et al.* 2013), the Hough transform (Lee & Kim 2004) and the division of droplet images between points of high boundary curvature (Blaisot 2012; Castanet *et al.* 2013; Fdida & Blaisot 2010), were trialled but performed poorly when applied to the non-circular droplet images common in this study. A new method was developed, based on the spatial rate of change in grey-level gradient along the image boundary. It involved four steps:

1. Identification of potential 'break points' (see Figure 3.7a), by calculating the grey-level gradient at each pixel on the image boundary, smoothing and fitting a spline to the profile formed by these values, and identifying peaks in the absolute value of the derivative of

the spline. Peaks that exceeded a threshold, τ_s, were considered as potential break points, and images with more than two potential break points were treated as the overlapping images of multiple droplets. The threshold, τ_s, was tuned to suit each spray.

2. Definition of secondary break points (see Figure 3.7b), translated from each of the original break points, towards the boundary segment in poorer focus, by a distance of $\frac{2}{3}S_{PSF}$, where S_{PSF} is the PSF half-width of the droplet image in poorer focus.
3. Completion of each droplet image boundary with arcs (see Figure 3.7c). The arc radii were determined from the chord length between each pair of break points and the perimeters of the existing image boundary segments, such that the arc would complete a circular image correctly.
4. Treatment of regions within each boundary as separate droplets thenceforth. Regions defined by the intersection of multiple droplet images were included in calculations of droplet sizes, but were neglected when determining the local contrast of each image.

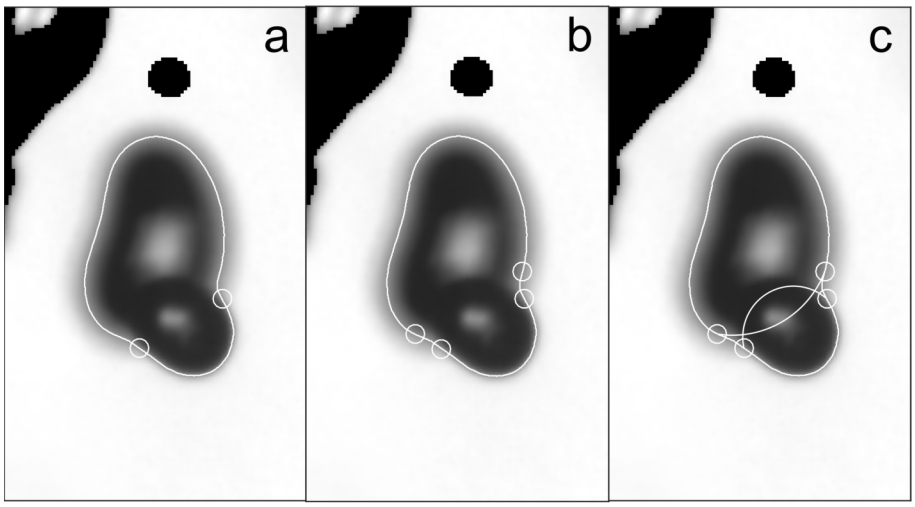

FIGURE 3.7: Detection and separation of overlapping droplet images, based on the grey-level gradient at the image boundary. Steps in the process included: (a) identification of potential 'break points' on the image boundary; (b) definition of secondary break points, translated towards the image that was in poorer focus; and (c) completion of each droplet boundary with arcs.

By separating overlapping droplet images in videos of the sprays, many inaccurate measurements of droplet size and local contrast were avoided. Furthermore, overlapping image separation allowed each of the respective droplets to be tracked through frames in which overlap occurred,

thereby reducing the number of droplets that were measured twice or tracked incorrectly. The method developed here was observed to be more robust than previously established methods that were also trialled, when applied to non-spherical droplets and images with a high degree of overlap, since it was not influenced by the shape of the image boundary. Completion of droplet boundaries using arcs, rather than straight lines, could be expected to improve the accuracy with which each separated droplet was measured, especially those that overlapped to a large degree.

Droplet volumes were estimated by dividing the region inside the droplet boundary into a large number of slices, assuming each slice to represent a disc and adding the volumes of the discs. The method for diameter correction of defocused droplet images proposed by Fdida and Blaisot (2010) was applied to the equivalent spherical diameters of each droplet. This method is based on an analytical model, which considers each defocused image to be the convolution of a binary circular image and a Gaussian PSF, and has been shown to agree well with predictions made using Lorenz Mie theory (Ren *et al.* 1996). However, the diameter correction method has typically overcorrected diameter measurements from actual droplets (Blaisot 2012; Blaisot & Yon 2005; Fdida & Blaisot 2010). So, in this study, the method was first trialled on images of isolated droplets and discs of known diameter (during the verification and calibration of the video analysis script). The corrected equivalent spherical diameter and location of each droplet were recorded.

The PSF half-width of droplet images were estimated from the mean grey-level gradient at the image boundary and the local contrast, using the method proposed by Blaisot (2012). The distance of each droplet from the focal plane was calculated from the PSF half-width, using models developed during the verification and calibration of the video analysis script.

3.4.4 Droplet Tracking

Once two subsequent video frames had been analysed, an attempt was made to pair any measured data obtained from the same droplet. Pairing of data through a sequence of frames produced a set of ‘tracks’, each corresponding to one droplet that had been measured. For each track, the cumulative sum of measured diameter values, droplet coordinates (η and ζ), distance from the

focal plane, and horizontal and vertical distances travelled between frames were recorded, so that the mean value of each parameter could be calculated at a later stage. The cumulative sum of each parameter squared was also recorded, to allow calculation of the variance of measured values associated with each track.

The method adopted to track droplets between frames was modelled closely on that outlined by Dalziel (1992) and implemented for PTV in the software 'Digiflow' (Dalziel 2006). 'Costs' were calculated for the pairing of each droplet image in one frame to each of those in another, such that low cost values indicated a high likelihood that the images were of the same droplet. The cost of pairing droplet i from one frame to droplet j in a subsequent frame was given by the sum of four sub-costs:

$$C_{ij} = C_{loc}(n_i, p_i, p_j) + C_{dia}(p_i, p_j) + C_{foc}(p_i, p_j) + C_{fee}(n_i) \tag{3.4}$$

where C_{loc}, C_{dia} and C_{foc} are functions for costs associated with droplet location, diameter and focus, respectively, C_{fee} is a 'joining fee', p represents the measured properties of a given droplet image, and n_i is the number of video frames already spanned by the track associated with droplet image i.

The location cost was defined by:

$$C_{loc} = \max\left\{ 0 , W_{loc}\left(\sqrt{\left(x_i + u_i\delta_t - x_j\right)^2 + \left(y_i + v_i\delta t - y_j\right)^2} - T_{loc}\right)\right\} \tag{3.5}$$

where W_{loc} and T_{loc} are weighting and threshold parameters, x_i and y_i are the horizontal and vertical coordinates of droplet i, u_i and v_i are the horizontal and vertical velocity components of droplet i, and δ_t is the time period separating the two video frames. Velocity components, u_i and v_i, were the average of those measured for the track associated with droplet i in previous tracking steps; droplets with no velocity history (i.e. those that had not been paired with droplet images in previous frames) were assigned an estimated velocity, defined by constants u_e and v_e. The threshold parameter, T_{loc}, was set as one of two values, depending on the length of the track associated with droplet i:

$$T_{loc} = \begin{cases} T_{loc,1} & n_i = 1 \\ T_{loc,2} & n_i > 1 \end{cases} \tag{3.6}$$

By setting $T_{loc,1} > T_{loc,2}$, new tracks could be established for droplets with a relatively wide range of velocities, but the continuation of existing tracks was more heavily constrained to maintain the established velocity history. The weighting parameter, W_{loc}, was a single fixed value. The diameter cost was defined by:

$$C_{dia} = \max\left\{ 0 , W_{dia}\left(\frac{2|d_i - d_j|}{d_i + d_j} - T_{dia}\right)\right\} \tag{3.7}$$

where W_{dia} and T_{dia} are weighting and relative threshold parameters, and d is the droplet equivalent spherical diameter. The focal cost was defined by:

$$C_{foc} = \max\left\{ 0 , W_{foc}\left(\frac{2|z_i - z_j|}{z_i + z_j} - T_{foc}\right)\right\} \tag{3.8}$$

where W_{foc} and T_{foc} are weighting and relative threshold parameters, and z is the droplet distance from the focal plane. The joining fee was zero for droplets that had been paired with droplets in previous video frames, and a fixed positive value for those that had not:

$$C_{fee} = \begin{cases} F & n_i = 1 \\ 0 & n_i > 1 \end{cases} \tag{3.9}$$

By tuning the value of F, the propensity for tracks to be erroneously interrupted by droplets as they arrived within the field of view could be minimised.

A single fixed cost, C_0, was also defined, for the pairing of any droplet with a hypothetical 'out of view' droplet. Droplet images that could not be paired with a cost less than C_0 were paired with the 'out of view' droplet, which prevented them from interfering with the tracking of other droplets. The parameters W_{loc}, $T_{loc,1}$, $T_{loc,2}$, W_{dia}, T_{dia}, W_{foc}, T_{foc}, u_e, v_e, F and C_0 were tuned to suit each spray.

The final allocation of droplet images from one frame to those in another was that which minimised the sum total cost. It was reached iteratively, by establishing an initial feasible solution, then progressively making changes that reduced the sum total cost until no more beneficial changes could be made. For an allocation to be feasible, each droplet image needed to

be paired to one other droplet image—either one from the other video frame under analysis, or a hypothetical 'out of view' droplet. The initial feasible solution was established by incrementally combining individual image pairs in order of increasing cost, except those that contained an image that had already been allocated, until every image was paired. Incremental improvements were made to the initial solution by identifying and swapping the two image pairs that, if swapped, caused the greatest decrease in the sum total cost; such changes were made until the optimal allocation had been reached. The number of potential changes was decreased by only considering pairs for which the cost was less than C_0, which sped up the tracking procedure substantially.

After droplets had been tracked between two sequential frames (say, frames p and $p+1$), an attempt was made to pair any unpaired droplet images from the second frame ($p+1$) to those that had not been tracked forward in the previous tracking step (from frame $p-1$ to frame p), using the same tracking procedure. Thus, droplets that had not been detected in isolated video frames could still form uninterrupted tracks.

3.4.5 Focal Criterion

Droplets more than 1.5 mm and 3 mm from the focal plane were disregarded from measurements taken at a working distance of 122 mm and 247 mm, respectively. The distance of a droplet from the focal plane was taken to be the mean of the values determined from each image of the droplet, which were calculated from measured PSF half-width values, as described in Sections 3.4.3 and 3.5.1. Thus, droplets that travelled into or out of the DOF, while in the field of view, were included in the measurement if they were within the DOF on average. This approach avoided much of the ambiguity encountered when using a lateral sheet of light to define a control volume, where droplets can be partially illuminated, or can disappear from view altogether.

3.4.6 Removal of Spurious Results

The tracking procedure was generally very robust but did produce some spurious tracks, which connected images of different droplets. Such tracks were typically due to the incorrect pairing of droplet images with no velocity history (i.e. those that formed new tracks). They rarely persisted

for more than one tracking step, since this would require an otherwise unpaired droplet image, of similar size and degree of defocus to the two incorrectly paired images, to be located in the third frame so as to continue the erroneous droplet trajectory. Tracks that spanned fewer than 3 frames were removed from analysis, to reduce the number of spurious results. Tracks with a standard deviation in horizontal velocity exceeding 2 pixels per video frame were also identified as likely spurious tracks and removed.

Spurious results were also caused by the presence of droplets in the field of view that had not originated directly from the nozzle. Such droplets were either produced by water splashing on surfaces in the test enclosure, or had travelled from the sprinkler, beyond the region being measured, and then had been forced back into the field of view. The influence of gravity on the larger of these droplets was relatively large, so they tended to fall, almost vertically, through the sprays, while the trajectories of smaller reentrained and splashed droplets were driven largely by drag forces (due to their low Stokes number), so they followed the induced airflow within the sprays more closely. Many of the spurious results associated with larger droplets were removed by disregarding tracks with a direction of travel outside of an acceptable range, the bounds of which were tuned to suit each spray. However, this is unlikely to have removed all spurious results associated with smaller reentrained droplets. Thus, the results of this study may be somewhat biased towards smaller droplets.

3.4.7 Correction for Sampling Bias

Rather than analysing the entire video record from each spray, discrete samples of n_f sequential video frames were taken from the video footage and analysed. Hundreds of such samples were analysed from each video file, each initiated n_p video frames after the start of the previous sample. The values n_f and n_p were set to 10 and 50, respectively, except when analysing time-varying sprays (i.e. spray B and spray IM when disrupted by the deflector paddle). For these sprays, n_f and n_p were set to 6 and 12, respectively, in order to improve the temporal resolution of the measurement. This approach was chosen to reduce the computational expense of the video

analysis process (by a factor of approximately n_p/n_f, which equalled 2 for time-varying sprays and 5 for all other sprays). The number of droplets analysed was not reduced by such a large factor, since droplets typically had a residence time within the field of view in the order of 10 frames, so many of the droplets recorded during the gaps between samples were also recorded within a sample.

The sampling method outlined above introduced a bias towards slower droplets, which needed to be corrected for. Slow droplets remained in the field of view for a greater number of video frames, so were more likely to be included in a sample. The probability that a given droplet would appear in enough sampled frames to be included in the measurement was given by:

$$P_i = \frac{n_{di} + n_f - 2n_{min}}{n_p} \tag{3.10}$$

where n_{di} is the number of frames in which droplet i was within the field of view and n_{min} is the minimum number of frames with which tracks would be included (which was set equal to 3, to remove spurious results, as discussed in section 3.4.6). The number of frames in which a droplet appeared could be estimated from the droplet speed:

$$n_{di} \approx \frac{f_{FR} w_{FOV}}{S_i} \tag{3.11}$$

where f_{FR} (s^{-1}) is the framerate, w_{FOV} (m) is the width of the field of view on the focal plane and S_i (m s^{-1}) is the speed of droplet i.

Another source of bias influenced measurements of sprays HC, B and DP, which were assumed to be axisymmetric. A greater portion of droplets emitted close to the axis of symmetry in these sprays were within the finite DOF than those emitted closer to $\eta = 0°$ (see Figure 3.8). Thus, results from the pseudo-planar measurements of axisymmetric sprays did not give an accurate representation of the distribution of liquid volume throughout the full range of η.

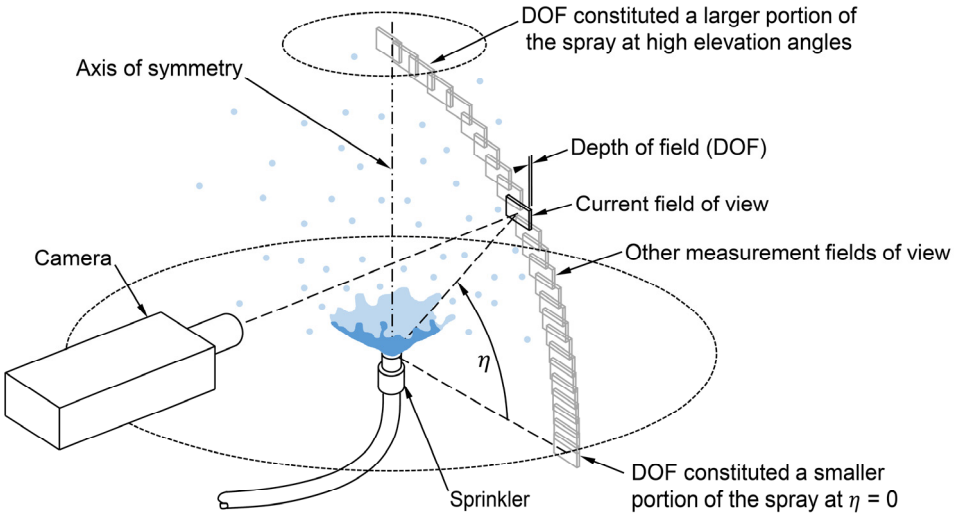

FIGURE 3.8: Geometry of measurements around axisymmetric sprays, which introduced bias towards droplets close to the axis of symmetry when results were converted to represent the distribution of liquid in the entire spray.

The two sources of bias mentioned above were addressed by weighting the contribution of each track by a correction factor, defined as:

$$\phi_i = \frac{W_i}{P_i} \tag{3.12}$$

where W_i is a factor for the correction of bias in data from axisymmetric sprays, given by:

$$W_i = \begin{cases} \cos \eta_i & \text{axisymmetric sprays} \\ 1 & \text{other sprays} \end{cases} \tag{3.13}$$

where η_i is the elevation angle at which droplet i was measured. Substitution of (3.10), (3.11) and $n_{min} = 3$ into (3.12) yields:

$$\phi_i = \left(\frac{S_i n_p}{f_{FR} w_{FOV} + S_i (n_f - 6)} \right) W_i \tag{3.14}$$

3.4.8 Interpretation of Results

Data from each spray was analysed in a number of ways. Four representative diameters and one representative speed were calculated from the distributions of measured droplet diameters and speeds. The arithmetic mean diameter was given by:

$$d_{10} = \frac{\sum_{i=1}^{n} \phi_i d_i}{\sum_{i=1}^{n} \phi_i} \tag{3.15}$$

where d_i is the equivalent spherical diameter of droplet i, ϕ_i is the weighting factor associated with droplet i, defined by (3.14), and n is the number of droplet tracks measured in the spray. The volume mean diameter, i.e. the diameter of a spherical droplet with a volume equal to the mean volume of droplets in the spray, was given by:

$$d_{30} = \left(\frac{\sum_{i=1}^{n} \phi_i {d_i}^3}{\sum_{i=1}^{n} \phi_i} \right)^{1/3} \tag{3.16}$$

The volume-length mean diameter, which has relevance to evaporation, was given by:

$$d_{31} = \left(\frac{\sum_{i=1}^{n} \phi_i {d_i}^3}{\sum_{i=1}^{n} \phi_i d_i} \right)^{1/2} \tag{3.17}$$

The Sauter mean diameter, which represents the ratio of liquid volume to surface area, was given by (Frohn & Roth 2000):

$$d_{32} = \frac{\sum_{i=1}^{n} \phi_i {d_i}^3}{\sum_{i=1}^{n} \phi_i {d_i}^2} \tag{3.18}$$

The mean characteristic speed was defined as the volume-weighted mean droplet speed:

$$S_{ch} = \frac{\sum_{i=1}^{n} S_i \phi_i {d_i}^3}{\sum_{i=1}^{n} \phi_i {d_i}^3} \tag{3.19}$$

where S_i is the speed of droplet i.

Continuous marginal distributions of droplet diameters, speeds, locations and, in the case of sprays B and IM, temporal locations, were formed using a kernel density estimation method. Gaussian kernels were used, the widths of which were tuned to avoid results that were noisy or overly smoothed. The contribution of each track to the continuous distribution was also weighted by the correction factor ϕ_i. The distributions were scaled using the water flowrates measured using the flow meter, and thus represented the spray liquid volume flux as a function of various droplet characteristics.

Variables representing the 'local' characteristic speed and 'local' Sauter mean diameter were defined, to allow two-dimensional spatial variations in droplet speed and diameter distributions to be plotted. The local characteristic speed was defined as:

$$\grave{S}_{ch}(\alpha,\varepsilon) = \frac{\sum_{i=1}^{n} S_i \phi_i {d_i}^3 e^{-\left(\frac{(\zeta-\zeta_i)^2+(\eta-\eta_i)^2}{2{\sigma_d}^2}\right)}}{\sum_{i=1}^{n} \phi_i {d_i}^3 e^{-\left(\frac{(\zeta-\zeta_i)^2+(\eta-\eta_i)^2}{2{\sigma_d}^2}\right)}} \tag{3.20}$$

where ζ_i and η_i are the azimuthal and elevation angles given by the location of droplet i, and σ_d is the standard deviation of a Gaussian kernel. The local Sauter mean diameter was defined as:

$$\grave{d}_{32}(\alpha,\varepsilon) = \frac{\sum_{i=1}^{n} \phi_i {d_i}^3 e^{-\left(\frac{(\zeta-\zeta_i)^2+(\eta-\eta_i)^2}{2{\sigma_S}^2}\right)}}{\sum_{i=1}^{n} \phi_i {d_i}^2 e^{-\left(\frac{(\zeta-\zeta_i)^2+(\eta-\eta_i)^2}{2{\sigma_S}^2}\right)}} \tag{3.21}$$

where σ_S is the standard deviation of a Gaussian kernel. The kernel widths σ_S and σ_d were tuned to produce functions that were not noisy or overly smoothed.

Standard functional forms were fitted to the marginal distribution of droplet diameters in each spray. Such functions allow the easy communication and comparison of droplet diameter distributions. Previous studies have found that no single functional form fits all sprays well (Paloposki 1994; Putorti, Everest & Atreya 2004), so four functional forms (Equations 3.19–3.21, 3.24) were trialled on data from the sprays in this study and the function that fit each dataset best was reported. The Rosin Rammler distribution defined the fraction of liquid contained in droplets with diameter less than d, or 'cumulative volume fraction', as:

$$F_{RR}(d) = 1 - e^{-(d/d_{RR})^{\gamma_{RR}}} \tag{3.22}$$

where d_{RR} and γ_{RR} are size and distribution parameters, respectively. The log-normal distribution defined the marginal distribution of liquid volume contained in droplets of diameter d as:

$$f_{LN}(d) = \frac{1}{d\sigma_{LN}\sqrt{2\pi}} e^{\frac{-(\ln d-\mu_{LN})^2}{2{\sigma_{LN}}^2}} \tag{3.23}$$

where μ_{LN} and σ_{LN} are size and distribution parameters, respectively. The upper-limit log-normal distribution (Mugele & Evans 1951) defined the marginal distribution of liquid volume contained in droplets of diameter d as:

$$f_{ULLN}(d) = \frac{\delta_{ULLN}\, d_{max}}{\sqrt{\pi} d(d_{max}-d)} e^{-{\delta_{ULLN}}^2\left(\ln\left(\frac{ad}{d_{max}-d}\right)\right)^2} \tag{3.24}$$

where d_{max} is the maximum diameter in the distribution, a is the ratio of d_{max} to a size parameter, d_{ULLN}:

$$a = \frac{d_{max}}{d_{ULLN}} \tag{3.25}$$

and δ_{ULLN} is a function of a distribution parameter, σ_{ULLN}:

$$\delta_{ULLN} = \frac{1}{\sqrt{2}\ln \sigma_{ULLN}} \tag{3.26}$$

A hybrid log-normal/Rosin Rammler distribution (Ren, Baum & Marshall 2011; You 1986) defined the cumulative volume fraction as:

$$F_{LNRR}(d) = \begin{cases} \frac{1}{\sqrt{2\pi}} \int_0^d \frac{\gamma_{LNRR}}{1.15\chi} e^{\left(\frac{-(\ln(\chi/d_{v50}))^2}{2(1.15/\gamma_{LNRR})^2}\right)} d\chi & (d < d_{v50}) \\ 1 - e^{-0.693(d/d_{v50})^{\gamma_{LNRR}}} & (d \geq d_{v50}) \end{cases} \tag{3.27}$$

where γ_{LNRR} is a distribution parameter and d_{v50} is a size parameter equal to the volume median diameter of the distribution. The parameters from each function were reached iteratively, by a least squares approach, except for those in the upper-limit log-normal distribution, which was fitted by the procedure outlined by Mugele and Evans (1951).

3.5 Results and Discussion

3.5.1 Model Calibration and Verification

The theoretical model for correction of diameter measurements from defocused droplet images, proposed by Fdida and Blaisot (2010), was found to perform poorly when applied to images of isolated droplets and opaque discs. This result is consistent with other published works employing the same model (Blaisot 2012; Blaisot & Yon 2005; Fdida & Blaisot 2010) and, as in these other works, an empirical model was developed for the specific optical setup used in this study.

The standard error of results obtained using the empirical diameter correction model was less than 7% within a 3 mm DOF at 122 mm working distance (see Figures 3.9 and 3.1) and less than 2.5% within a 6 mm DOF at 247 mm working distance. Outside of these DOFs, estimates of the diameter of droplets and discs were typically much less accurate (see, for example, outliers 10mm

behind the focal plane in Figure 3.1). However, since the focal criterion was used to eliminate droplets outside a narrow DOF, these inaccuracies had no effect on measurements of the six sprays. Some parallax error remained in the data after correction (visible in Figures 3.9 and 3.1, as a trend for objects closer to the camera to appear larger). The use of a telecentric lens could have avoided this error (Fdida & Blaisot 2010), however the 90 mm macro lens used in this study introduced an error of less than 3.5% within the DOFs of interest.

The diameter correction model served two functions: it corrected for the overestimation of droplet diameters from highly defocused images (see inset in Figure 3.9), and it corrected for inaccuracy in the scale used to convert droplet measurements from pixels to millimetres (observed as a common relative offset between raw and corrected values in Figures 3.9 and 3.1). The former function, which is typically the stated purpose of PSF-based diameter correction models, substantially improved the accuracy with which small droplets were measured in this study. Images of larger droplets could reach higher degrees of defocus before the 'blurred' outer edges influenced the image centre, so were predominantly corrected for the inaccurate scale.

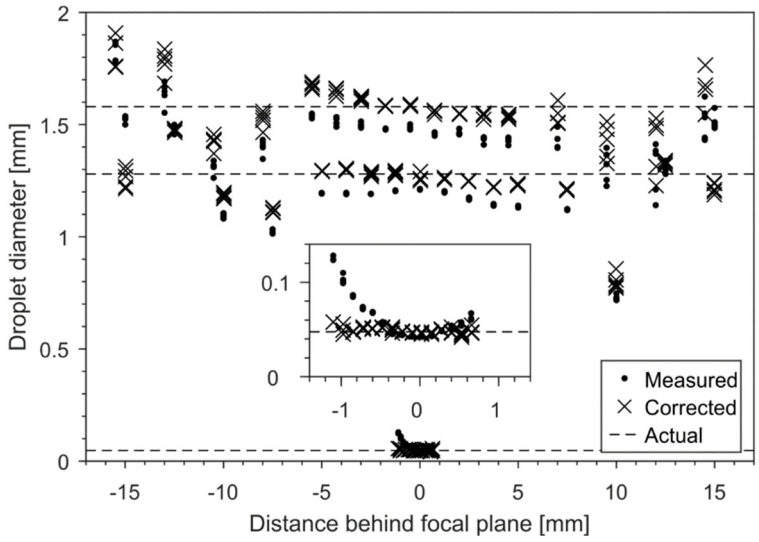

FIGURE 3.9: Calibration results showing the measured, corrected and actual diameters of droplets, at various locations relative to the focal plane. Data presented here is for a working distance of 122 mm. The inset shows a magnified view of data in the lower part of the figure.

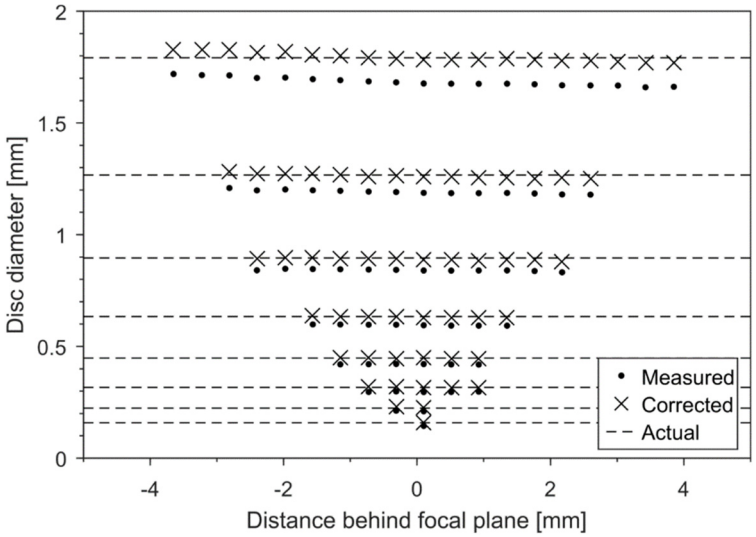

FIGURE 3.10: Calibration results showing the measured, corrected and actual diameters of opaque discs, at various locations relative to the focal plane. Data presented here is for a working distance of 122 mm.

The analytical model for estimation of PSF half-widths of droplet images, proposed by Blaisot (2012), performed well in this study. A common linear trend, increasing with distance from the focal plane, was clearly evident in the calculated PSF half-widths from objects of all diameters (see Figure 3.11). Within the DOF, linear models fitted to this data were able to predict the distance of objects from the focal plane with a mean absolute error of 0.075 mm. These models provided a basis for a focal criterion that did not introduce bias towards larger or smaller droplets.

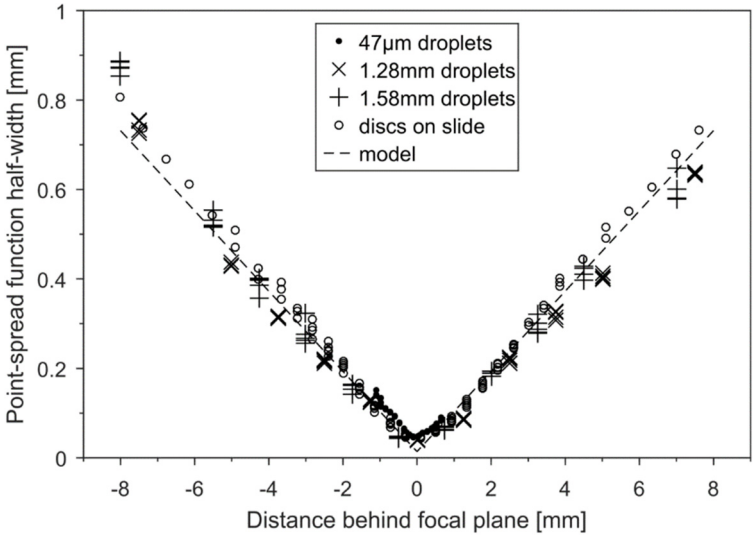

FIGURE 3.11: Image point-spread function (PSF) half-width at varying degrees of defocus. The model to estimate object distance from the focal plane, based on PSF half-width measurements, was based on a fit to this data and is specific to the optical setup and working distance that was used. Data presented here is for a working distance of 122 mm.

3.5.2 Bulk Spray Properties

Between 91,000 and 323,000 droplets were measured in each spray. Most slow-moving droplets were relatively small (see Figure 3.12)—a trend that has been identified in data from other sprays (Dorr *et al.* 2013; Nuyttens *et al.* 2009; Zhou, D'Aniello & Yu 2012). Nuyttens *et al.* (2009) attributed this to the diameter dependence of droplet relaxation times, meaning that smaller droplets are slowed more rapidly by drag forces, while travelling from where they were formed to where they were measured. Such behaviour could also be expected in the sprays considered here. This trend reveals a sensitivity in the experimental results to the distance from each nozzle at which measurements were taken. Thus, the spray characteristics reported herein are specific to the locations at which measurements were taken.

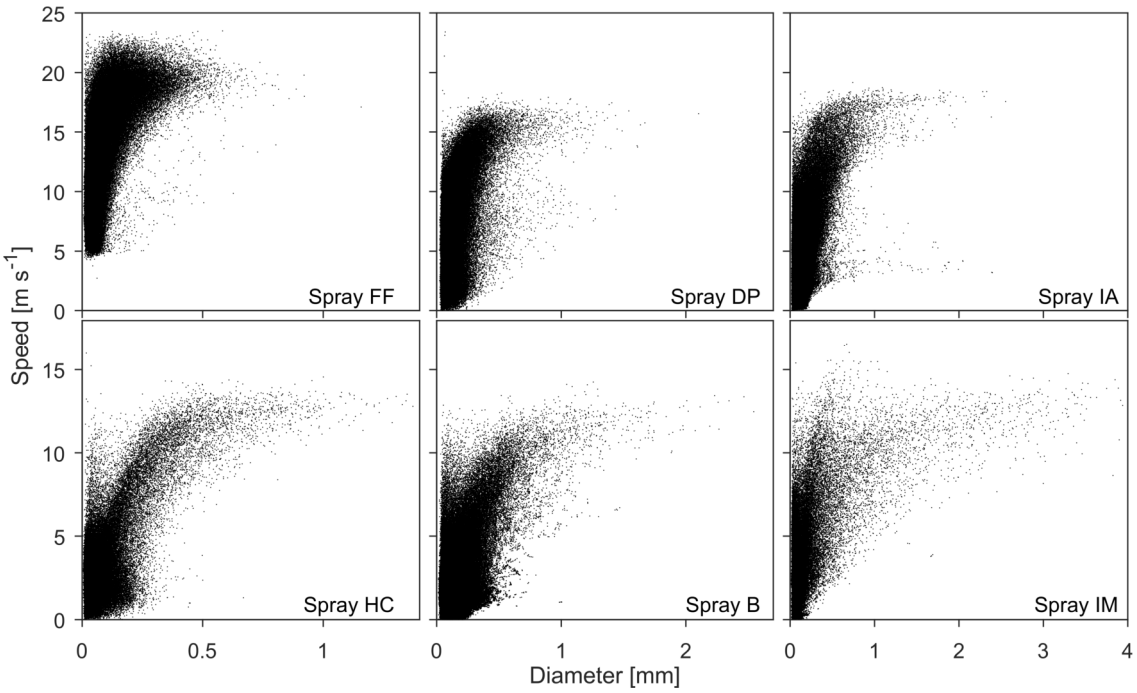

FIGURE 3.12: Comparison of droplet speeds and diameters measured in sprays produced by the flat-fan nozzle (spray FF), hollow-cone nozzle (spray HC), deflector-plate spray head (spray DP), butterfly sprinkler (spray B), impact sprinkler auxiliary nozzle (spray IA) and impact sprinkler main nozzle (IM). Some outlying results have been omitted for clarity. The majority of slow droplets that were observed were small, which could be explained by the relatively large influence of aerodynamic drag on these droplets.

Marginal distributions of droplet diameters and speeds, presented in Figures 3.13–3.16, reveal the spatiotemporally averaged characteristics of each spray. The sprays were dominated by droplets with diameters ranging from 100 μm to 1.8 mm, and speeds between 2 and 22 m s^{-1}. Compared

to other sprays used for fire suppression, spray B was the most similar to previously characterised 'pendant' and 'upright' sprinklers (Zhou, D'Aniello & Yu 2014; Zhou, D'Aniello & Yu 2012), while sprays FF, HC and DP were comprised of smaller droplets, and sprays FF, IA and DP expelled droplets at higher velocities. Sprays FF, HC and DP are near the upper limit of what is considered a 'water mist' in current fire protection standards (ISO 2005; NFPA 2010; Standards Australia 1999); although, they are not mists in a scientific sense (Mawhinney & Back 2016). Spray FF, in particular, could be considered a relatively coarse water mist, in the context of sprays for fire suppression. Various metrics describing the sprays, including characteristic diameters, characteristic speeds and details of the standard functional forms found to fit the diameter distributions best, are presented in Table 3.3.

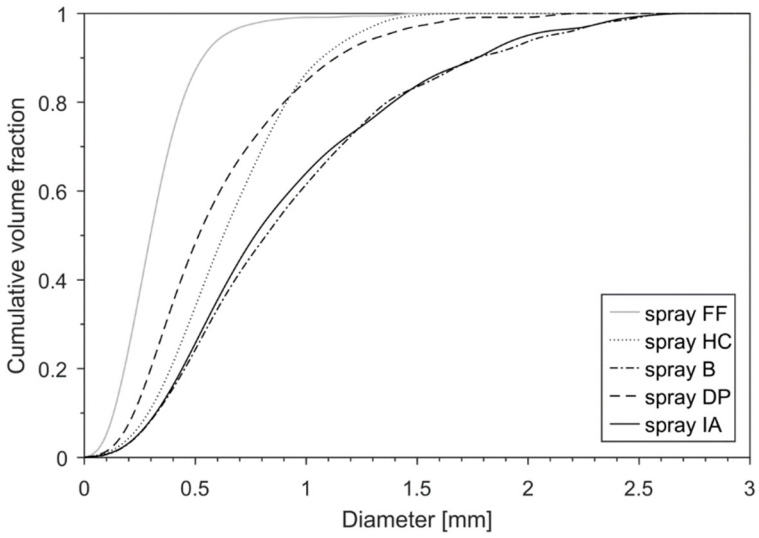

FIGURE 3.13: Comparison of droplet diameter marginal distributions in sprays produced by the flat-fan nozzle (spray FF), hollow-cone nozzle (spray HC), deflector-plate sprinkler (spray DP), butterfly sprinkler (spray B), and impact sprinkler auxiliary nozzle (spray IA).

Characteristics of spray IM were not heavily influenced by the disrupted mode (see Figures 3.15 and 3.16), because that mode occurred for a small portion of the spray oscillatory period. Despite having been taken 6m from the sprinkler nozzle, measurements of the undisrupted jet included a number of large (~5 mm) droplets, which were likely to have subsequently undergone secondary atomisation further downstream. These large, unstable droplets significantly influenced the diameter distributions presented in Figure 3.15, due to the large volume that they comprised.

Consequently, none of the standard functional forms fitted data from spray IM with satisfactory accuracy.

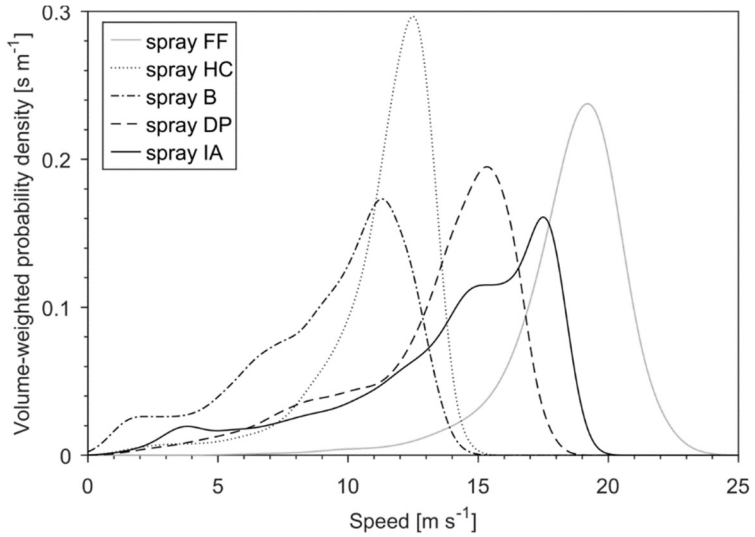

FIGURE 3.14: Comparison of droplet speed marginal distributions in sprays produced by the flat-fan nozzle (spray FF), hollow-cone nozzle (spray HC), deflector-plate sprinkler (spray DP), butterfly sprinkler (spray B), and impact sprinkler auxiliary nozzle (spray IA).

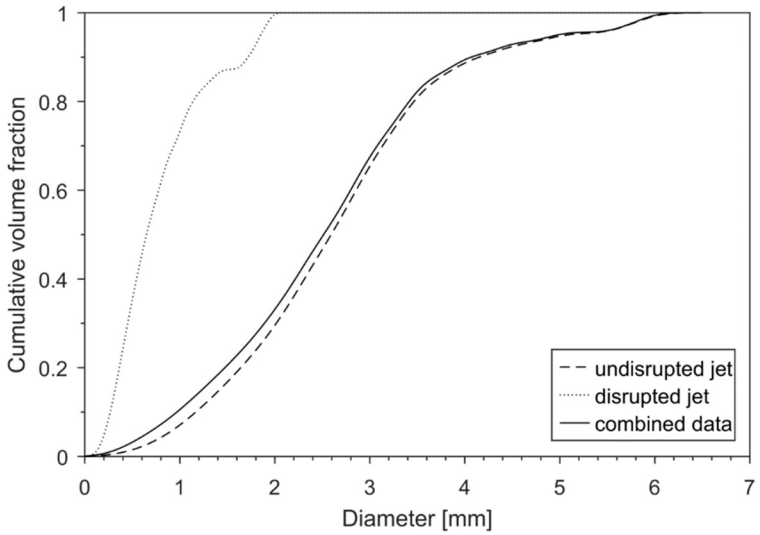

FIGURE 3.15: Comparison of droplet diameter distributions in spray IM when disrupted by the deflector paddle, and undisrupted, with the combined (i.e. time-averaged) data. The disrupted jet had little effect on the time-averaged spray characteristics, as it occurred for only a 13% of the spray period. A small number of large (~5 mm) droplets had not yet undergone secondary atomisation, but were measured in the undisrupted jet.

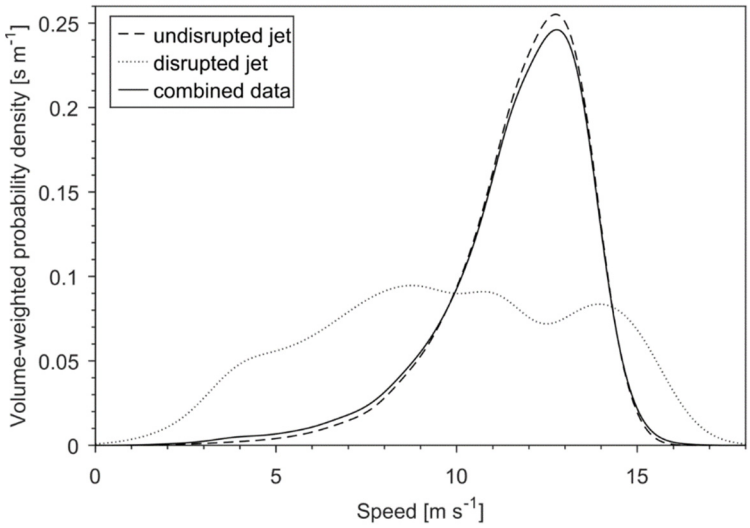

FIGURE 3.16: Comparison of droplet speeds measured in spray IM when disrupted by the deflector paddle, and undisrupted, with the combined (i.e. time-averaged) data. The disrupted jet had relatively little effect on the time-averaged spray behaviour since it occurred for only 13% of the spray period.

TABLE 3.3: Characteristics of sprays produced by the flat-fan nozzle (FF), hollow-cone nozzle (HC), deflector-plate spray head (DP), butterfly sprinkler (B), impact sprinkler auxiliary nozzle (IA) and impact sprinkler main nozzle (IM). Four common functional forms were trialled on the spray data; the functions that best fit each dataset are presented here, with the relevant parameters.

	FF	HC	B	DP	IA	IM		
						Disrupted	Undisrupted	Combined
Measurement distance from nozzle [mm]	100	326	533	221	536	300	6,000	-
Number of droplets measured ($\times 10^3$)	155	91	343	120	160	18	29	47
Arithmetic mean diameter, d_{10} [µm]	102	122	183	176	196	219	336	273
Volume mean diameter, d_{30} [µm]	159	263	341	273	354	336	912	720
Volume-length mean diameter, d_{31} [µm]	199	387	465	340	475	416	1,504	1,168
Sauter mean diameter, d_{32} [µm]	240	496	615	419	610	517	2,002	1,731
Best functional fit to diameter distribution[1]	LN/RR	ULLN	ULLN	ULLN	LN/RR	-	-	-
Size parameter, d_{RR}, μ_{LN}, d_{ULLN} or d_{v50}	0.2899	0.9039	0.9917	0.5133	0.7496	-	-	-
Distribution parameter, γ_{RR}, σ_{LN}, σ_{ULLN} or γ_{LNRR}	2.0163	2.1388	2.3027	1.9147	1.4825	-	-	-
Maximum size parameter, d_{max}	-	1.9114	4.3431	21.5965	-	-	-	-
Mean characteristic speed, S_{ch} [m s^{-1}]	18.5	11.3	9.1	13.2	13.9	9.7	11.8	11.7

1 – Functional forms trialled on the spray data included the Rosin-Rammler distribution, log-normal distribution, upper-limit log-normal distribution (ULLN) and a hybrdid log-normal/Rosin-Rammler distribution (LN/RR).

3.5.3 Spatiotemporal Spray Variations

Substantial spatial and temporal variations were evident in the distributions of droplet sizes, speeds and flow rates within the sprays (see Figures 3.17–3.23**Error! Reference source not found.**). Such characteristics may influence the spray behaviour significantly, so could be vital to the accurate simulation of these sprays. Analysis of spatiotemporal variations in the sprays also provided some insight into the physical processes involved in their formation.

Each spray exhibited a core region of fast, polydisperse droplets. Regions of slower droplets surrounded these core regions, except towards the centre of the hollow cone formed by spray HC and the top of spray IM when undisrupted. Air flow, induced by the sprays, is likely to have been fastest in these core regions, due to the dense spacing of droplets and surrounding regions of induced air flow. The resulting reduction in drag forces acting on droplets there could have caused the fast core regions to form. It is possible that sufficient air movement was established in the central region encompassed by spray HC to substantially reduce the drag forces on droplets adjacent to this region as well. Spray IM is likely to have induced air flow with particular efficiency, due to the relatively high liquid volume fraction in this spray. Liquid in spray IM was also observed to travel more than 1 m before atomising (see Figure 3.5). Combined, these two factors may explain the relative uniformity of droplet speeds observed 6 m from the impact sprinkler (see Figure 3.20**Error! Reference source not found.**).

Spatial variations in droplet size distributions varied between the different sprays. Generally, larger droplets tended to be concentrated towards the fast, core regions of the sprays. However, regions at both ends of the ‘fan’ formed by spray FF, and at the end of the ‘fan’ extending to high azimuthal angles in spray IA, were dominated by relatively large droplets (see Figures 3.21 and 3.22). The formation of these two sprays was similar, in that a liquid jet was projected onto an inclined surface, producing a liquid sheet which subsequently atomised. The large droplets were produced through the primary breakup process at the ends of the liquid sheets that were produced.

Rotation of the impact sprinkler head about the y-axis occurred with a mean period of 27.7 s, which influenced sprays IM and IA. Oscillation of the deflector paddle, into and out of the liquid jet in spray IM, occurred with a mean frequency of 4.89 Hz. Spray IM was disrupted by the deflector paddle for only 13% of the resulting 0.2045 s period; hence the relatively small influence that characteristics of the disrupted jet had on time-averaged data for this spray (see Figures 3.15 and 3.16). The butterfly sprinkler deflector rotated with an average frequency of 43.56 Hz, producing an outward-moving spiral of droplets, with a spacing of approximately 255 mm. Smaller droplets in spray B typically travelled slower and lagged somewhat behind larger droplets in the spiral, to an extent that the smallest droplets formed a constant, slow (< 6 m s^{-1}) flow throughout the spray (see Figure 3.23**Error! Reference source not found.**). The relatively large influence of aerodynamic drag on small droplets is likely to have caused them to slow and lag behind the spiral of larger droplets in this manner. However, complexities in the breakup process and re-entrainment of small droplets into the spray (see Section 3.4.6) may have also contributed to the constant flow of small, slow droplets observed 533 mm from the butterfly sprinkler.

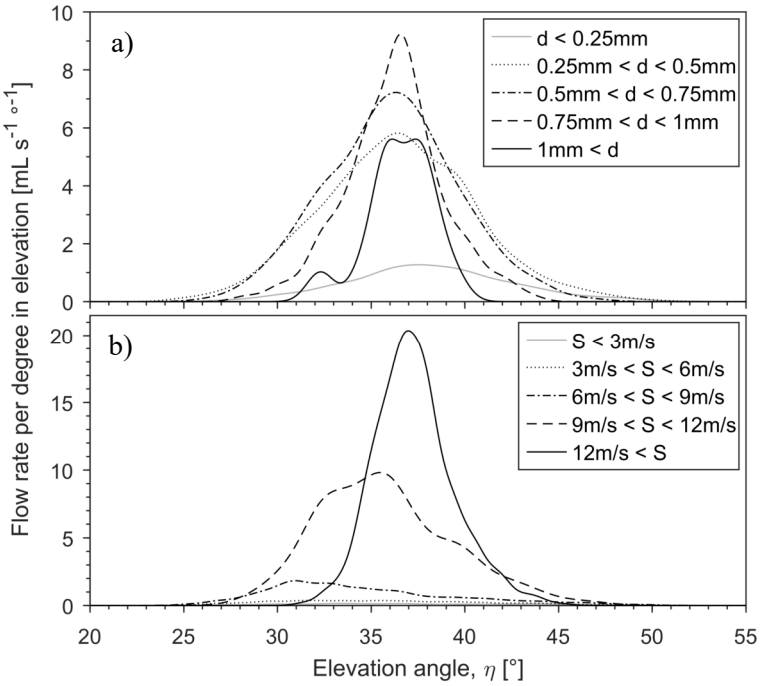

FIGURE 3.17: Spatial distributions of the liquid volume flux, 326 mm from the hollow-cone nozzle, for a number of discrete a) diameter (d) and b) speed (S) classes. These profiles, rotated about the axis of symmetry (η = 90°), represent the distribution of droplets within spray HC.

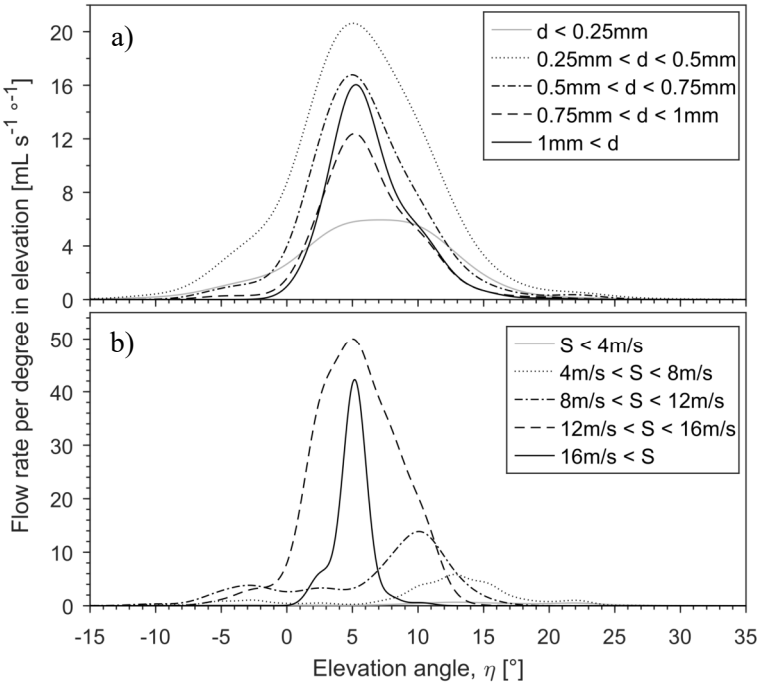

FIGURE 3.18: Spatial distributions of the liquid volume flux, 221 mm from the deflector-plate sprinkler, for a number of discrete a) diameter (d) and b) speed (S) classes. These profiles, rotated about the axis of symmetry (η = 90°), represent the distribution of droplets within spray DP.

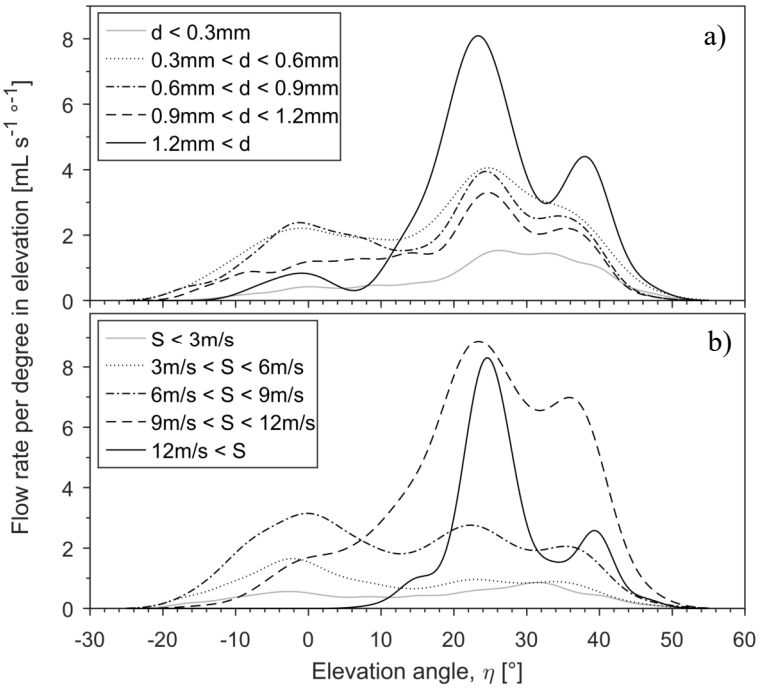

FIGURE 3.19: Spatial distributions of the liquid volume flux, 533 mm from the butterfly sprinkler, for a number of discrete a) diameter (d) and b) speed (S) classes. These profiles, rotated about the axis of symmetry (η = 90°), represent the time-averaged distribution of droplets within spray B.

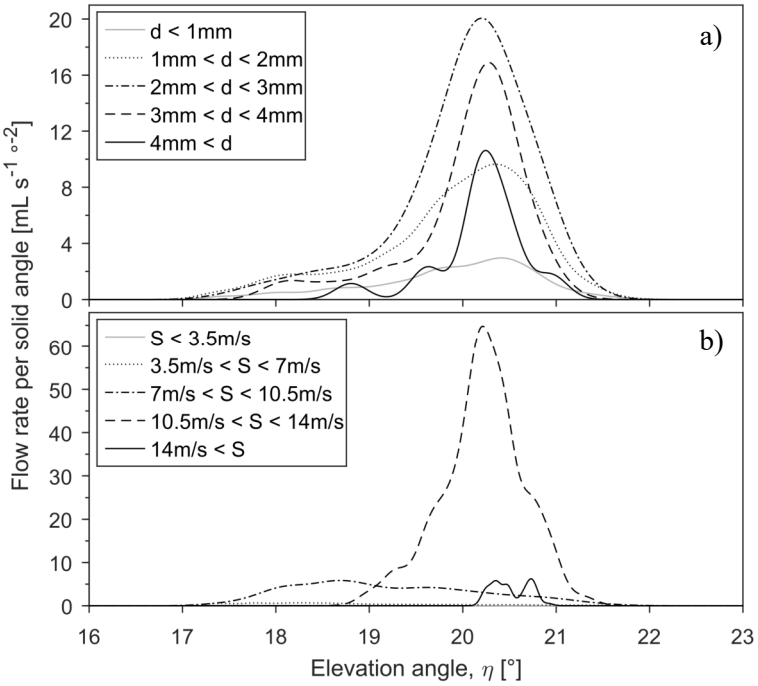

FIGURE 3.20: Spatial distributions of liquid volume flux through the vertical centre plane (i.e. at $\zeta = 0°$) of the spray generated by the impact sprinkler main nozzle, measured 6 m from the nozzle. Results are presented in terms of the liquid volume flux per solid angle, for a number of discrete a) diameter (d) and b) speed (S) classes. The sprinkler was inclined forward during measurement, such that $(\eta, \zeta) = (15°, 0°)$ was horizontal. Separate measurements found the sprinkler rotation period to be 27.7s. The initial mean velocity of the jet was 19 m s^{-1} at $\eta = 26°$.

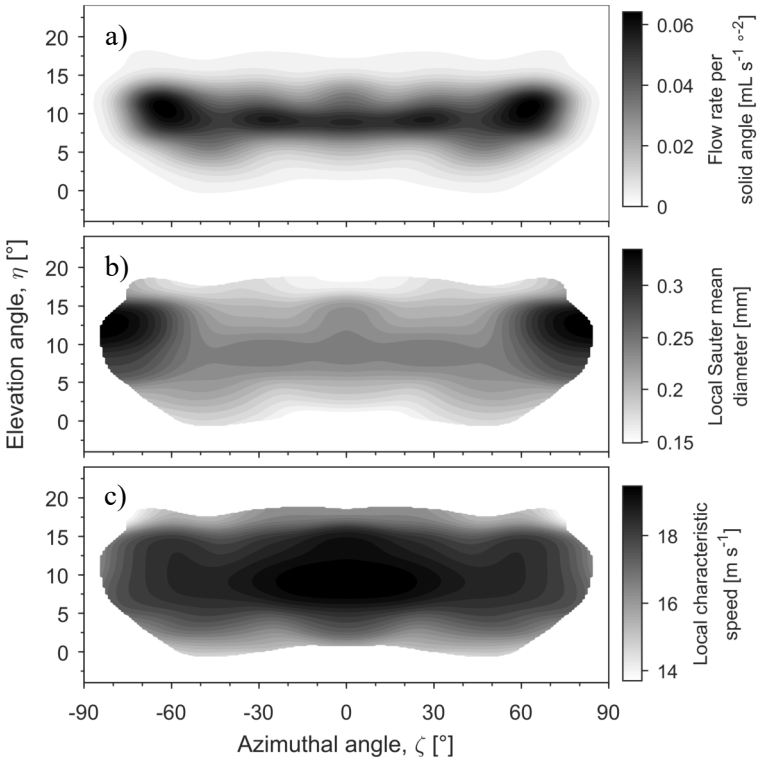

FIGURE 3.21: Spatial distributions of: a) liquid volume flux, b) local Sauter mean diameter ($\grave{d}_{32}$), and c) local characteristic speed ($\grave{S}_{ch}$), 100 mm from the flat-fan nozzle (in spray FF).

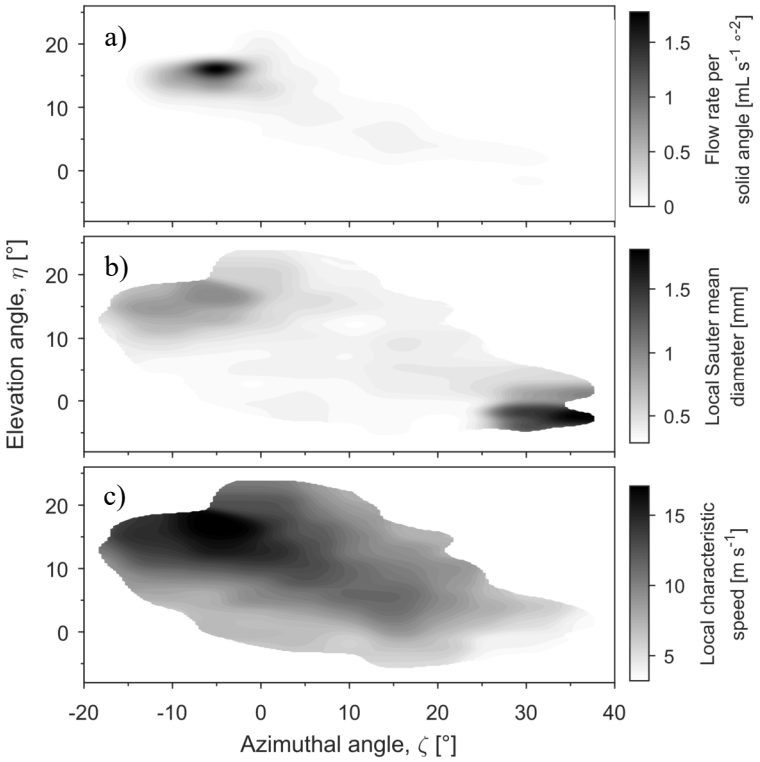

FIGURE 3.22: Spatial distributions of: a) liquid volume flux, b) local Sauter mean diameter ($\grave{d}_{32}$), and c) local characteristic speed ($\hat{S}_{ch}$), 536 mm from the auxiliary impact sprinkler nozzle (in spray IA). The sprinkler was restrained during measurement, to prevent rotation about the y-axis.

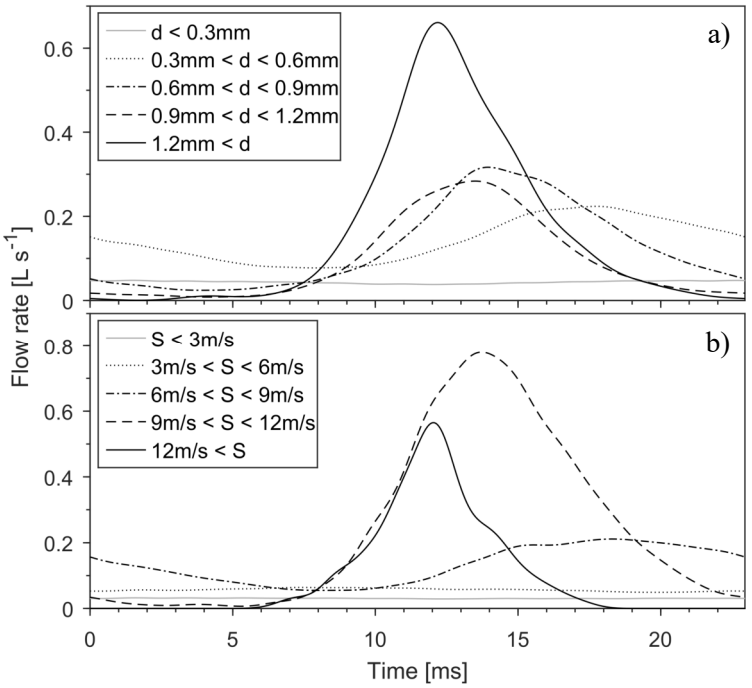

FIGURE 3.23: Temporal variations in spray B, measured at a fixed azimuthal angle (ζ = 0), 533 mm from the sprinkler, and plotted for one rotation of the sprinkler deflector. Results are expressed in terms of the volume flow rate of droplets within discrete a) diameter (d) and b) speed (S) classes. Slower, smaller droplets tended to lag behind the predominant, outward-moving spiral of droplets in this spray.

3.6 Conclusion

Six sprays have been experimentally characterised. Each spray was produced by a sprinkler similar to those mentioned in reports and technical guidance related to wildfire sprinkler systems. Droplet diameters and speeds were measured at a fixed distance from each sprinkler; each sprinkler was supplied with water at one pressure. Kernel density functions and standard functional forms were fitted to the marginal distributions of droplet diameters and speeds. Spatial and, where relevant, temporal variations in the distributions were also investigated. Such information on the characteristics of each spray is suitable for use in defining spray source conditions for CFD simulations, or other, similar work. Moreover, this new evidence appears to be the first of its kind for the sprinklers investigated here. Results presented here are specific to the five sprinklers investigated, at one operating pressure and distance from the sprinkler nozzle in each case. Nevertheless, accurate simulations of these sprinklers are now made possible, and the methods developed in doing so may be extended to other sprinklers in the future.

A back-lit high-speed videography technique was employed to measure the sprays. A focal criterion, based on the point-spread function half-width of defocused droplet images, was used to define a distinct DOF for the measurements. This experimental approach proved to be a relatively inexpensive method to obtain detailed information pertaining to droplet properties, beyond the primary breakup region of a spray. Furthermore, the experimental method was particularly well-suited to large, non-spherical droplets, which were common in the sprays investigated. Experimental parameters, such as working distance, frame rate, spray orientation and the distance from the sprinkler at which measurements were taken, needed to be optimised for each spray. A detailed calibration procedure was also necessary; however, this was only required once for a given optical setup.

A custom-built script was developed to analyse videos of the sprays. The combination of new and existing methods that were employed proved to be effective and accurate within the DOFs of interest. A new method to automatically detect and separate overlapping droplet images, based on the grey-level gradient at the image boundary, performed better than previously established

methods based on watershed algorithms or the curvature of image outlines, especially when applied to images of non-spherical droplets. Tracking of droplets between video frames was formulated as an optimisation problem, using cost functions based on droplet image properties.

A number of potential sources of error were identified and addressed in the characterisation procedure. Spurious results, caused by incorrect initial pairings in the tracking process, were removed by disregarding droplets that had been tracked between fewer than three frames, or had a high standard deviation in horizontal velocity. Some droplets, formed by splashing on surfaces in the test enclosure, or reentrained back into the field of view, were eliminated from the results by setting limits on the acceptable droplet direction of travel. However, smaller reentrained and splashed droplets tended to follow the bulk flow of droplets more closely, so they were not all removed. Thus, results presented here may include some bias towards smaller droplets. Such bias could be reduced in future studies through the use of a larger test enclosure. Bias in the data towards slower droplets, due to the video sampling procedure that was adopted, and droplets close to the axis of symmetry, in axisymmetric sprays, were eliminated by weighting the influence of each measured droplet on the results.

Chapter 4

Wind–Spray Interaction: Full-Scale Experiments

This chapter presents an experimental study into the dispersion of water, emitted by a sprinkler, around a bluff body that is immersed in the atmospheric boundary layer (ABL). The primary aim of the study was to produce data suitable for the validation of CFD simulation methodologies, intended for the analysis of bushfire sprinkler system operation in windy conditions. Results from the experiments have been used to validate a simulation methodology in Chapter 5.

4.1 Introduction

The field of wind engineering has developed significantly since the pioneering work on boundary layer flows by von Karman, Prandtl and Taylor in the early 1900s (Baker 2007). Improved technology and techniques have enabled researchers to better understand the complex physical phenomena involved in wind flow over the surface of the earth, which has, in-turn, led to more sophisticated designs for buildings and other human-made structures. In particular, the application of computational fluid dynamics (CFD) techniques to wind engineering has enhanced the ability of researchers to model complex problems, by enabling them to obtain comprehensive 'whole flow field' data, at full-scale and under well-controlled conditions (Blocken 2014). However, the numerous sources of uncertainty that must be understood and minimised to produce accurate results with CFD have been widely acknowledged, and it is also recognised that

erroneous CFD results can often be interpreted as realistic or accurate by unskilled researchers (Blocken 2014; Britter & Schatzmann 2007; Franke *et al.* 2007; Stathopoulos 2002; Tominaga & Stathopoulos 2013). Thus, high-quality experimental data remains indispensable to the field of wind engineering, for use in the validation of CFD methodologies and development of empirical sub-models, as well as for purely experimental investigations.

Measurements of ABL flow around buildings can be obtained through full-scale experiments in natural wind, or at reduced scale in boundary layer wind tunnels. Both approaches have advantages and disadvantages. Wind tunnels can produce flows with specific characteristics and replicate the same flow for comparison studies. However, due to the reduced scales involved, it can be extremely difficult or impossible to produce air flow in a wind tunnel that accurately matches every important characteristic of the ABL flow of interest, especially in cases involving additional physical phenomena, e.g. significantly non-isothermal or multiphase flows (Cermak 2003; Holmes 2015; Tanaka 1990; Tieleman 2003). In contrast, full-scale, on-site experiments do not require compromises to be made in terms of flow similitude, but they offer little or no control over test conditions and no opportunity to exactly reproduce conditions from past experiments.

Ideally, test cases for CFD validation are as simple as possible, in terms of the flow geometry, physical phenomena involved and influence on the flow from outside of the region of interest, while still capturing the fundamental details that are of interest. Many previous experimental campaigns in the field of wind engineering have focused on boundary layer flow around cubes and over trenches, e.g. Castro and Robins (1977); Jiang *et al.* (2003); Li and Meroney (1983); Meinders, Hanjalic and Martinuzzi (1999); Oke (1988); Pavageau and Schatzmann (1999); Richards *et al.* (2007); Richards, Hoxey and Short (2001). The ability of different simulation techniques to replicate the complex features of flow around isolated buildings and urban street canyons can be tested, by comparison to results from such studies. Cubes have often been adopted to represent buildings in such studies, since they are simple in form but have similar sharp edges to those that establish the dominant flow features that form around buildings.

The work described in this chapter was undertaken to produce validation data for simulations of water spray dispersion around buildings in windy conditions. Experiments were conducted using a 2.4-metre sharp-edged cube, exposed to natural wind. Isolated sprinklers were operated near the cube and measurements were taken of water deposition at various locations on the cube and ground surfaces. ABL properties were also measured near the cube during the experiments. Sprays that were characterised in Chapter 3 were used in this study, so that they could be accurately represented in simulations of the test cases investigated here. Details of the experimental method are outlined in Section 4.2, and detailed results are presented in Section 4.3.

4.2 Method

4.2.1 Experimental Site

The experiments were conducted in a field, with a relatively long, flat, unobstructed fetch to the north-east (see Figure 4.1 and Figure 4.2). The cube was orientated with one face pointing north-east and experiments were conducted only when the mean wind direction was approximately from that direction. Thus, the nearest 200 m of terrain to the cube, in the upwind direction, was typically characterised by short (~100mm high) grass, and a further 120 m was unobstructed by buildings or large vegetation. In experiments with a more northerly wind direction, a carpark containing irregularly spaced cars was 75 m upwind and two four-storey buildings were located 200 m upwind. A meteorological mast, fitted with equipment to measure the ABL, was located 15.6 m south-east of the cube.

FIGURE 4.1: Photograph of the cube and meteorological mast, looking north-east.

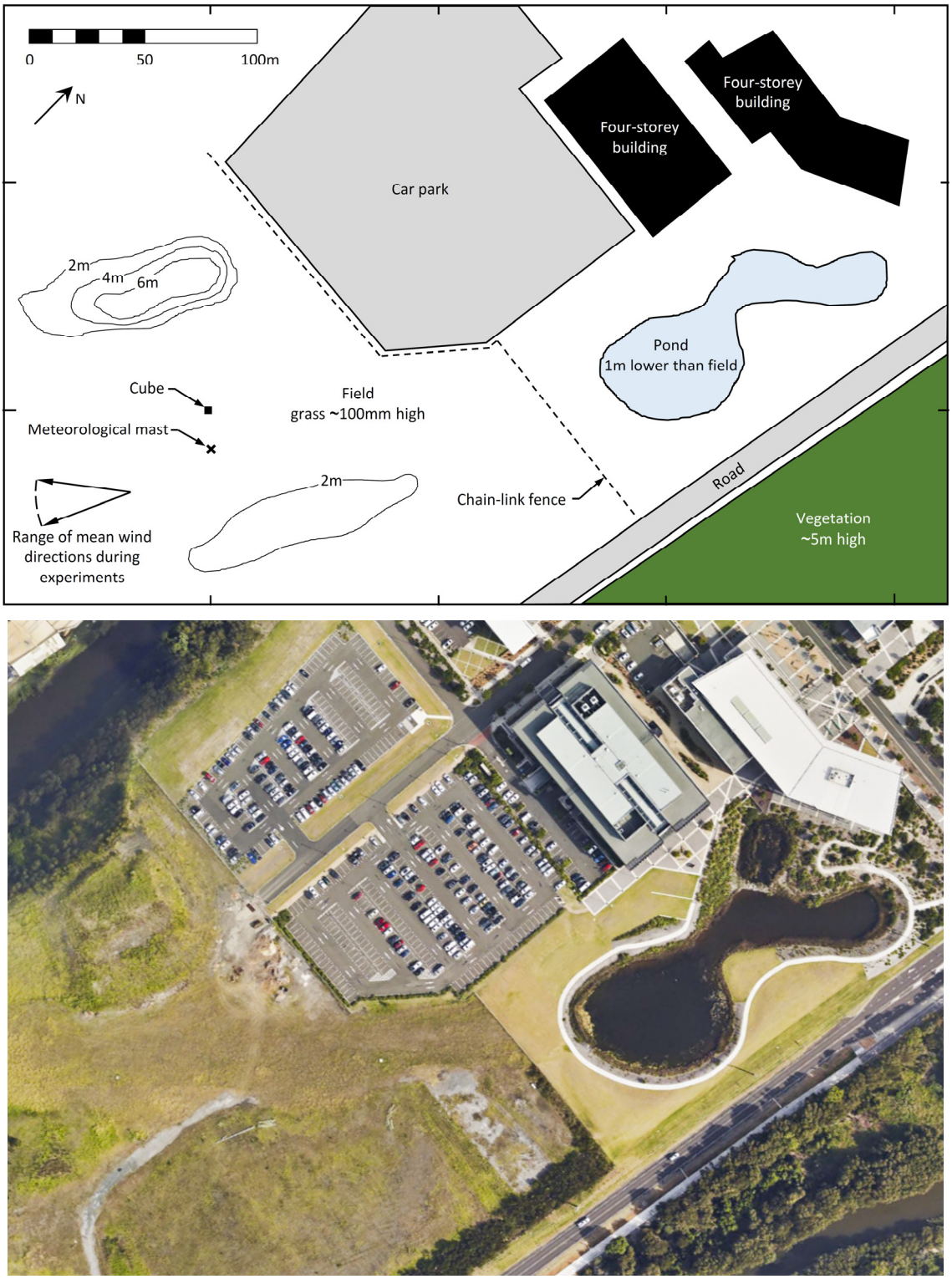

FIGURE 4.2: Map of the experimental site (top) and a corresponding aerial photograph (bottom). Heights on contour lines on the map refer to height above the ground level surrounding the cube. The cube and meteorological mast were not installed when the photograph was taken.

4.2.2 Test Cases

Experiments were conducted with an isolated sprinkler operating near the cube. Four cases were investigated involving the butterfly and hollow-cone sprinklers characterised in Chapter 3, each was operated at two different locations relative to the cube (see Figure 4.3 and Table 4.1). The butterfly sprinklers were upright for all tests, and the hollow-cone sprinklers were orientated such that the centre of the cone pointed in the negative x direction (i.e. north-east). The water supply to the sprinklers was maintained at pressures within ±5% of the values reported in Table 4.1 during the experiments, using a centrifugal pump, pressure regulator and Wika™ analogue pressure gauge.

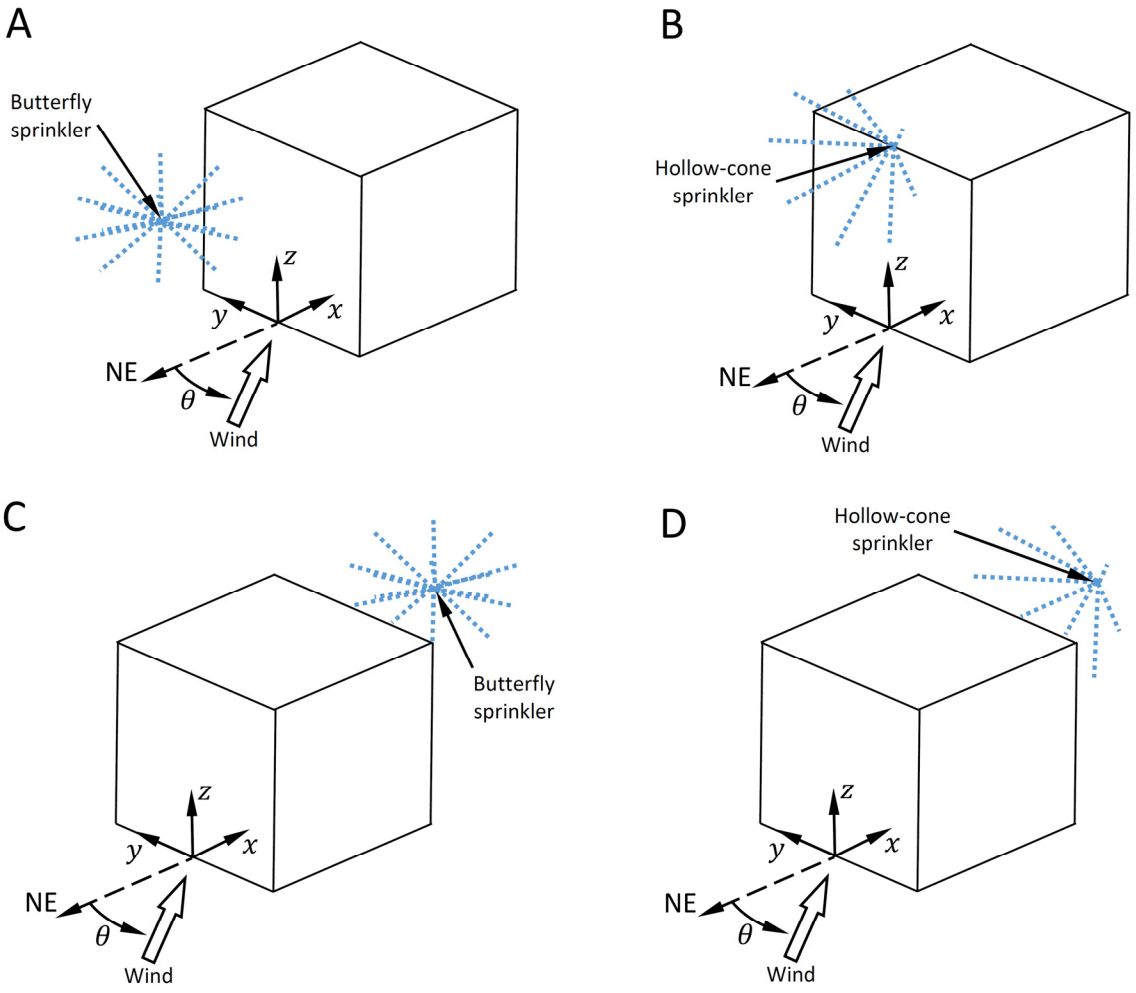

FIGURE 4.3: Outdoor spray test geometries. The butterfly sprinkler was upright in cases A and C, while the hollow-cone sprinkler was orientated such that the centre of the cone pointed in the negative x direction in cases B and D.

TABLE 4.1: Details of the four test cases (A, B, C and D).

Case	Sprinkler model	Location	Pressure [kPa]	Flow rate [L min^{-1}]
A	Holman ½-inch brass butterfly sprinkler	Windward	200	34
B	½-inch Champion S9F hollow-cone nozzle	Windward	345	12.5
C	Holman ½-inch brass butterfly sprinkler	Leeward	200	34
D	½-inch Champion S9F hollow-cone nozzle	Leeward	345	12.5

Four separate experiments were conducted for each case. The exact locations of the sprinklers varied somewhat between experiments, and the locations for each test are listed in Table 4.2. Images of the experiments were analysed, to determine the sprinkler locations in the z-x plane with more accuracy than was practicable at the time of the tests (see Table 4.2). However, it was not possible to accurately determine the lateral location of the sprinklers (i.e. in the y-direction) from the photographs. Therefore, an uncertainty of approximately ±100 mm applies to the y-locations presented in Table 4.2, except for those relating to Case B since the sprinkler was mounted directly to the cube, at exactly $y = 0$ in that case.

TABLE 4.2: Sprinkler locations in each experiment. The butterfly sprinkler was upright in cases A and C; the hollow-cone sprinkler was orientated such that the centre of the cone pointed in the negative x direction in cases B and D.

	Experiment															
	A1	**A2**	**A3**	**A4**	**B1**	**B2**	**B3**	**B4**	**C1**	**C2**	**C3**	**C4**	**D1**	**D2**	**D3**	**D4**
Case	A	A	A	A	B	B	B	B	C	C	C	C	D	D	D	D
x **[m]**	-1.87	-1.87	-1.91	-1.90	0	0	0	0	4.26	4.26	4.19	4.19	3.33	3.33	3.31	3.31
y **[m]**	0	0	0	0	0	0	0	0	0	0	0	0	0	0	0	0
z **[m]**	1.87	1.87	1.86	1.88	2.43	2.43	2.43	2.43	1.95	1.95	1.94	1.94	1.83	1.83	1.81	1.81

4.2.3 Wind Measurement

The meteorological mast was fitted with two Gill WindMaster three-axis, ultrasonic anemometers (see Figure 4.4), located at heights of 2 m and 10 m and with a sampling frequency of 20 Hz, and a two-axis Vaisala WMT700 Windcap anemometer, which took measurements of horizontal wind velocity, 6 m from the ground, at a frequency of 4 Hz. The ambient dry-bulb and wet-bulb

temperatures (referred to hereafter as T and T_{WB}, respectively) were measured once per experiment, at a height of 1 m, 1 m from the base of the mast.

FIGURE 4.4: Photograph of the experimental setup, showing the meteorological mast near the cube. Three-axis ultrasonic anemometers were fitted at heights of 2 m and 10 m on the mast, and a two-axis ultrasonic anemometer was fitted at a height of 6 m.

Data from the three anemometers was analysed, to determine time-averaged properties of the ABL, as well as various turbulence characteristics. The mean wind direction, relative to the normal to the upwind face of the cube, $\bar{\theta}$, was determined for each experiment using air velocity measurements taken at $z = 10$ m and the measured velocity components, u, v and w, were transposed into streamwise, lateral and vertical components (U, V and W, respectively). The mean streamwise velocity, $\overline{U}(z)$, was evaluated at the height of each anemometer, for each experiment. The turbulence intensity at each elevation was also calculated, as follows (Stull 1988):

$$I_i(z) = \frac{\sigma_i(z)}{\overline{U}(z)} \tag{4.1}$$

where I_i and σ_i are the turbulence intensity and root mean-square (RMS) of velocity fluctuations in coordinate direction i, respectively. Note that in the streamwise direction, velocity fluctuations were defined as deviations from the mean, i.e:

$$\sigma_U = \sqrt{\overline{(U - \overline{U})^2}} = \sqrt{\overline{(U')^2}} \tag{4.2}$$

Turbulence was further characterised by estimating the Eulerian integral scales of time and length from each velocity time-series. The Eulerian integral timescale of turbulence in i^{th} coordinate direction was defined as:

$$\tau_i(z) = \int_0^\infty R_{i,z}(s)\, ds \tag{4.3}$$

where $R_{i,z}$ is the temporal autocorrelation of the velocity fluctuations in the i^{th} coordinate direction, at height z. Solution of the semi-infinite integral in (4.3) is often not possible in practice, since $R_{i,z}(s)$ cannot reliably be evaluated for $s \gtrsim P_t/2$, where P_t is the length of the time-series, and $R_{i,z}$ often contains oscillatory components that decay slowly with respect to s. O'Neill *et al.* (2004) compared four methods to approximate the integral length scale within a finite domain, which is analogous to the estimation of an integral timescale from a finite time-series, and concluded that integration of R to the first zero-crossing produced consistent results. In this study, a linear function was first fitted to, and then subtracted from, the time-series of velocity measurements. Integral timescales were then estimated by numerically integrating the autocorrelation of each pre-processed time-series, from zero to the first zero-crossing.

Eulerian integral length scales were estimated by invoking Taylor's 'frozen turbulence' hypothesis, which states that turbulent eddies are approximately stationary relative to the mean flow (Taylor 1938). Thus, the turbulence integral length scale in the i^{th} coordinate direction was given by:

$$\Lambda_i(z) \approx \tau_i(z)\overline{U}(z) \tag{4.4}$$

Turbulence energy spectra were also analysed. Velocity data, from which linear trends had already been removed, were further pre-processed by imposing a 'bell taper', formed using a sine

curve, to the first and last 10% of the duration of each time-series. Discrete spectral energy profiles were calculated from the pre-processed data using the fast Fourier transform (Ogata 1998) and continuous energy density spectra were estimated from the discrete profiles. Each energy density spectrum was smoothed using a moving-average filter, the width of which was increased with increasing frequency, for presentation in a log-log space.

4.2.4 Water Deposition Measurement

Spray deposition gauges were designed and built to collect water that impinged on regions of the cube external surfaces. A preliminary design was developed (see Figure 4.5), based on that of many 'horizontal rain gauges' that have been used to measure wind-driven rain on building facades (Blocken & Carmeliet 2004, 2006). Water that struck, adhered to and then flowed from the 200 mm × 200 mm collection plate was funnelled into a measuring cylinder. Blocken and Carmeliet (2006) found that, counterintuitively, vertical rain gauges with collection plates made of hydrophilic materials, such as glass, retained less water than surfaces that were more hydrophobic. This was due to the contact angle of droplets adhered to the collection surfaces; hydrophilic materials produced a lower contact angle, thereby reducing the volume of adhered droplets. Any water retained on the collection surfaces of the spray gauges would not flow down to the measuring cylinder, and thus would not be measured. For this reason, the preliminary spray gauge design of the present project featured a glass collection plate.

Testing of the prototype spray gauge revealed that a substantial portion of water impinging on the collection plate was not measured due to splashing. A second spray gauge design was developed (see Figure 4.6), based on one presented by Högberg (2002) and included in the review of Blocken and Carmeliet (2006). It featured a deep collection chamber rather than a collection plate, to minimise splashing losses. Testing of the second spray gauge design confirmed that much less water was splashed from that gauge than was from the preliminary design. 'Vertical' and 'horizontal' versions of the second gauge design were developed, to collect water that would otherwise strike the cube walls or top surface, respectively.

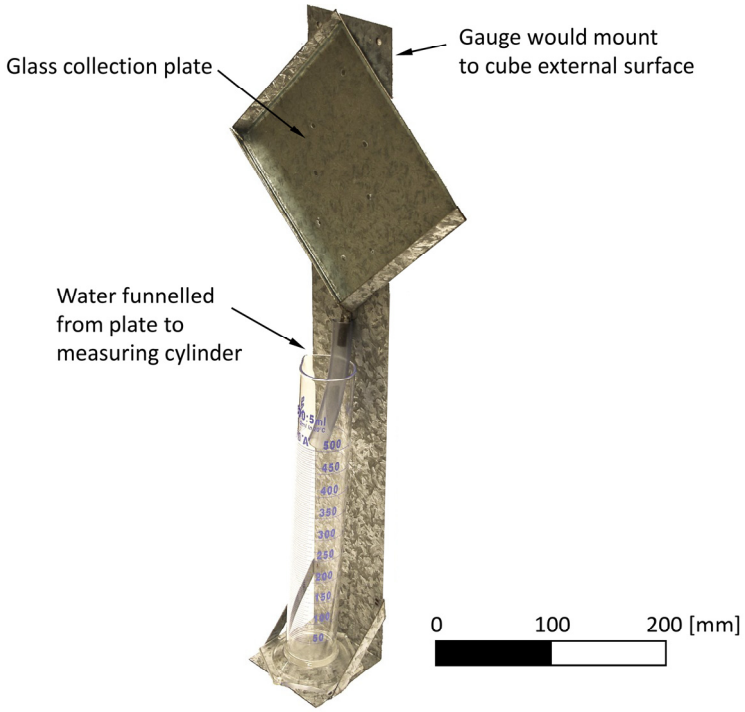

FIGURE 4.5: Vertical spray gauge preliminary design. A substantial portion of the water impinging on to the gauge collection plate was observed to splash beyond the gauge during early trials, so an improved design was developed.

The gauges and measuring cylinders were designed to be almost entirely contained within the cube, to minimise their influence on air flow around the cube. However, the gauge openings were deliberately made to project 10 mm beyond the cube outer surfaces, so as to form channels that would prevent water from flowing from the cube external surfaces into the gauges. Gaps between the gauges and the cube outer surfaces were sealed with tape, to prevent airflow into or out of the cube. Gaps between the spray gauges and measuring cylinders were also sealed, to prevent air flow through the gauges.

Immediately prior to each experiment, the spray gauges were sprayed with water, to prime the gauge internal surfaces with adhered water, thereby offsetting error caused by water left on those surfaces after the experiments. The total volume of water collected by each spray gauge, during each experiment, was read directly from the measuring cylinders. Mean deposition fluxes were calculated from the volumetric measurements, gauge opening areas (which were accurately measured from photographs) and the duration of each experiment.

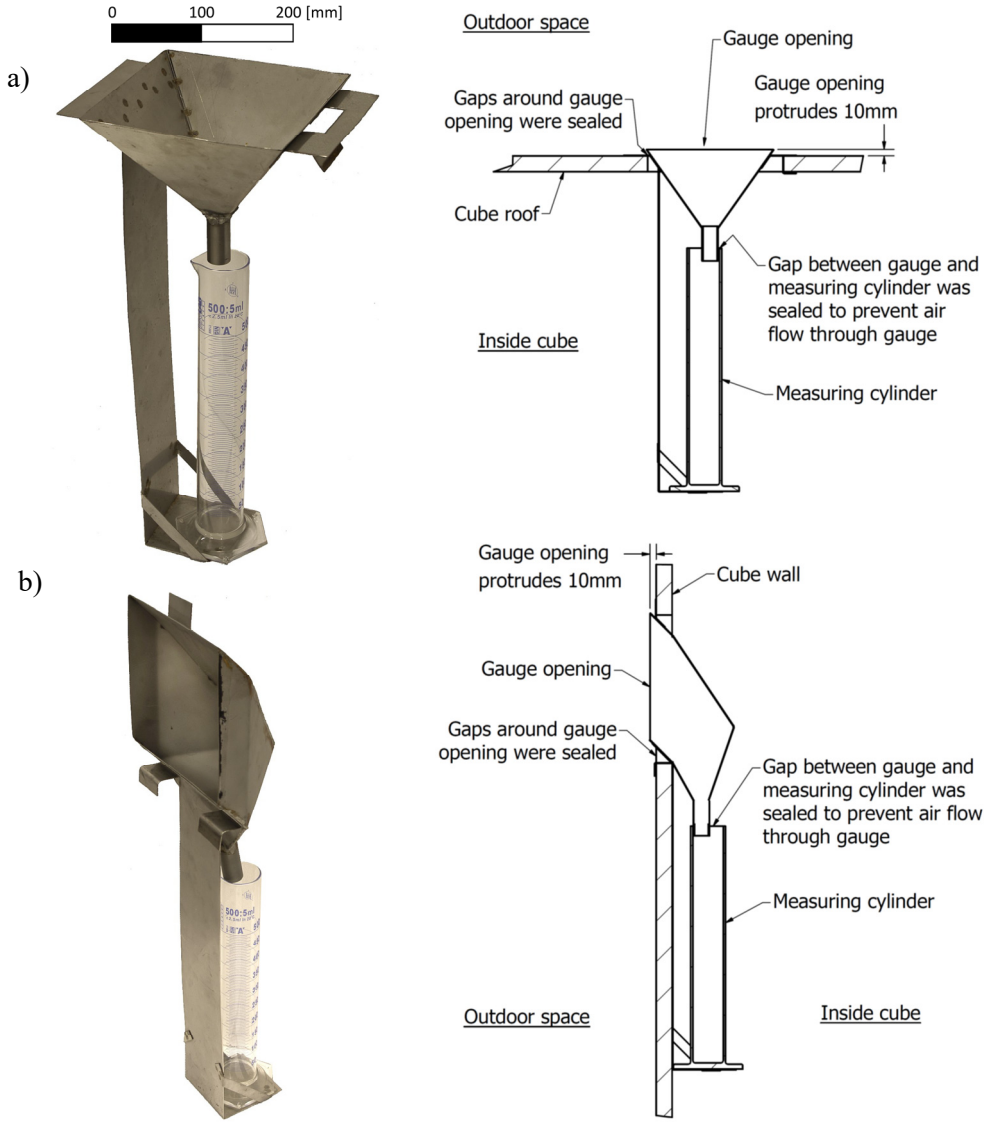

FIGURE 4.6: Horizontal (a) and vertical (b) spray gauges that were used to measure water deposition. The deep collection chambers formed by these gauges were located within the cube during experiments, which minimised their influence on airflow around the cube.

Water was also collected at ground level during experiments of Cases C and D (i.e. when sprinklers were located on the leeward side of the cube). Plastic containers, each with an open top approximately 130×100 mm^2 in size, were placed in a frame that was buried below ground level, such that the container openings protruded ~10mm above ground level (see Figure 4.7). The outer rim of each container opening was formed into a sharp edge, to reduce the portion of droplets that would be partially collected after striking the edge and splashing. The mass of each ground collection container, when empty, was measured before and after the full set of experiments, and the total volume of water deposited in the containers was determined by weighing the plastic containers after each experiment and subtracting the relevant empty container

masses. Volumetric measurements from the ground collectors were treated in the same way as volumetric measurements from the spray gauges, i.e. they were divided by the relevant container opening area (which was accurately measured from photographs) and the duration of the relevant experiment, to produce mean volumetric fluxes.

FIGURE 4.7: Photograph of the experimental setup for case D. Ground collectors are visible in the foreground (set in a frame and separated by sections of black plastic sheet).

Three horizontal spray gauges and three vertical spray gauges were installed on the cube for all sixteen experiments. The locations of the gauges varied between windward and leeward cases (see Figures 4.9 and 4.8), and were selected to resolve visible variations in the water flux incident on the cube. Ground collectors were installed in four pairs, at distances of 1 m, 3 m, 3.5 m and 4 m from the cube leeward face in experiments of case C, and distances of 2 m, 2.5 m, 3 m and 3.5 m from the cube leeward face in experiments of case D (see Figure 4.8). Experiments were continued until any one of the spray gauge measuring cylinders, or ground collection containers, was close to full capacity. The duration of each experiment was recorded, so that mean deposition fluxes could be calculated.

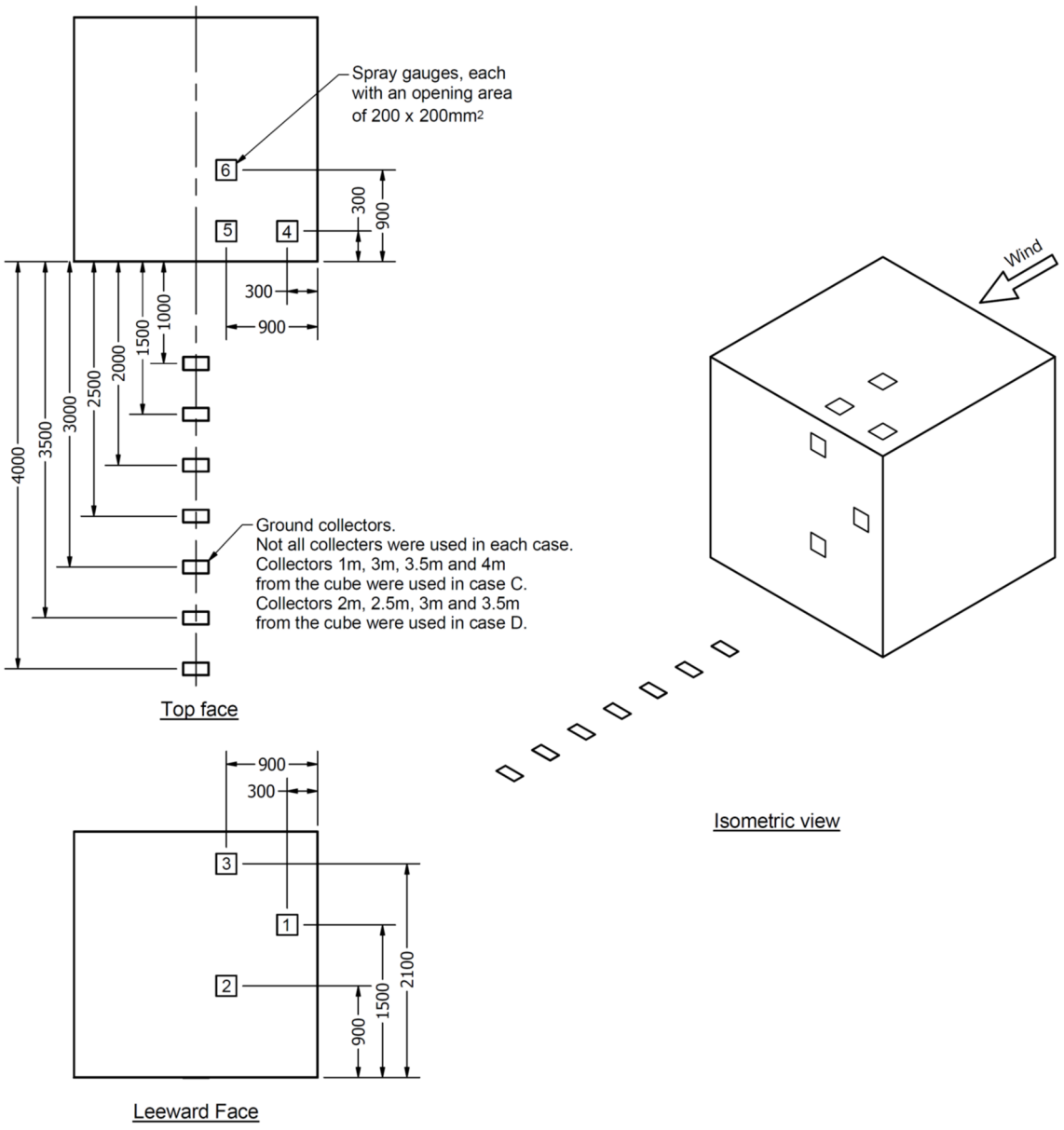

FIGURE 4.8: Spray gauge and ground collector locations for cases C and D (i.e. when sprays were implemented on the leeward side of the cube). Gauge reference numbers are indicated on the gauge. Dimensions are given to the centre of each gauge and collector; all dimensions are in mm.

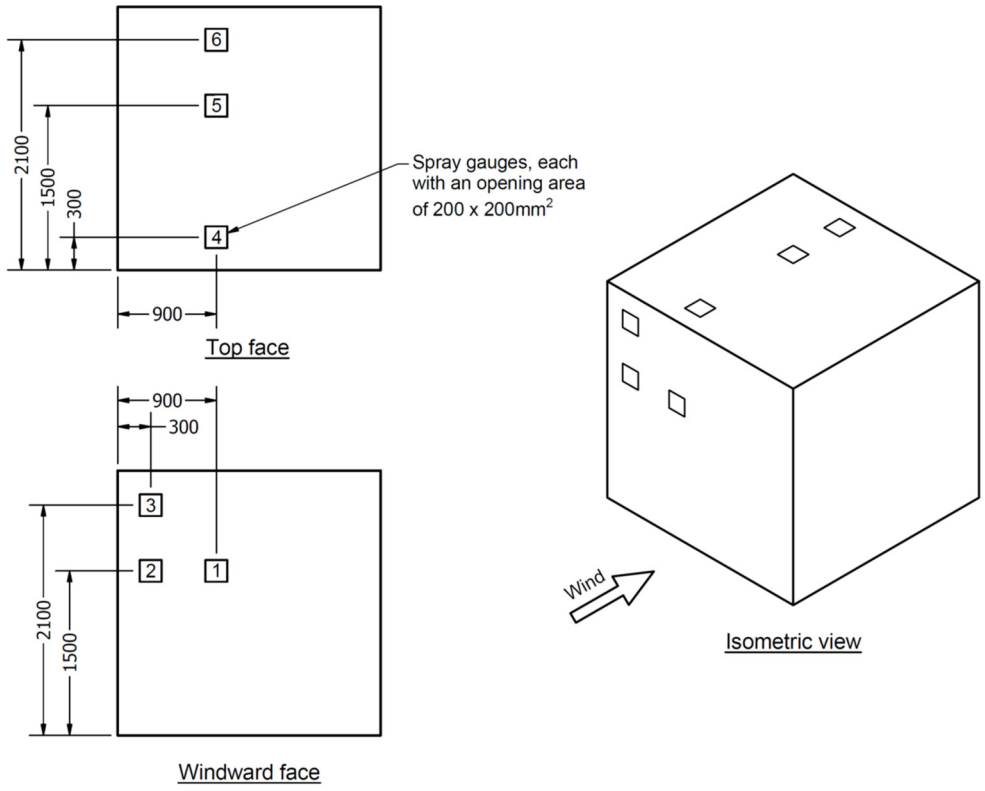

FIGURE 4.9: Spray gauge locations for cases A and B (i.e. when sprays were implemented on the windward side of the cube). Gauge reference numbers are indicated on the gauge. Dimensions are given relative to the centre of each gauge; all dimensions are in mm.

4.3 Results and Discussion

In total sixteen experiments were conducted and the duration of experiments ranged from 451 s to 1,566 s, and averaged 840 s. In addition to measurements of water deposition and wind characteristics, a number of qualitative observations were also made.

4.3.1 Qualitative Observations

The relatively large influence of drag on small droplets, compared to larger droplets, was clearly visible during the experiments. Streams of large droplets were observed to travel several metres upwind of the spray source, whereas finer water droplets of the sprays were entrained into the air flow before travelling 0.5 m from the sprinklers (see Figure 4.10). The influence of the cube on the surrounding air flow was also evident, due to spatial and temporal variations in the concentration of small airborne droplets, which allowed a number of flow features to be visualised. A highly turbulent, unsteady flow was observed near the cube leeward face (see Figure

4.10), for example, and a point of flow separation, fixed by the sharp leading edge of the cube, was also clearly visible (see Figure 4.11).

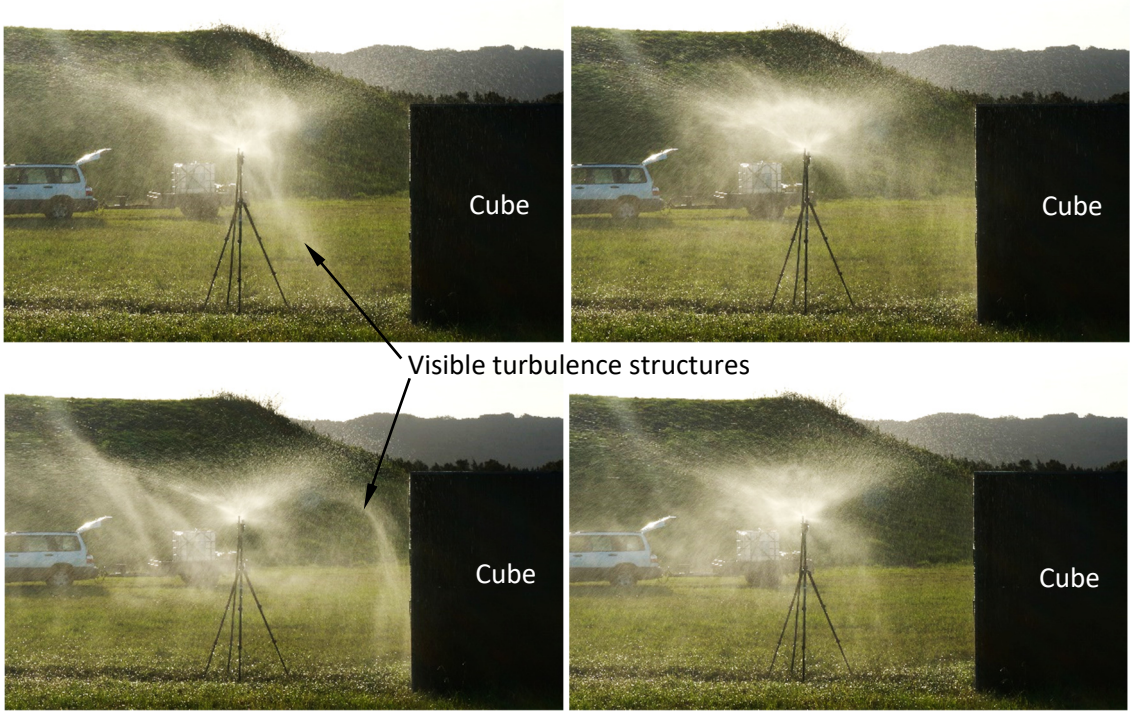

FIGURE 4.10: Series of photographs from experiment C4 ($\bar{U}(10)$ = 5.04 m s^{-1}), taken at 10 s intervals, illustrating the unsteady airflow near the cube leeward face and the relatively large influence of drag on the trajectories of small droplets, compared to larger droplets. Air flow was from right to left.

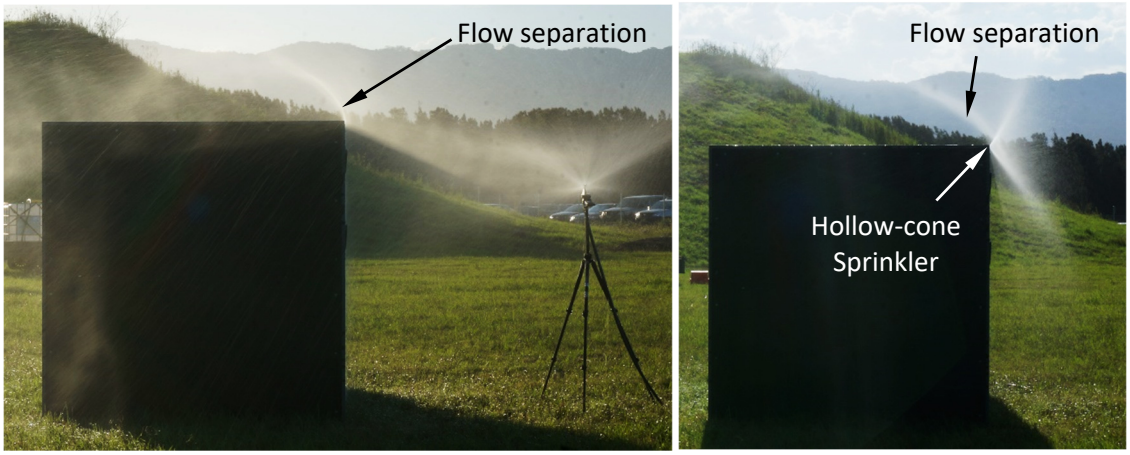

FIGURE 4.11: Photographs from experiments A4 (left; $\bar{U}(10)$ = 3.38 m s^{-1}) and B4 (right; $\bar{U}(10)$ = 3.97 m s^{-1}), showing flow separation from the cube leading edge. Air flow was from right to left.

The unsteady spray produced by the butterfly sprinkler was comprised of a 'swirl' of droplets, emitted from the rotating deflector plate within the sprinkler (see Figure 4.12). However, the dispersion of droplets tended to become more homogeneous with increasing distance from the

sprinkler, so very little periodicity was observed in the stream of droplets impinging on the cube and ground surfaces. Fluctuations in the wind velocity were observed to cause much larger temporal variations in water deposition fluxes than those resulting from the unsteady flow from the deflector plate. Gusts of wind frequently caused the location of regions of intense water deposition to move up to several metres, in all four of the cases that were tested.

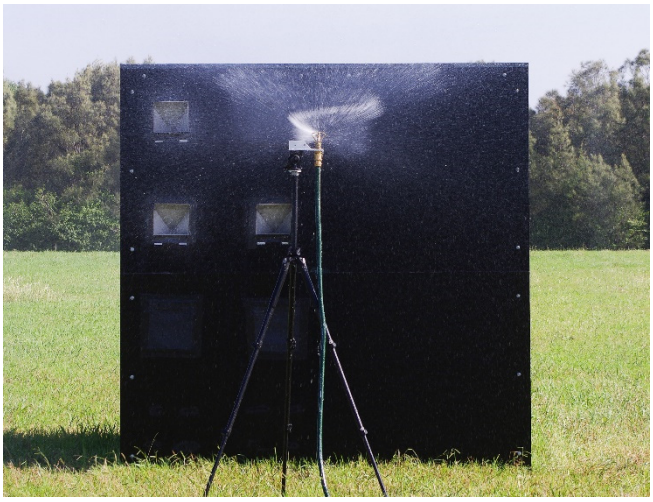

FIGURE 4.12: Photograph from Experiment A1, showing the concentrated 'swirl' of droplets emitted by the butterfly sprinkler.

4.3.2 Wind Characteristics

The mean wind speed, measured at a height of 10 m and averaged over the duration of each experiment, ranged from 3.32 m s^{-1} to 7.17 m s^{-1} (see Figure 4.13 and Table 4.3), which corresponded to Reynolds numbers between 5.3×10^5 and 1.2×10^6 based on the characteristic cube length of 2.4 m. These wind speeds did influence droplet trajectories significantly in the experiments but do not represent the full range of wind speeds that occur during wildfires (Blanchi *et al.* 2010); therefore, further testing at higher wind speeds would be worthwhile. Mean wind direction during the experiments, θ, ranged from -7.9° to 20.9°. Two four-storey buildings and a ground level open carpark were upstream of the cube when $\theta \gtrsim 17°$ (see Figure 4.2). However, there was no discernible correlation between mean wind direction and the vertical velocity profile, turbulence intensity, integral length or time scales, or energy spectra. It was concluded that the buildings and carpark did not significantly affect air flow around the cube during any of the experiments.

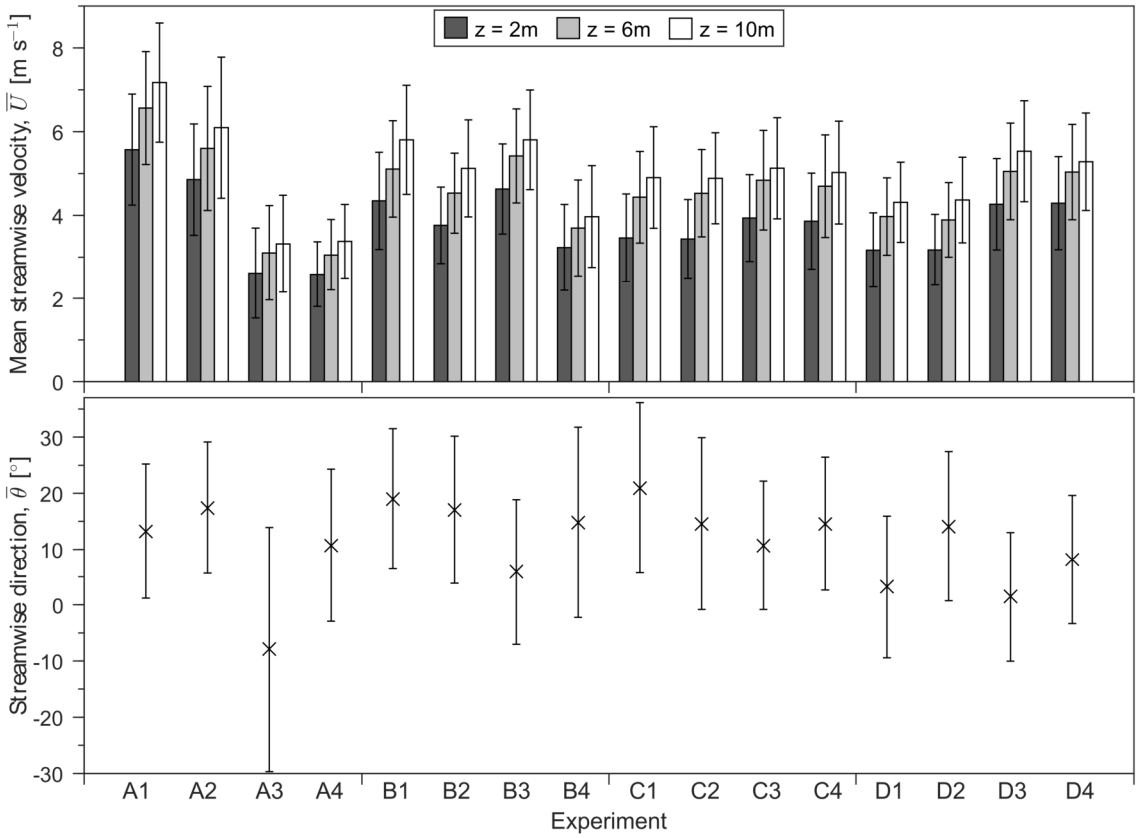

FIGURE 4.13: Measured mean streamwise wind velocities and directions from each experiment. Error bars show the RMS fluctuation in streamwise velocity, σ_U, (top) and standard deviation in streamwise direction (bottom).

A distinct anisotropy was observed in the turbulence measurements, with vertical components characterised by lower intensity and smaller length scales. Such anisotropy is a well-documented feature of boundary layer flow and is attributable to the disruption of large, low-frequency eddies by the ground (Stull 1988). Streamwise and lateral turbulence intensities were typically similar, averaging between 18% and 25% at the heights of all three anemometers. Vertical turbulence intensity was significantly lower, with mean values of 12% at $z = 10$ m and 8% at $z = 2$ m. The integral length scale of vertical turbulence was approximately equal to z at both $z = 10$ m and $z = 2$ m, while horizontal turbulence exhibited similar integral length scales at all three heights (i.e. at 2 m, 6 m and 10 m), the magnitude of which varied between experiments, but was on the order of 10–100 m (see Figures 4.14 to 4.16). Measured turbulence energy spectra were similar in the streamwise and lateral directions, but vertical turbulence contained significantly less energy at lower frequencies (see Figure 4.17).

TABLE 4.3: Mean wind characteristics for each experiment, measured at three heights (z [m]). Results include the mean wind direction ($\bar{\theta}$), mean streamwise velocity ($\overline{U}(z)$), three components of turbulence intensity (streamwise $I_U(z)$, lateral $I_V(z)$ and vertical $I_W(z)$), dry-bulb temperature (T) and wet-bulb temperature (T_{WB}).

	Experiment															
	A1	**A2**	**A3**	**A4**	**B1**	**B2**	**B3**	**B4**	**C1**	**C2**	**C3**	**C4**	**D1**	**D2**	**D3**	**D4**
$\bar{\theta}$ **[°]**	13.2	17.4	-7.9	10.7	19.0	17.0	5.9	14.8	20.9	14.5	10.7	14.5	3.2	14.1	1.5	8.1
$\overline{U}$**(10) [m s^{-1}]**	7.17	6.10	3.32	3.38	5.80	5.12	5.81	3.97	4.91	4.89	5.13	5.02	4.31	4.37	5.53	5.28
$\overline{U}(6)/\overline{U}(10)$	0.937	0.940	0.934	0.904	0.903	0.909	0.934	0.931	0.904	0.927	0.944	0.935	0.921	0.891	0.913	0.954
$\overline{U}(2)/\overline{U}(10)$	0.777	0.797	0.788	0.766	0.749	0.735	0.798	0.813	0.706	0.704	0.768	0.769	0.735	0.727	0.771	0.813
$I_U(10)$ **[%]**	19.8	27.6	35.0	26.0	22.4	22.6	20.4	30.7	24.7	22.2	23.5	24.5	22.2	23.4	21.8	22.0
$I_V(10)$ **[%]**	21.7	21.6	42.3	25.5	22.5	24.6	24.1	33.6	27.4	28.8	20.5	20.3	24.1	25.3	19.4	20.1
$I_W(10)$ **[%]**	10.5	11.3	15.5	13.1	11.1	11.5	10.6	14.0	10.7	11.0	11.7	12.6	11.4	11.4	11.9	12.7
$I_U(6)$ **[%]**	18.8	24.3	34.2	25.1	19.9	18.7	19.3	28.9	22.3	21.3	23.2	24.4	21.4	20.4	20.8	21.5
$I_V(6)$ **[%]**	20.2	20.5	30.7	25.8	20.1	21.1	22.2	25.5	17.2	18.6	11.1	12.7	17.7	15.8	8.7	11.0
$I_U(2)$ **[%]**	18.5	21.8	32.7	23.2	20.0	17.9	18.5	26.0	21.4	19.3	20.3	22.9	20.7	19.5	19.7	21.1
$I_V(2)$ **[%]**	17.1	17.6	27.9	17.5	16.8	17.6	18.0	26.0	18.9	19.5	17.9	19.7	16.3	18.0	19.7	21.2
$I_W(2)$ **[%]**	7.3	7.0	9.4	7.9	7.4	7.6	7.4	8.4	7.3	7.5	7.9	8.0	7.8	7.5	8.0	8.3
T **[°C]**	25.9	25.9	29.0	25.9	25.1	25.1	28.5	30.5	23.0	29.6	24.5	23.5	22.0	20.6	26.1	25.2
T_{WB} **[°C]**	19.2	19.2	20.0	20.2	20.0	20.0	20.7	20.6	17.0	16.1	17.4	16.9	18.0	17.2	17.8	17.6

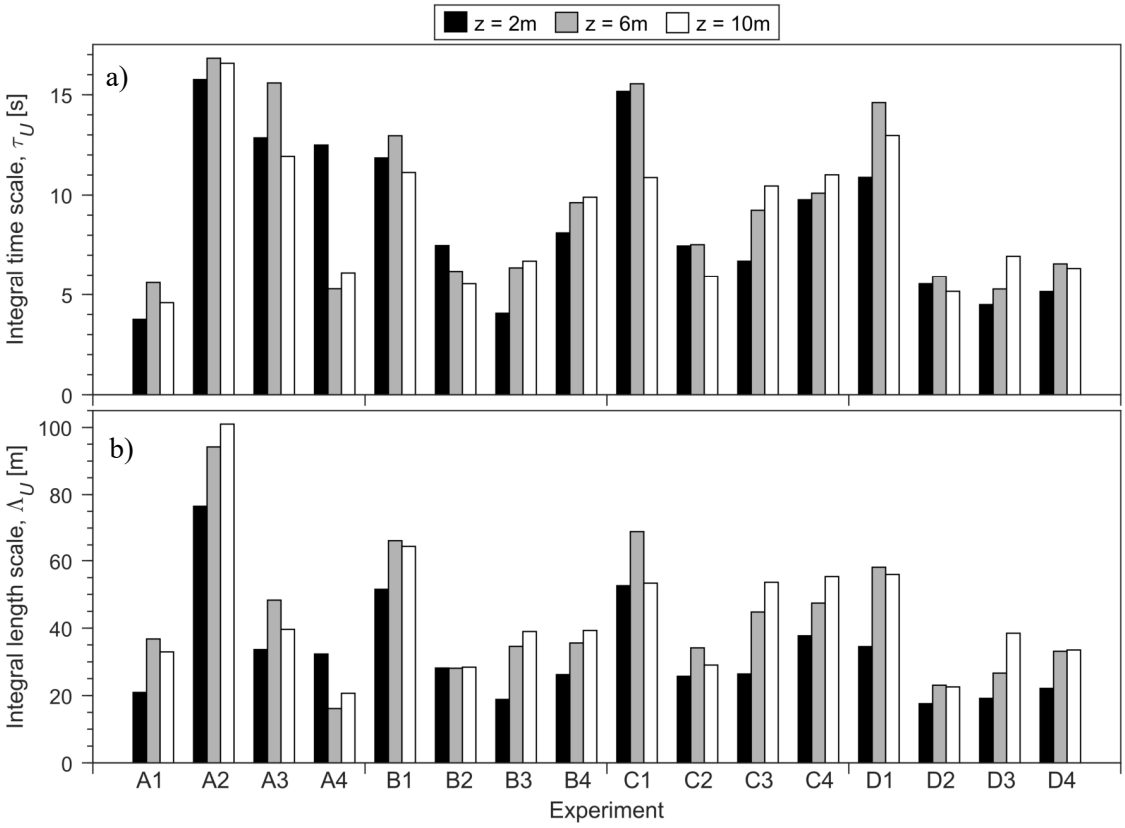

FIGURE 4.14: Integral a) time and b) length scales of streamwise turbulence, measured at three heights.

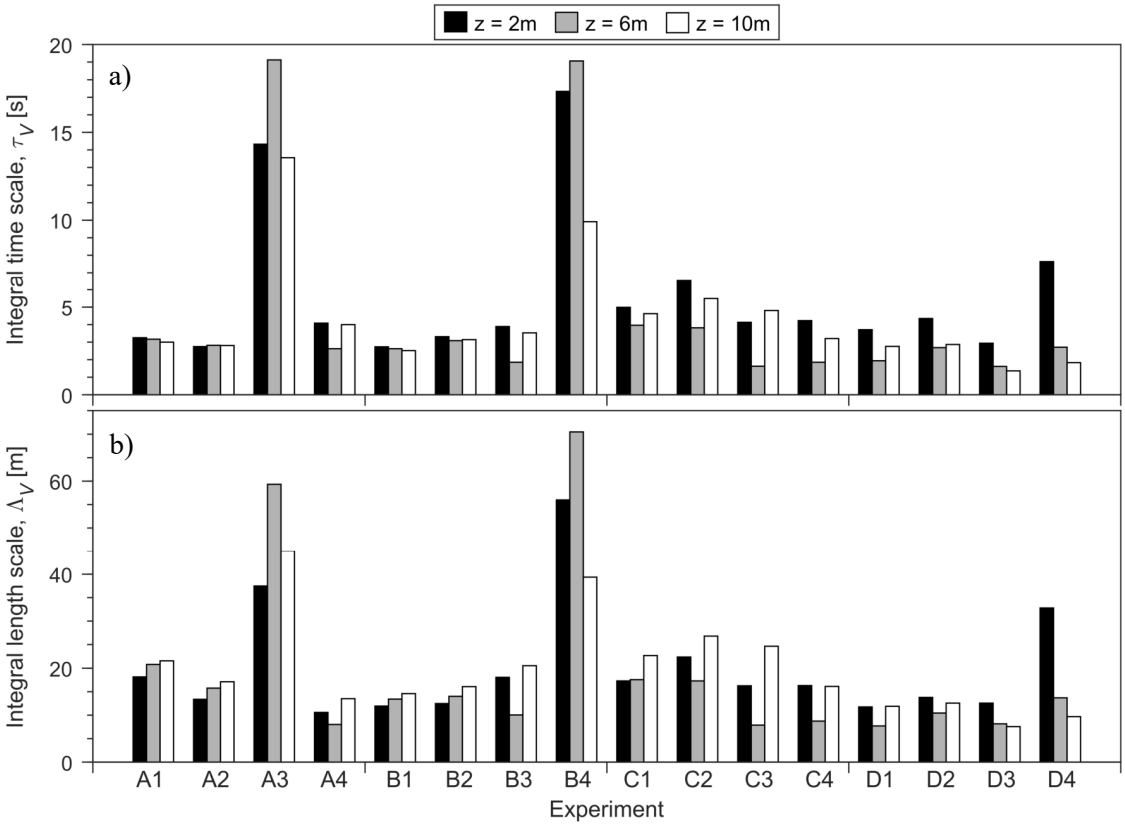

FIGURE 4.15: Integral a) time and b) length scales of lateral turbulence, measured at three heights.

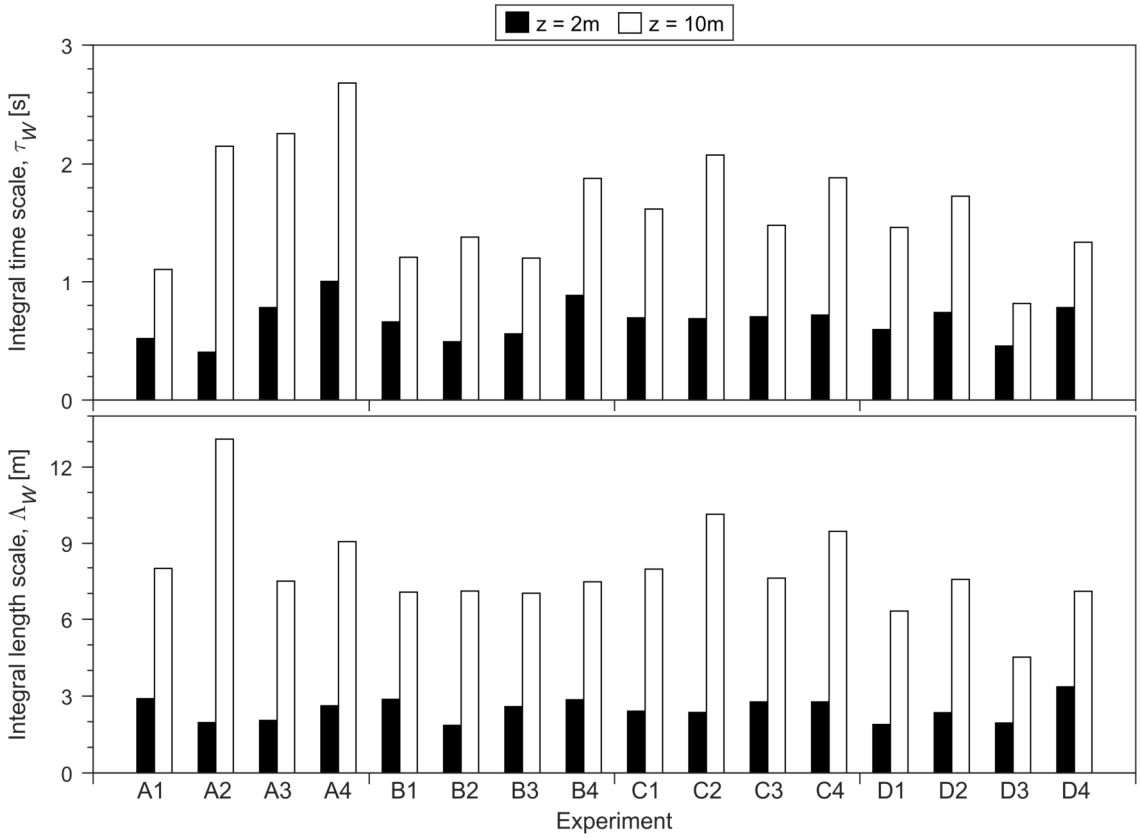

FIGURE 4.16: Integral a) time and b) length scales of vertical turbulence, measured at two heights.

The inertial subrange was identifiable, in all measured turbulence spectra, as a region of -5/3 slope (see Figure 4.17). The inertial subrange represents a range of frequencies through which there is very little turbulence production or dissipation; most turbulent energy is generated at lower frequencies, and then 'cascades' through the inertial subrange, transferring energy to smaller and smaller eddies, until it approaches the Kolmogorov scale, where it is dissipated as heat (Stull 1988). Therefore, little turbulence production was evident at frequencies greater than 2×10^{-2} (corresponding to a timescale of 50 s) in the measured energy spectra, except in the vertical direction, where the inertial subrange was confined to higher frequencies. Such deviation of vertical spectra from those in other directions is likely to have been a transition to a low-frequency range where vertical turbulent energy is dominated by large detached eddies and the blocking effect of the wall, so does not in-fact indicate the production of turbulent energy by shear (Högström, Hunt & Smedman 2002).

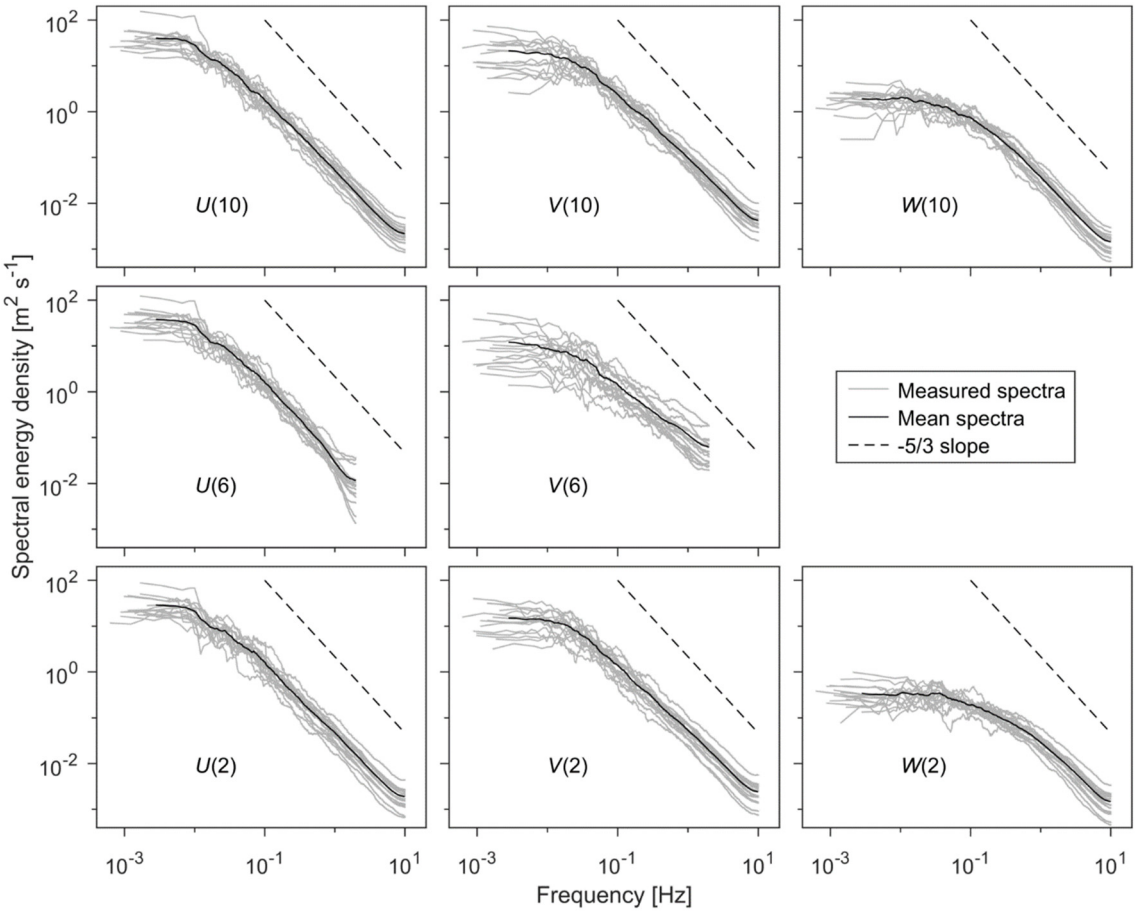

FIGURE 4.17: Turbulence energy spectra calculated from streamwise ($U(z)$), lateral ($V(z)$), and vertical ($W(z)$) velocity measurements, taken at three heights (z [m]). Lines of -5/3 slope are also shown, indicating the spectral slope predicted for the inertial subrange by similarity theory. Deviations from the general trend that are evident at the high-frequency end of each spectrum were introduced by the smoothing algorithm. In reality, the spectra are likely to have maintained a steady trend through the inertial subrange, to a frequency corresponding to the Kolmogorov scale (at ~5 kHz, corresponding to ~1 mm (Garratt 1994)).

4.3.3 Water Deposition

Mean water deposition fluxes, measured using the spray gauges and ground collectors, are presented in Figure 4.18. It was difficult to assess the repeatability of the water deposition results since the wind characteristics were different during each experiment. However, the mean absolute correlation between deposition flux and wind speed was 0.986 and 0.911 in cases A and D, respectively. In both of these cases there was a significant difference in mean wind speed between the first two experiments (A1 and A2, or D1 and D2, respectively) and the last two experiments (A3 and A4, or D3 and D4, respectively), which produced the correlations that have been observed. If the experiments were not repeatable, no such correlation could be expected.

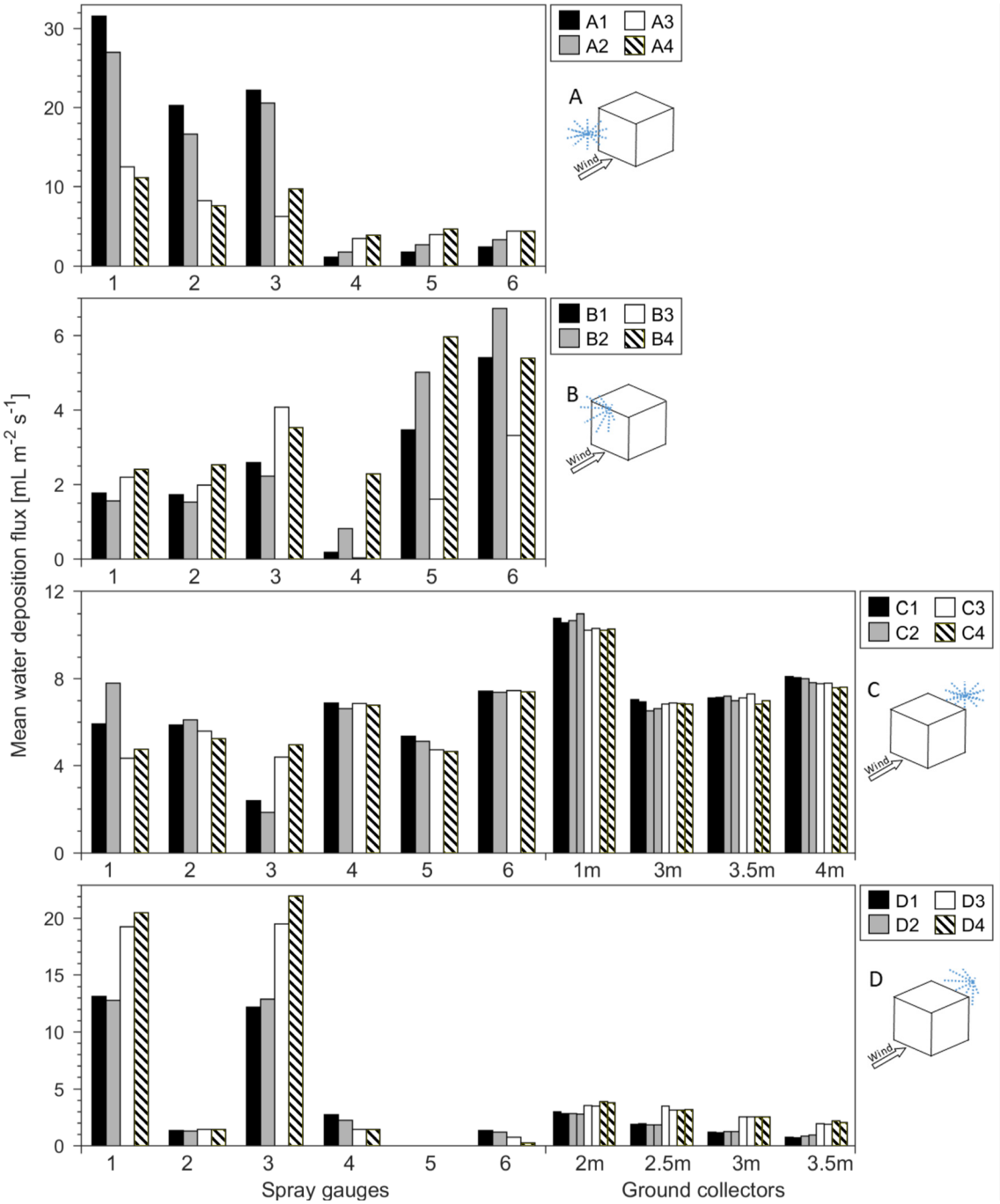

FIGURE 4.18: Mean water deposition fluxes measured during each experiment. The numbers used to identify spray gauges correspond to those presented in Figures 4.9 and 4.8, and the distances used to identify ground collectors indicate the collector distance from the cube leeward face (see Figure 4.8).

4.4 Conclusion

An experimental campaign was undertaken to investigate the dispersion of an isolated water spray around a bluff body located on the ground and immersed in an atmospheric boundary layer flow. Sixteen experiments were conducted, with either a butterfly sprinkler or a hollow-cone sprinkler

implemented on either the windward or leeward side of a 2.4 m cube, producing four distinct test cases. The cube was located in a flat, open field, with an unobstructed upwind fetch of approximately 200 m. Detailed (4-20 Hz) measurements of wind velocity were taken at three heights near the cube, and the ambient temperature and humidity were also measured. Water was collected using custom-designed spray deposition rate gauges on the cube walls and roof, as well as at various locations at ground level.

Mean wind speeds at a height of 10m ranged from 3.32 m s^{-1} to 7.17 m s^{-1} during the experiments, with an angle of incidence on the cube windward face between -7.9° and 20.9°. Turbulence intensities were of the order of 20%, except in the vertical direction where they were closer to 10%. Turbulence integral time and length scales, and energy spectra, also exhibited this anisotropy, with vertical length scales approximately equal to the height at which they were measured and a noticeable deficit at the low-frequency end of vertical energy spectra. The anisotropy measured in the present experiments aligned closely with previous literature on this well-documented feature of boundary layer flow.

Water deposition fluxes on the cube and ground surfaces ranged up to ~32 mL m^{-2} s^{-1}. Some observations can be made as to the distribution of water from the sprinklers under various wind conditions, however, that was not the primary purpose of this study. Rather, the primary aim of the experimental campaign was to produce data suitable for validation of CFD spray simulations, and a detailed comparison of the experiments and CFD simulations in the present study is presented in Chapter 5. In addition, the detailed results presented above may prove useful to other CFD researchers in future validation studies.

Chapter 5

Wind–Spray Interaction: Development and Validation of a Simulation Methodology

This chapter presents a comparison of various methods to simulate wildfire sprinkler systems operating in windy conditions using CFD. Test cases from the experiments reported in Chapter 4 were simulated, and the capabilities of different simulation methodologies were assessed by comparing the simulations to experimental results. The most suitable methodology developed here was then applied to the assessment of the performance of several wildfire sprinkler configurations, as described in Chapter 6.

5.1 Introduction

For the effectiveness of wildfire sprinkler systems to be properly evaluated, the influence of wind and evaporation on the dispersion of water droplets must be understood. Investigation of the fluid dynamics processes involved is challenging, since there is no straight-forward and safe method to replicate the conditions of a wildfire while conducting full-scale experiments at reasonable cost, and the coupled behaviour of the continuous phase (i.e. air) and discrete phase (i.e. water droplets) cannot be accurately represented at a reduced scale. Thus, simulation techniques such as CFD offer the only viable methodology to determine the likely effectiveness of wildfire sprinklers at the present time.

Two issues were encountered in the application of CFD to the investigation of wildfire sprinklers in the present work:

1. The accuracy of different CFD methods, when applied to the dispersion of droplets around bluff bodies immersed in a turbulent boundary layer, had not previously been established; and
2. There was no clearly established method to translate the characteristics of specific sprays, such as those presented in Chapter 3, into boundary/input conditions for CFD simulations.

A simulation study was therefore undertaken to address these issues. The investigation focused on CFD methods that were relatively inexpensive in terms of computational cost, since it was desirable that a methodology for design or performance assessment purposes be developed. Various CFD techniques were compared, to assess:

1. Whether sprays with time-varying characteristics can be accurately represented by quasi-steady simulations;
2. Whether the influence of turbulence on droplet dispersion can be replicated by time-averaged turbulence models; and
3. Whether the influence of sprays on the surrounding air flow can be ignored without significant reductions in simulation accuracy.

The sensitivity of simulations to the initial locations and velocities of droplets was also investigated, so as to provide some insight into how spray characteristics determined in 'quiescent' laboratory conditions (i.e. without externally forced airflow) could best be applied in CFD simulations involving wind.

The present work focused on simulations of atmospheric boundary layer flows around isolated buildings, and the dispersion and evaporation of airborne water droplets within such flows. Water transport after droplet impacts with solid surfaces (e.g. via processes such as splashing, runoff, absorption and post-impact evaporation) were outside the scope of this study, however some modelling of such processes has been included in Chapter 6. The influence of strong localised

sources of heat in close proximity to the building, such as flames or accumulated embers, were also not included in the simulation study reported here. The buoyancy-driven flow and heat transfer caused by such heat sources could affect sprinkler performance significantly during the passage of a wildfire, but are likely to have less of an effect for the majority of the duration of sprinkler operation, prior-to and after the passage of the fire front.

Details of the simulation study are presented in the proceeding sections of this chapter. First, a brief overview of the CFD method is provided and relevant CFD methods are discussed with reference to previous research. The simulation study methodology and results are then discussed, and several important conclusions are outlined.

5.2 A Brief Overview of CFD

Fluid flow is governed by three fundamental laws: i) mass is conserved, ii) energy is conserved, and iii) the net force acting on the fluid equals the product of its mass and acceleration (known as Newton's second law). Expressed mathematically, these laws form a set of partial differential equations known as the Navier-Stokes equations, which can be solved numerically to simulate the fluid flow within a finite spatial domain if adequate information is defined in terms of 'boundary conditions' (i.e. details of the flow at the bounds of a finite spatial domain) and 'initial conditions' (i.e. a complete description of fluid properties within the domain at one point in time). The term 'computational fluid dynamics' describes the variety of methods used to simulate fluid flows in this way. A wealth of information is publicly available on CFD, including many books that cover the fundamentals comprehensively, e.g. Anderson (1995), and Versteeg and Malalasekera (1995). For this reason, a detailed account of the underlying mathematics and basic principles has not been included in this thesis. However, a few key concepts from CFD have been described very briefly below, and aspects of CFD modelling that are particularly pertinent to the simulation of wildfire sprinklers have been covered in more detail in Section 5.3.

CFD allows the solution of the Navier-Stokes equations at a discrete set of locations within the domain, which are defined by a computational 'grid' (or 'mesh'). The partial differential Navier-

Stokes equations can be 'discretised', i.e. approximated algebraically at each grid point, in relation to neighbouring grid points, using either finite difference, finite volume or finite element formulations. The form of the discretised governing equations varies, depending on which of these formulations is used, and the type of flow being simulated (e.g. compressible or incompressible, viscous or inviscid, etc.). The range of methods able to solve the equations depends on their form, and the selection of a method from within the range that is appropriate is usually based on a compromise between accuracy, stability and computational efficiency. Due to the large number of solution methods used in CFD, they have not been reviewed in detail here; the interested reader is directed to the books cited earlier, (Anderson 1995; Versteeg & Malalasekera 1995).

One particularly challenging aspect of CFD is the simulation of turbulence. Exact reproduction of turbulence requires an extremely fine computational grid and short time step, in order to fully resolve turbulence structures down to the Kolmogorov scale; this approach is termed 'direct numerical simulation' (DNS). A much more economical approach is to resolve only the time-averaged flow, and use numerical models to approximate the most important properties of turbulence throughout the domain and the effects of that turbulence on the mean flow. This separation of mean and turbulent flow behaviour is achieved using the Reynolds-averaged Navier-Stokes (RANS) equations. Large-eddy simulation (LES) offers a compromise between the complete representation of turbulence achieved by DNS and the computational efficiency of RANS by resolving the larger scales of turbulence, which tend to have the largest effect on mean flow properties, and modelling smaller eddies. Hybrid RANS/LES methods also exist, such as detached-eddy simulation (DES), which provide CFD practitioners with more options with regard to this compromise between accuracy and computational cost.

A variety of turbulence closure models (often referred to simply as 'turbulence models') have been developed for use with the RANS equations. 'One-and-a-half order' eddy viscosity models approximate the influence of local turbulence stresses using an additional viscous term. Examples of such models include various versions of k-ε model, which calculate the transport of turbulence

kinetic energy, k, and turbulence dissipation rate, ε, as well as k-ω models, which utilise k and the turbulence specific dissipation rate, ω, (sometimes referred to as the mean turbulence frequency). Second-order closure models, such as Reynolds stress models (RSM), offer a more complete description of local turbulence properties, but entail a larger computational cost than eddy viscosity models.

Ultimately, the most appropriate method to represent turbulence CFD depends on the case at hand. None of the RANS, LES or hybrid methods developed so far can exactly model turbulence, so it is important that CFD practitioners understand what kinds of flow each model has been validated for, in order to minimise the errors introduced by turbulence modelling. The commercial CFD code ANSYS Fluent 14.5 was used in the present work. This code adopts a finite volume method and offers a wide range of solution methods and options for the representation of turbulence. A more detailed discussion of these options, and evidence from previous studies as to their appropriateness for simulations of wildfire sprinklers, is provided in the following section.

5.3 Review of Appropriate CFD Methods

A review of published literature related to numerical simulations of wind flow around buildings and liquid sprays was undertaken. No previous validation studies were found that focused specifically on the simulation of spray dispersion around buildings by wind, but simulation methodologies for a number of other relevant types of flow have been reported.

Several previous studies have used CFD to simulate the dispersion of droplets from indoor fire sprinklers; for example, see (Chatterjee & Geiman 2017; Chen *et al.* 2015; Chow 1999; McGrattan, Hamins & Evans 1998; Myers, Trouvé & Marshall 2018; Novozhilov *et al.* 1997; O'Grady & Novozhilov 2009; Yuan & Smith 2015). However, these previous studies differ from the cases of interest here in that wind was not present.

Previous research into the wind drift of agricultural sprays (used for the application of pesticides and irrigation) has included numerous simulation studies, such as: Baetens *et al.* (2007); Butler Ellis and Miller (2010); Delele *et al.* (2007); Holterman *et al.* (1997); Molle *et al.* (2012);

Walklate (1992); Weiner and Parkin (1993). However, these studies were concerned with the dispersion of sprays in open fields, and therefore did not include the influence of large bluff bodies like buildings.

A range of approaches to the simulation of wind-driven rain deposition on building facades have been published (Abuku *et al.* 2009; Blocken & Carmeliet 2007; Blocken & Carmeliet 2010; Blocken, Poesen & Carmeliet 2006; Briggen, Blocken & Schellen 2009; Choi 1993; Huang & Li 2010; Kubilay *et al.* 2013, 2014; Kubilay *et al.* 2015a; Kubilay *et al.* 2015b). However, the relatively uniform spatial distribution of droplets in rain differs from that formed by concentrated droplet sources like sprinklers. Therefore, simulation techniques developed for wind-driven rain may not be well suited to simulations of wildfire sprinkler systems, which, for example, are likely to involve localised regions of relatively strong air entrainment.

Water dispersion from rooftop cooling towers is also a potentially relevant flow type. This has been investigated by Meroney (2006), who proposed a set of guidelines for CFD simulations of this type of flow, and has also been looked at more recently by others (Consuegro *et al.* 2014). Methods developed for such cooling tower simulations are not necessarily suitable for simulations of wildfire sprinkler systems, since the droplet sources in such simulations have typically been distributed in large, upward-moving air jets, representing the cooling tower outlet flow.

Despite differences between the abovementioned spray dispersion scenarios and those considered here, much of the physics is similar. The selection of CFD simulation techniques that were tested in the present study was informed by the findings of previous studies reported in the literature, i.e. those related to the dispersion problems mentioned above, and from the broader fields of computational wind engineering and spray simulation. A summary of relevant findings from previous research is presented below.

5.3.1 Simulation of the Continuous Phase

CFD has been used to investigate atmospheric flow at a wide range of spatial scales. Simulations concerned with flow around individual buildings or small groups of buildings with computational

domains ranging from approximately 100 m to several kilometres are typically classified as 'microscale' simulations (Blocken 2014; Blocken, Tominaga & Stathopoulos 2013; Toparlar *et al.* 2017). The discussion in the following sections is focused on such microscale simulations, since they are most relevant to the present case of wildfire sprinkler systems.

Turbulence

Both turbulence-resolving techniques, such LES, and time-averaged techniques based on the RANS equations, are often employed in simulations of air flow around buildings. The RANS approach involves a significantly lower computational cost, but cannot accurately replicate all physical processes. Comparisons between RANS and turbulence-resolving techniques in the field of computational wind engineering have typically shown the latter to produce results that are more accurate, especially near the side, top and leeward surfaces of buildings where flow separation occurs (Liu & Niu 2016; Meroney 2009; Tominaga & Stathopoulos 2010, 2013; van Hooff, Blocken & Tominaga 2017). However, the simpler RANS-based simulations have produced results of comparable accuracy in some cases, e.g. in the cross-ventilation of simple structures (Meroney 2009) and in pollutant dispersion near buildings (Lateb *et al.* 2014).

Thus, the choice between RANS and turbulence-resolving approaches should be made on a case-by-case basis, and should take into account both the computational cost and required accuracy of results. This conclusion has been stated in a number of relevant best-practice guidelines and review papers (Blocken 2014; Franke & Hellsten 2011; Tominaga *et al.* 2008; Tominaga & Stathopoulos 2013). The suitability of RANS for simulations of wildfire sprinkler systems was investigated in the present work.

Turbulence Stationarity and 'Inactive' Turbulence

Simulation of transient flows as simplified, pseudo-steady cases was found to be a common approach adopted in the CFD studies that were reviewed. This approach reduces the computational cost of simulations significantly, and can reproduce the flow features of interest in many cases. However, pseudo-steady CFD simulations not only neglect changes in the mean flow field over time, they also fail to account for the influence of turbulence structures with spatial

scales much larger than the computational domain, since the influence of such structures would appear in the computational domain as fluctuations in the mean velocity field. Turbulence at such scales has often been referred to as 'inactive' turbulence in the literature (Bottema 1997; Bradshaw 1967; Högström, Hunt & Smedman 2002; Katul & Albertson 1996; Richards & Norris 2011; Townsend 1961).

Wind-tunnel experiments have demonstrated that some time-averaged variables (e.g. pressure coefficients across buildings) are not significantly affected by inactive turbulence (Durbin & Hunt 2006; Melbourne 1979; Richards *et al.* 2007; Richards & Norris 2011). However, in the present case, it was conceivable that fluctuations in the local mean velocity field could disperse sprayed water over a larger area, thereby influencing the performance of wildfire sprinkler systems. For this reason, the sensitivity of simulated results to inactive turbulence was assessed in the present work.

Turbulence Closure

When RANS-based CFD techniques are adopted to simulate air flow around buildings, the choice of turbulence model can influence results significantly, as has been demonstrated in many comparison studies (Meroney 2009; Murakami 1993; Tominaga & Stathopoulos 2009). No single turbulence model has consistently performed better than others, so it is good practice to base the selection of turbulence models on comparison studies involving flows very similar to that which is to be simulated. No such comparison study was found for simulations of particle dispersion near buildings, so one was conducted in the present work. The set of candidate models for comparison was selected based on studies of similar flow cases.

The standard k-ε model (Launder & Spalding 1974) has repeatedly been shown to perform poorly in regions of flow separation, including those triggered by building edges (Meroney 2009; Murakami 1993; Tominaga & Stathopoulos 2009). Revised versions of the k-ε model, particularly the renormalisation group (RNG) and realisable k-ε models, have typically produced more accurate results. Similarly, the standard k-ω model has typically not performed as well as

the shear stress transport (SST) k-ω model in simulations of wind flow around buildings (Meroney 2009; Ramponi & Blocken 2012b).

RSM can be adopted to resolve turbulence anisotropy, but they entail a higher computational cost than the abovementioned 'one-and-a-half order' eddy viscosity models. Previous studies have shown that turbulence anisotropy is important in simulations of the dispersion of pollutants (Tominaga & Stathopoulos 2013) and fine particles (Dehbi 2008a, 2008b). However, RSM have typically been found to offer little-to-no benefit over the simpler 'one-and-a-half order' models (Blocken 2014; Bradshaw 1999; Richards & Norris 2011; Tominaga & Stathopoulos 2013). This was highlighted by Bradshaw (1999) and later quoted by Richards and Norris (2011), "it is so obvious that stress-transport models are more realistic in principle than eddy viscosity models that the improvements they give are very disappointing".

In the present investigation, comparisons were made between the performance of the RNG and realisable k-ε models in simulations of wildfire sprinklers. These comparisons formed the basis for selection of a turbulence model in subsequent simulations.

Wall Treatment

Wall functions are employed in the vast majority of ABL simulations, due to the high Reynolds numbers and large spatial scales involved. The wall functions available in commercial CFD packages (including ANSYS Fluent 14.5, which was used in the present work) are generally based on 'sand-grain' roughness coefficients, derived from pipe flow experiments. Blocken, Stathopoulos and Carmeliet (2007) identified four conflicting requirements for accurate simulations of the ABL using such wall functions: 1) a sufficient wall-normal resolution in the computational mesh to capture the flow behaviour of interest; 2) boundary layer flow upstream and downstream of the region of interest that is horizontally homogeneous; 3) computational cells immediately adjacent to the wall that are larger than the physical 'sand grain' roughness imposed at the wall; and 4) appropriate selection of physical 'sand grain' roughness values for the aerodynamic roughness length of the terrain. The authors noted that it is often impossible to meet all four of these requirements, but that it is advisable to ensure that 1, and 3 are satisfied, and to

check the boundary layer horizontal homogeneity in an empty computational domain before undertaking the final simulations. These guidelines were adhered to in the present work.

5.3.2 Representation of the Discrete Phase

Discrete particles can be represented in several ways in CFD simulations. Particles that follow the continuous-phase flow very closely can be treated as a miscible fluid and tracked by calculating the particle concentration in each computational cell. This approach can be extended to flows involving particles that do not follow the continuous-phase streamlines exactly, by calculating a representative discrete-phase velocity in each cell. Thus, momentum transfer between the phases can be simulated. Further complexity can be added to simulate heat and mass transfer, as well as particle breakup and collisions. This group of approaches can be classified as Eulerian-Eulerian, since both phases are dealt within an Eulerian framework.

Lagrangian-Eulerian simulations take a different approach, in which individual particle trajectories are calculated within a Lagrangian framework. Typically, a relatively small number of particles are tracked and each is used to represent a set of similar trajectories within the particle field. Particles are often considered as point-masses in this approach, although volume-resolved methods do exist. As with Eulerian-Eulerian simulations, various physical processes can be included or neglected in Lagrangian-Eulerian simulations, as needed. The interested reader is directed to the comprehensive reviews of Loth (2000), Elghobashi (1994), Balachandar and Eaton (2010) and Subramaniam (2013) for more detailed descriptions of the Eulerian and Lagrangian approaches.

The Eulerian-Eulerian approach was adopted in several previous studies, for simulations of wind-driven rain (Huang & Li 2010; Kubilay *et al.* 2013, 2014; Kubilay *et al.* 2015a; Kubilay *et al.* 2015b). The authors reported a good agreement with experimental results and a significantly reduced computational cost, compared to Lagrangian-Eulerian simulations. However, a comparison of the two approaches in simulations of a single solid-cone spray revealed that the accuracy and computational cost of Lagrangian-Eulerian and Eulerian-Eulerian simulations were

very similar in that case (Nijdam *et al.* 2006). Nijdam *et al.* (2006) also noted two potential disadvantages of the Eulerian-Eulerian approach for simulations of sprays:

1. Simulations requiring many discrete size classes could become prohibitively expensive, since transport equations would need to be solved for each size class throughout the entire domain.
2. Spray interactions may not be accurately represented, since a single representative velocity would be calculated for each size class in each computational cell, prohibiting droplets of the same size from passing close by each other.

The latter issue could be addressed by representing droplets from different sprays as separate phases, but this would exacerbate the former issue. The vast majority of spray simulations that were reviewed in the present study adopted the Lagrangian-Eulerian approach.

In the present study, the considerations outlined above, and an inspection of the droplet Stokes' numbers, St, formed the basis of decisions related to the representation of the discrete phase.

5.3.3 Interactions between Phases

Coupling between the discrete and continuous phases can be classified as one, two or four-way. Two-way coupled simulations allow a two-way interaction between the phases, while one-way coupling only allows the continuous phase to influence the discrete phase. 'Four-way' coupling implies that particles are able to collide with each other, in addition to two-way coupling between the phases. A general 'rule of thumb' has been proposed, which suggests that two-way coupling should be employed in cases where the particle volume fraction, Φ, is greater than 10^{-6}, and particle collisions should be taken into account when $\Phi \gtrsim 10^{-3}$ (Elghobashi 1994). In reality, the sensitivity of CFD results to interphase coupling settings will depend on other aspects of the flow as well as the particle volume fraction.

Momentum Transfer

Regardless of the coupling option chosen, a variety of analytical and empirical drag laws can be used to model momentum transfer between phases (Ishii & Zuber 1979; Mashayek & Ashgriz

2011; Turton & Levenspiel 1986). The appropriate choice of drag law depends on the drag regime being simulated, which can be estimated using Re_d (see Section 3.2). Droplet deformation should also be considered, since drag forces on deformed droplets can be significantly different to those that act on spherical droplets with the same volume. The dimensionless parameters We and Oh provide some insight into droplet stability and the propensity for deformation (see Section 3.2). In the present study, Re_d, We and Oh were used to form the basis of decisions as to whether droplets could be accurately represented by spherical particles, and whether droplet breakup should be modelled in simulations.

Heat and Mass Transfer

Heat and/or mass transfer can be included in both Eulerian and Lagrangian spray simulations. Particles are generally assumed to be isothermal and homogeneous in composition. Convective heat transfer can be modelled using theoretical heat transfer coefficients, e.g. Ranz and Marshall (1952). Droplet vaporisation can be modelled in a similar manner, if it is assumed that the continuous phase gas is saturated at the droplet surface, and latent cooling can be calculated from the vaporisation rate.

The accuracy of heat and mass transfer models in CFD simulations of sprays has been investigated by Sureshkumar, Kale and Dhar (2008b), and Montazeri, Blocken and Hensen (2015b). Both groups simulated a hollow-cone spray operating in a wind tunnel, and compared the air temperature and humidity downwind of the spray to the experimental results of Sureshkumar, Kale and Dhar (2008a). Both simulation studies produced results that qualitatively matched the experimental results. However, quantitatively, the CFD results varied from experimental results by up to 30%.

Droplet Collision

Droplet collisions in sprays can result in bouncing, splashing, persistent coalescence or coalescence followed by breakup (Brenn 2011; Frohn & Roth 2000; Orme 1997). Modelling of such phenomena in simulations, where droplet fields are represented by Eulerian phases or sets

of Lagrangian point-particles, is largely based on geometry and empirical relations (Nijdam *et al.* 2006; O'Rourke 1981; Ruger *et al.* 2000).

The importance of coalescence in spray simulations has not been quantified in many previous studies. Ruger *et al.* (2000) showed that, within two hollow-cone sprays, coalescence was probably the primary cause of an increase in Sauter mean diameter with increasing distance from the spray nozzles. The droplet collision model used for simulations in that study reduced the discrepancy between experimental and CFD results by approximately 50%. However, droplet collisions were not included in the majority of studies reviewed in the present work, and no other direct comparison was found between experimental measurements and CFD results obtained with and without droplet collision models.

Droplet Breakup

As discussed in the context of momentum transfer above, the breakup of droplets can be predicted, based on the dimensionless parameters We and Oh. Thus, the importance of breakup in spray simulations can be assessed quite easily, given a cursory understanding of the flow and its boundary conditions (e.g. droplet initial sizes and velocities). Several models can be used to account for spray breakup, e.g. (O'Rourke & Amsden 1987; Reitz 1987). These models have not been reviewed in-detail here, since they were not required in the present work. Detailed descriptions of the models can be found in the abovementioned references, and several other sources, e.g. ANSYS (2014). For further information on the physics of droplet breakup, the interested reader is directed to the numerical simulations of Jain *et al.* (2015) and the experimental work of Faeth, Hsiang and Wu (1995); Hsiang and Faeth (1992, 1995).

5.3.4 Turbulence and Droplet Dispersion

In RANS-based simulations of sprays, the interphase interactions described in the previous section only take the mean continuous-phase flow field into account. However, in reality, turbulent eddies can influence the dispersion of droplets significantly. It is therefore often

necessary to augment the drag forces calculated in the discrete phase momentum balance, to model the effects of turbulence on droplet trajectories.

Turbulent dispersion models for Lagrangian-Eulerian simulations can be categorised into two groups: 1) eddy-interaction models, which aim to replicate the effects of a succession of turbulent eddies on each particle by introducing terms with a stochastic component into the particle momentum balance; and 2) particle 'cloud' tracking models, which compute the probability distribution associated with each particle's location directly. Eddy-interaction models can be further categorised as either: a) discrete random-walk (DRW), b) continuous random-walk (CRW), or c) Langevin stochastic differential equation models. Differences between models have not been described in-detail here; the interested reader is directed to the summaries produced by of Loth (2000); MacInnes and Bracco (1992), as well as works on DRW models by: Call and Kennedy (1992); Dehbi (2008a); Gosman and loannides (1981); Graham (1998, 2001); Kallio and Reeks (1989); discussion on CRW models by Amani and Nobari (2013); the Langevin stochastic differential equation model proposed by Dehbi (2008b); and the work on 'cloud' tracking models by Jain (1998); Litchford and Jeng (1991).

There is no established method to determine whether particular flow simulations require a turbulent dispersion model, or to select the most appropriate model when one is required. As with many decisions in CFD, the computational cost and accuracy of each option should be understood, and an appropriate compromise made. In the case of wildfire sprinkler simulations, some insight was available in previous published works concerned with similar flows.

Kubilay *et al.* (2015a) demonstrated the importance of turbulent dispersion in simulations of wind-driven rain deposition on building facades; they noted a decrease in the deviation between experimental and CFD results from 24% to 15% when a DRW turbulent dispersion model was included. CFD studies of particle deposition in idealised wall-bounded flows were also relevant, some of which had noted the importance of turbulence anisotropy (Call & Kennedy 1992; Dehbi 2008a, 2008b; Parker, Foat & Preston 2008; Tian & Ahmadi 2007). When the continuous phase flow field is calculated using RANS and 'one-and-a-half' order eddy viscosity models (which do

not resolve anisotropy), modelled velocity components can force droplets directly into walls, whereas, in reality, wall-normal velocity fluctuations are dampened. The authors reported improvements in the accuracy of simulated wall-deposition rates when RSM were adopted. However, for particle diameters greater than 10 μm, simulations conducted with RSM and 'one-and-a-half' order models produced similar results (Parker, Foat & Preston 2008; Tian & Ahmadi 2007).

In the present work, the importance of turbulent dispersion in simulations of wildfire sprinkler systems was investigated. The investigation scope was limited to include only the DRW model implemented in ANSYS Fluent 14.5 (ANSYS 2014) and turbulence anisotropy was not considered.

5.4 CFD Simulation Methodology

CFD simulations were conducted, to compare the performance of various modelling approaches to wildfire sprinkler system analysis. Steady-state RANS CFD simulations were conducted using the CFD code Ansys Fluent 14.5. The coupled pressure-based solver was used, with least-squares 'cell-based' (as opposed to node-based) spatial discretisation of gradients and second order discretisation of advection terms in all governing equations.

5.4.1 Test Cases

Five test cases were defined for the simulation study. Four were taken from Chapter 4, each involving either a Holman ½-inch brass butterfly sprinkler or a ½-inch Champion S9F hollow-cone nozzle, operating in wind, at either the windward or leeward side of a 2.4 m cube. Simulations of the butterfly sprinkler were included, to assess whether time-averaged representations of such periodic sprays could provide accurate CFD results. Experiments A2, B3, C1 and D4 were selected, and have been hereafter referred to as Cases A, B, C and D, respectively. The fifth test case involved the undisturbed liquid jet emitted from a Vyrsa VYR 35 ¾-inch 360° impact sprinkler main nozzle, replicating the characterisation experiment described in Chapter 3. In that experiment, the sprinkler was inclined forwards (towards the main nozzle) by 15° and the

deflector paddle was restrained so that it did not rotate into the path of the liquid jet, thus also preventing rotation of the sprinkler head. Thus, the fifth test case was a steady liquid jet, emitted into quiescent air at an angle of 11° above the horizontal.

5.4.2 Computational Domain and Mesh

One computational domain was defined for simulations of Cases A–D, i.e. the cases involving a cube immersed in the atmospheric boundary layer. The domain dimensions were set according to recommendations found in relevant best-practice guidelines (Franke *et al.* 2007; Tominaga *et al.* 2008), with boundaries located 5*H* above, 5*H* laterally and 15*H* downstream from the cube (see Figure 5.1), where *H* is the cube edge length. The upstream boundary was located 3*H* from the cube, instead of the generally recommended distance of 5*H*. Such a reduction in the extent of the domain has been shown to have negligible effect on simulations of flow around isolated buildings, and can reduce the effects of boundary layer inhomogeneity in cases where the ground roughness does not maintain the inlet profiles of velocity or turbulence (Blocken, Carmeliet & Stathopoulos 2007; Blocken, Stathopoulos & Carmeliet 2007; Ramponi & Blocken 2012a; Ramponi & Blocken 2012b). The generation of inlet boundary conditions is described later, in Section 5.4.5.

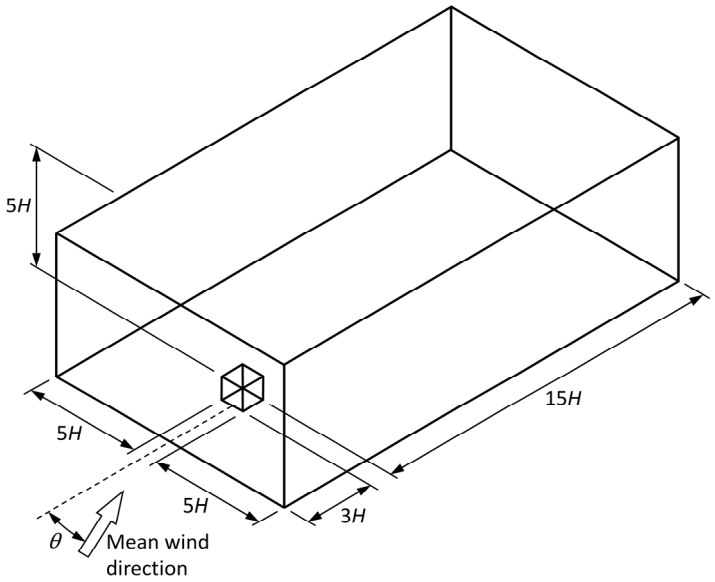

FIGURE 5.1: Computational domain used for simulations of Cases A, B, C and D. Dimensions are expressed in terms of the cube edge length, *H*, which was 2.4 m.

A second computational domain was defined for simulations of the impact sprinkler. This domain was a rectangular prism, 25 m long, 10 m wide and 8 m high. The sprinkler nozzle was located 1 m from the base of the domain and 5 m from three of its sides (see Figure 5.2).

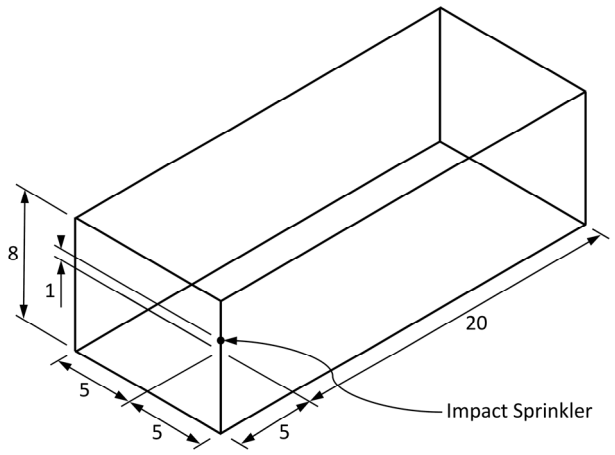

FIGURE 5.2: Computational domain used for the impact sprinkler test case. Dimensions are shown in metres.

Computational meshes were generated in each domain (see Figure 5.3 and Figure 5.2). The meshes were designed for use with wall functions, so, in the cube domain, elements in contact with the ground surface were formed with sufficient height to ensure that the centre of each element was further from the ground than the sand-grain roughness length set there. The cube surfaces and the ground surface in the impact sprinkler domain would be set as smooth walls, so no such constraint was relevant to those surfaces. A grid sensitivity analysis was conducted using three versions of each mesh, which had incrementally refined grid spacing, according to a grid refinement ratio of approximately 1.5. Grid sensitivity study was conducted with all sub-models (e.g. turbulent droplet dispersion), to test the sensitivities of these models to grid spacing as well.

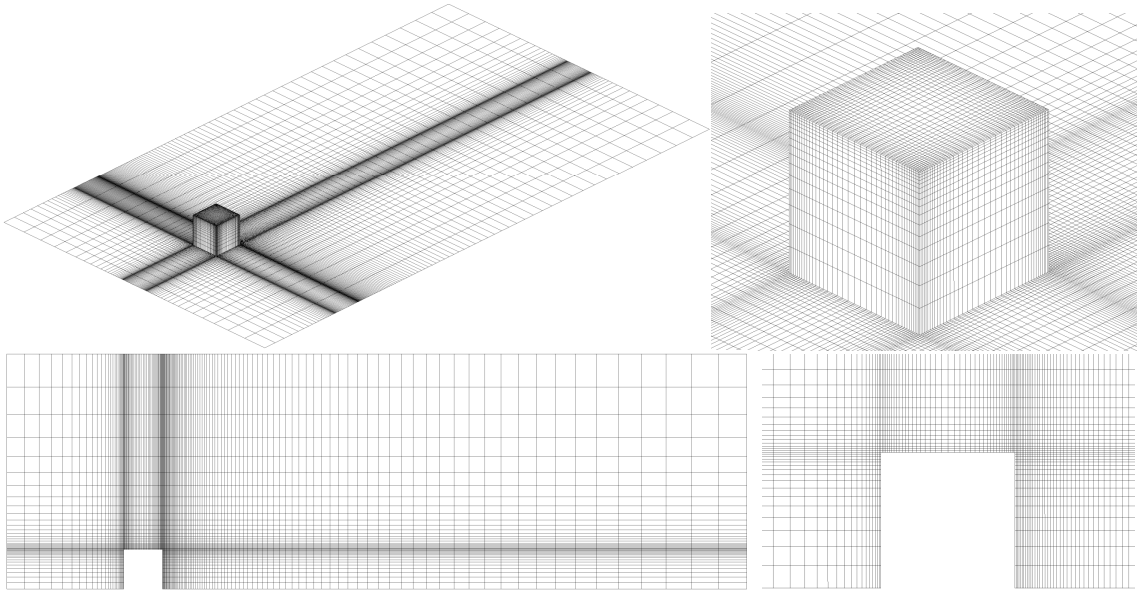

FIGURE 5.3: Computational mesh used for Cases A–D. The top two images show isometric views of the mesh on solid boundaries (mean flow from bottom-left to top-right), the lower two images show the mesh on the streamwise vertical centre-plane (mean flow from left to right). Meshes with finer and coarser grid spacing than that shown here were also trialled during the mesh sensitivity analysis.

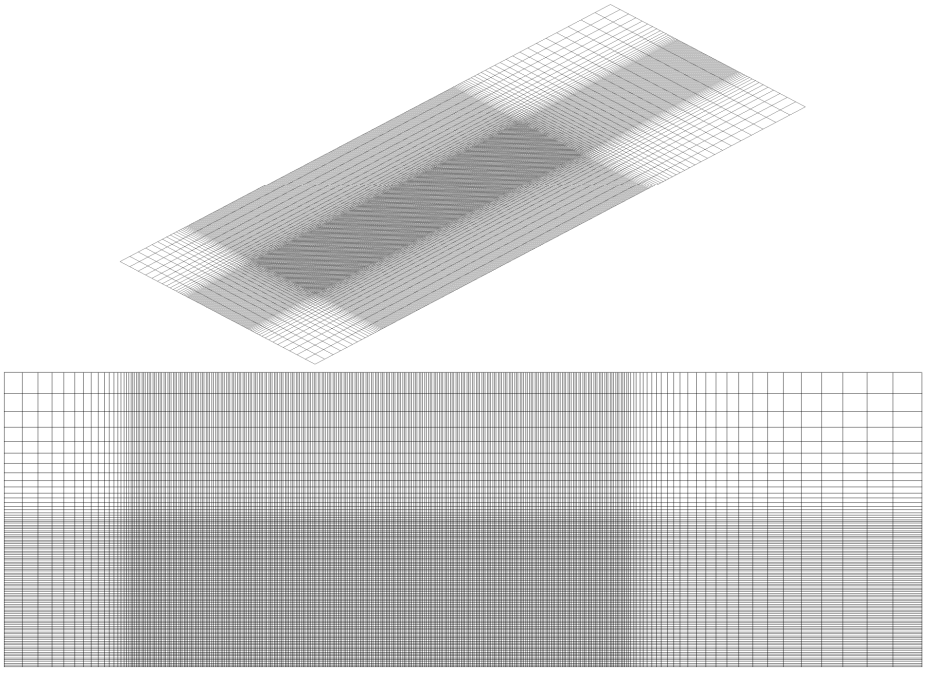

FIGURE 5.4: Computational mesh used for the impact sprinkler case. The top image shows an isometric view of the mesh on the solid boundary, the lower image shows the mesh on a centre-plane. Meshes with finer and coarser grid spacing than that shown here were also trialled during the mesh sensitivity analysis.

5.4.3 Continuous Phase Modelling

The continuous phase flow field was simulated using the incompressible RANS equations. The realisable k-ε (ANSYS 2014; Shih *et al.* 1995) and RNG k-ε (ANSYS 2014; Yakhot *et al.* 1992) models have performed best in previous validation studies concerned with pollutant dispersion around buildings (Tominaga & Stathopoulos 2009), especially near the top, side and leeward surfaces of building-like objects. Therefore, these two turbulence models were compared in the present work. Unless stated otherwise, simulations in this chapter were conducted using the realisable k-ε model.

The continuous phase was modelled as a mixture of dry air and water vapour using the 'species transport' method in Fluent. Thus, the mass-fraction of water vapour in each computational cell was calculated from advection, diffusion and production terms, but the velocity and temperature of water vapour was assumed to be equal to those of dry air in each cell.

5.4.4 Discrete Phase Modelling and Interphase Coupling

The sprays were modelled as sets of pre-formed droplets by tracking point-particles in a Lagrangian framework. Sensible heat transfer, droplet evaporation and the associated latent cooling were included in the simulations.

The Stokes' numbers, St, and liquid volume fractions, Φ, relevant to Cases A–D were estimated using: i) the droplet diameter measurements from Chapter 3; ii) the mean 10 m-elevation wind speed from the measurements in Chapter 4; and iii) the cube side-length of 2.4 m. The calculated St were between 3×10^{-7} and 3×10^{-4}, and Φ ranged from approximately 3×10^{-4} to 2×10^{1} (see Figure 5.5). According to the 'rules of thumb' described in Sections 5.3.2 and 5.3.3, these values indicated that: i) some particle trajectories were likely to follow continuous-phase streamlines quite closely, while others would not; ii) droplets were likely to have a significant effect on the local air flow; and iii) droplet collisions were unlikely to have a large effect on the sprays. Based on these observations, both one and two-way coupled CFD simulations were run in the present work and the results were compared, but droplet collisions were not simulated.

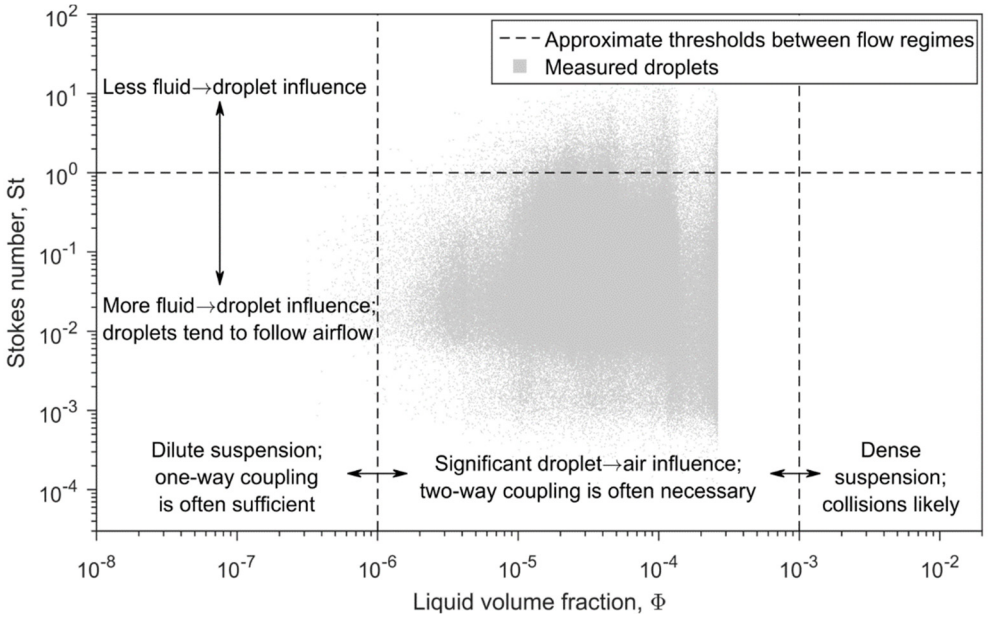

FIGURE 5.5: Stokes number plotted against liquid volume fraction, estimated from the measurements of the butterfly and hollow-cone sprays in Chapter 3, wind measurements in Chapter 4 and the cube side-length (2.4 m). Different flow regimes are also shown, based on general 'rules of thumb' for simulations of particle-laden flow proposed in the literature (ANSYS 2014; Elghobashi 1994).

Drag coefficients were calculated using the expression proposed for spherical particles by Morsi and Alexander (1972). This approach was justified by an analysis of droplet Reynolds numbers, Re_d, and Weber numbers, We, which were calculated from the relevant droplet velocities and diameters reported in Chapter 3, with an assumption that the ambient air was quiescent. This simplified approach neglected wind and air entrainment into the spray, but provided some insight into the cases of interest. Calculated Reynolds numbers, Re_d, ranged from 1×10^{-1} to 3×10^{3} (see Figure 5.6), i.e. from Stokes' drag regime to the onset of significant droplet deformation (Ishii & Zuber 1979). The majority (>95%) of calculated Weber numbers were less than 0.6 (see Figure 5.7), indicating that a spherical drag law may be appropriate. The simplified analysis adopted here could have overestimated Re_d and We by neglecting air entrainment into the sprays, but could also have underestimated these values by neglecting wind. Considering the air and droplet velocities involved in the cases of interest, such simplifications are unlikely to have influenced the calculated Re_d and We by more than factors of ~0.4 and ~2, respectively. Based on the ranges of Re_d and We, and the 'rules of thumb' outlined in Section 5.3.3, the CFD simulations were conducted with drag laws for spherical particles and droplet breakup was not considered.

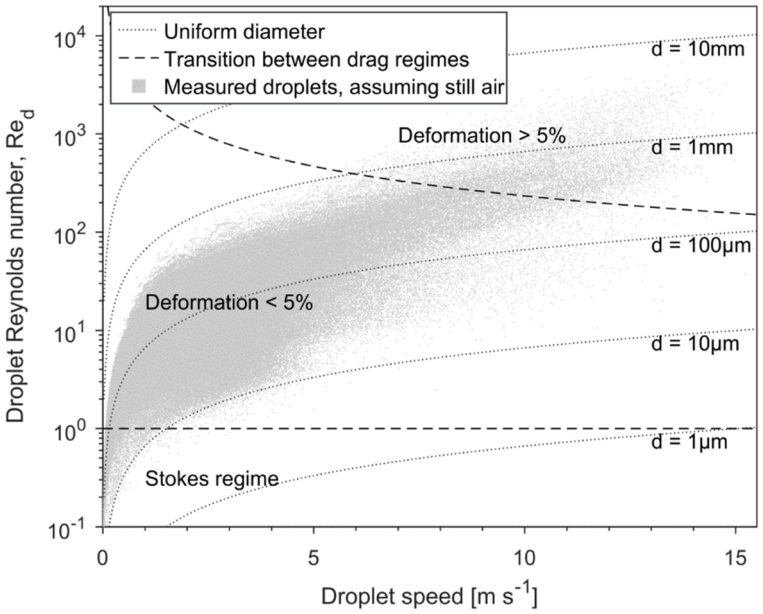

FIGURE 5.6: Reynolds numbers of spherical droplets travelling through still air. Data obtained from measurements (described in Chapter 3) of sprays produced by the butterfly, hollow-cone and impact sprinklers are presented, with an assumption that the ambient air was quiescent. Actual droplet Reynolds numbers would have been different in the test cases, due to the effects of air entrainment into the sprays and wind.

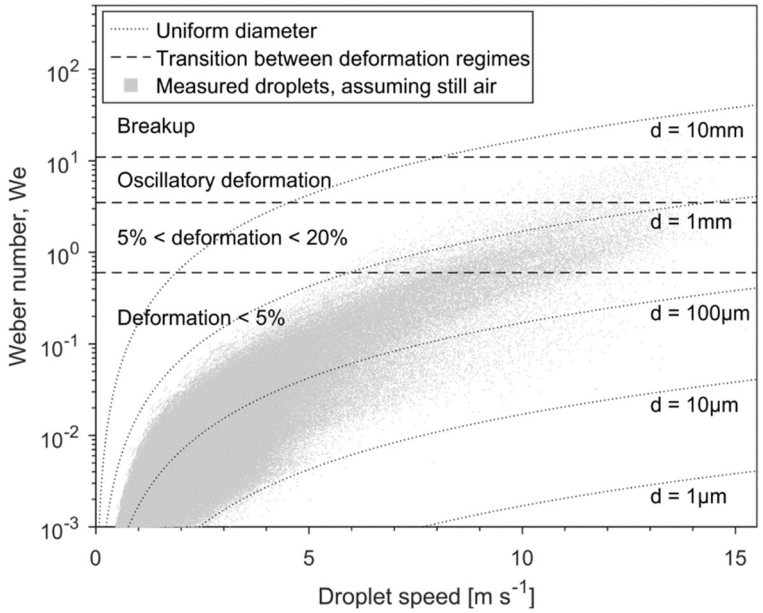

FIGURE 5.7: Weber numbers of spherical water droplets travelling through still air. Data obtained from measurements (described in Chapter 3) of sprays produced by the butterfly and hollow-cone sprinklers are presented, with an assumption that the surrounding air was still. Actual droplet Weber numbers would have been different in the test cases, due to air entrainment into the sprays and wind.

Simulations were run with and without a turbulent dispersion model, and with various numbers of stochastic iterations, n_{td}, to investigate the sensitivity of results to these settings. The DRW model available in ANSYS Fluent 14.5 (ANSYS 2014) was used.

5.4.5 Boundary Conditions

For Cases A–D the velocity, turbulence kinetic energy (k), turbulence dissipation rate (ε), temperature and water vapour mass fraction were fixed at the inlet boundaries. The vertical profiles of velocity, k and ε were defined by the standard power law (Tominaga *et al.* 2008), fitted to measured values from the experiments corresponding to each case (see Figure 5.8). The standard k profiles were of a similar magnitude as the measured values, but differed significantly in shape. To investigate whether such discrepancies had a significant effect on the CFD results, simulations were run with the standard profiles and with custom profiles, which fitted the experimental data more closely. The custom profiles did not have a basis in boundary layer theory, and were unrealistic in that k approached infinity with increasing height, but they did match the measured values well close to the ground, in flow surrounding the sprays. The temperatures and water vapour mass fractions assigned to inlet boundaries were constant with height, and matched the temperature and humidity measurements from the relevant experiments.

The outlet boundaries in Cases A–D, downstream of the cube, were assigned constant pressure. The top boundary was assigned the same fixed parameters that were set at the top of the inlets. In the impact sprinkler case, all four side boundaries and the top boundary were set with fixed pressure, since there was no wind in that case.

Solid boundaries were set as adiabatic, non-slip walls in all five cases. The wall functions outlined by (Launder & Spalding 1974) were adopted, with a correction to enforce a logarithmic velocity profile when the dimensionless wall distance was below 11.225, which was referred to as 'scalable wall functions' in the ANSYS Fluent documentation (ANSYS 2014). The aerodynamic roughness of the cube surfaces in Cases A–D and the ground in the impact sprinkler case were set as zero (smooth walls), and the roughness of the ground in Cases A–D were set to match the inlet boundary layer profiles. Droplets that hit any boundary (solid or open) were removed from the simulation.

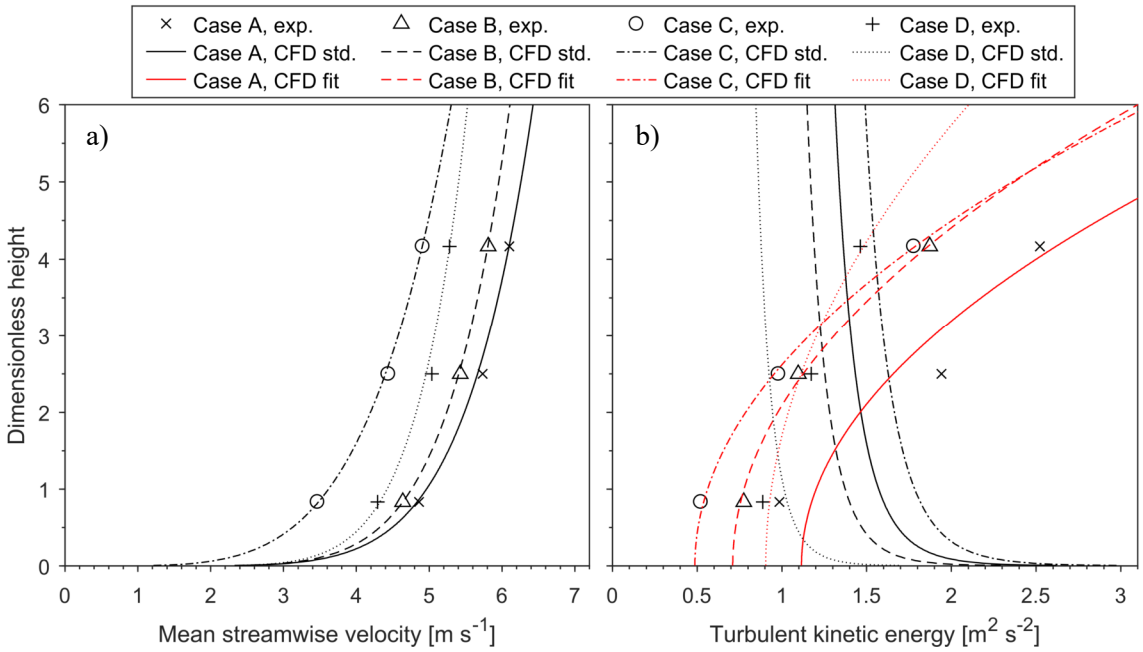

FIGURE 5.8: Vertical profiles of a) mean streamwise velocity and b) turbulence kinetic energy for simulations of Cases A–D, compared to results from the corresponding experiments in Chapter 4. Two sets of turbulence kinetic energy profiles were trialled, those matching the standard power-law boundary layer (labelled 'std.') and those fitted to the experimental data (labelled 'fit'). Height has been non-dimensionalised using the cube height, $H = 2.4$ m.

The effect of inactive turbulence on the dispersion of droplets in Cases A–D was also investigated, by running nine simulations with different inlet boundary conditions for each case and combining the results into weighted averages. In this way, results were obtained that represented the each case with varying mean wind velocities, without incurring the significant computational cost of particle tracking throughout transient simulations spanning ~10 min. Clearly, this approach was unlikely to generate exactly the same results as transient simulations, but it did give an indication of the magnitude of error that was introduced by not including inactive turbulence in the individual steady simulations.

Inlet boundary conditions were defined for each set of nine simulations by a 5-step process:

1. The turbulent length scale modelled by the DRW turbulent dispersion model was determined, using the relation: $L_e = \left({C_\mu}^{3/4} k^{3/2}\right)/\varepsilon$, where $C_\mu = 0.09$ is the k-ε model constant, and k and ε were evaluated at the reference height, 10m.
2. The relation: $t_e = L_e/\overline{U}$ was used to estimate a time scale corresponding to L_e; here, $\overline{U}$ is the mean velocity, also evaluated at the reference height.

3. A low-pass filter, with a cut-off frequency of $1/t_e$, was applied to the time-series of velocity measurements taken at the reference height during the relevant experiment, thereby removing velocity fluctuations that would be accounted for by the turbulent dispersion model.
4. Within the set of wind speeds and directions in the large-scale 'inactive' fluctuations that remained, nine evenly spaced reference velocities were defined, using each combination of the mean, mean plus $^4/_3$ the standard deviation, and mean minus $^4/_3$ the standard deviation, of wind speed and direction, respectively (see Figure 5.9).
5. The direction and magnitude of the inlet velocity profiles were set according to the nine reference velocities. Vertical profiles of k and ε were also affected by these adjustments, due to their reliance on the velocity magnitude to the power-law ABL profile equations.

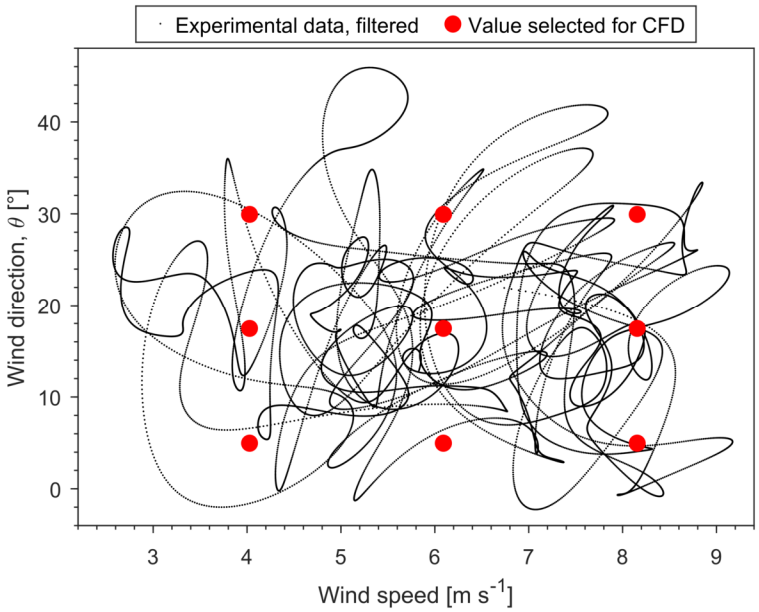

FIGURE 5.9: Filtered wind speed and direction measurements, taken at a height of 10m during the experiment corresponding to Case A, and the nine velocities selected for use in steady simulations of that case. High-frequency fluctuations have been filtered out, since they would be modelled by the turbulent dispersion model.

Results from each set of nine simulations were combined into one weighted-average. Weighting factors were assigned to each result according to probability density estimates, which represented the portion of time during the experiment that the wind velocity (at 10 m) had been close to the

simulated value. A kernel-based estimating method with Gaussian kernels was used to generate the probability density estimates.

5.4.6 Droplet Sources

Each spray was represented by a relatively small number of pre-formed droplets, which were defined by initial locations, velocities, diameters and temperatures, as well as mass flow-rates (since each one represented a set of similar droplets). For each simulation, a set of n_d distinct initial diameters was selected, and a set of n_s spatially unique source points were defined within the computational domain. During each tracking procedure, one droplet with each of the initial diameters was tracked from each source point. The mass flow-rate and initial velocity associated with each of these $n_d n_s$ droplets were calculated from the probability density functions reported in Chapter 3. Thus, distributions of diameter and velocity that had been measured in the actual sprays were replicated in the simulations, as were correlations between diameter and velocity, and spatial variations thereof. All droplet initial temperatures were set as 24.5°C, which was within ±2°C of values measured during the experiments.

Simulation of the impact sprinkler case by such a method was not straight-forward, since the spray characteristics had been measured 6 m from the sprinkler, beyond the regions of primary and secondary breakup. If the droplet source points were implemented so far from the sprinkler in simulations with wind, the effects of the wind would be greatly underestimated. Two alternative approaches were to define droplet source points much closer to the sprinkler, or to introduce a liquid jet into the domain and simulate its breakup. The former approach was tested in the present study. A set of droplets, with appropriate distributions of diameter and mass-flow, were released from a single source point ($n_s = 1$) at the sprinkler location (see Figure 5.10). The initial velocity of all droplets was set in the direction of the liquid jet flow, with a magnitude matching the initial jet speed.

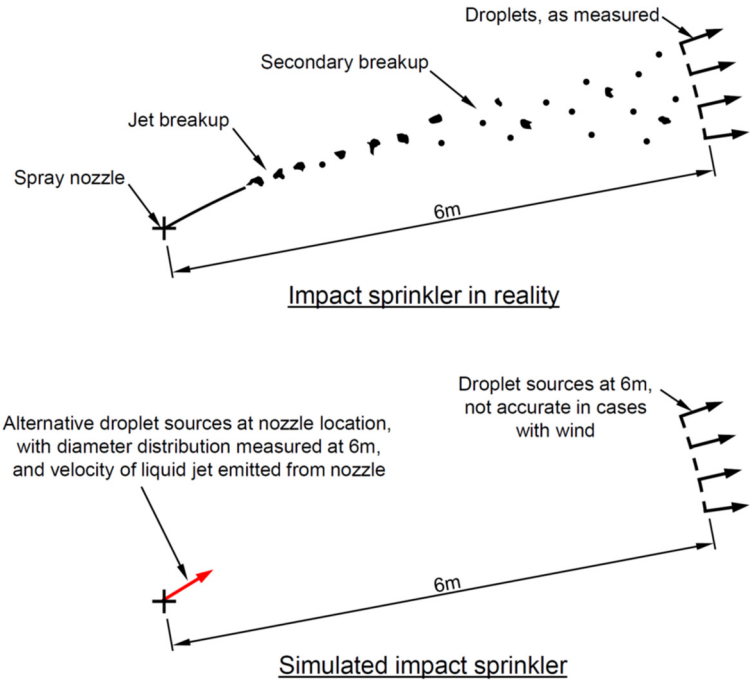

FIGURE 5.10: Challenges associated with the application of measured spray characteristics to the simulation of the liquid jet emitted by the impact sprinkler. Droplet characteristics had been measured 6m from the sprinkler. If droplet source points were located so far from the sprinkler in simulations involving wind, the effects of wind would likely be underestimated. The approach tested in the present study was to release pre-formed droplets from a single point at the sprinkler location, with velocities equal to the jet initial velocity.

This approach was highly simplified. Two potential issues were identified with it: 1) the spray may not penetrate as far as it should into the domain, since drag forces on discrete droplets are significantly different to those that act on a liquid column; and 2) the only mechanism by which the trajectories of droplets with the same initial diameter would deviate from each other would be the stochastic forces introduced by the turbulent dispersion model, while, in reality, droplet trajectories would deviate as a product of the breakup process. However, the approach did produce a spray with a diameter distribution matching that which had been measured, and it allowed interaction between the phases through the full droplet trajectories. The method tested here also avoided the computational expense associated with simulating liquid jet breakup. The results of simulations were compared to the measurements taken 6 m from the sprinkler in Chapter 3, to determine whether accurate results could be obtained, despite the highly simplified approach that had been taken. The sensitivity of results to the number of distinct initial diameters, n_d, was also tested.

In Cases A–D, droplet source points were located on a sphere, with the sprinkler at its centre and the droplet initial velocities directed radially outwards. The source points were evenly spaced in a lattice pattern throughout the range of solid angles in which droplets had been measured. The sensitivity of results to the number of initial diameters, n_d, and spatially unique source points, n_s, was investigated, to ensure that the final results were not significantly affected by these settings.

The radius of the sphere on which the droplet source points were located, hereafter referred to as the 'spray source radius', was also varied between simulations, to investigate the influence of this parameter on results. In the same line of reasoning as has been presented for the impact sprinkler case above, it was possible that simulations in which droplets were introduced 'as measured', i.e. some distance from the sprinkler, could underestimate the effects of wind (see Figure 5.11). A spray source radius reduction factor, δ, was defined, such that:

$$r_s = \delta r_m \tag{5.1}$$

where r_s is the spray source radius and r_m is the distance from the sprinkler at which measurements had been taken (326 mm and 533 mm for the hollow-cone and butterfly sprinklers, respectively). Several simulations were conducted for each case, with progressively reduced spray source radius according to $\delta = \{1, 0.8, 0.6, 0.4, 0.2\}$.

Reduction of the spray source radius led to another research question: should droplet initial velocities be set 'as measured' when the droplets are released from points closer to the nozzle, or should the velocities be augmented somehow, to correct for the acceleration they would undergo before reaching the point at which measurements were taken? Previous studies had reported significant changes in droplet velocity distributions in the near-field, close to spray nozzles (Dorr *et al.* 2013; Nuyttens *et al.* 2007; Nuyttens *et al.* 2009). Augmentation of the droplet initial velocities may be beneficial in simulations with reduced spray source radius, since it could correct for such acceleration. To test this theory, simulations with reduced spray source radius were run with initial droplet velocities implemented 'as measured' and in an augmented form, and the results were compared.

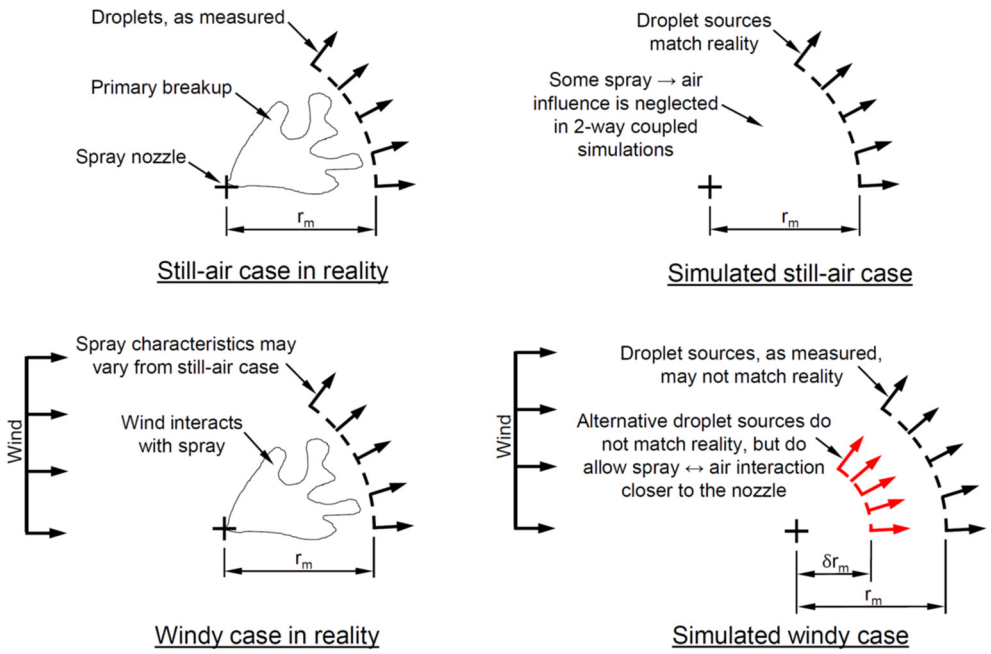

FIGURE 5.11: Challenges associated with the application of 'still-air' spray measurements to simulations with wind, and the spray source reduction factor, δ, that was trialled to address these challenges. Reduction of the droplet source radius does not replicate reality, but does allow some momentum, mass and energy transfer between phases closer to the nozzle, which may replicate a wind-affected spray more accurately. This hypothesis was tested.

It was not possible to calculate a set of augmented droplet initial velocities that would correct for the reduction in spray source radius exactly, since the air velocity field close to the sprinkler was not known. However, a simple method was developed which approximately corrected for the acceleration that the simulated droplets would undergo while travelling from δr_m to r_m. The droplets were assumed to be spherical and all forces except drag were neglected—the effect of gravity was assumed to be negligible compared to drag over the short trajectory of interest. The local air velocity was also assumed to be aligned with the droplet direction of travel. Thus, the acceleration of each droplet could be calculated in one-dimension. The change in droplet momentum over time was given by:

$$m_d \frac{du}{dt} = \frac{-1}{2} C_d \rho_a (u - u_a)^2 A_d \tag{5.2}$$

where m_d, u and A_d are the mass, velocity and frontal area of the droplet, respectively, C_d is the drag coefficient, t is time, and ρ_a and u_a are the density and local velocity of the air, respectively. Substitution of equations for the droplet mass and area, and replacement of du/dt with $u\,du/dr$ yielded:

$$\rho_d \frac{\pi d^3}{6} u \frac{du}{dr} = \frac{-1}{8} C_d \rho_a (u - u_a)^2 \pi d^2 \tag{5.3}$$

where r represents the droplet distance from the sprinkler and ρ_d is the droplet density. An expression containing the new, augmented, initial droplet velocity, u_1, was obtained by rearranging (5.3) and integrating both sides from the point of release to the point at which measurements had been taken:

$$\int_{u_1}^{u_m} \frac{u}{C_d (u - u_a)^2} du = \frac{-3\rho_a}{4\rho_d d} \int_{\delta r_m}^{r_m} dr \tag{5.4}$$

Here, u_m droplet velocity that was measured in Chapter 3.

Two issues prevented the direct solution of (5.4) to find u_1: 1) the local air velocity, u_a, was unknown and could vary along the path of the droplet; and 2) the drag coefficient, C_d, varies as a function of u. To overcome these issues, C_d was assumed to be constant for each droplet and was calculated based on the average of u_1 and u_m. u_a was also assumed to be constant along the path of each droplet. It was observed that the magnitude of u_a would be likely to lie between 0 (still air) and the lowest measured droplet speed in that region of the spray—typically the speed of a very small droplet, which would act somewhat like a tracer particle (Melling 1997). Thus, the constant air velocity was estimated using the expression:

$$u_a = f_a u_{m,min} \tag{5.5}$$

Here, f_a is a factor between 0 and 1, and $u_{m,min}$ is the minimum droplet velocity that was measured in the region of the spray surrounding the droplet of interest. There was no obvious basis for the selection of a value for f_a. A value of 0.95 was adopted, based on the thesis that the smallest, slowest droplets within the sprays were small enough and had travelled far enough from the breakup region to act acceptably well as tracer particles.

Integration and simplification of (5.4) then yielded:

$$\ln(u_1 - u_a) - \frac{u_a}{u_1 - u_a} = \frac{3\rho_a (1 - \delta) r_m C_d}{4\rho_d d} + \ln(u_m - u_a) - \frac{u_a}{u_m - u_a} \tag{5.6}$$

This equation was solved numerically, by iteratively recalculating u_a until the solution converged. The empirical relationship for spherical particles proposed by Morsi and Alexander (1972), and implemented in ANSYS Fluent, was used to calculate C_d.

It is acknowledged that the procedure described above contains several important assumptions. Its use in the present work was intended to provide an approximate correction for the effects of a reduced spray source radius, thereby allowing the influence of such velocity augmentation to be estimated. It may be that more sophisticated methods exist, which reduce the uncertainty in the augmented velocity, u_1.

5.4.7 Post-Processing of CFD Results

The details of droplets were recorded when they impacted on solid surfaces during the CFD simulations. However, it was only possible to record the values one time-step prior to impact. To estimate the location of each impact, the droplets were assumed to maintain a constant velocity during their final time-step—typically covering a distance of several millimetres. The recorded diameter, temperature and mass flow-rate of such droplets were not changed. A kernel density estimation method with Gaussian kernels used to convert the droplet impact data into continuous deposition fluxes on the solid surfaces. Band-widths of the kernels were tuned, to produce deposition flux profiles that were relatively smooth, but not overly so.

A dimensionless deposition flux was defined using the local water deposition flux on a surface, q [L s^{-1} m^{-2}], water flow rate through the sprinkler, Q [L s^{-1}], and the height of the cube, $H = 2.4$ m, as follows:

$$q^* = \frac{qH^2}{Q} \tag{5.7}$$

This variable has been used to compare results in the following sections. The standard deviation of simulated q^* in sets of results, σ_{q^*}, has also been referred to at some points in the following discussion, as a measure of the repeatability of results.

5.5 Results and Discussion

Simulations of the five test cases were qualitatively similar to the corresponding experiments (see Figure 5.12). The relatively large influence of drag forces (including the effects of the turbulent dispersion model) on smaller droplets was evident in all four cases involving wind (Cases A–D). Figure 5.13 displays an example of the continuous water deposition flux data obtained from the simulations. Fluxes in regions corresponding to the collection gauge apertures have been compared to experimental results through the remainder of this chapter.

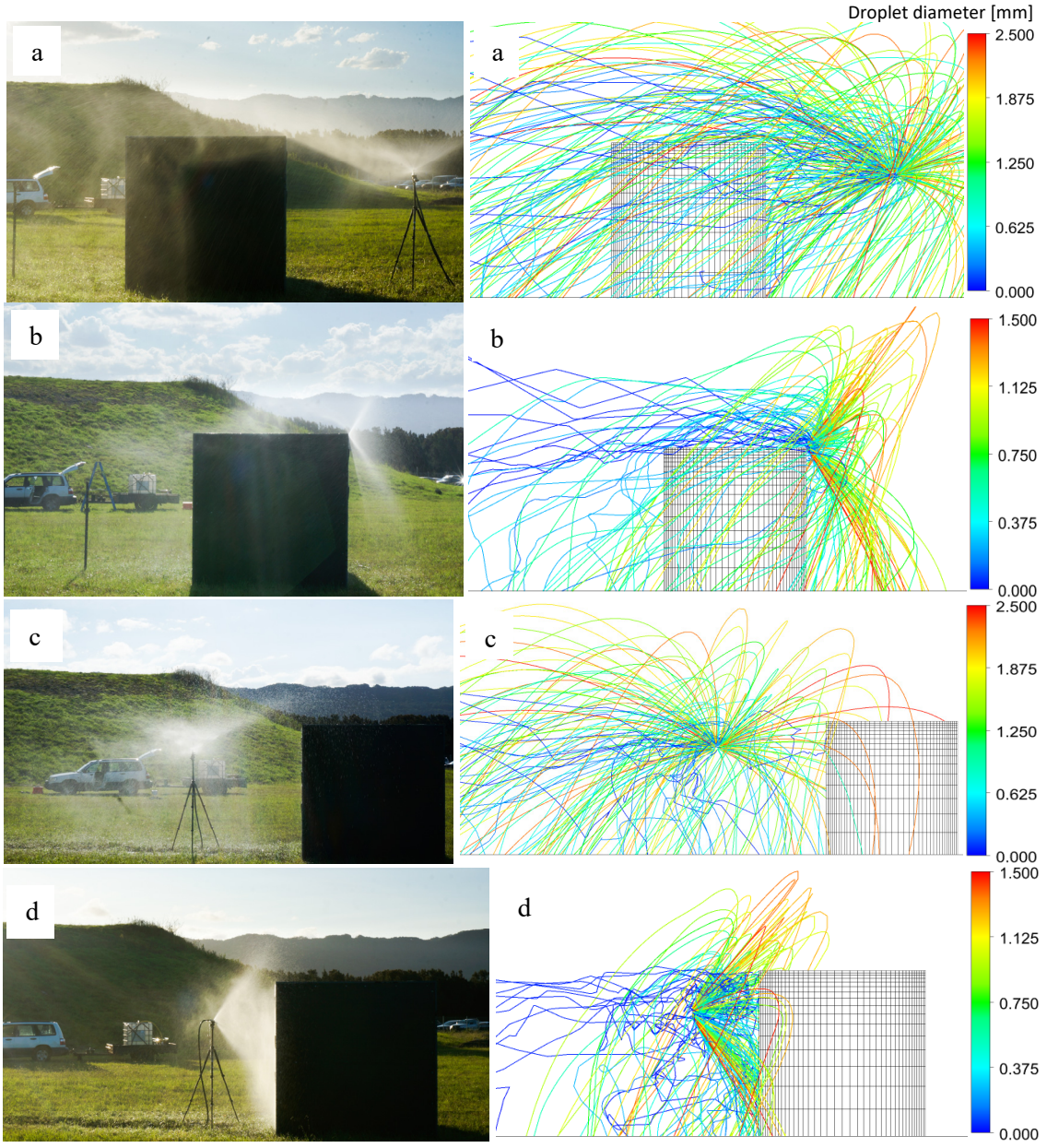

FIGURE 5.12: Comparison of CFD simulations with the corresponding experiments, for Cases A–D. Only a small sample of simulated droplet trajectories have been shown, coloured according to diameter (mm). The mean wind flow is from right to left in each image.

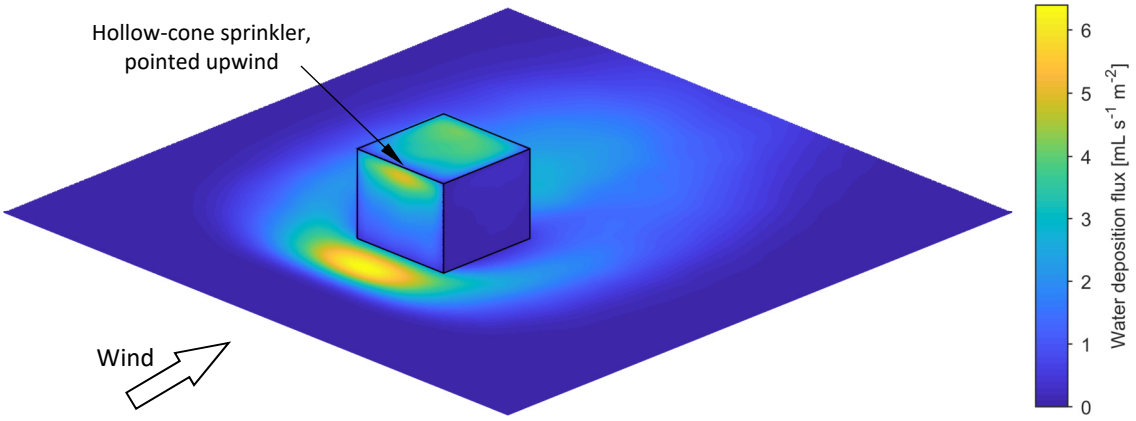

FIGURE 5.13: Simulated water deposition flux on the cube and ground surfaces in Case B.

5.5.1 Mesh Sensitivity

Water deposition fluxes simulated using coarse, medium and fine meshes were qualitatively very similar (see Figure 5.15 and Figure 5.14). The mean deviation between results obtained using the medium and fine meshes ranged from 3.1% to 5.9%, while the coarse meshes generated results that deviated from the fine-mesh results by 4.3% to 15.2%, on average. The largest variations were observed downwind of the cube in Case C and in the impact sprinkler case. Case C involved relatively large, slow droplets, which were emitted in the highly turbulent region at the leeward side of the cube, so it is likely that much of the variation in results from that case was caused by stochastic elements of the turbulent dispersion model. Droplets were able to penetrate further into the domain in the impact sprinkler case when a finer mesh was used, since regions of air entrainment around the concentrated stream of droplets could be resolved more accurately. The medium meshes were deemed to provide an acceptable degree of accuracy for the present investigation, so they were used for all subsequent simulations.

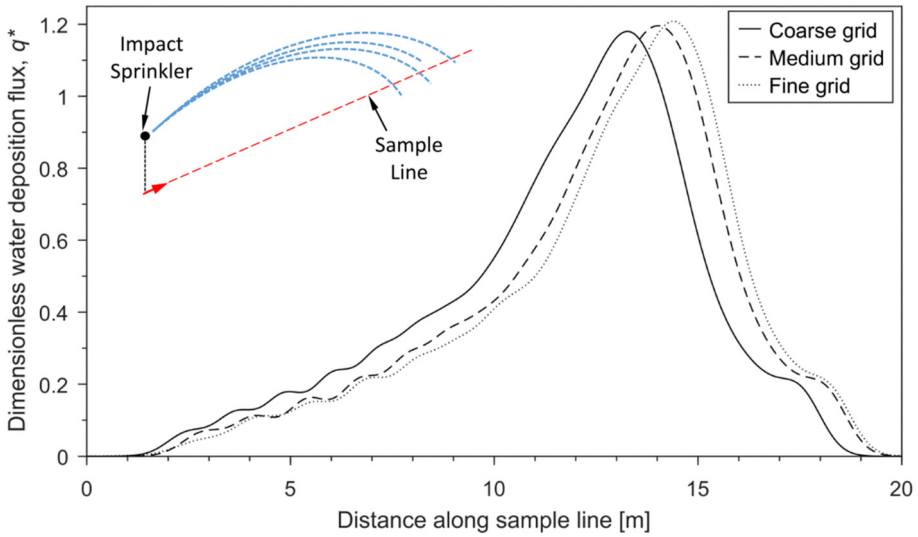

FIGURE 5.14: Sensitivity of simulated water deposition flux to refinement of the computational mesh, for the impact sprinkler case. Results have been sampled along a line at the base of the domain, starting directly below the sprinkler.

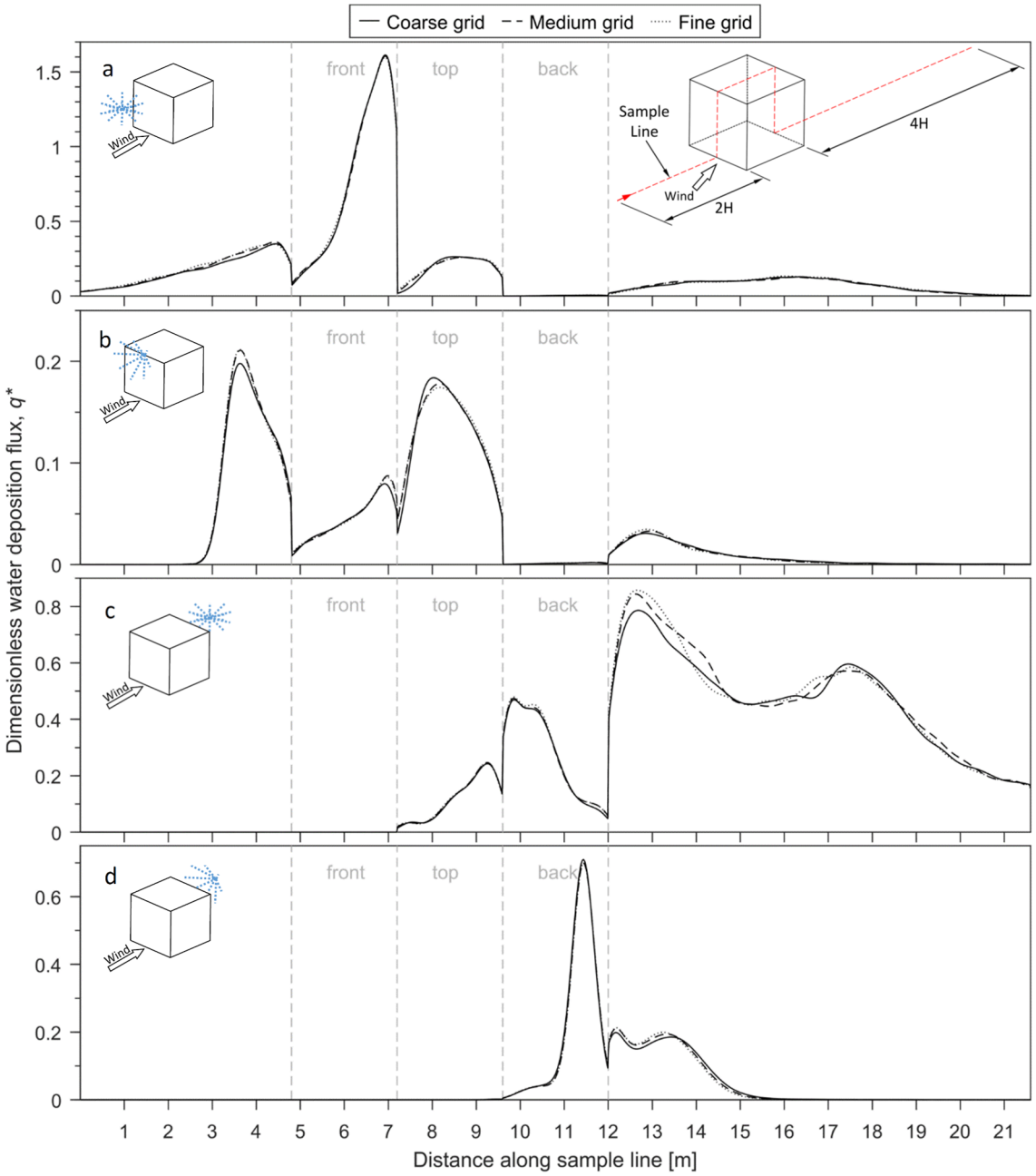

FIGURE 5.15: Sensitivity of simulated water deposition flux to refinement of the computational mesh. Results have been sampled along a line across the centre of the cube windward, top and leeward faces, starting on the ground, a distance 2*H* upwind of the cube and ending on the ground, 4*H* downwind of the cube, where *H* is the cube height of 2.4 m. Each plot presents results from one of the four cases: (a) butterfly sprinkler windward of the cube, (b) hollow-cone spray windward of the cube, (c) butterfly sprinkler leeward of the cube, and (d) hollow-cone spray leeward of the cube.

5.5.2 Horizontal Homogeneity

Simulations conducted in a long, empty, two-dimensional domain demonstrated that the computational mesh, turbulence model and boundary conditions could maintain a horizontally homogeneous velocity profile fairly well, but that the inlet profiles of k and ε deteriorated significantly within several cube edge-lengths of the inlet (see Figure 5.16). The deterioration of atmospheric boundary layer turbulence profiles in RANS-based CFD simulations has been well documented (Blocken, Stathopoulos & Carmeliet 2007; Richards & Norris 2011). As discussed in Section 5.4.2, the upstream extent of the domain was set $3H$ from the cube in simulations of Cases A–D, which minimised differences between the boundary layers incident on the cube and those measured in the field. The most significant deviations from the standard boundary layer profiles observed $3H$ from the domain inlet were reductions in k close to the ground. Such deviations from the standard k profile actually brought the k profile into closer agreement with measured values (see Section 5.4.5 and Figure 5.8), so they were not considered to be a cause for significant concern.

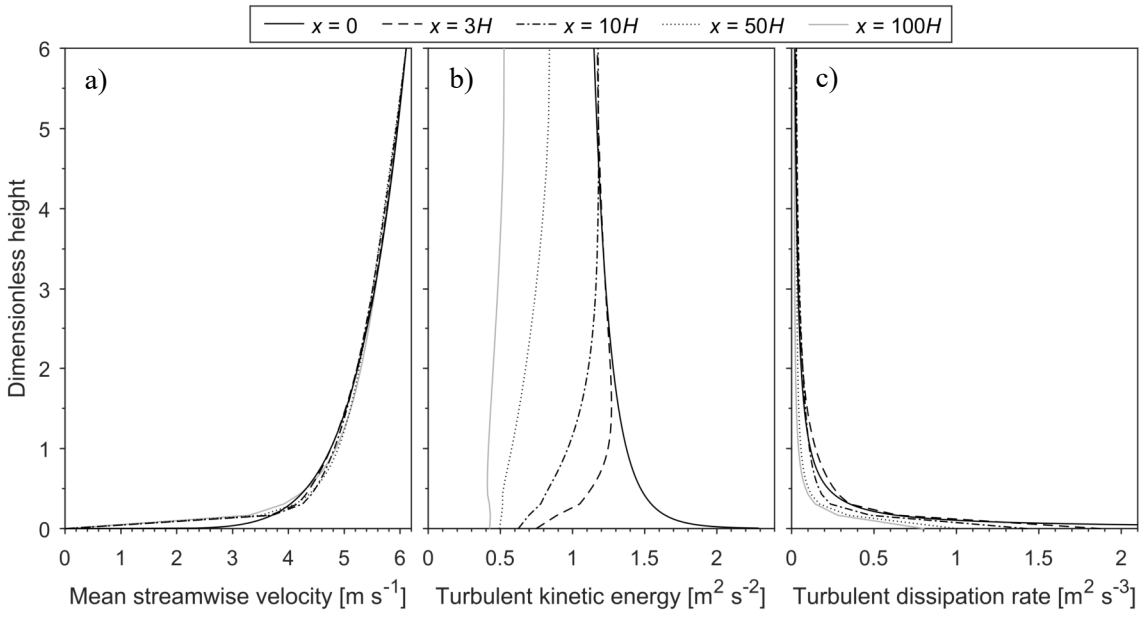

FIGURE 5.16: Horizontal homogeneity of vertical profiles of a) velocity, b) turbulent kinetic energy, and c) turbulent dissipation rate, when implemented in a long, empty, two-dimensional domain. Profiles are compared from several horizontal distances from the domain inlet (x). Lengths have been non-dimensionalised using the cube edge length, $H = 2.4$ m.

5.5.3 Sensitivity to Inlet Turbulence Kinetic Energy Profile

Simulations of Cases A–D conducted with the standard and custom inlet profiles of k produced results that were very similar (see Figure 5.17). The standard profiles produced results that agreed more closely with experimental results on the ground behind the cube in Cases C and D, and on the leeward face of the cube in Case D. Flow in these regions was highly turbulent, but much of the turbulence was introduced by flow interactions with the cube. It is likely that some of the variation that was observed in results was caused by stochastic elements of the turbulent dispersion model. However, the consistency with which results leeward of the cube were improved by adopting the standard profiles did indicate that such changes may also be important. All subsequent simulations were conducted with the standard inlet profiles of k.

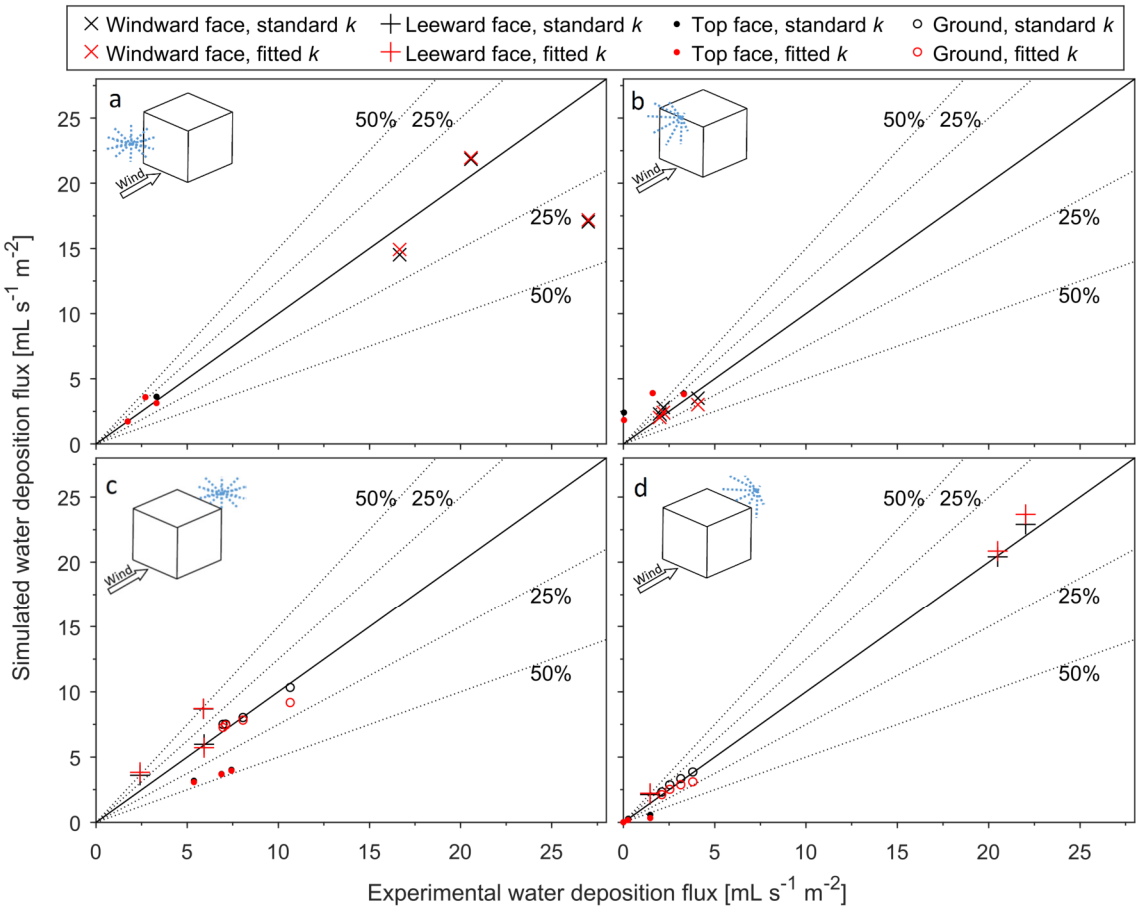

FIGURE 5.17: Water deposition fluxes simulated with the standard turbulence kinetic energy (k) profile for the power-law boundary layer, and with a custom k profile fitted to experimental data, plotted against the corresponding experimental results. Results are presented for four cases: a) butterfly sprinkler windward of the cube, b) hollow-cone spray windward of the cube, c) butterfly sprinkler leeward of the cube, and d) hollow-cone spray leeward of the cube.

5.5.4 Sensitivity to Droplet Source Settings

In Cases A–D, simulations with increasing numbers of droplet source points, n_s, and size classes, n_d, produced distributions of water deposition flux that appeared to converge towards a limit (see Figure 5.18). Simulations with fewer than 10 droplet size classes or 1,000 source points produced results that deviated significantly from the reference results, which were obtained with $n_s =$ 10,000 and $n_d = 20$. Considering each case separately, the mean deviation of results obtained using $n_s =$ 1,000 and $n_d = 10$ from the reference results ranged from 2.9% to 5.3%, while those obtained using $n_s =$ 3,160 and $n_d = 15$ deviated from the reference by between 1.4% and 3.7%.

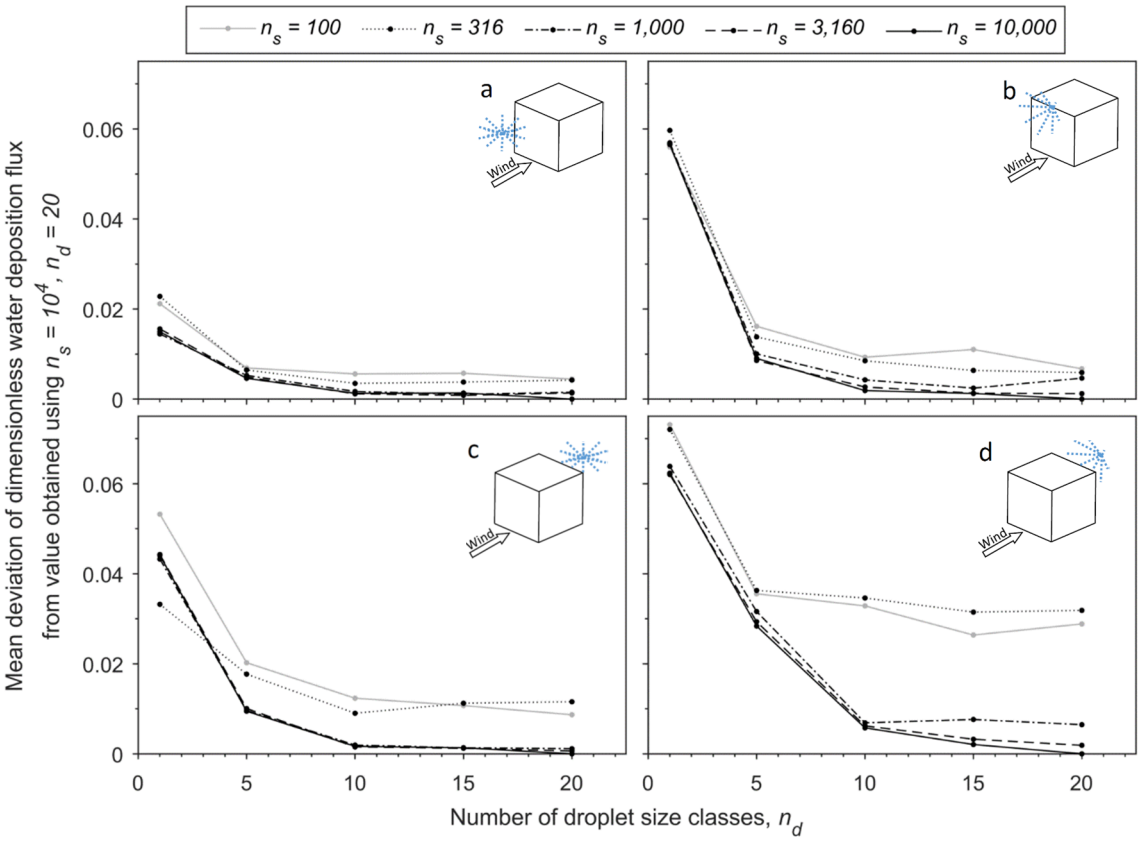

FIGURE 5.18: Sensitivity of simulated water deposition, on and around the cube, to the number of spatially unique droplet source points (n_s) and the number of droplet size classes (n_d). Results are presented for four cases: (a) butterfly sprinkler windward of the cube, (b) hollow-cone spray windward of the cube, (c) butterfly sprinkler leeward of the cube, and (d) hollow-cone spray leeward of the cube.

Similar results were obtained in the impact sprinkler case, except that all simulations of that case were conducted with $n_s = 1$. Simulations conducted with fewer than 20 droplet size classes deviated significantly from the reference simulation, which was run with $n_d = 30$ (see Figure

5.19). The mean deviation of water deposition fluxes simulated with $n_d = 20$ and $n_d = 25$ from the reference result, were 4.7% and 2.7%, respectively.

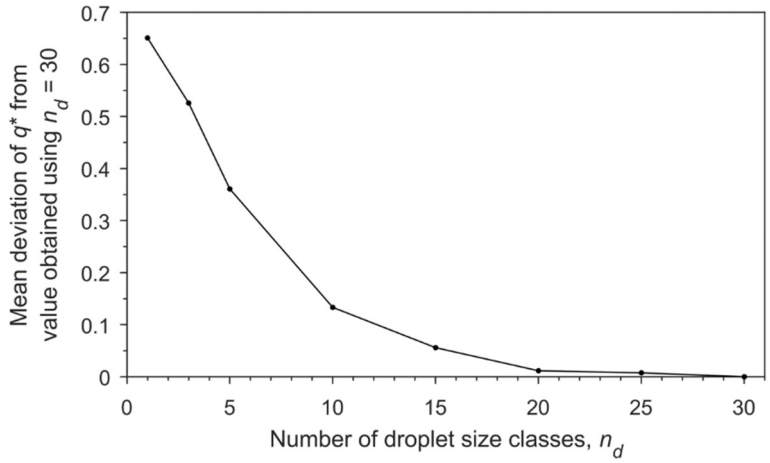

FIGURE 5.19: Sensitivity of simulated water deposition on the ground near the impact sprinkler, to the number of droplet size classes (n_d). The number of spatially unique droplet source points (n_s) was fixed as 1 for simulations of the impact sprinkler.

The total number of particles tracked per iteration was given by the product of n_s, n_d and, when the turbulent dispersion model was implemented, the number of stochastic iterations, n_{td}. Thus, the computational cost of simulations was strongly influenced by changes to n_s or n_d, and selection of values for n_s or n_d is a balance between accuracy and computational cost. In the present study, all subsequent simulations of Cases A–D were conducted with $n_s = 3{,}160$ and $n_d = 15$, and simulations of the impact sprinkler case were conducted with $n_d = 25$.

The spray source radius also had a significant effect on simulated water deposition flux. Simulations of Cases B and C were observed to deviate more from experimental results when the droplet source points were located closer to the sprinkler nozzle (see Figure 5.20). Simulations of Cases A and D were improved by small (20–40%) reductions in the source radius but began to deviate more from the experiments when the source radius was reduced further. When droplet initial velocities were augmented to account for the reduced spray source radius, the mean error in Cases B and C was affected less by reductions in the spray source radius, and simulations of Cases A and D exhibited gradual improvement as the droplet sources were moved closer to the sprinkler. One and two-way coupled simulations were effected similarly by changes in the droplet source radius.

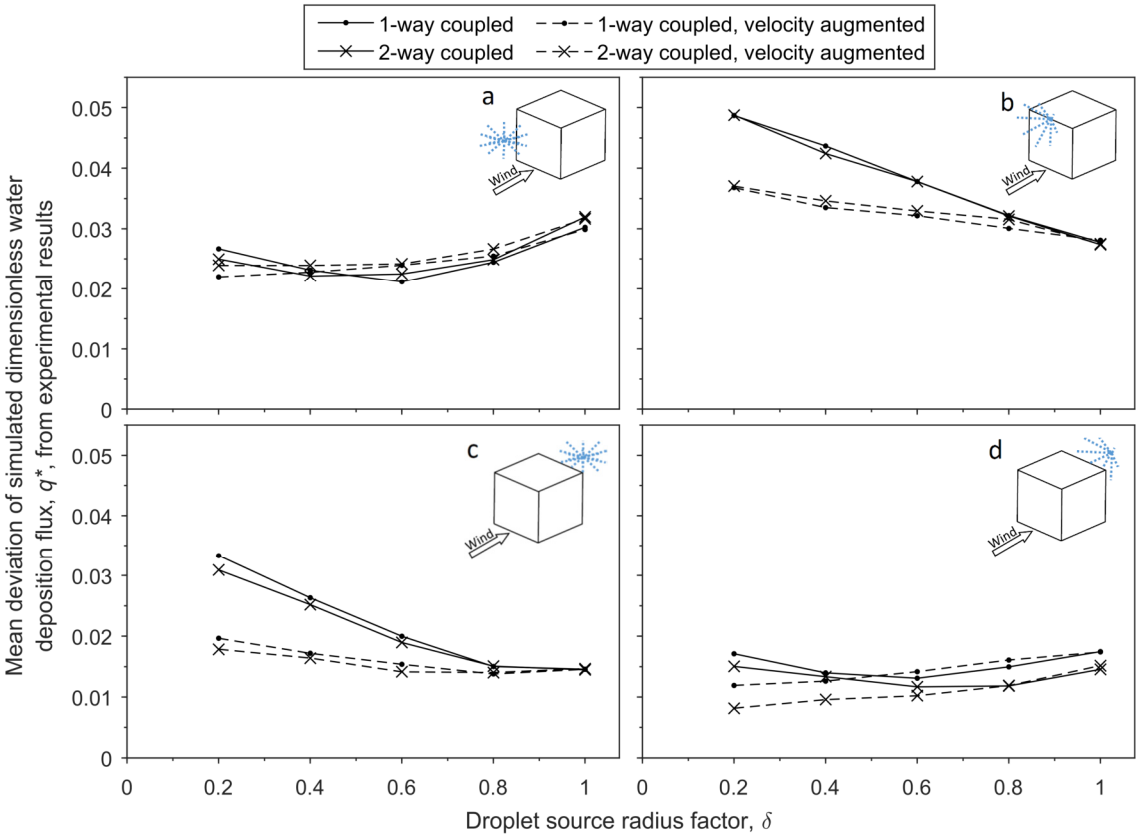

FIGURE 5.20: Influence of spray source radius on simulation accuracy. Droplets were introduced into the simulations at various distances from the sprinkler nozzle, defined by $r = \delta r_{meas}$, where r_{meas} is the distance from the sprinkler nozzle at which the sprays were characterised in Chapter 3. In some simulations the initial velocities of the droplets were equal to those measured in Chapter 3, and in others they were augmented to account for any acceleration between the point of release and r_{meas}. Results are presented for four cases: (a) butterfly sprinkler windward of the cube, (b) hollow-cone spray windward of the cube, (c) butterfly sprinkler leeward of the cube, and (d) hollow-cone spray leeward of the cube.

It was not possible to reach a definitive conclusion based on the results presented here, as to whether droplet source points in all CFD simulations of sprays should be located 'as measured' or closer to the spray nozzle. However, the results did highlight the sensitivity of some spray simulations to such choices, and the benefits that augmentation of initial droplet velocities can have when the droplet source locations are not set 'as measured'. In the four cases examined here, the best overall agreement with experimental results was obtained with reduced spray source radii, such that $\delta = 0.2$, and augmented initial droplet velocities. With these settings, the mean deviation of Cases A and D from experimental results was reduced by 24% and 46%, respectively, compared to simulations with droplets released 'as measured', while the deviation between

simulations of Cases B and C and the corresponding experiments was increased by 35% and 22%, respectively. These settings were used for all subsequent simulations in the present work.

5.5.5 Influence of Turbulent Dispersion

Simulations of all five cases exhibited decreased sensitivity to the number of stochastic iterations used in the DRW turbulent dispersion model, n_{td}, as n_{td} was increased (see Figure 5.21 and Figure 5.22). Increases in n_{td} above approximately 20 had a relatively small effect on the repeatability of simulated water deposition fluxes, since a good statistical representation of the spray had been established. Similar to n_d and n_s, selection of n_{td} was a compromise between computational cost and accuracy. All subsequent simulations employing the turbulent dispersion model were conducted with n_{td} =30.

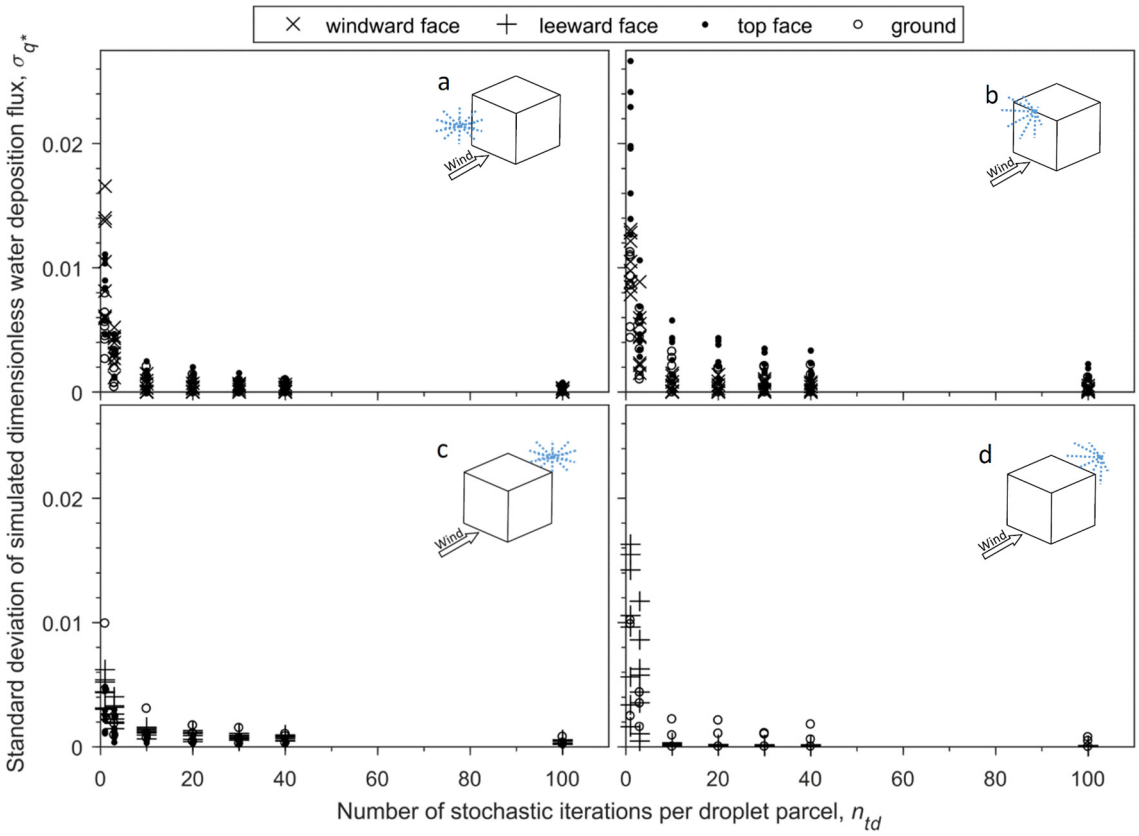

FIGURE 5.21: Influence of the number of stochastic iterations, n_{td}, used in the discrete-random-walk turbulent dispersion model, on the repeatability of simulated water deposition fluxes. Each data point represents the normalised standard deviation of water deposition fluxes predicted, at a single point, by 20 simulations run with the same settings. Results are presented for four cases: (a) butterfly sprinkler windward of the cube, (b) hollow-cone spray windward of the cube, (c) butterfly sprinkler leeward of the cube, and (d) hollow-cone spray leeward of the cube.

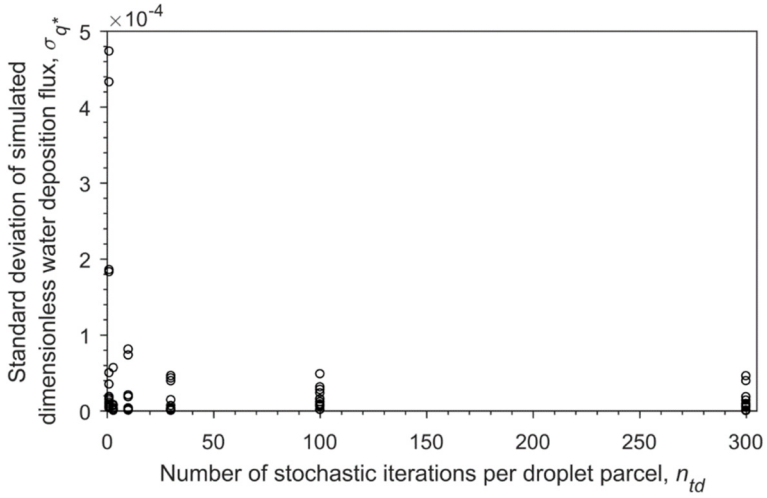

FIGURE 5.22: Influence of the number of stochastic iterations, n_{td}, used in the discrete-random-walk turbulent dispersion model, on the repeatability of simulated water deposition fluxes in the impact sprinkler case. Each data point represents the normalised standard deviation of water deposition fluxes predicted, at a single point, by 20 simulations run with the same settings.

Comparison of results obtained with and without the turbulent dispersion model revealed that, in some cases, the agreement between CFD and experimental results was improved significantly by the turbulent dispersion model (see Figure 5.23). The most notable improvements were observed on the ground at the leeward side of the cube in Cases C and D, on the leeward surface of the cube in Case D, on the windward surface of the cube in Case B and on the top surface of the cube in Case A. Turbulence could be expected to have the largest influence droplet trajectories in such regions, since turbulence would have been significantly more intense in regions of separated flow, close to the top cube surface and at the leeward side of the cube, and near the stagnation point at the cube windward surface.

Droplets travelling directly from the butterfly sprinkler to the nearest cube surface (i.e. the windward surface in Case A and leeward surface in Case C) were also influenced significantly by the turbulent dispersion model, but with no clear improvement in the correlation between CFD and experimental results. This may have been caused by the simplified representation of that spray in simulations, as a steady conical spray rather than the swirling stream of droplets that it was in reality. The dense grouping of droplets within the actual spray would have been influenced less by the mean airflow, and turbulent fluctuations thereabout, than the time-averaged version of the spray that was simulated.

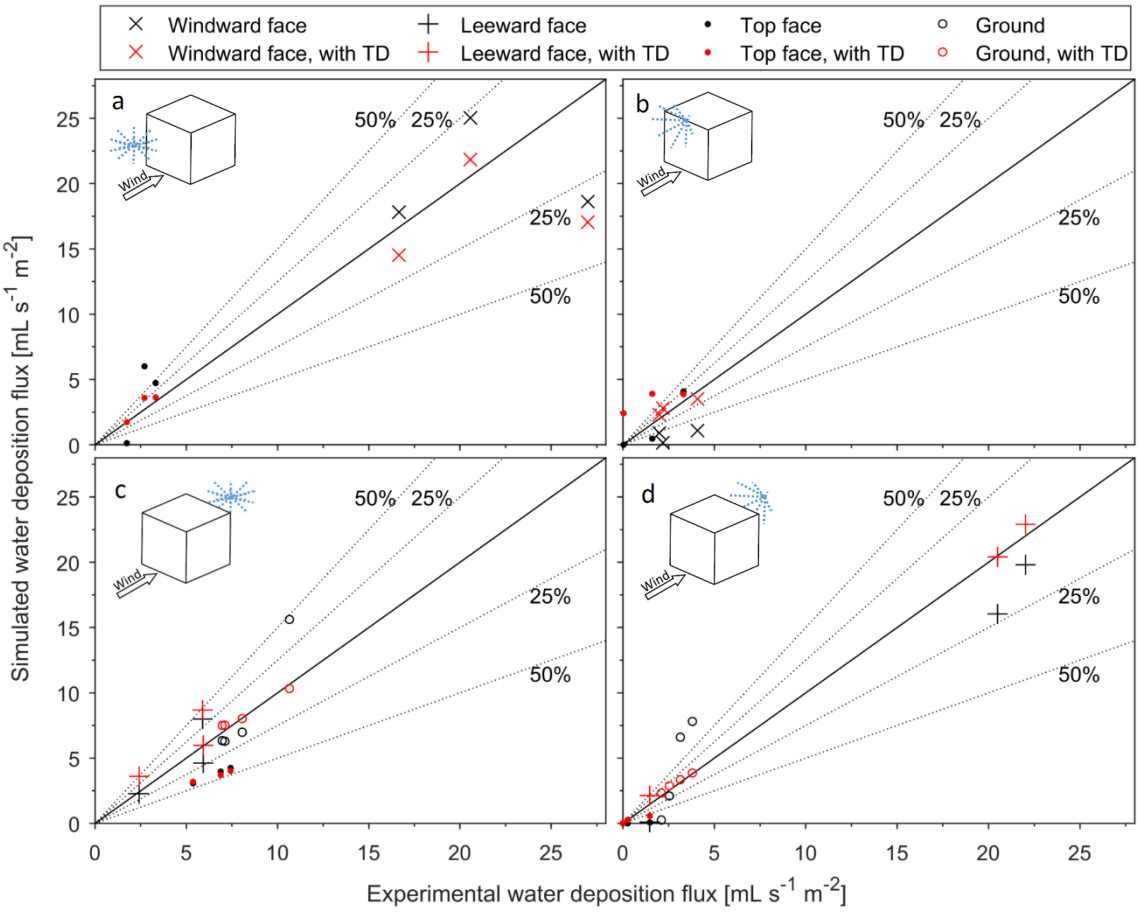

FIGURE 5.23: Water deposition fluxes simulated with and without the turbulent dispersion model (TD) enabled, plotted against the corresponding experimental results. Results are presented for four cases: a) butterfly sprinkler windward of the cube, b) hollow-cone spray windward of the cube, c) butterfly sprinkler leeward of the cube, and d) hollow-cone spray leeward of the cube.

5.5.6 Comparison of Turbulence Models

Results obtained using the RNG k-ε turbulence model were qualitatively very similar to those produced using the realisable k-ε model (see Figure 5.24). Neither model was distinctly superior for a majority of the test cases, although some individual results did differ by up to 2 mL s^{-1} m^{-2}, which amounted to a relative difference of 50% in the case of one result. The RNG k-ε model did replicate experimental deposition fluxes on the top cube surface with slightly better accuracy in Cases A, B and D, which may indicate that the RNG model simulated the separated flow above the cube more accurately. However, comparison to a larger experimental dataset would be required before such a conclusion could be made with confidence. For the sake of consistency, and since the performance of both turbulence models was acceptable in the cases tested here, subsequent simulations in the present work were run using the realisable k-ε turbulence model.

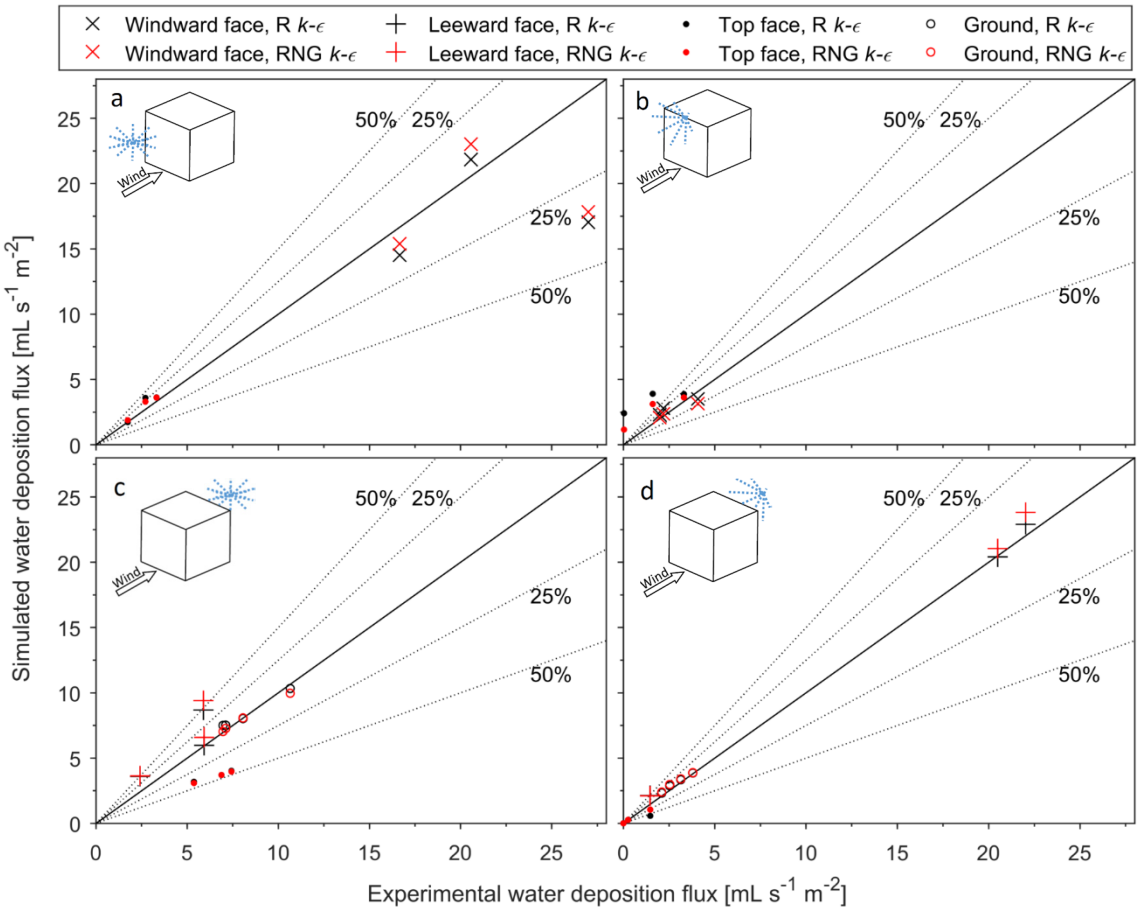

Figure 5.24: Comparison of water deposition fluxes simulated with the realisable *k-ε* (R *k-ε*) and renormalisation group *k-ε* (RNG *k-ε*) turbulence models. Results are presented for four cases: a) butterfly sprinkler windward of the cube, b) hollow-cone spray windward of the cube, c) butterfly sprinkler leeward of the cube, and d) hollow-cone spray leeward of the cube.

5.5.7 Interphase Coupling

Simulations of Cases A–D conducted with one-way coupling produced results that were within 10% of two-way coupled solutions, in 31 of the 32 results that were compared (see Figure 5.25). The largest differences were observed on the windward and leeward cube surfaces, in cases where the sprinklers were emitting droplets directly towards these surfaces. This was probably due to the high liquid volume densities and velocities in the regions between the sprinklers and cube in such cases, which would have had a relatively large influence on the local air flow.

The results presented here indicate that, for many cases, acceptable accuracy may be achieved using one-way coupled simulations. This is a significant finding, since the computational requirements of such simulations can be 1–2 orders of magnitude less than those of two-way coupled simulations. However, it is apparent that the relative importance of droplet-air influence

can be greater in cases involving spray impingement onto solid surfaces from a relatively close range. Furthermore, two-way coupled simulations must be used for cases in which the heat and/or mass transfer from droplets to the continuous phase is important, e.g. for cases in which the cooling effect of sprays on the air flow is of interest, or when the local accumulation of water vapour may have a significant effect on droplet evaporation rates.

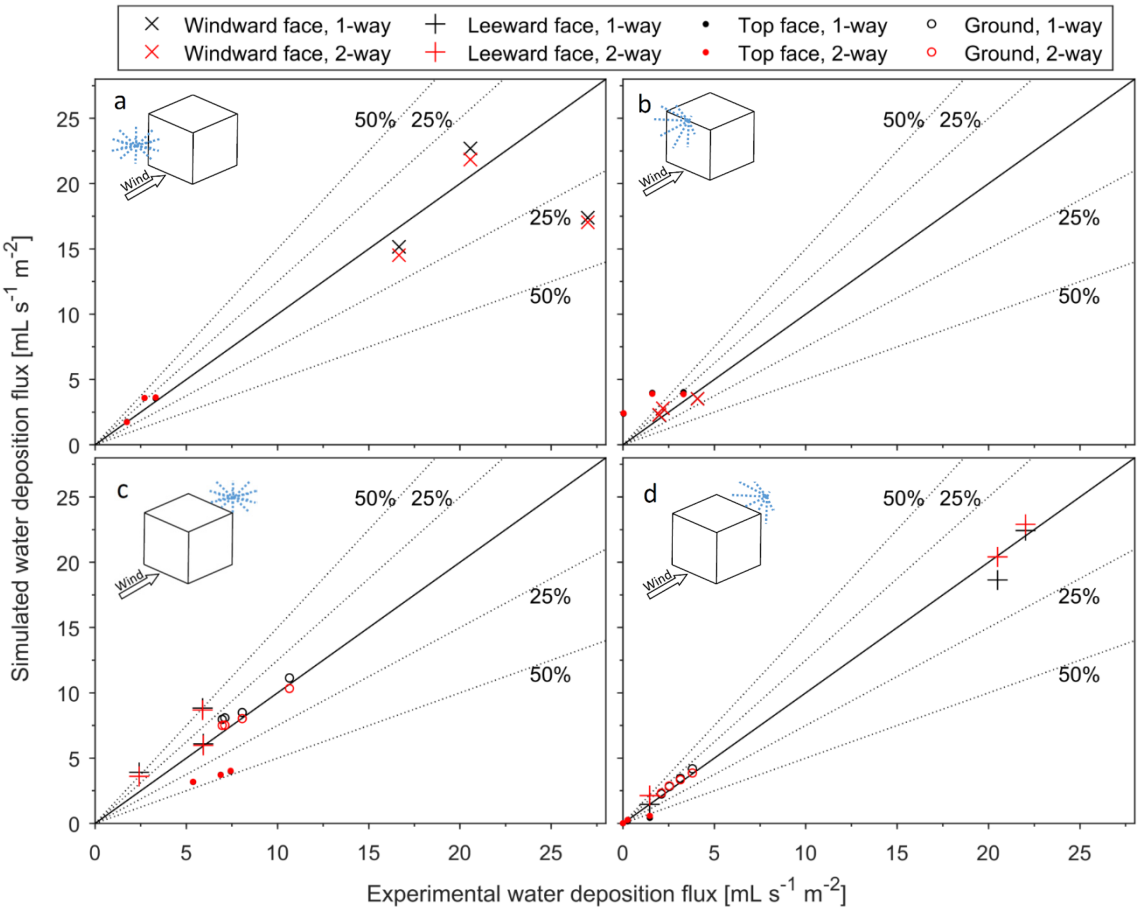

FIGURE 5.25: Water deposition fluxes from one and two-way coupled simulations, plotted against the corresponding experimental results. Results are presented for four cases: a) butterfly sprinkler windward of the cube, b) hollow-cone spray windward of the cube, c) butterfly sprinkler leeward of the cube, and d) hollow-cone spray leeward of the cube.

Simulations of the impact sprinkler case were strongly influenced by the interphase coupling setting (see Figure 5.26). In two-way coupled simulations, droplets were subjected to reduced drag forces due to induced air flow within the spray, which caused them to penetrate further into the domain. The trajectories of small droplets were influenced more by the difference in drag than larger droplets. Consequently, two-way coupled simulations produced a narrower stream of droplets, with much higher liquid volume density but with a lower mean droplet diameter.

Droplets 6 m from the sprinkler were also travelling slower in the one-way coupled simulation, due to the large drag forces to which they were subjected.

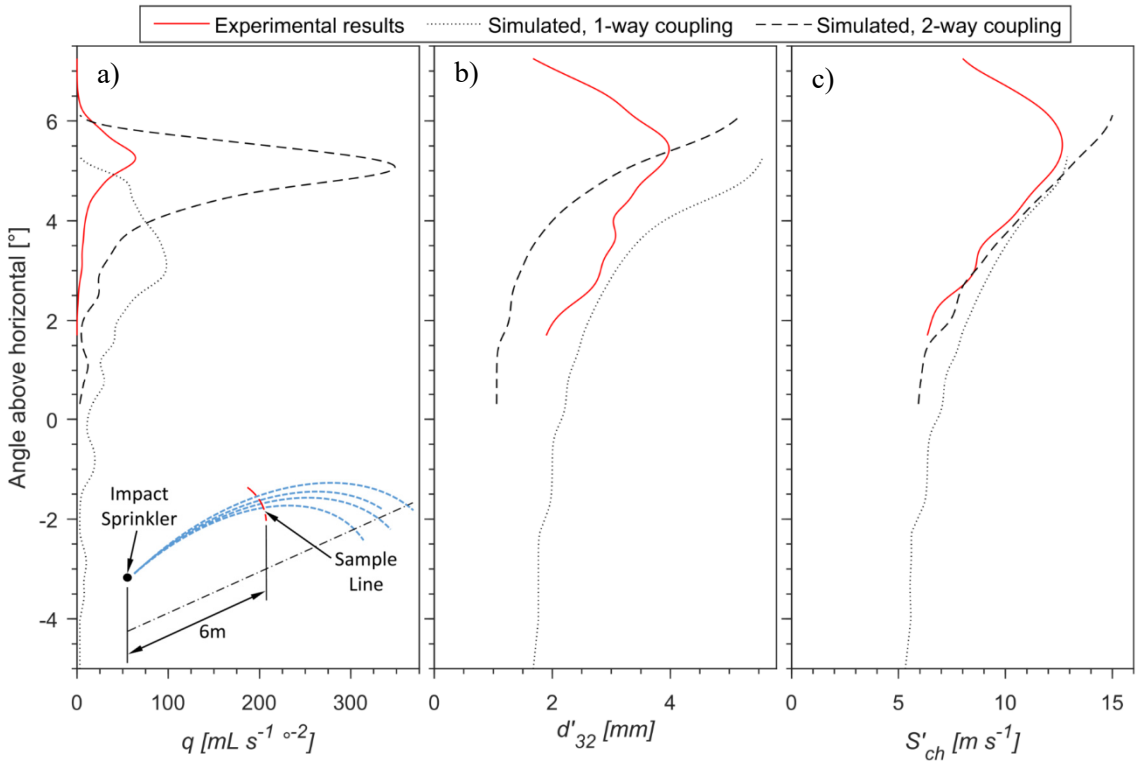

FIGURE 5.26: Comparison of simulated and experimental: a) liquid volume flux (q), b) local Sauter mean diameter (d'_{32}), and c) local characteristic speed (S'_{ch}), for the impact sprinkler. These profiles were sampled along an arc in the vertical centre-plane of the spray, centred at the sprinkler nozzle and with a radius of 6 m.

Both one and two-way coupled simulations failed to produced liquid volume flux distributions similar to the measured profile from Chapter 3 (see Figure 5.26). Two-way coupled simulations produced a narrow stream of droplets, similar to the real spray, but the liquid volume flux in the vertical centre-plane was approximately five times larger than the measured value. One-way coupled simulations produced a stream of droplets that was much more widely dispersed in the vertical direction, and that also contained a higher total liquid volume flux in the vertical centre-plane than had been measured in the real spray. The simulated sprays had the same total liquid flow-rate as the real spray, so the larger fluxes observed in the vertical centre-plane indicated that both one and two-way coupled simulations had greatly under-predicted the lateral dispersion of droplets. This was probably due to the highly simplified method that was adopted to simulate the impact sprinkler spray, in which pre-formed droplets were emitted from the sprinkler location. In

the absence of an external force, such as wind, the only mechanism by which droplets could disperse laterally in such simulations would be in response to velocity fluctuations imposed by the turbulent dispersion model. The results presented here indicate that a concentrated stream of pre-formed droplets cannot be used to accurately represent a liquid jet undergoing breakup. It is possible that in simulations with stronger global turbulence (e.g. simulations of the impact sprinkler in wind) the turbulent dispersion model would disperse droplets in a manner more similar to the breakup processes, but no reliable experimental data was available in the present study to investigate such a possibility.

The failure of the turbulent dispersion model to accurately replicate droplet dispersion, which was, in reality, caused by liquid breakup processes as well as turbulent velocity fluctuations, is also evident in the profiles of local Sauter mean diameter in Figure 5.26. The simulated droplet streams clearly exhibit decreasing droplet mean diameter with decreasing elevation angle, which was caused by the relatively large influence that drag had on the velocities of small droplets. The turbulent dispersion model did not cause enough small droplets to travel to the top of the stream to significantly reduce the mean diameter there, while the profile measured from the actual spray exhibits mean diameters that decreased above and below a core stream of relatively large droplets.

5.5.8 Inactive Turbulence

Changes to the mean wind speed and/or direction, within the range of measured values from the experiments, influenced simulated water deposition fluxes significantly in some cases (see Figure 5.27). However, the weighted average of results from such simulations did not differ significantly from results obtained from the single, steady simulations. It is possible that transient simulations, taking the effects of 'inactive' turbulence into account by imposing a constantly varying inlet velocity, would have produced different results from the weighted averages presented here. It is also possible that 'inactive' turbulence did have a significant effect on water deposition in some or all of the test cases, just not at the locations at which measurements were taken. However, in the absence of contradictory evidence, the results presented here indicate the accuracy of results would not be improved by taking the effects of 'inactive' turbulence into account.

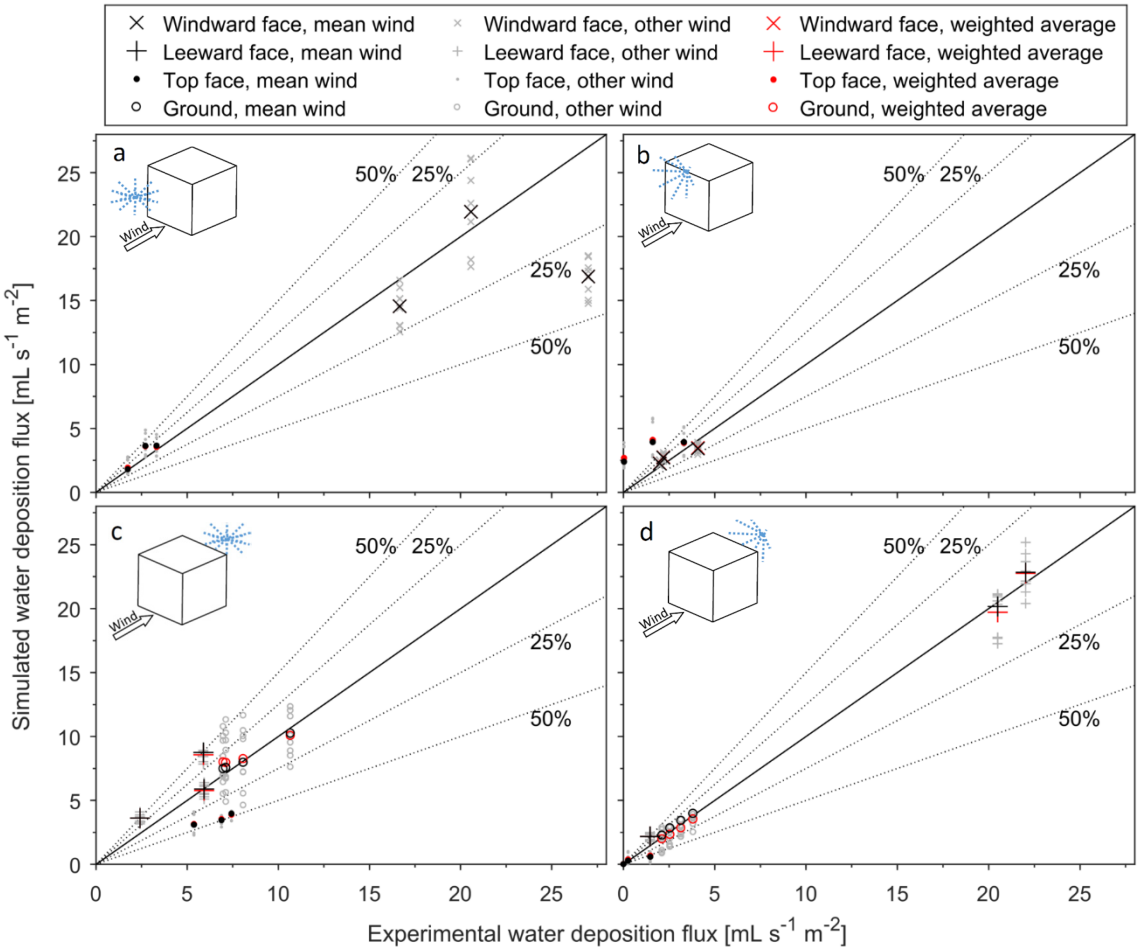

FIGURE 5.27: Simulation sensitivity to 'inactive' turbulence. Results are presented from simulations with the measured mean wind speed and direction; with altered mean wind speeds and/or directions, which were taken from within the range of measured values (labelled 'other wind'); and the weighted average of results from such 'other wind' simulations. Results are presented for four cases: a) butterfly sprinkler windward of the cube, b) hollow-cone spray windward of the cube, c) butterfly sprinkler leeward of the cube, and d) hollow-cone spray leeward of the cube.

5.6 Conclusion

A literature review and simulation study were conducted, to investigate whether steady, RANS-based CFD techniques could accurately simulate spray dispersion around buildings in wind, and how computational cost could be minimised by simplifying such simulations, without compromising the accuracy of results. Different methods to implement measured spray characteristics in CFD simulations were also tested. Two questions of particular interest where whether transient sprays, such as those produced by 'butterfly' sprinklers, could be accurately simulated in a time-averaged form, and whether a range of sprays, including liquid jets, could be accurately simulated without modelling primary or secondary breakup processes.

Simulations of five test cases were compared to experimental results. Four of the cases (Cases A–D) involved atmospheric boundary layer flow around an isolated 2.4m cube, with a single hollow-cone or butterfly sprinkler operating close to the windward or leeward cube surfaces. Water deposition fluxes on the cube surfaces, and on the ground nearby, were compared to measured values. The fifth case involved a steady liquid jet, emitted into quiescent air at an angle of 11° above the horizontal. Simulated results were compared to measured liquid volume flux, droplet diameter and droplet velocity measurements that had been taken 6m from an impact sprinkler emitting such a jet.

Reasonably good agreement was observed between the CFD and experimental results of Cases A–D. Simulated deposition fluxes on the cube walls and ground were all within ±50% of the measured values, and 17 out of 20 of such results were within ±15% of the experimental results. Simulated deposition fluxes on the cube top surface did not match the experimental values as closely; they were generally over-predicted in simulations involving a sprinkler upwind of the cube and under-predicted in simulations involving a sprinkler downwind of the cube. Considering the simplified nature of the simulations, including the representation of a transient 'butterfly' sprinkler spray as steady, such results do not entirely diminish the value of RANS-based methods in simulating cases such as those considered here. Thus, the combination of methods adopted in the present study is capable of predicting water deposition by wildfire sprinkler systems in windy conditions, with an uncertainty of approximately ±50% in the deposition flux magnitude at any given point. Further validation studies would be warranted, and further investigation into discrepancies in the deposition flux on the roofs of structures would be very worthwhile.

Simulation of the steady liquid jet as a concentrated stream of pre-formed droplets did not produce results that matched the experimental measurements. Reliance on the turbulent dispersion model to disperse droplets laterally in such simulations led to greatly underestimated lateral spread compared to the real spray, in which droplets were dispersed laterally by the primary and secondary breakup processes. A different approach would be required to simulate water dispersion from an undisrupted liquid jet, perhaps including a model for the breakup of the jet

into droplets. It is not clear how measured spray properties could be translated into such an approach, so they may be more useful for validation purposes than as an input for simulations of such sprays. Further challenges would be encountered in CFD simulations of impact sprinklers in full operation, since the periodic disruption of the jet by the paddle arm, and the rotation of the sprinkler head, would need to be taken into account. The computational expense of a transient CFD simulation encompassing the full rotation of an impact sprinkler—a time period of 27.7 s in the present case—could be several orders of magnitude larger than that of the steady simulations reported in this chapter.

The sensitivity of results to various aspects of the CFD method was also investigated, which led to several interesting findings:

- One and two-way coupled simulations produced very similar results in Cases A–D, despite the fact that liquid volume fractions close to the sprinklers were on the order of 10^{-4}—far in excess of the 'rule of thumb' threshold above which two-way coupling should be used, 10^{-6}. One-way coupled simulations would be much more appropriate for application to wildfire sprinkler system design or performance assessment tasks, due to their significantly reduced computational cost, provided that the influence of the spray on its surroundings (e.g. the cooling of gases) is not of interest.
- The implementation of droplet source points closer to the sprinkler than the distance at which the spray characteristics had been determined caused simulations to deviate significantly more from the experiments, in some cases. However, when the droplet initial velocities were augmented, to correct for such a change in initial position, the agreement with experimental results was improved. A slight net improvement was observed in the Cases A–D when they were all simulated with droplet source points much closer to the sprinkler and with augmented initial velocities. These observations have implications to CFD simulations in which droplet sources are not implemented exactly 'as measured'.

- The combination of results from several steady simulations, with various mean wind speeds and directions, into one weighted average produced results that were very similar to those obtained with a single steady simulation. This indicated that 'inactive' turbulence had a relatively small influence on the dispersion of water in the cases considered here. Thus, the simulation of wildfire sprinkler systems in pseudo-steady states can be warranted.
- Turbulent dispersion was found to improve the agreement between CFD and experimental results significantly.
- The RNG k-ε and realisable k-ε turbulence models produced similar results in simulations of Cases A–D, although the RNG model did predict deposition fluxes on the cube top surface that were slightly closer to the experimental results.
- Reasonably consistent results were obtained when 1000 or more spatially unique droplet source points and 10 or more distinct initial droplet diameters were used to represent each spray, and when 20 or more stochastic iterations were conducted in the turbulent dispersion model.

The present investigation was limited in scope. It is possible that better agreement with experimental results could be obtained using turbulence-resolving CFD methods (e.g. LES or DES), an Eulerian-Eulerian multiphase method, more sophisticated turbulent dispersion models, or by allowing droplet collisions or breakup. However, such changes would increase the computation expense of simulations, except perhaps for the adoption of an Eulerian-Eulerian multiphase method. Comparison of results presented here with such simulations would be worthwhile.

The method developed here could justifiably be applied to wildfire sprinkler systems, with care. In addition to the uncertainty in simulation accuracy, discussed above, the present work did not consider the influence of wildfire on the continuous phase (e.g. buoyant plumes), or on the discrete phase (e.g. radiant heat transfer to droplets). The post-impact transport of water, by processes such as splashing, runoff, absorption and evaporation, was also not considered. Results

from this chapter could be used as a ‘first step’, from which to develop validation studies involving strong localised heat sources, flying embers and/or post-impact water transport. Alternatively, the method presented here can be applied directly to estimate the dispersion of water around buildings prior-to and after the passage of a wildfire.

Chapter 6

Wildfire Sprinkler System Performance Comparison

This chapter outlines the investigation into the performance of nine wildfire sprinkler configurations, typical of those reported in the literature. The CFD methods developed in Chapter 5 were applied to estimate the effects of wind drift and evaporation on droplet dispersion from each system, and bespoke post-processing techniques were used to estimate the system capacity to cool building surfaces and attenuate radiant heat. Thus, this chapter provides both a demonstration of how CFD methods, developed in previous chapters, can be applied to practical problems, and a quantitative comparison of typical wildfire sprinkler systems.

6.1 Introduction

A review of scientific publications and technical guidance related to wildfire sprinkler systems revealed that very few scientific investigations had focused on such systems, and as a result, much of the advice available to system designers was inconsistent and lacked detail (see Chapter 2). Various configurations of sprinklers had been recommended, however, at the time of writing no previous analyses appeared to have been undertaken that quantified the performance of wildfire sprinklers protecting buildings. Without quantitative data on the effects of different sprinkler configurations regarding the mitigation of radiant heat, ember attack or flame contact, taking into account the strong, hot, dry winds that typically occur during wildfires, it would not be possible

to design sprinkler systems that make the best use of a given water resource, or to understand the protection that could be provided by such sprinkler systems.

The CFD method developed in Chapter 5 provided a means by which to quantify the dispersion of sprays in wind with a reasonably high degree of accuracy (see evaluations of simulation accuracy in that chapter). Its application in this chapter demonstrates how specific wildfire sprinkler arrangements can be simulated in realistic wind conditions. However, as identified in Chapter 2, other fundamental aspects of wildfire sprinkler performance are still not well understood. For example, the various mechanisms by which wildfire sprinklers could mitigate the effects of wildfire on buildings have not been quantified (see Section 2.4). Thus, the accurately simulated water deposition fluxes presented here represent only one 'piece of the puzzle'; further investigation into other aspects of wildfire sprinklers is needed before their full value can be realised. Furthermore, several important simplifications were necessary in the simulations presented here, which should be noted:

1. The influence of a wildfire on the air velocity, temperature and humidity fields within the computational domain was neglected, i.e. the simulations represent sprinkler operation prior-to or after, but not during, the passage of a fire; and
2. A neutral ABL was simulated, i.e. the inlet flow and ground surface were isothermal, neglecting the influence of heat from the sun.

Therefore, the work presented in this chapter should be viewed as a demonstration of how CFD can be applied to investigate droplet dispersion from specific wildfire sprinkler systems, and as a useful 'first step' towards the accurate quantification of wildfire sprinkler effectiveness.

6.2 Method

6.2.1 Computational Domain and Mesh

A fundamental residential building geometry was modelled (see Figure 6.1) such that the building footprint was 15 m × 8 m, and the building walls were 2.4 m high. A 'double-hip' roof with four

pitches of 22.5° extended beyond the four building walls, creating 0.5 m-wide eaves around the building perimeter. The total building height, H, was 4.264 m.

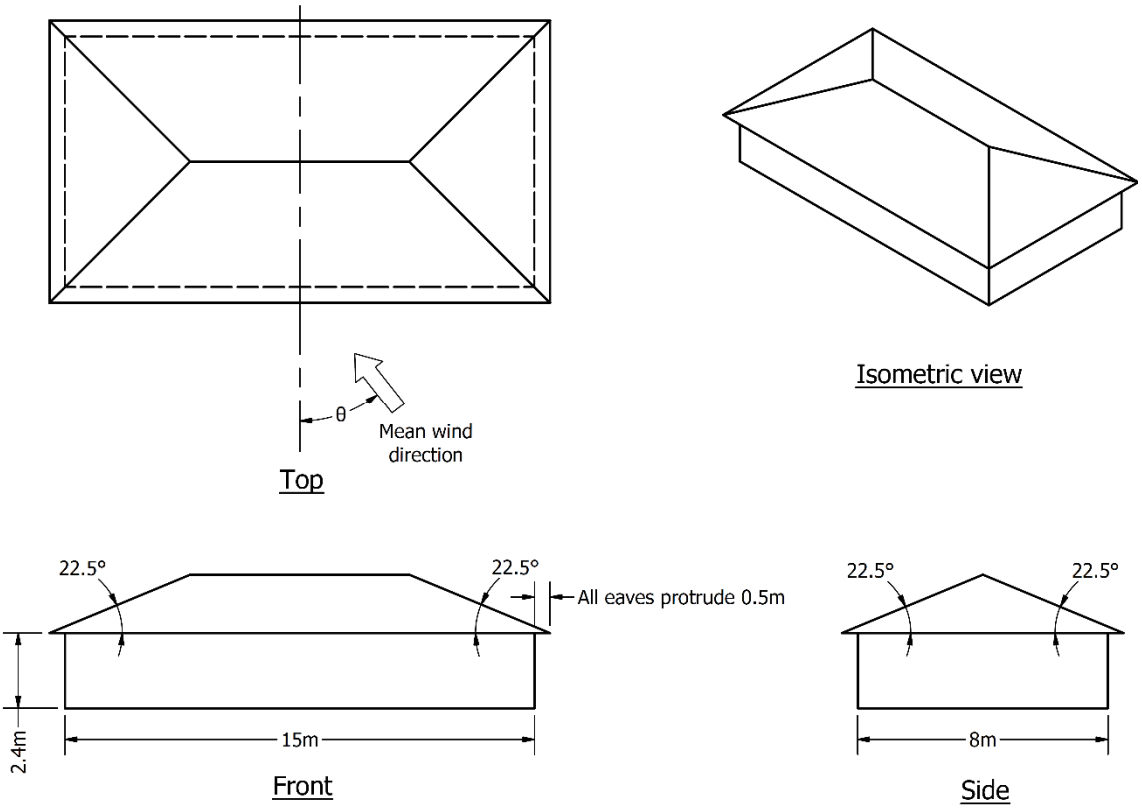

FIGURE 6.1: Building geometry, around which the sprinkler configurations were simulated.

The building was modelled in a rectangular computational domain that extended 5H from the building walls in the two upwind directions, and 15H from the building walls in the two downwind directions (see Figure 6.2). The total computational domain height was 6H. A computational mesh was formed within the domain, with a total of 1,282,297 hexahedral, tetrahedral and triangular-prism elements. The wall-normal spacing of elements was designed for use with wall functions. Coarse, medium and fine versions of the mesh were generated, for use in a mesh sensitivity analysis, using a grid-refinement ratio of approximately 1.5.

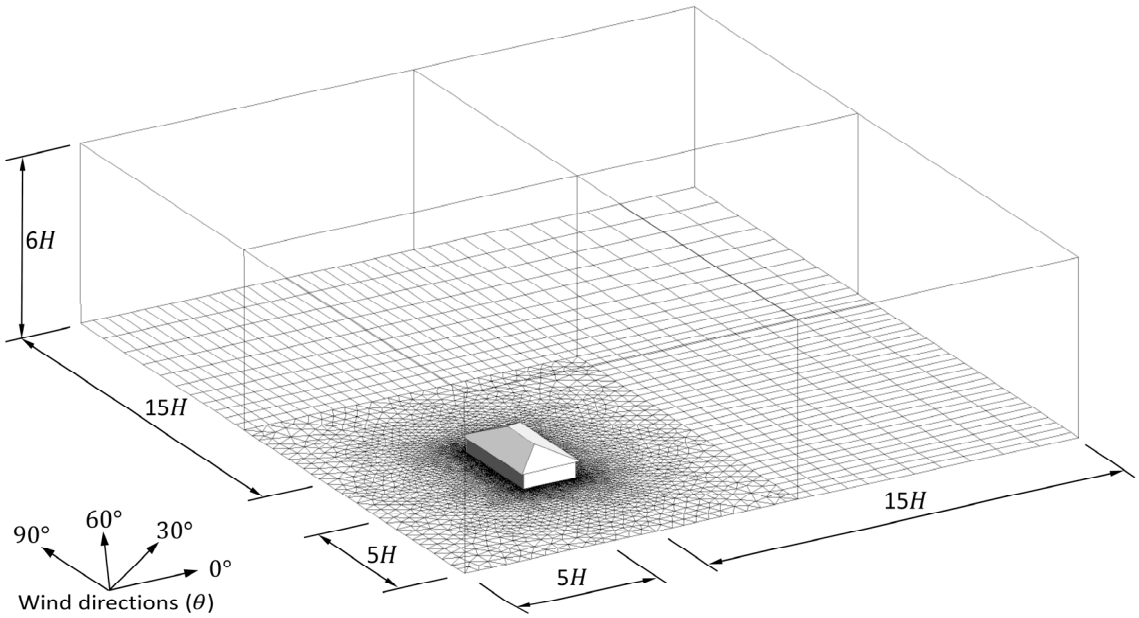

FIGURE 6.2: Computational domain used in simulations of the different sprinkler configurations, with the computational mesh shown on the ground surface. Dimensions are expressed in terms of the building height, $H = 4.264$ m.

6.2.2 Sprinkler Configurations

Nine different sprinkler configurations were simulated (see Figure 6.3, Figure 6.4, Figure 6.5 and Table 6.1), each based on wildfire sprinkler systems reported in the literature. Configurations with sprinklers installed around building perimeter (i.e. not above the roof ridge) were simulated with sprinklers on only one side of the building, to reduce the computational cost of simulations. The side of the building on which they were implemented was varied between simulations, so both windward and leeward sprinklers in such configurations were investigated, but in separate simulations. The configurations have been identified by the letters A–I:

A. Five of the ½-inch 'butterfly' sprinklers characterised in Chapter 3, installed on 2 m risers, 4.5 m from the building wall. This configuration was documented in the survey conducted by FPAA (2000). The stated intent of the system was to produce a 'curtain' of droplets between the wildfire and the building.

B. Three of the ½-inch 'butterfly' sprinklers characterised in Chapter 3, installed above the roof ridge. This configuration matched several wildfire sprinkler systems that were commercially available at the time of writing.

C. Three of the ‘deflector plate’ sprinklers characterised in Chapter 3, installed on the roof ridge. This configuration was similar to B, except that sprinklers with no moving parts were used, in compliance with the Australian standard for wildfire sprinkler systems (Standards Australia 2012). This configuration was also similar to one recommended by the South Australian Country Fire Service (CFS 2011).

D. Ten of the ‘flat fan’ sprinklers characterised in Chapter 3, installed above the perimeter of the roof, spraying inwards. This configuration represented part of one of the systems documented and recommended by FPAA (2000), and also matched several commercially available wildfire sprinkler systems at the time of writing.

E. Five of the ½-inch ‘butterfly’ sprinklers characterised in Chapter 3, installed above the perimeter of the roof. This configuration was documented by FPAA (2000), and was recommended by the South Australian Country Fire Service (CFS 2011).

F. Five of the ‘deflector plate’ sprinklers characterised in Chapter 3, installed above the perimeter of the roof. This configuration corresponds to one recommended in the Australian standard for wildfire sprinkler systems (Standards Australia 2012), although the exact type of sprinkler was not specified in the standard.

G. Ten of the ‘flat-fan’ sprinklers characterised in Chapter 3, installed upside-down under the eaves of the building, spraying towards the wall. This configuration was similar to one documented and recommended by FPAA (2000), and the Australian standard for wildfire sprinkler systems (Standards Australia 2012), although the flat-fan sprinklers may produce a finer spray than the ‘large droplet nozzles’ specified in the standard.

H. Seven of the ‘hollow-cone’ sprinklers characterised in Chapter 3, installed under the perimeter of the roof, pointing outwards. This configuration closely replicated the ‘wind-enabled ember dousing system’ (WEEDS) proposed by Mitchell (2006).

I. Five of the ‘deflector plate’ sprinklers characterised in Chapter 3, installed upside-down (as pendent sprinklers), under the eaves of the building. This configuration corresponds to one recommended in the Australian standard for wildfire sprinkler systems (Standards Australia 2012).

TABLE 6.1: Details of each sprinkler configuration investigated.

	Sprinkler configuration	Sprinkler type	Nozzle Pressure [kPa]	Number of sprinklers simulated	Total flow rate [L min^{-1}]
A	Butterfly sprinklers on risers around building	Holman ½-inch brass butterfly sprinkler	200	5	169.5
B	Butterfly sprinklers above roof ridge	Holman ½-inch brass butterfly sprinkler	200	3	101.7
C	Deflector-plate sprinklers above roof ridge	Lechler 525.049 sprinkler	245	3	125.4
D	Flat-fan sprinklers above gutters, spraying inwards	Tecpro KHW-1390 180° flat-fan nozzle	400	10	41
E	Butterfly sprinklers above gutters	Holman ½-inch brass butterfly sprinkler	200	5	169.5
F	Deflector-plate sprinklers above gutters	Lechler 525.049 sprinkler	245	5	209
G	Flat-fan sprinklers under eaves, spraying inwards	Tecpro KHW-1390 180° flat-fan nozzle	400	10	41
H	Hollow-cone sprinklers in WEEDS arrangement	½-inch Champion S9F hollow-cone nozzle	345	7	87.5
I	Deflector-plate sprinklers under eaves	Lechler 525.049 sprinkler	245	5	209

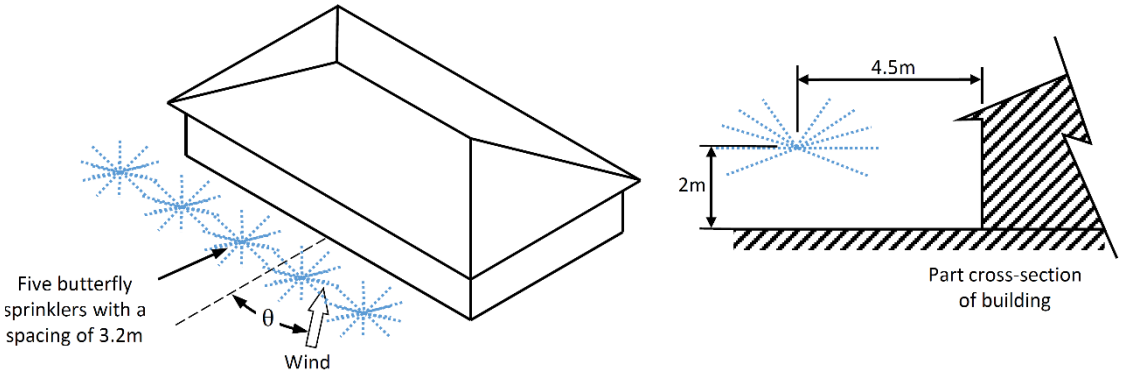

A) Butterfly sprinklers on risers around building

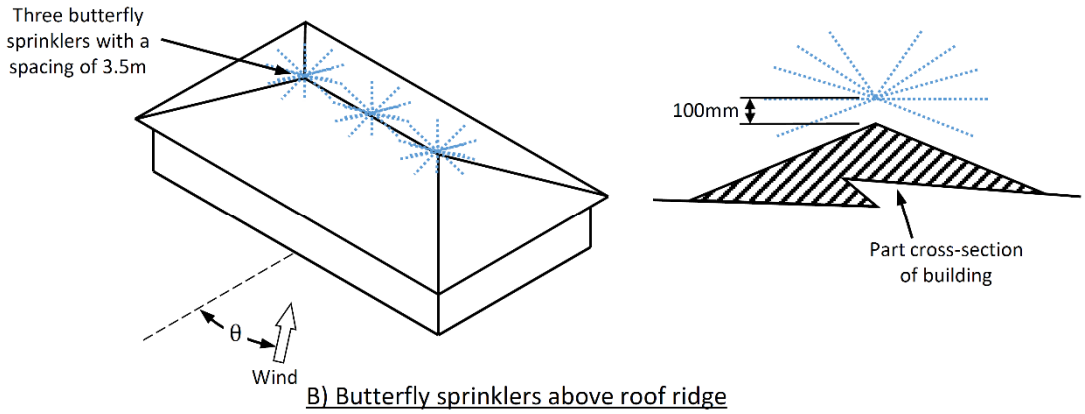

B) Butterfly sprinklers above roof ridge

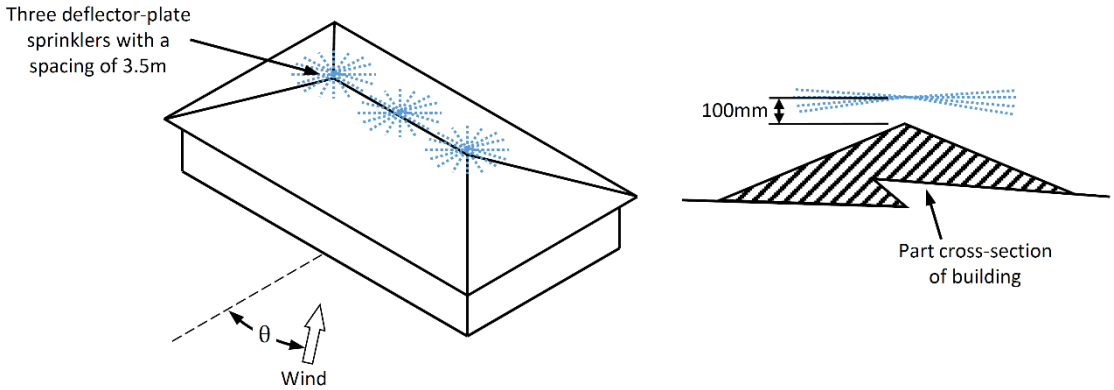

C) Deflector-plate sprinklers above roof ridge

FIGURE 6.3: Sprinkler configurations A–C.

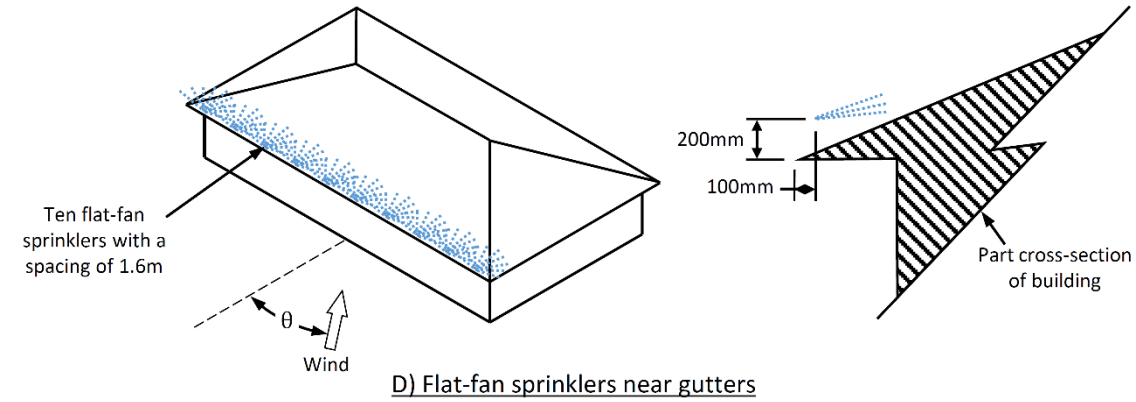

D) Flat-fan sprinklers near gutters

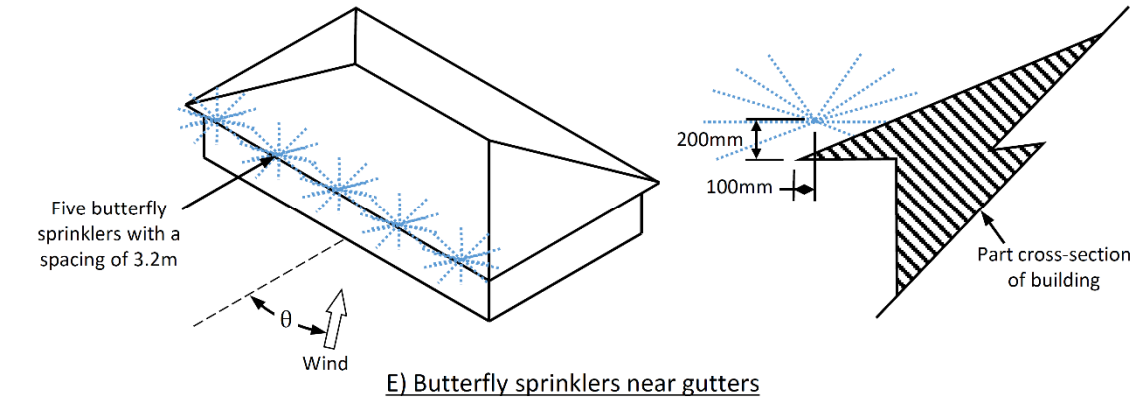

E) Butterfly sprinklers near gutters

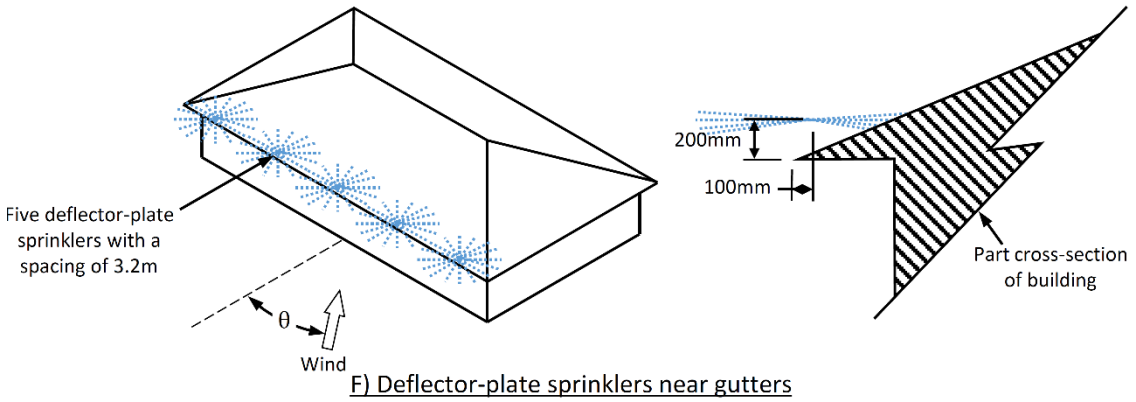

F) Deflector-plate sprinklers near gutters

FIGURE 6.4: Sprinkler configurations D–F.

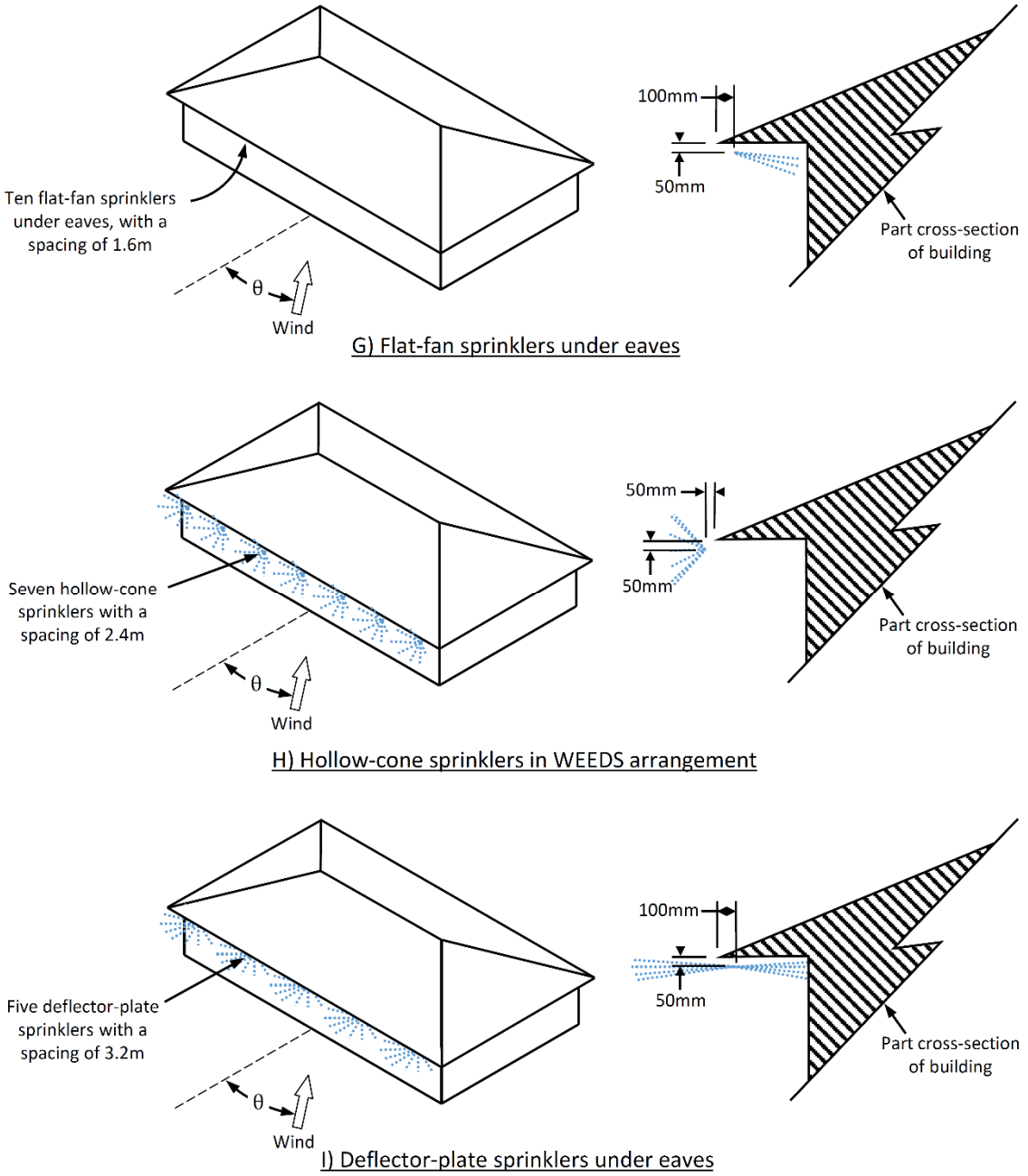

FIGURE 6.5: Sprinkler configurations G–I.

6.2.3 Weather Conditions

Three sets of weather conditions, referred to hereafter as 'moderate', 'severe' and 'extreme' (see Table 6.2), were defined using the data on building destruction by wildfire in Australia reported by Blanchi *et al.* (2010). Each wildfire that was reported was weighted by the number of buildings that had been destroyed. The 'building-weighted' mean temperature, humidity and reference wind speed (measured at a height of 10 m) from the data were defined as the 'severe' set of conditions. The 'moderate' and 'extreme' conditions were defined in a similar manner, using,

respectively, the building-weighted 5th and 95th percentile temperature, humidity and reference wind speed values.

TABLE 6.2: Weather conditions applied in CFD simulations. The forest fire danger index (FFDI) has also been presented, given a drought factor (DF) of 5 and 10.

Description	Temperature [°C]	Relative humidity [%]	Reference wind speed (at 10 m height) [m s^{-1}]	FFDI (DF=5)	FFDI (DF=10)
Moderate	35	19	7.7	20	40
Severe	42	12	14.1	56	111
Extreme	47	7	18.5	114	226

The McArthur forest fire danger index (FFDI) is a metric used to indicate the influence of weather on wildfire behaviour (Dowdy *et al.* 2009; Luke & McArthur 1978), given by:

$$FFDI = 2\exp(-0.45 + 0.987\ln(DF) - 0.0645RH + 0.0338T + 0.0234\bar{u}) \quad (6.1)$$

where RH is the ambient relative humidity (expressed as a percentage), T is the ambient air temperature (°C), $\bar{u}$ is the mean wind speed (km h^{-1}), and DF is the drought factor (a measure of fuel moisture content that ranges from 0 to 10, with 10 representing the driest conditions). In the 1960's, an FFDI of 100 was considered to represent the worst possible conditions likely to occur in Australia (Luke & McArthur 1978). However, this value has been exceeded during several of the most destructive Australian wildfires, to which can be attributed approximately 64% of the houses lost during wildfires in Australia between 1959 and 2009 (Blanchi *et al.* 2010). The weather conditions simulated in the present study could not be represented by single FFDI values, since drought factors were not defined by simulation variables. Given a drought factor of 5 , the 'moderate', 'severe' and 'extreme' conditions would represent FFDI values ranging from 20 to 114, while a drought factor of 10 would produce FFDI values ranging from 40 to 226.

6.2.4 Simulation methodology

The computational strategy in the present chapter was developed using methods that were tested in Chapter 5. Steady RANS CFD simulations were conducted with the realisable k-ε turbulence model, using ANSYS Fluent 14.5. The coupled pressure-based solver was used, with least-squares cell-based spatial discretisation of gradients and second order discretisation of advection terms in all governing equations.

Droplet trajectories were tracked in a Lagrangian framework, and were two-way coupled with the continuous-phase flow field. Drag coefficients for spherical particles were employed, and heat and mass transfer were allowed between the phases. The discrete random walk (DRW) turbulent dispersion model available in ANSYS Fluent 14.5 was employed, with 30 stochastic iterations performed for each droplet during each computational iteration. Thus, after a preliminary steady-state solution had been reached for the continuous phase flow field, 30 sets of lagrangian droplets were tracked; the continuous-phase flow was then resolved to convergence, and this process was repeated until the simulated droplet dispersion reached a converged state. Droplets were removed from the simulations when they collided with the domain boundaries (i.e. splashing, runoff, post-impact evaporation, etc. were not simulated).

6.2.5 Boundary Conditions

Each spray was represented by 3,160 droplet source points, spaced in a lattice pattern on a virtual spherical surface surrounding the sprinkler location. Fifteen droplet size classes were simulated, and one droplet of each size was released from each source point. The distance between the source points and sprinkler location was 0.2 times that at which the sprinklers had been measured in Chapter 3 (i.e. 106.6 mm for butterfly sprinklers, 44.1 mm for deflector-plate sprinklers, 20 mm for flat-fan sprinklers, and 65.2 mm for hollow-cone sprinklers). The droplet initial velocities, taken from Chapter 3, were augmented to correct for this change in initial location, following the procedure outlined in Chapter 5. Thus, spatial variations in droplet diameter distributions, velocities and diameter-velocity correlations were represented in the CFD simulations.

Simulations were run with four different mean wind directions: $\theta = \{0°, 30°, 60°, 90°\}$, where θ is the azimuthal angle from a line normal to the 15-m-long walls of the building (see Figure 6.1). The upstream boundaries were assigned fixed velocity, temperature, humidity, and turbulence quantities, as detailed in Section 6.2.3, and the top boundary was assigned the same fixed values as the top of the inlet. Boundaries parallel to the mean flow direction (in simulations with $\theta = \{0°, 90°\}$) were assigned 'symmetry' boundary conditions (i.e. zero flux of all quantities), and

downstream boundaries in all simulations were assigned a fixed static pressure. Solid boundaries were adiabatic and were assigned representative roughness values, for use with standard wall functions.

Vertical profiles of wind speed, turbulence kinetic energy and turbulence dissipation rate were assigned at the domain inlets (see Figure 6.6). Canopy-flow profiles were adopted, rather than standard boundary-layer profiles, to mimic scenarios in which the region surrounding the computational domain was forest and the region of the domain was a clearing. Such scenarios are more relevant to wildfire sprinkler systems, since wildfire-prone buildings are typically in relatively close proximity to highly vegetated areas. The inlet flow was isothermal and uniform in humidity.

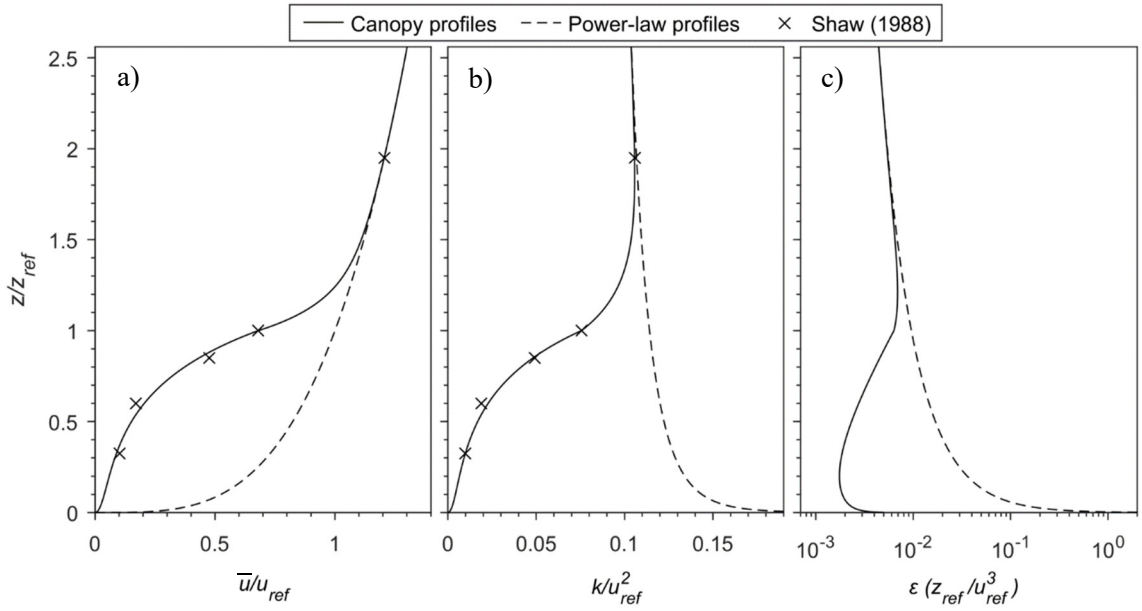

FIGURE 6.6: Canopy flow vertical profiles of: a) mean streamwise velocity ($\bar{u}$), b) turbulence kinetic energy (k), and c) turbulence dissipation rate (ε), non-dimensionalised by the reference height (z_{ref}) and reference wind speed (u_{ref}). The standard power-law atmospheric boundary layer profiles (Tominaga *et al.* 2008) and experimental data reported by Shaw, Den Hartog and Neumann (1988) have been included for comparison. The canopy height was set equal to z_{ref} in the present study.

The canopy-flow velocity and turbulence kinetic energy profiles were defined using different functions below and above the canopy height, z_c (10 m in the present study). Below z_c the profiles proposed by Cowan (1968) were adopted, and above z_c the standard 'power-law' atmospheric boundary layer profiles were used, which have been presented in detail by Tominaga *et al.* (2008).

The exponent, α, and boundary layer depth, z_g, were set to 0.28 and 400 m, respectively, which were the values proposed for forests and suburbs by Davenport (1960). A blending function was employed to form a smooth transition between the two regions, as follows:

$$\frac{\bar{u}}{u_{ref}} = \begin{cases} \delta_u \sqrt{\dfrac{\sinh\left(\beta \dfrac{z}{z_c}\right)}{\sinh(\beta)}} & z \le z_c \\ \delta_u + \left(\left(\dfrac{z}{z_{ref}}\right)^{\alpha} - \delta_u\right)\left(1 - e^{\gamma_u\left(\frac{z_c - z}{z_{ref}}\right)}\right) & z > z_c \end{cases} \tag{6.2}$$

where $\bar{u}$ is the mean wind speed, z is the height above ground-level, u_{ref} is the reference wind speed (see Table 6.2), z_{ref} is the reference height (10m in the present study), β is a parameter tuned to represent the influence of a forest canopy (assigned a value of 6 in the present study), and δ_u and γ_u are parameters used to blend the two profiles (assigned values of 0.56 and 15, respectively, in the present study). In a similar fashion, the turbulence kinetic energy profile was defined as follows:

$$\frac{k}{k_{ref}} = \begin{cases} \delta_k \sqrt{\dfrac{\sinh\left(\beta \dfrac{z}{z_c}\right)}{\sinh(\beta)}} & z \le z_c \\ \delta_k + \left(\left(\dfrac{z}{z_{ref}}\right)^{-0.1} - \delta_k\right)\left(1 - e^{\gamma_k\left(\frac{z_c - z}{z_{ref}}\right)}\right) & z > z_c \end{cases} \tag{6.3}$$

where δ_k and γ_k are parameters used to blend the two profiles (assigned values of 0.71 and 7, respectively, in the present study), and k_{ref} is the turbulence kinetic energy of the standard power-law profile, at z_{ref}, given by (Tominaga *et al.* 2008):

$$k_{ref} = \left(0.1\left(\frac{z_{ref}}{z_g}\right)^{-\alpha-0.05} u_{ref}\right)^2 \tag{6.4}$$

The turbulence dissipation rate was calculated from the velocity and turbulence dissipation rate profiles, following the procedure outlined for the power-law profiles by Tominaga *et al.* (2008).

6.2.6 Film Runoff and Cooling Potential

Results from the CFD simulations were post-processed, to provide an estimate of the quantity of heat that each sprinkler configuration could remove from the building walls, by evaporation and

convection within the liquid runoff. It was assumed that all droplets impinging on the building windward wall formed a statistically steady liquid film flow, down the surface. The film properties (e.g. impinging droplet flux, film flow rate and film temperature) were averaged over the wall width, and the film was assumed to be isothermal across its thickness. Thus, a one-dimensional finite difference problem could be formulated which gave a simplified representation of water flow down the wall, and heat removal therefrom (see Figure 6.7).

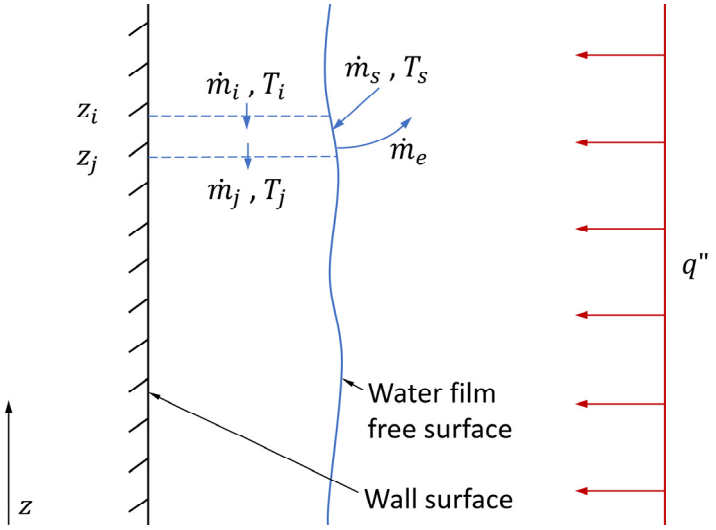

FIGURE 6.7: Simple finite difference formulation used to represent the water film on the building wall, exposed to a uniform heat flux (q").

Various scenarios were considered in which a uniform heat flux of magnitude q" was incident on the wall. The vertical film mass flow rate (per unit width) as a function of height, $\dot{m}_j$ at height z_j, was assumed to be governed by the conservation of mass on a control volume (see Figure 6.7), and could be calculated from: the film mass flow entering from above, $\dot{m}_i$; the mass flow rate of droplets impinging on the free surface of the control volume, $\dot{m}_s$; and the mass of water vapour released from the film free surface per unit time, $\dot{m}_e$:

$$\dot{m}_j = \dot{m}_i + \dot{m}_s - \dot{m}_e \tag{6.5}$$

Convective heat transfer from the film free surface, conduction into the wall, and vertical conduction within the film were neglected, since they were several orders of magnitude smaller than energy fluxes caused by the water mass flux (during impingement, film flow and

evaporation). Thus, the control volume energy balance could be expressed in terms of the incident heat flux, convection of heat by the liquid film flow, and latent heat removal, as follows:

$$q"(z_i - z_j) = (\dot{m}_j T_j - \dot{m}_s T_s - \dot{m}_i T_i) C_p + \dot{m}_e h_e \quad (6.6)$$

where T_i and T_j are the film temperatures at heights z_i and z_j, respectively, T_s is the mass-weighted mean temperature of droplets impinging on the wall between heights z_i and z_j, $C_p =$ 4.195 kJ kg^{-1} K^{-1} is the specific heat capacity of water and $h_e = 2257$ kJ kg^{-1} is the latent heat of vaporisation of water.

Details of the impinging droplets, $\dot{m}_s$ and T_s, were obtained at each height from CFD simulations conducted with zero mean wind angle and the 'severe' set of weather conditions (i.e. $\theta = 0°$, $T =$ 42°C, $RH = 12\%$, and $u_{ref} = 14.1$ m s^{-1}). A set of four different heat fluxes ($q" = \{0, 10, 30, 50\}$ kW m^{-2}) were investigated for each spray configuration. Evaporation of the film was ignored when the film temperature was below 100°C, which allowed Equations (6.5) and (6.6) to be solved over the discretised height of the wall, starting at the top. In areas where the film flow rate became zero, the fraction of the incident heat flux not removed by the water (and therefore absorbed by the wall surface) was recorded.

Several significant simplifications were made in the procedure outlined above.

- Processes such as splashing and bouncing were ignored.
- Flow of water from the film away from the wall, e.g. at door frames, window sills or other horizontal edges, was not considered.
- Only uniform heat fluxes were considered, which may represent the radiant heat emitted by nearby flames reasonably well, but do not include the localised areas of strong heating that are likely to arise near accumulated embers and from direct flame contact.
- Convective heat transfer from the free surface of the falling water film was neglected.
- Vertical conduction was ignored within the film.
- Conduction of heat into the building wall was ignored.

- The film runoff flow was decoupled from the CFD simulations and droplet trajectory calculations.

Although the approach outlined here was relatively simple to implement, it served two important purposes: 1) it put the water deposition fluxes predicted by CFD simulations into context, giving an indication of the maximum cooling potential of each sprinkler configuration; and 2) it provided some insight into the performance of different water application methods (e.g. the 'run-down' method, as compared to a more even application of droplets to a surface).

6.2.7 Radiation Attenuation

The magnitude of radiant heat that could be attenuated by airborne droplets was also estimated by post-processing the CFD results. A simple model, similar to that proposed by Dombrovsky, Dembele and Wen (2016), was adopted to approximate the interaction between a diffuse radiant heat flux and a uniform 'curtain' of airborne droplets. This approach was computationally inexpensive and took into account the important spectral behaviour of water droplets in the infrared band. However, the sprays were represented in a highly simplified manner, so the analysis produced results that were more of an 'order-of-magnitude estimate' than an exact solution. The value of this procedure was that it put the CFD results in context, by quantifying the effect that each sprinkler configuration could have in a wildfire situation, taking into account the effects of wind drift and evaporation, and it facilitated a comparison of the effectiveness of the different sprinkler configurations.

Scenarios were considered in which a uniform, diffuse heat flux of magnitude q'', was incident on the sprays. The power spectrum of incident radiation was based on the spectral radiance of a hot body, which was determined throughout the band of wavelengths 1 μm $< \lambda <$ 14 μm using the Planck radiation law:

$$B = \frac{2hc^2}{\lambda^5 \left(\frac{hc}{e^{\lambda k_B T_f}} - 1 \right)} \tag{6.7}$$

where T_f is the radiation source temperature, $h \approx 6.626\times10^{-34}$ J s is the Planck constant, $k_B \approx 1.381\times10^{-23}$ J K^{-1} is the Boltzmann constant, and $c \approx 2.998\times10^{8}$ m s^{-1} is the speed of light. In the present study, the flame temperature was assumed to be 1200 K, which is commensurate with measured values from full-scale experiments (Butler *et al.* 2004; Sullivan, Ellis & Knight 2003). Equation (6.7) produced the spectral radiance of the flame, in units of W sr^{-1} m^{-3}. A conversion factor, f_q, was defined, to convert B into the power spectrum of radiation that was incident on the spray (units W m^{-2}), such that:

$$q'' = f_q \int_0^\infty B \, d\lambda \tag{6.8}$$

Thus, f_q had units sr, and could be tuned to produce incident radiant spectra with a desired total intensity, and with a spectral profile matching that produced by a 1200 K flame. Total incident radiant heat fluxes of up to 55 kW m^{-2} were investigated, which represents an approximate upper-limit of radiant heat that could be expected incident on a building surrounded by a small fuel break (Cohen 2004; Maughan *et al.* 1999; Standards Australia 2009).

Airborne droplets were assumed to be falling in between the source of radiant heat and the building windward wall, forming a statistically steady 'curtain' of droplets. Properties of the spray curtain were averaged over the width of the wall and assumed to be constant through the thickness of the curtain, which allowed the curtain to be formulated as a one-dimensional finite difference problem (see Figure 6.8). The important parameters which described the spray curtain at a given height, denoted here by the subscript i, were the vertical liquid mass flow rate, $\dot{m}_l$, the liquid mass per unit curtain frontal area, ξ_i, the droplet temperature, T_i, and the droplet diameter, d_i. Thus, the field of droplets was assumed to be horizontally isothermal and monodisperse, which is clearly a significant simplification. However, this simplification has been made in several similar investigations (Dombrovsky, Dembele & Wen 2016; Godoy & DesJardin 2007).

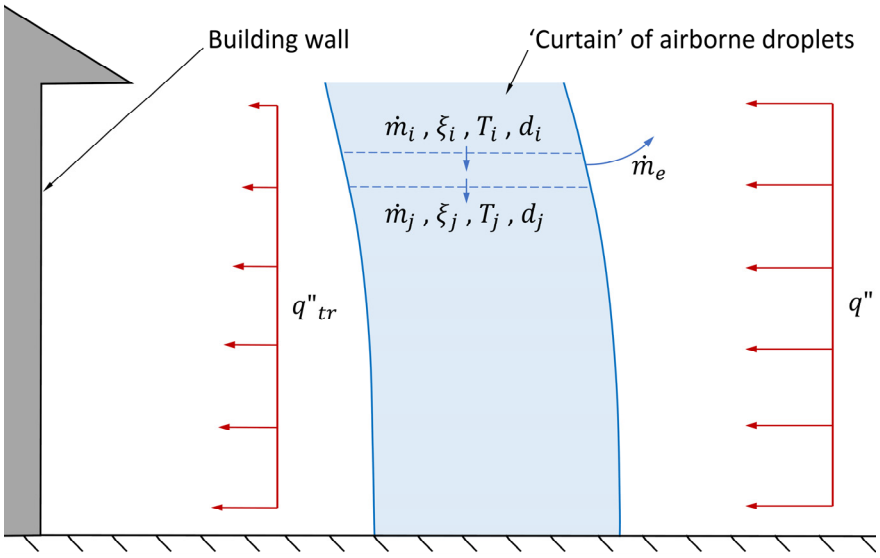

FIGURE 6.8: Attenuation of uniform heat flux, of magnitude $q"$, by a 'curtain' of airborne droplets. Variables describing the spray curtain at two heights are shown, illustrating the finite difference formulation used in the analysis. $q"_{tr}$ is the (non-uniform) transmitted heat flux.

At each height, the heat flux transmitted through the spray, $q"_{tr}$, and the absorbed heat flux, $q"_{abs}$, were calculated using the following expressions:

$$q"_{tr} = 2f_q \int_0^\infty q_* B \, d\lambda \tag{6.9}$$

$$q"_{abs} = 2f_q \int_0^\infty w_* B \, d\lambda \tag{6.10}$$

where q_* and w_* are the dimensionless spectral radiative flux transmitted through the spray, and spectral profile of absorbed radiation power, respectively. Both of these variables were functions of λ, and were calculated from ξ_i, d_i, and the absorption and scattering characteristics of spherical water droplets, using the methods outlined by Dombrovsky, Dembele and Wen (2016).

The boundary conditions at the top of the spray curtain were obtained from the results of CFD simulations conducted with zero mean wind angle (i.e. $\theta = 0°$). All droplets that had landed on the ground upwind of the building, or on the lowest 1m of the building windward wall, were considered to have contributed to the attenuation of radiant heat, and were included in the analysis. The total mass flux, mass-weighted mean temperature and Sauter mean diameter of the set of droplets were applied as boundary conditions at the top of the spray curtain. The mean liquid volume per unit spray frontal area was calculated from the mass flow rates and residence times

of the set of droplets, and was also imposed as a boundary condition at the top of the spray curtain. The spray curtain was discretised with respect to height, and Equations (6.9) and (6.10) were solved, together with mass and energy conservation equations, to determine the fluxes of transmitted and absorbed radiant heat, and changes in the mean droplet diameter, mass flux and liquid volume per unit spray frontal area. Thus, the vertical profile of transmitted heat was calculated, taking into account the effects of droplet heating and evaporation.

6.3 Results and Discussion

6.3.1 Wind Drift and Evaporation

The simulated distributions of water deposition on the various building surfaces, and the ground, are presented in Figure 6.10, Figure 6.11 and Figure 6.12. To quantify rates of water deposition on the ground surface close to the building (where it could extinguish accumulated embers and spot-fires threatening the building), a 'near building' region was defined, which included parts of the ground surface that were within 2 m of the building walls. The remainder of the ground surface was divided into 'upwind' and 'downwind' regions, which were separated by a line, normal to the wind direction and passing through the centre of the building footprint (see Figure 6.9).

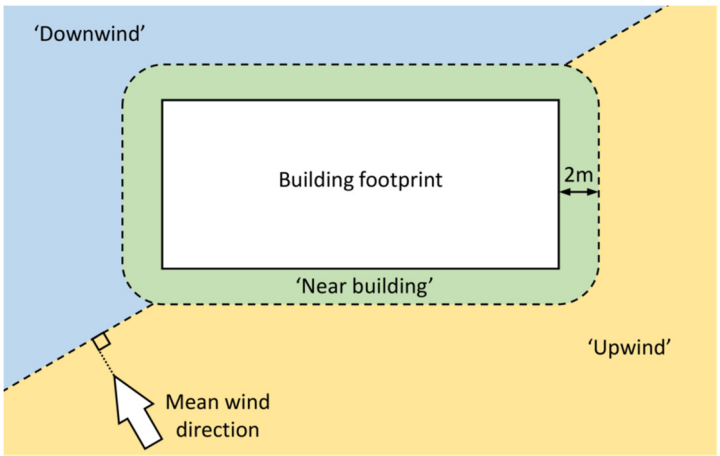

FIGURE 6.9: Definition of the 'upwind', 'downwind' and 'near building' regions of ground surface, surrounding the building. 'Near building' included the ground surface within 2m of the building walls. The line separating 'upwind' and 'downwind' regions was normal to the mean wind direction and passed through the centre of the building footprint.

The majority of water sprayed by the butterfly sprinklers on risers (in configuration A) landed on the ground, away from the building; a maximum of 15% landed on the building (when the sprinklers were upwind of the building), and a maximum of 23% landed on the ground surface within 2 m of the building. Such performance would not diminish the effectiveness of the sprinklers in attenuating radiant heat or extinguishing airborne embers, but it would limit the system capacity to cool or extinguish the building directly.

Sprinklers mounted on the ridge of the building roof (in configurations B and C) delivered between 42% and 76% of water to the roof surface; the remainder was deposited on the ground or evaporated. The deflector-plate sprinklers emitted smaller droplets, at a lower angle above horizontal, than the butterfly sprinklers did, and on-average they deposited 8% more water on the roof. Flat-fan sprinklers, installed near the perimeter of the roof and directed towards the roof surface (in configuration D) delivered a larger fraction (55–83%) of water to the roof surface, and also deposited a small fraction (~2%) on the building walls in some simulations. Thus, the flat-fan and deflector-plate sprinklers were able to deliver a significant fraction of water to building surfaces during wildfires, despite the relatively high susceptibility to wind drift and evaporation of the small droplets that they emitted. In systems designed to wet the roofs of buildings during wildfires, it appears to be more important that droplets are projected at a low angle above horizontal, towards the roof surface where possible. Even when this is achieved (e.g. in configuration D), approximately 20% of water that is sprayed can be blown away from the building, and a further 20% can evaporate.

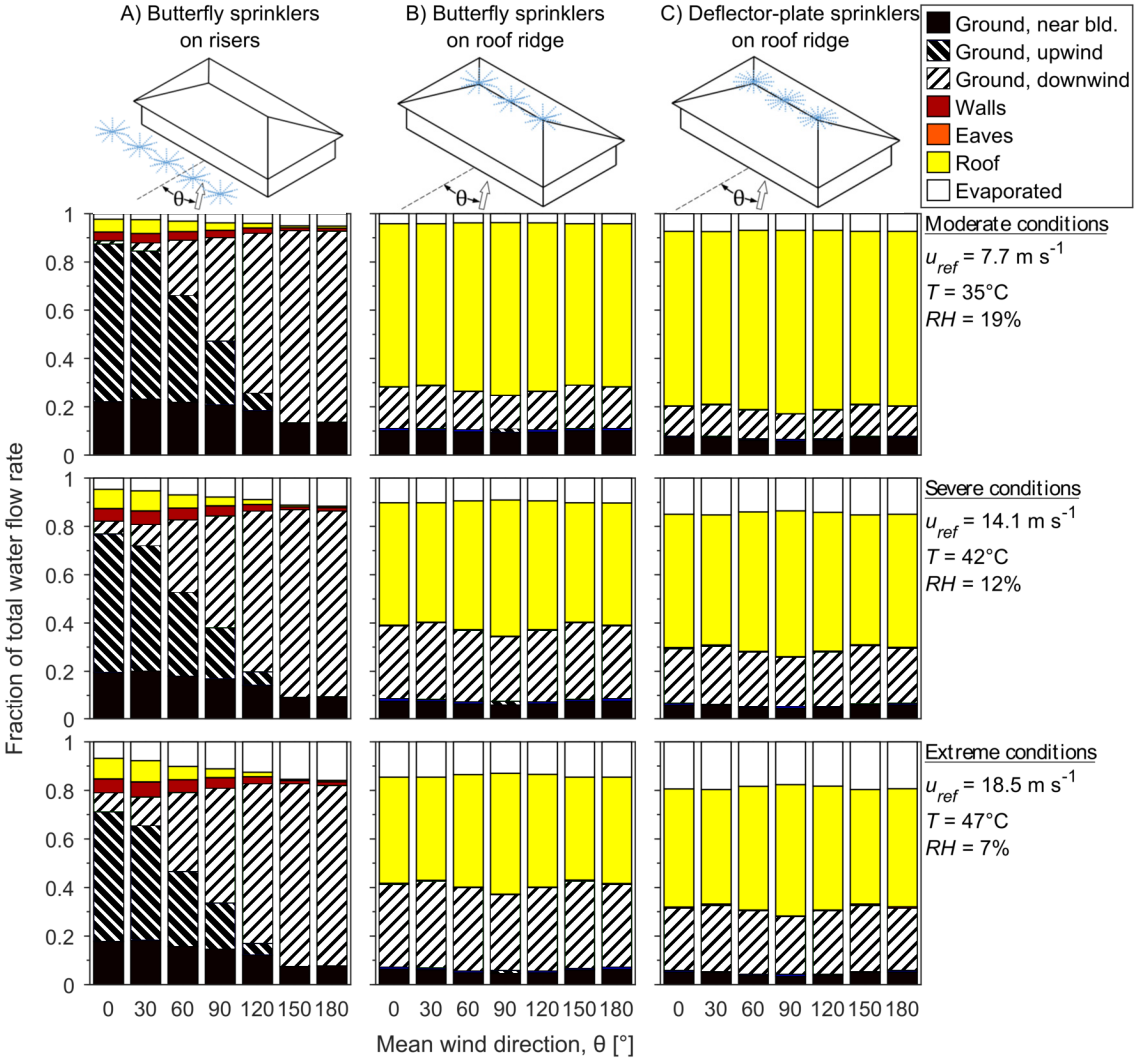

FIGURE 6.10: Distributions of water deposited by sprinkler configurations A–C. Water categorised as 'evaporated' includes the mass of water evaporated from droplets before they collided with solid boundaries, droplets that evaporated completely while airborne, and droplets that were blown beyond the computational domain.

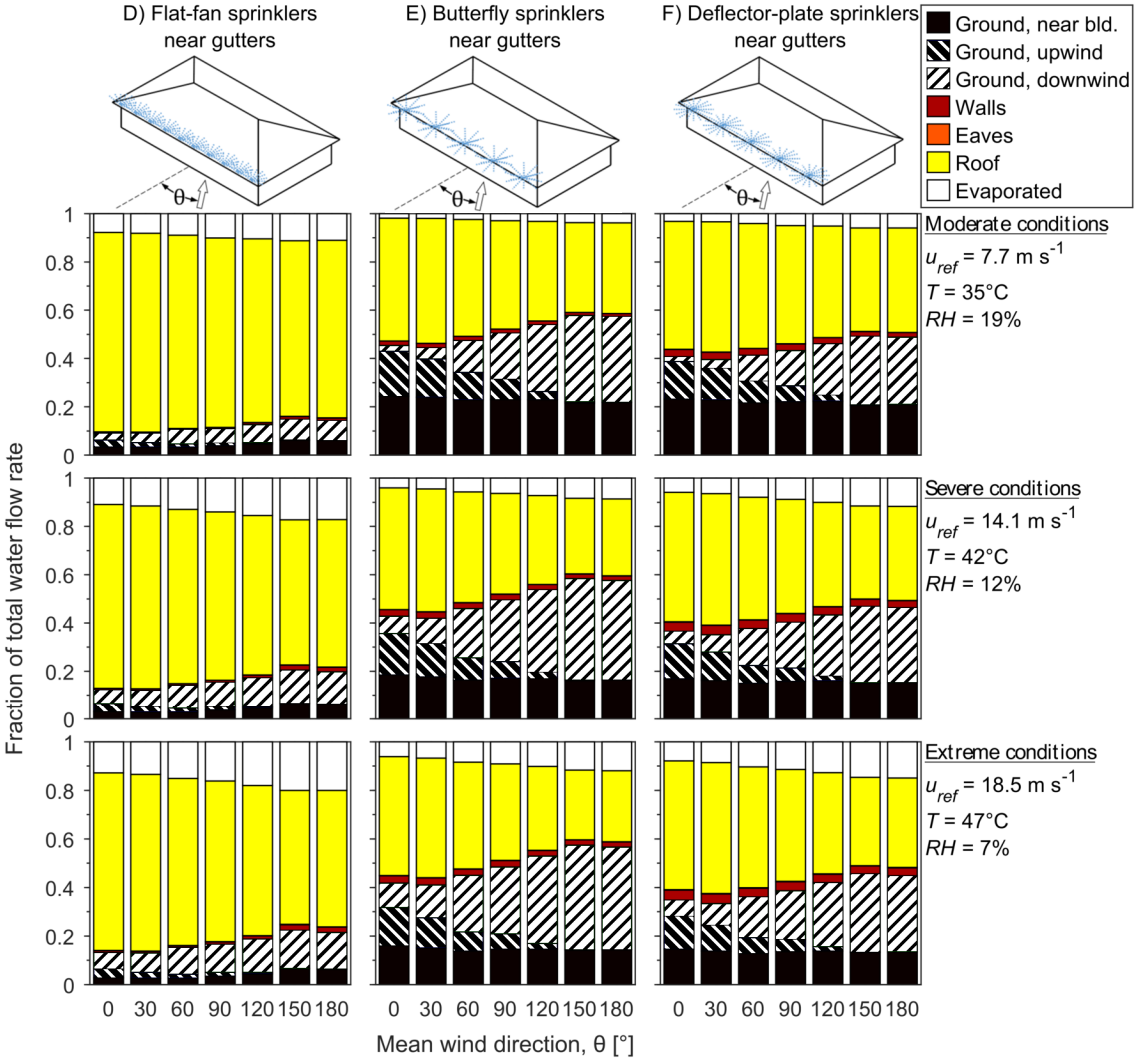

FIGURE 6.11: Distributions of water deposited by sprinkler configurations D–F. Water categorised as 'evaporated' includes the mass of water evaporated from droplets before they collided with solid boundaries, droplets that evaporated completely while airborne, and droplets that were blown beyond the computational domain.

Butterfly and deflector-plate sprinklers mounted above the perimeter of the roof (in configurations E and F, respectively) deposited 23–54% of water on the building roof, and 13 – 24% of water on the ground within 2 m of the building. Even in simulations with a strong wind directing droplets back towards the building (i.e. 'extreme' conditions with $\theta = 0$), a maximum of 4% of water was deposited on the building walls by such sprinklers. The fraction of water deposited on the roof by sprinkler configurations E and F was affected most strongly by the wind direction; sprinklers on the leeward side of the building deposited approximately half the amount that sprinklers on the windward side did. The mass flux of water to the ground within 2 m of the building was affected more by the wind speed, temperature and humidity. Thus, the results presented here

indicate that gutter-mounted sprinklers, such as those in configurations E and F, 1) do not deposit a significant quantity of water on the building walls; and 2) can be affected significantly by wind drift and evaporation, especially when implemented on the leeward side of a building, where as much as 55% of the water that is sprayed can be blown away from the building or evaporated in some cases.

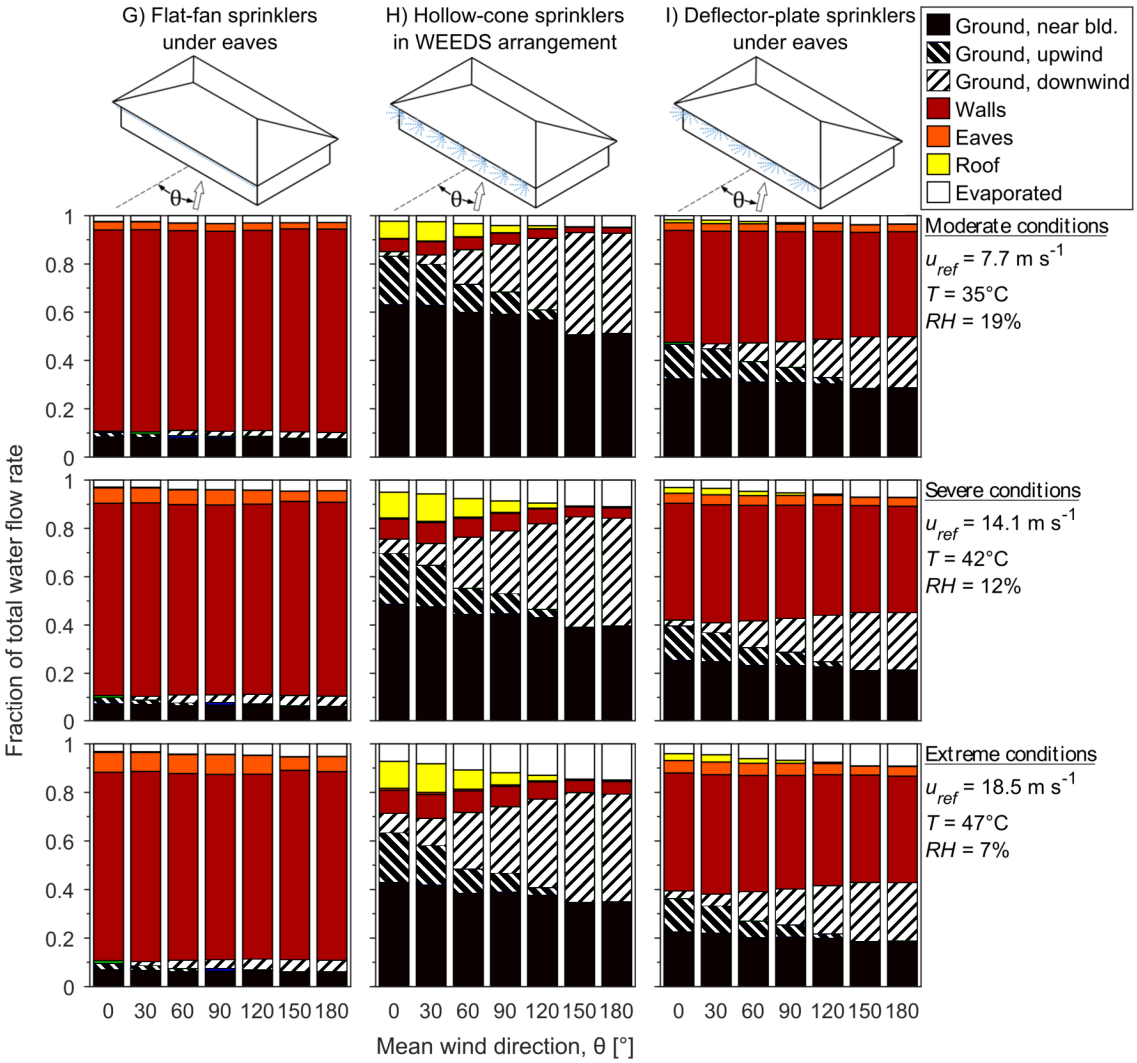

FIGURE 6.12: Distributions of water deposited by sprinkler configurations G–I. Water categorised as 'evaporated' includes the mass of water evaporated from droplets before they collided with solid boundaries, droplets that evaporated completely while airborne, and droplets that were blown beyond the computational domain.

Flat-fan sprinklers mounted under the building eaves (in configuration G) were affected relatively little by changes in wind direction, or in the weather conditions (i.e. wind speed, temperature and humidity). Between 76% and 84% of water was deposited on the building walls in simulations of such sprinklers. Deflector-plate sprinklers installed in a similar location (in configuration I),

deposited 43–49% of water on the building walls and 18–32% of water on the ground within 2 m of the building. Both configurations (G and I) sprayed water directly towards the top of the building walls from a relatively short range, in what is sometimes referred to as a 'run-down' method. The result appears to have been a relatively consistent water deposition flux on the walls, despite changes in weather conditions. The fraction of water projected away from the building by the deflector-plate sprinklers (due to the 360° spray pattern formed by those sprinklers) was affected more by evaporation and wind drift.

Hollow-cone sprinklers, installed under the perimeter of the roof and directed outwards in configuration H, corresponding to the WEEDS proposed by Mitchell (2006), were affected much more strongly by the wind speed and direction. When the wind was forcing droplets back, towards the building (i.e. when $\theta = 0$), 12–20% of water was deposited on the building walls and roof, and 43–63% of water was deposited on the ground within 2 m of the building. The relatively low wind speed simulated as part of the 'moderate' conditions caused a higher deposition flux on the ground, while the high wind speeds involved in the 'extreme' case caused a higher deposition flux on the building surfaces. Thus, the CFD simulations indicated that the WEEDS design was relatively ineffective at depositing water on the building surfaces, compared to other sprinkler configurations that employ a 'run-down' approach. This was true for all wind directions and speeds that were tested, but was especially true of sprinklers implemented on the leeward side of the building. While these findings indicate that WEEDS are relatively ineffective at wetting building surfaces, such systems could still be effective at extinguishing airborne embers or attenuating radiant heat.

6.3.2 Cooling Potential

Estimates of the liquid film flow rate on the building windward wall, and the fraction of incident heat that the film flow would remove via convection and as latent heat, demonstrated some implications of the water deposition fluxes that were predicted using CFD. Figure 6.13 contains an example of such estimated film flow, obtained for sprinkler configuration A operating in the

'severe' set of weather conditions and with a mean wind incidence angle of $\theta = 0$. From the plots it is evident that:

i) When no heat flux is incident on the wall, impinging droplets would form a liquid film with a flow-rate that increases as it approaches the ground.

ii) The film flow would be greatly diminished by incident radiant heat fluxes as low as 10 kW m^{-2}, due to evaporation.

iii) In the scenario involving an incident heat flux of 10 kW m^{-2}, 100% of the incident heat would be removed by the water film, except in narrow regions at the top and bottom of the wall; at these locations, impinging droplets from the sprinklers would not remove all incident heat, so the wall would increase in temperature.

iv) In scenarios involving incident heat fluxes of 30 kW m^{-2} and 50 kW m^{-2}, the rate of droplet evaporation would match the rate of deposition over the entire wall height and the heat removal rate would be significantly less than the incident heat flux, but the sprinklers would reduce the heat flux absorbed by the wall by approximately 15–35%.

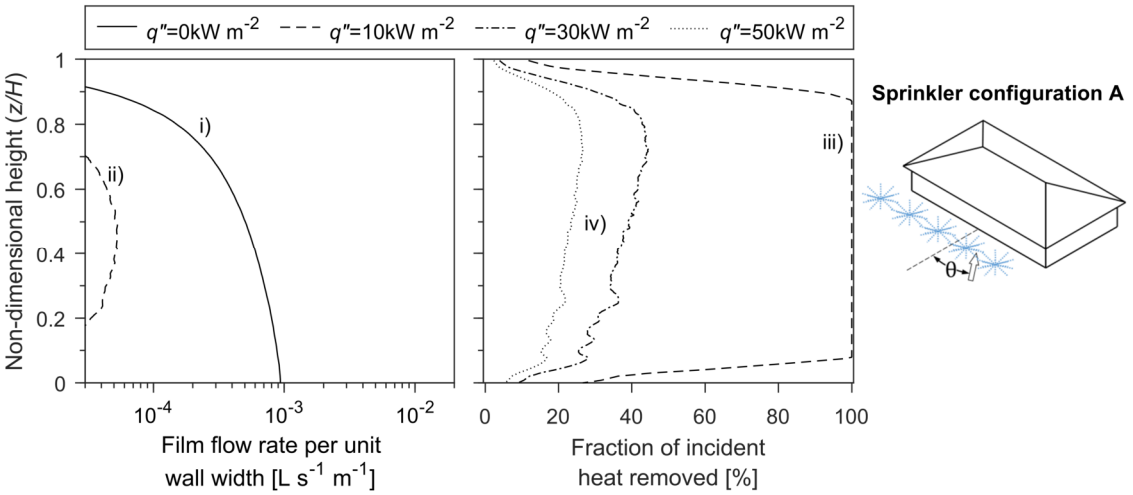

FIGURE 6.13: Example of the vertical profiles of liquid film flow rate on the building windward wall (left) and fraction of heat incident on the wall that would be removed by the film (right), which were estimated based on CFD results, given four different incident heat fluxes (q"). The annotations i–iv correspond to observations outlined in the text, above.

Modelling of liquid films produced by all nine sprinkler configurations revealed that they could be grouped into three distinct categories, based on the ability of each system to cool the windward

wall of a building. The first category contained sprinkler configurations G and I (i.e. flat-fan or deflector-plate sprinklers installed under the building eaves), which both employed a 'run-down' method. The majority of water deposited on the windward wall by these sprinkler systems landed near the top of the wall, producing liquid films with relatively high flow-rates over most of the wall height (see Figure 6.14). Such liquid films were very effective at cooling the windward wall; configuration I was estimated to remove 100% of all incident heat fluxes that were modelled (up to 50 kW m^{-2}), and configuration G was predicted to remove 100% of incident heat fluxes from a large fraction of the wall height, excluding a ~85 mm band at the top of the wall, where insufficient water was deposited, and the lower 25% of the wall when a 50 kW m^{-2} heat flux was applied.

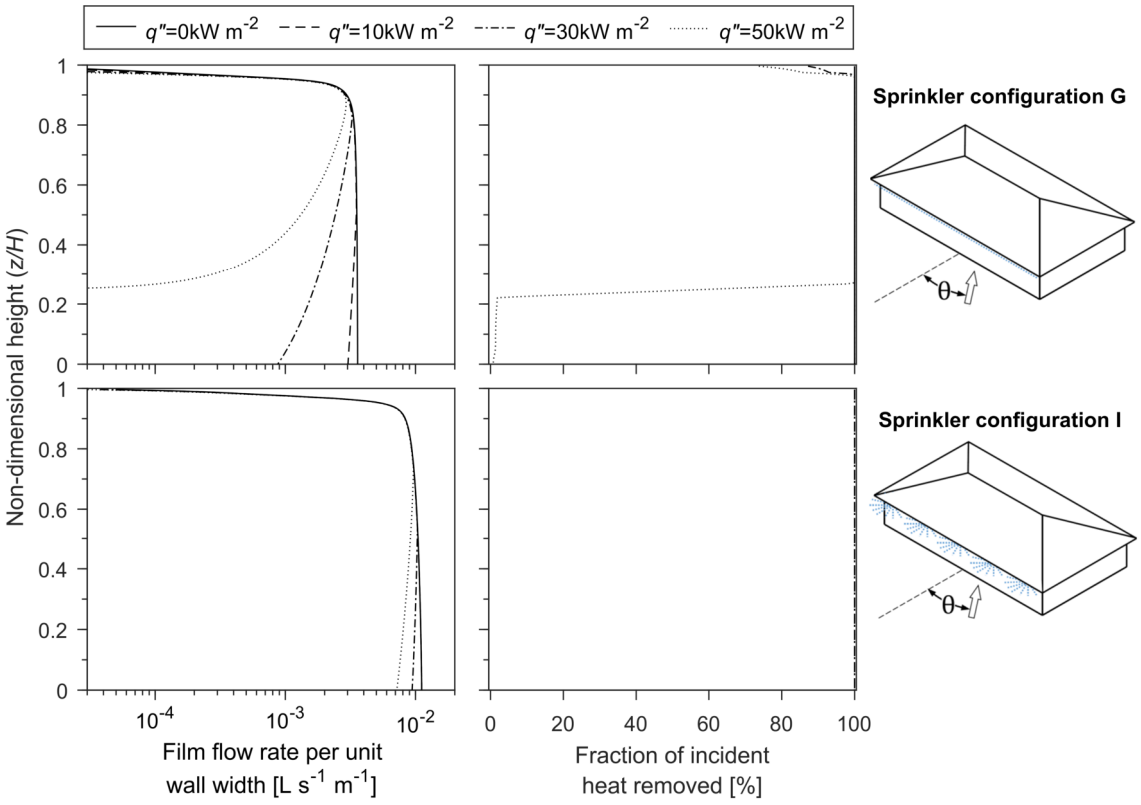

FIGURE 6.14: Vertical profiles of liquid film flow rate on the building windward wall (left) and fraction of heat incident on the wall that would be removed by the film (right), calculated for sprinkler configurations G (top) and I (bottom).

The second category contained sprinkler configurations A, E, F and H, i.e. configurations in which butterfly sprinklers were implemented on risers 4.5 m from the building, butterfly or deflector-plate sprinklers were implemented above the edges of the roof, or hollow-cone sprinklers were

implemented near the edges of the roof pointing outwards (in a 'WEEDS' arrangement). These configurations deposited less water on the windward wall than those in the previous category, and the water was deposited more evenly over the wall height (i.e. a 'run-down' method was not employed). Consequently, the liquid films modelled for these sprinkler configurations were not able to remove 30 kW m^{-2} or 50 kW m^{-2} heat fluxes from any portion of the wall, and left significant portions of the wall (or the entire wall, in the case of configuration E) without complete protection in scenarios with an incident heat flux of 10 kW m^{-2} (see Figure 6.15).

Sprinkler configurations B, C and D comprised the third category. These configurations involved sprinklers above the roof ridge, or above the edges of the roof directed inwards, and so deposited very little water on the building walls. Modelling of the water films produced by these configurations revealed that they would not cool building walls significantly in a wildfire; less than 5% of the incident heat flux was removed from the entire wall height in all cases investigated.

Despite the highly simplified method used to model the water films in the present work, the analysis did provide an 'order-of-magnitude' estimate of the quantity of cooling that could be provided by each sprinkler configuration, taking into account the effects of wind drift and the evaporation of airborne droplets (which were included in the preceding CFD analysis). Sprinklers aimed directly at the top of the building walls, in configurations G and I, appear to provide sufficient cooling to address radiant heat loads typical of those incident on buildings during wildfires, which are on the order of 10–50 kW m^{-2} (Cohen 2004; Maughan *et al.* 1999; Standards Australia 2009), while sprinklers implemented on the roofs of buildings did not cool the building walls significantly. The remaining configurations (i.e. A, E, F and H) deposited water on the windward wall primarily due to the effects of wind drift. The quantity of cooling affected by these systems would be significant, but would not be sufficient to completely address all radiant heat loads that can be expected during wildfires.

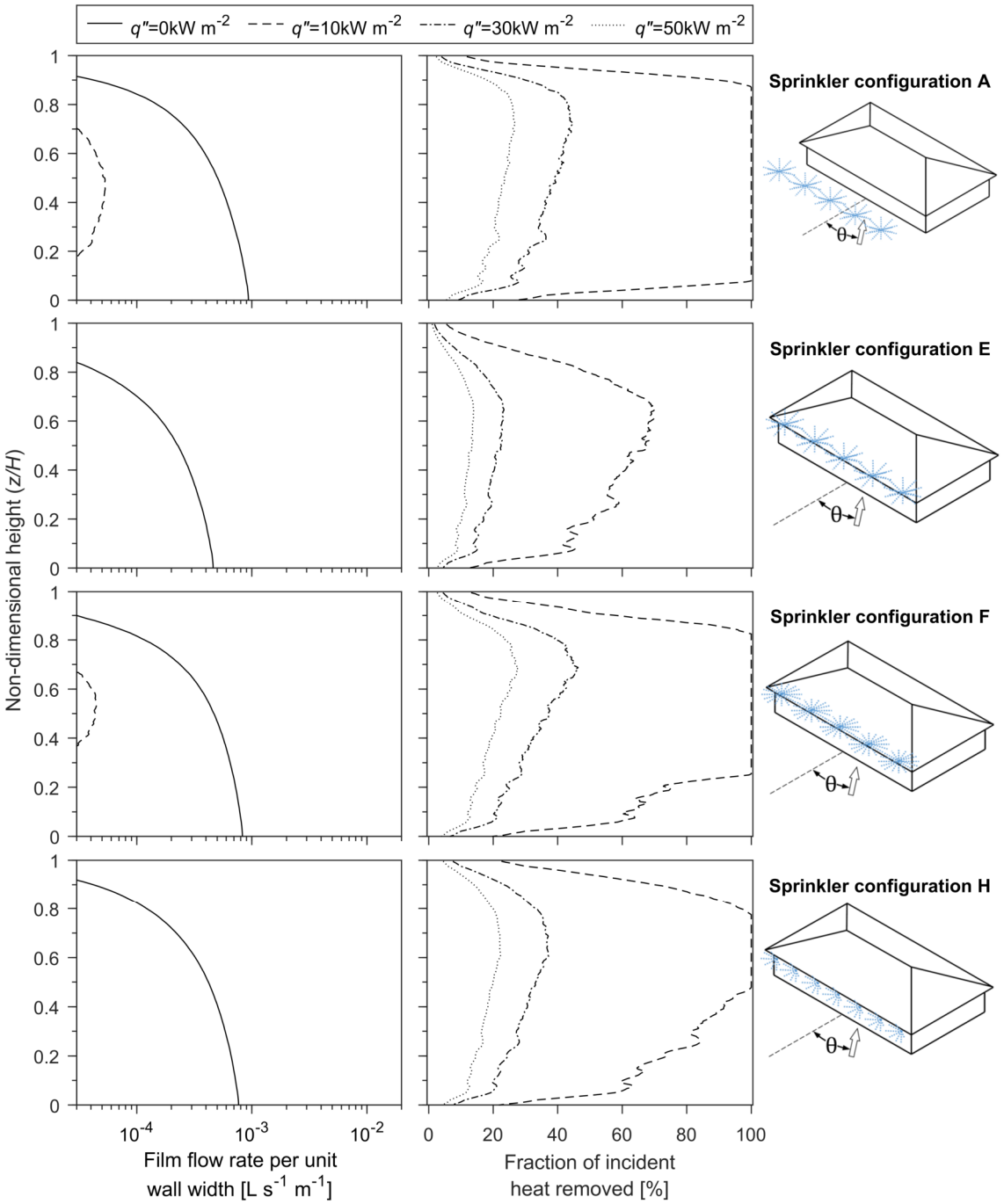

FIGURE 6.15: Vertical profiles of liquid film flow rate on the building windward wall (left) and fraction of heat incident on the wall that would be removed by the film (right), calculated for sprinkler configurations A (top), E (centre-top), F (centre-bottom) and H (bottom).

6.3.3 Radiation Attenuation

The quantity of radiant heat that could be attenuated by airborne droplets varied significantly between the nine sprinkler configurations (see Figure 6.16). Butterfly sprinklers installed on risers (in configuration A) were most effective, attenuating 15–25% of the incident heat flux, depending on the weather conditions. Configurations involving the deflector-plate sprinklers near

the roof perimeter (i.e. configurations I and F) attenuated 10–22% of the incident heat flux, and configurations H and E attenuated 6–13% of the incident heat flux. The remaining sprinkler configurations, which projected water primarily onto the roof or walls of the building, attenuated very little (< 3.5%) of the incident heat flux.

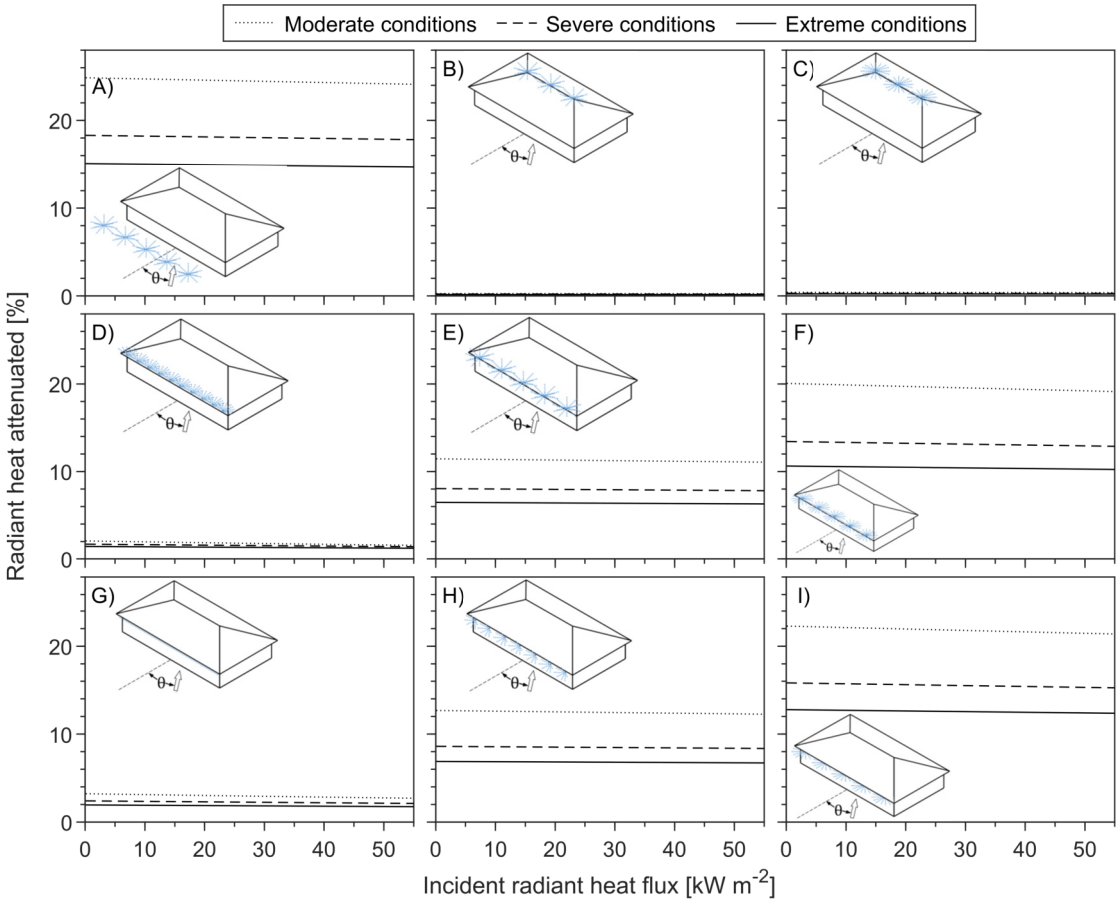

FIGURE 6.16: Radiant heat attenuated by airborne droplets, in sprinkler configurations A–I, given three sets of weather conditions.

Wind drift and evaporation significantly reduced the quantity of radiant heat attenuated by each sprinkler configuration. The five configurations that attenuated more than 5% of the incident heat flux (i.e. configurations A, E, F, H and I) attenuated 39–47% less radiant heat in 'extreme' conditions than they did in 'moderate' conditions. However, within the range of incident heat fluxes investigated (0–55 kW m^{-2}), the evaporation of droplets due to absorbed radiant heat had a relatively small effect on the sprinkler performance.

The sprinklers investigated here produced droplets with diameters predominantly in the range 150–2000 µm. However, as has been established in previous studies (Coppalle, Nedelka & Bauer

1993; Dembele, Wen & Sacadura 2001; Murrell, Crowhurst & Rock 1995), droplets closer to the size of the radiant heat wavelength (~1–10 μm) attenuate radiant heat much more effectively. Figure 6.17 presents the spectra of radiant heat predicted to be transmitted through monodisperse 'curtains' of droplets with the same liquid volume per unit spray frontal area, but with various droplet diameters. It is clear that, if 'curtains' of 10 μm droplets could be established between a building and wildfire, water resources could be used much more effectively than was predicted in the current investigation. However, such a spray would be highly susceptible to the effects of wind drift and evaporation. The trade-off between radiation attenuation capacity and resilience to the effects of wind, with respect to droplet size, would be a worthy subject for further investigation. The methods adopted in the present study would be suitable for such an investigation.

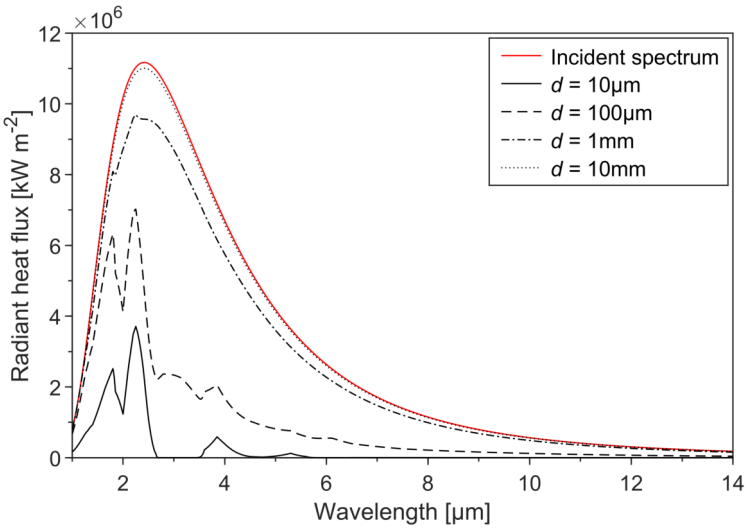

FIGURE 6.17: Radiant heat power spectra, including: an incident spectrum with total intensity of 40 kW m^{-2}, generated by a 1200 K flame; and the fractions of such a heat flux that would transmit through monodisperse 'curtains' of water droplets with various diameters (d), but all with the same liquid volume per unit curtain frontal area (0.1 L m^{-2}).

6.4 Conclusion

The dispersion of water by nine different wildfire sprinkler configurations has been simulated using two-way coupled RANS CFD modelling and Lagrangian particle tracking. Each sprinkler configuration was based on those reported in the literature, or commercially available at the time of writing. Three sets of weather conditions were simulated, representing the range of conditions

that have been recorded during destructive wildfires in Australia. The deposition of water on and around a generic residential building was calculated in each simulation, and the results were post-processed, to estimate the potential for each sprinkler configuration to cool the building walls and attenuate radiant heat. Table 6.3 summarises the performance of each sprinkler configuration.

TABLE 6.3: Comparison of the performance of different wildfire sprinkler configurations. Water consumption values represent the total consumption of a system designed to protect the building from all directions.

	Sprinkler configuration	Cooling of walls	Radiation attenuation	Water consumption [L s^{-1}]
A	Butterfly sprinklers on risers around building	Moderately effective	Effective	13.6
B	Butterfly sprinklers above roof ridge	Not effective	Not effective	1.7
C	Deflector-plate sprinklers above roof ridge	Not effective	Not effective	2.1
D	Flat-fan sprinklers above gutters, spraying inwards	Not effective	Not effective	2.1
E	Butterfly sprinklers above gutters	Moderately effective	Moderately effective	9.0
F	Deflector-plate sprinklers above gutters	Moderately effective	Effective	11.1
G	Flat-fan sprinklers under eaves, spraying inwards	Effective	Not effective	2.1
H	Hollow-cone sprinklers in WEEDS arrangement	Moderately effective	Moderately effective	4.6
I	Deflector-plate sprinklers under eaves	Effective	Effective	11.1

Wind drift and evaporation affected the performance of the sprinklers significantly. In some cases 20% of the water evaporated while airborne, and in other cases more than 35% of water was blown downwind, away from the building. Within the set of sprinkler configurations investigated, the system susceptibility to wind drift and evaporation was influenced more by the location and orientation of the sprinklers than it was by the spray characteristics (i.e. droplet initial sizes and velocities). Sprinkler configurations that sprayed water towards the target surfaces, over a relatively short range, were much less susceptible to the effects of wind and evaporation. When installed in such a configuration, even sprinklers that produced relatively small droplets (e.g. flat-fan or deflector-plate sprinklers, which produced sprays with Sauter mean diameters of 240 μm and 419 μm, respectively) were able to deposit a large fraction of water on building surfaces in high winds.

Cooling of the building windward wall by deposited droplets, via convection within a liquid film flow and as latent heat during evaporation, was found to vary widely between the different sprinkler configurations. Three distinct categories were identified in this regard: 1) systems that sprayed water directly onto the top of the wall from a short range, which could effectively mitigate incident heat fluxes of up to 50 kW m^{-2} over all or most of the wall height; 2) systems that sprayed water outwards from near the building gutters, or from risers located 4.5m from the building perimeter, which deposited sufficient water on the windward wall to remove 5–45% of incident heat fluxes of 30–50 kW m^{-2}; and 3) systems that sprayed water from the roof ridge, or from inward-facing sprinklers at the roof perimeter, which did not deposit sufficient water on the building walls to cool it significantly. The scenarios investigated here involved uniform heat fluxes applied to the entire windward wall; it would be worthwhile to extend this work to include localised high-intensity heat sources, like those generated by burning items or accumulated embers near the building. The extinguishment of accumulated embers on windowsills, etc., and at the base of walls, would also be worth investigating in future work. Combined with simulated droplet flux distributions like those presented here, such knowledge would allow different sprinkler systems to be evaluated in terms of how effectively they extinguish accumulated embers.

The quantity of radiant heat that could be attenuated by airborne droplets varied significantly between the sprinkler configurations, depending on the sizes of droplets that were sprayed, the sprinkler locations, and the weather conditions (e.g. wind speed). Five of the nine configurations attenuated between 6% and 26% of the radiant heat flux incident on the building, but the other four configurations did not have a significant effect. Wind-drift and evaporation had a large effect on properties of the 'curtain' of droplets that each sprinkler system could establish in front of the building; the quantity of heat attenuated was typically 39–47% less in 'extreme' weather conditions ($u_{ref} = 18.5$ m s^{-1}, $T = 47$°C, $RH = 7\%$) than it was in 'moderate' conditions ($u_{ref} = 7.7$ m s^{-1}, $T = 35$°C, $RH = 19\%$). The absorption of radiant heat by the droplets, and subsequent evaporation, did not significantly diminish the amount of radiant heat that could be attenuated, within the range of incident heat fluxes investigated (0–55 kW m^{-2}). It is possible that wildfire

sprinkler systems can be designed to attenuate much more radiant heat than the configurations investigated here, since droplets of a similar size to the radiant heat wavelength (~1–10 μm) are much more effective at doing so than the larger droplets in the present study (~150–2000 μm). However, further investigation would be required to quantify the effects of wind drift and evaporation on such fine sprays in a wildfire context.

To the best of the present author's knowledge, the effects of wind and evaporation on the performance of wildfire sprinkler systems had not previously been quantified, nor had the ability of such systems to cool building surfaces or attenuate radiant heat. The analysis of nine typical systems presented here has demonstrated that the impacts of wildfires can be mitigated significantly by external water sprays, but that the location, orientation and type of sprinklers need to be selected appropriately. Furthermore, the present study demonstrated how relatively simple methods, as developed in this project, can be used to simulate wind-spray interaction and to quantify the performance of different sprinkler configurations. With an improved understanding of the mechanisms by which water sprays can mitigate the effects of wildfire on a building (e.g. where and how much water needs to be applied to protect certain building features, or whether droplets can effectively intercept airborne embers), the simulation methods demonstrated here would provide the necessary means to design sprinkler systems to meet specific performance requirements.

Chapter 7

Conclusion

The primary aim of the present work was to develop a much more complete and rigorous understanding of wildfire sprinkler system operation, particularly in windy conditions. Although such sprinkler systems have been recommended in sources of technical guidance for owners of wildfire-prone buildings, the published design guidelines available at the time of writing were inconsistent in terms of the recommended sprinkler types and configurations. These inconsistencies appear to have resulted from a lack of rigorous scientific investigation; no previous studies appear to have evaluated and compared the various mechanisms by which water sprays could mitigate the effects wildfires on buildings, or the performance of different sprinkler configurations in the hot, windy conditions of a wildfire.

In the present work, experiments and simulations were conducted to quantify the performance of wildfire sprinklers. Due to the lack of previous research on the topic, the present investigation necessarily involved the development of several new research tools and techniques, and the validation of existing techniques for application to wildfire sprinkler systems. The investigation was comprised of five primary activities:

1. A comprehensive literature review;
2. Sprays generated by six typical sprinklers in quiescent conditions were experimentally characterised using a custom-built video-analysis program;
3. Outdoor experiments in windy conditions to validate CFD simulation methods;

4. CFD simulations of the test cases to determine whether computationally inexpensive methods could accurately model the dispersion of water from wildfire sprinkler systems; and
5. The CFD method developed was applied to nine typical wildfire sprinkler configurations, to quantify the effects of wind-drift and evaporation on the sprays, and to estimate the effectiveness of each system at cooling the building walls and attenuating an incident radiant heat flux.

The first experimental campaign was conducted indoors to fully characterise the droplet fields generated by the six sprinklers in quiescent air. A back-lit high-speed videography technique and a custom-built suite of image analysis software were used to form spatiotemporal maps of the co-distribution of droplet diameters and velocities within six sprays. High-speed video footage was generated of several hundred regions within the sprays, with a narrow depth-of-field. A computer script was developed to automatically identify droplet silhouettes in the videos, and eliminate droplets that had been outside a distinct control volume, based on the degree of image focus. A new automated method to detect and separate overlapping images of non-spherical droplets was developed that was more reliable than previously established methods. The resulting set of droplet diameter and velocity data will be of significant value for definition of spray source conditions in future CFD simulations, or other similar work

The second set of experiments investigated sprinkler operation in windy conditions, close to an isolated 2.4 m cube. The deposition of water was measured at several locations on the cube surfaces and ground, and high-frequency air velocity measurements were taken at three heights to characterise the atmospheric boundary layer flow. Four test cases were established; each involved either a hollow-cone or 'butterfly' sprinkler, implemented on either the windward or leeward side of the cube. Data from the experiments have been reported in-detail, including water deposition fluxes, and vertical profiles of mean wind velocity and turbulence characteristics.

An extensive investigation was conducted into the suitability of different CFD techniques for simulations of wildfire sprinkler systems. Simulated water deposition fluxes were compared to measurements from the outdoor experiments. Steady RANS-based simulations with Lagrangian

particle tracking and a discrete-random-walk turbulent dispersion model were able to replicate measured deposition fluxes on the vertical cube surfaces and ground reasonably well; 17 out of 20 of such results were within ±15% of the experimental results, and the remaining three results disagreed by less than 50%. However, simulated deposition fluxes on the cube top surface deviated from the experimental results by a greater margin. Comparison of results obtained using different simulation settings revealed the following.

- Differences between CFD and experimental results were much larger when a turbulent dispersion model was not used.
- One-way and two-way coupled simulations produced results that were very similar, despite the relatively high liquid volume fractions observed close to the sprays.
- Results obtained using the RNG k-ε and realisable k-ε turbulence models were very similar, although the RNG k-ε model did produce deposition fluxes on the top surface of the cube that were slightly closer to the experimental results.
- Deviations between CFD and experimental results did not appear to be caused by large-scale 'inactive' turbulence.
- The radius of the virtual spherical surface, from which droplets were introduced into the computational domain, had a large effect on CFD results. However, augmentation of droplet velocities in this 'droplet source' boundary condition could negate such effects.

The CFD methodology that was developed throughout this process provides a means to model droplet trajectories in hot windy conditions, such as those that occur during wildfires, with reasonably high accuracy and low computational expense. However, turbulence-resolving methods such as LES may be able to predict water deposition fluxes more accurately in the region of separated flow above the cube, so may be worth investigating further.

The performance of nine typical wildfire sprinkler configurations was then quantitatively evaluated using the CFD methodology that had been developed. The dispersion of water around a generic residential building was modelled in three hot, windy weather condition scenarios,

corresponding to conditions recorded during actual destructive wildfires in Australia. In many cases less than half of the water being sprayed impacted on or near the building, due to wind drift and the evaporation of airborne droplets. The primary factor that influenced the efficiency of the system in wetting building surfaces appeared to be the location and orientation of the sprinklers. Even sprinklers that emitted relatively small droplets ($d_{32} = 240$ μm) were able to deposit more than 75% of water on the target surfaces in high winds, when they were positioned to spray directly onto the surfaces over a short range. Sprinkler configurations that have often been recommended in sources of technical guidance, such as rotating 'butterfly' sprinklers above the roof ridge or gutters, deposited as little as 45% of water on the building in some cases, despite the relatively large droplets that they emit (which should be relatively insusceptible to wind drift and evaporation).

In order to understand the implications of the water deposition fluxes predicted using CFD for the effectiveness of each sprinkler configuration, the results were post-processed to estimate: i) the quantity of heat that could be removed from the building windward wall by water runoff film flow, and ii) the quantity of radiant heat that could be attenuated by airborne droplets upwind of the building. One-dimensional finite difference models were formulated for this analysis, which provided a relatively simple method to obtain 'order-of-magnitude' estimates of system performance, taking into account important phenomena such as the optical scattering characteristics of water droplets.

Two sprinkler configurations, which sprayed water towards the top of the wall surface from under the building eaves, were able to remove a uniform 30 kW m^{-2} heat flux from almost the entire wall surface, and could remove a 50 kW m^{-2} heat flux from 75–100% of the wall area. Water blown back onto the windward wall from sprinklers mounted above the roof perimeter, or pointing outwards from below the gutters (in a 'WEEDS' arrangement), was only able to remove 5–45% of incident heat fluxes of 30–50 kW m^{-2}, and sprinklers mounted to predominantly spray water on the roof surface did not cool the windward wall significantly.

Five of the nine sprinkler configurations established a 'curtain' of airborne droplets upwind of the building that could attenuate a significant fraction (6–26%) of incident radiant heat fluxes. The fraction of incident radiant heat that could be attenuated was strongly influenced by the weather conditions, due to wind drift and evaporation, but was affected much less by the intensity of the incident radiant heat flux (within the range 0–55 kW m^{-2}). It is possible that water resources could be used much more effectively by wildfire sprinklers designed to emit smaller (~10–100 μm) droplets, due to their optical scattering characteristics. However, further research would be required to determine whether 'curtains' of such small droplets can be established around buildings in the hot, windy conditions of a wildfire. The methods that were developed in the present work would be well-suited for such an investigation.

Considering the significant benefits that indoor sprinkler systems have been shown to provide in extinguishing structural fires, wildfire sprinkler systems have received surprisingly little attention from the scientific community. It is true that the complex thermo-physical phenomena that occur in the outdoor environment during wildfires render such systems difficult to investigate, and could diminish their effectiveness compared to indoor sprinklers, but these barriers are not insurmountable. Methods have been developed in the present work which allow wildfire sprinkler performance to be quantified with a reasonable degree of accuracy. Furthermore, the results obtained using these methods indicate that external sprinklers could be very effective at mitigating the impacts of wildfire on buildings, if implemented correctly. Continued development of a robust and comprehensive understanding of wildfire sprinkler performance would enable the owners of wildfire-prone buildings to make informed risk-management decisions, ultimately saving lives and property. It is the author's hope that the work presented here can serve as the basis for further investigations in this area.

References

Abuku, M, Blocken, B, Nore, K, Thue, JV, Carmeliet, J & Roels, S 2009, 'On the validity of numerical wind-driven rain simulation on a rectangular low-rise building under various oblique winds', *Building and Environment*, vol. 44, no. 3, pp. 621-32.

Albini, F, Brown, J, Reinhardt, E & Ottmar, R 1995, 'Calibration of a large fuel burnout model', *International Journal of Wildland Fire*, vol. 5, no. 3, pp. 173-92.

Amani, E & Nobari, MRH 2013, 'Systematic tuning of dispersion models for simulation of evaporating sprays', *International Journal of Multiphase Flow*, vol. 48, pp. 11-31.

Anderson, JD 1995, *Computational fluid dynamics: The basics with applications*, McGraw-Hill, Inc., New York, USA.

ANSYS 2014, *Academic research fluent, version 15.0, help system*, ANSYS, Inc.

Ashgriz, N, Li, X & Sarchami, A 2011, 'Instability of liquid sheets', in N Ashgriz (ed.), *Handbook of atomization and sprays: Theory and applications*, Springer US, Boston, MA, pp. 75-95.

Babinsky, E & Sojka, PE 2002, 'Modeling drop size distributions', *Progress in Energy and Combustion Science*, vol. 28, no. 4, pp. 303-29.

Bachalo, W 2000, 'Spray diagnostics for the twenty-first century', *Atomization and Sprays*, vol. 10, no. 3-5, pp. 439-74.

Baetens, K, Nuyttens, D, Verboven, P, De Schampheleire, M, Nicolaï, B & Ramon, H 2007, 'Predicting drift from field spraying by means of a 3d computational fluid dynamics model', *Computers and Electronics in Agriculture*, vol. 56, no. 2, pp. 161-73.

Baker, CJ 2007, 'Wind engineering—past, present and future', *Journal of Wind Engineering and Industrial Aerodynamics*, vol. 95, no. 9, pp. 843-70.

Balachandar, S & Eaton, JK 2010, 'Turbulent dispersed multiphase flow', *Annual Review of Fluid Mechanics*, vol. 42, no. 1, pp. 111-33.

Batarseh, FZ, Roisman, IV & Tropea, C 2010, 'Characterization of a spray generated by an airblast atomizerwith prefilmer', *Atomization and Sprays*, vol. 20, no. 10, pp. 887-903.

Bautista-Capetillo, C, Robles, O, Salinas, H & Playán, E 2014, 'A particle tracking velocimetry technique for drop characterization in agricultural sprinklers', *Irrigation Science*, vol. 32, no. 6, pp. 437-47.

Bautista-Capetillo, CF, Salvador, R, Burguete, J, Montero, J, Tarjuelo, J, Zapata, N, González, J & Playán, E 2009, 'Comparing methodologies for the characterization of water drops emitted by an irrigation sprinkler', *Transactions of the ASABE*, vol. 52, no. 5, pp. 1493-504.

Beason, D 1986, 'Fire endurance of sprinklered glass walls', *Annual Technology Review*, p. 59.

Black, DL, McQuay, MQ & Bonin, MP 1996, 'Laser-based techniques for particle-size measurement: A review of sizing methods and their industrial applications', *Progress in Energy and Combustion Science*, vol. 22, no. 3, pp. 267-306.

Blaisot, J 2012, 'Drop size and drop size distribution measurements by image analysis', paper presented to International Conference on Liquid Atomization and Spray Systems: ICLASS, Heidelberg, Germany, September 2-6, 2012.

Blaisot, JB & Yon, J 2005, 'Droplet size and morphology characterization for dense sprays by image processing: Application to the diesel spray', *Experiments in Fluids*, vol. 39, no. 6, pp. 977-94.

Blanchi, R & Leonard, J 2005, *Investigation of bushfire attack mechanisms resulting in house loss in the act bushfire 2003*, Bushfire CRC Report CMIT Technical Report-2005-478, Bushfire Cooperative Research Centre.

Blanchi, R, Leonard, J, Haynes, K, Opie, K, James, M & Oliveira, FD 2014, 'Environmental circumstances surrounding bushfire fatalities in australia 1901–2011', *Environmental Science & Policy*, vol. 37, no. 0, pp. 192-203.

Blanchi, R, Leonard, J, Holland, M & Kearsley, D 2011, *Community vulnerability discussion paper: Wind, interface fuels & egress*, USP2011/EP114795, CSIRO Ecosystems Sciences and Country Fire Authority.

Blanchi, R, Leonard, J & Maughan, D 2004, 'Towards new information tools for understanding bushfire risk at the urban interface', in *Bushfire 2004 - Australian Bushfire Conference*, Adelaide.

Blanchi, R, Leonard, J, White, N, Sargeant, A, Bicknell, A & Andersson, S 2007, *Research into the performance of water tanks in bushfire*, USP2007/014, BlueScope Steel Limited and CSIRO Sustainable Ecosystems (CSE) Urban Systems Program, St Lucia, Queensland.

Blanchi, R, Leonard, JE & Leicester, RH 2006, 'Lessons learnt from post-bushfire surveys at the urban interface in australia', paper presented to Proceedings of the V International Conference on Forest Fire Research, Figuera da Foz, Portugal, November 27-30, 2006.

Blanchi, R, Lucas, C, Leonard, J & Finkele, K 2010, 'Meteorological conditions and wildfire-related houseloss in australia', *International Journal of Wildland Fire*, vol. 19, no. 7, pp. 914-26.

Blocken, B 2014, '50 years of computational wind engineering: Past, present and future', *Journal of Wind Engineering and Industrial Aerodynamics*, vol. 129, no. 0, pp. 69-102.

Blocken, B & Carmeliet, J 2004, 'A review of wind-driven rain research in building science', *Journal of Wind Engineering and Industrial Aerodynamics*, vol. 92, no. 13, pp. 1079-130.

Blocken, B & Carmeliet, J 2006, 'On the accuracy of wind-driven rain measurements on buildings', *Building and Environment*, vol. 41, no. 12, pp. 1798-810.

Blocken, B & Carmeliet, J 2007, 'Validation of cfd simulations of wind-driven rain on a low-rise building facade', *Building and Environment*, vol. 42, no. 7, pp. 2530-48.

Blocken, B & Carmeliet, J 2010, 'Overview of three state-of-the-art wind-driven rain assessment models and comparison based on model theory', *Building and Environment*, vol. 45, no. 3, pp. 691-703.

Blocken, B, Carmeliet, J & Stathopoulos, T 2007, 'Cfd evaluation of wind speed conditions in passages between parallel buildings—effect of wall-function roughness modifications for the atmospheric boundary layer flow', *Journal of Wind Engineering and Industrial Aerodynamics*, vol. 95, no. 9–11, pp. 941-62.

Blocken, B, Poesen, J & Carmeliet, J 2006, 'Impact of wind on the spatial distribution of rain over micro-scale topography: Numerical modelling and experimental verification', *Hydrological Processes*, vol. 20, no. 2, pp. 345-68.

Blocken, B, Stathopoulos, T & Carmeliet, J 2007, 'Cfd simulation of the atmospheric boundary layer: Wall function problems', *Atmospheric Environment*, vol. 41, no. 2, pp. 238-52.

Blocken, B, Tominaga, Y & Stathopoulos, T 2013, 'Cfd simulation of micro-scale pollutant dispersion in the built environment', *Building and Environment*, vol. 64, no. 0, pp. 225-30.

Bottema, M 1997, 'Turbulence closure model “constants” and the problems of “inactive” atmospheric turbulence', *Journal of Wind Engineering and Industrial Aerodynamics*, vol. 67, pp. 897-908.

Boulet, P, Collin, A & Parent, G 2006, 'Heat transfer through a water spray curtain under the effect of a strong radiative source', *Fire Safety Journal*, vol. 41, no. 1, pp. 15-30.

Bowditch, P, Sargeant, A, Leonard, J & Macindoe, L 2006, *Window and glazing exposure to laboratory-simulated bushfires*, Bushfire Cooperative Research Centre.

Bowditch, PA, Leonard, J & O'Brien, DJ 2004, *Full-scale fire truck performance measurements*, Report to the Bushfire CRC, CSIRO, Highett, Victoria, Australia.

Bowman, DMJS, Williamson, GJ, Abatzoglou, JT, Kolden, CA, Cochrane, MA & Smith, AMS 2017, 'Human exposure and sensitivity to globally extreme wildfire events', *Nature Ecology & Evolution*, vol. 1, p. 0058.

Bradshaw, P 1967, '‘Inactive’ motion and pressure fluctuations in turbulent boundary layers', *Journal of Fluid Mechanics*, vol. 30, no. 2, pp. 241-58.

Bradshaw, P 1999, 'The best turbulence models for engineers', *ICASE LARC Interdisciplinary Series in Science and Engineering*, vol. 7, pp. 9-28.

Bradstock, RA, Cary, GJ, Davies, I, Lindenmayer, DB, Price, OF & Williams, RJ 2012, 'Wildfires, fuel treatment and risk mitigation in australian eucalypt forests: Insights from landscape-scale simulation', *Journal of Environmental Management*, vol. 105, no. 0, pp. 66-75.

Brenn, G 2011, 'Droplet collision', in N Ashgriz (ed.), *Handbook of atomization and sprays*, Springer, pp. 157-81.

Briggen, PM, Blocken, B & Schellen, HL 2009, 'Wind-driven rain on the facade of a monumental tower: Numerical simulation, full-scale validation and sensitivity analysis', *Building and Environment*, vol. 44, no. 8, pp. 1675-90.

Britter, R & Schatzmann, M 2007, *Model evaluation guidance and protocol document*, European Cooperation in Sciences and Technology, COST Office Brussels.

Butler, B, Cohen, J, Latham, D, Schuette, R, Sopko, P, Shannon, K, Jimenez, D & Bradshaw, L 2004, 'Measurements of radiant emissive power and temperatures in crown fires', *Canadian Journal of Forest Research*, vol. 34, no. 8, pp. 1577-87.

Butler Ellis, MC & Miller, PCH 2010, 'The silsoe spray drift model: A model of spray drift for the assessment of non-target exposures to pesticides', *Biosystems Engineering*, vol. 107, no. 3, pp. 169-77.

Butry, D & Donovan, G 2008, 'Protect thy neighbor: Investigating the spatial externalities of community wildfire hazard mitigation', *Forest Science*, vol. 54, no. 4, pp. 417-28.

Calkin, DE, Cohen, JD, Finney, MA & Thompson, MP 2014, 'How risk management can prevent future wildfire disasters in the wildland-urban interface', *Proceedings of the National Academy of Sciences*, vol. 111, no. 2, pp. 746-51.

Call, CJ & Kennedy, IM 1992, 'Measurements and simulations of particle dispersion in a turbulent flow', *International Journal of Multiphase Flow*, vol. 18, no. 6, pp. 891-903.

Castanet, G, Dunand, P, Caballina, O & Lemoine, F 2013, 'High-speed shadow imagery to characterize the size and velocity of the secondary droplets produced by drop impacts onto a heated surface', *Experiments in Fluids*, vol. 54, no. 3, pp. 1-17.

Castro, IP & Robins, AG 1977, 'The flow around a surface-mounted cube in uniform and turbulent streams', *Journal of Fluid Mechanics*, vol. 79, no. 2, pp. 307-35.

Caton, SE, Hakes, RSP, Gorham, DJ, Zhou, A & Gollner, MJ 2016, 'Review of pathways for building fire spread in the wildland urban interface part i: Exposure conditions', *Fire Technology*, pp. 1-45.

Cermak, JE 2003, 'Wind-tunnel development and trends in applications to civil engineering', *Journal of Wind Engineering and Industrial Aerodynamics*, vol. 91, no. 3, pp. 355-70.

CFS 2011, *Cfs fact sheet - sprinkler systems*, 10 Febuary 2017, <http://www.cfs.sa.gov.au/site/resources.jsp#TemporaryFactSheets>.

Chatterjee, P & Geiman, J 2017, *Numerical simulation of sprinkler activation and spray transport under obstructed, sloped ceilings*, FM Global.

Chen, Y, Su, C, Tseng, J & Li, W 2015, 'Experimental and numerical analysis of the cooling performance of water spraying systems during a fire', *PLoS ONE*, vol. 10, pp. e0118306-e.

Chigier, N 1991, 'Optical imaging of sprays', *Progress in Energy and Combustion Science*, vol. 17, no. 3, pp. 211-62.

Choi, ECC 1993, 'Simulation of wind-driven-rain around a building', *Journal of Wind Engineering and Industrial Aerodynamics*, vol. 46–47, no. 0, pp. 721-9.

Chow, WK 1999, 'Selection of differencing schemes on simulating the sprinkler hot-air layer problem', *Numerical Heat Transfer, Part A: Applications*, vol. 35, no. 3, pp. 311-30.

Chueng, WY 2009, 'Radiation blockage of water curtains', *International Journal on Engineering Performance-Based Fire Codes*, vol. 1, pp. 7-13.

Cohen, JD 1995, 'Structure ignition assessment model (siam)', paper presented to The Biswell Symposium: Fire Issues and Solutions in Urban Interface and Wildland Ecosystems, Walnut Creek, CA, USA, 15 - 17 February 1994, <http://www.fs.fed.us/psw/publications/documents/psw_gtr158/psw_gtr158_05_cohen.pdf>.

Cohen, JD 1999, *Reducing the wildland fire threat to homes: Where and how much?*, USDA Forest Service General Technical Report PSW-GTR-173, U.S. Forest Service, Pacific Southwest Research Station, Albany, California.

Cohen, JD 2000, 'Preventing disaster: Home ignitability in the wildland-urban interface', *Journal of Forestry*, vol. 98, no. 3, pp. 15-21.

Cohen, JD 2004, 'Relating flame radiation to home ignition using modeling and experimental crown fires', *Canadian Journal of Forest Research*, vol. 34, no. 8, pp. 1616-26.

Consuegro, AJ, Kaiser, AS, Zamora, B, Sánchez, F, Lucas, M & Hernández, M 2014, 'Numerical modeling of the drift and deposition of droplets emitted by mechanical cooling towers on buildings and its experimental validation', *Building and Environment*, vol. 78, no. 0, pp. 53-67.

Coppalle, A, Nedelka, D & Bauer, B 1993, 'Fire protection: Water curtains', *Fire Safety Journal*, vol. 20, no. 3, pp. 241-55.

Cova, T, Drews, F, Siebeneck, L & Musters, A 2009, 'Protective actions in wildfires: Evacuate or shelter-in-place?', *Natural Hazards Review*, vol. 10, no. 4, pp. 151-62.

Cowan, I 1968, 'Mass, heat and momentum exchange between stands of plants and their atmospheric environment', *Quarterly Journal of the Royal Meteorological Society*, vol. 94, no. 402, pp. 523-44.

Dalziel, S 2006, *Digiflow user guide*, DL Research Partners, <http://www.damtp.cam.ac.uk/lab/digiflow/digiflow.pdf>.

Dalziel, SB 1992, 'Decay of rotating turbulence: Some particle tracking experiments', *Applied scientific research*, vol. 49, no. 3, pp. 217-44.

Davenport, AG 1960, *Rationale for determining design wind velocities*, National Research Council of Canada Ottowa (Ontario) div. of Building Research.

Dehbi, A 2008a, 'A cfd model for particle dispersion in turbulent boundary layer flows', *Nuclear Engineering and Design*, vol. 238, no. 3, pp. 707-15.

Dehbi, A 2008b, 'Turbulent particle dispersion in arbitrary wall-bounded geometries: A coupled cfd-langevin-equation based approach', *International Journal of Multiphase Flow*, vol. 34, no. 9, pp. 819-28.

Delele, MA, Jaeken, P, Debaer, C, Baetens, K, Endalew, AM, Ramon, H, Nicolaï, BM & Verboven, P 2007, 'Cfd prototyping of an air-assisted orchard sprayer aimed at drift reduction', *Computers and Electronics in Agriculture*, vol. 55, no. 1, pp. 16-27.

Dembele, S, Wen, JX & Sacadura, JF 2001, 'Experimental study of water sprays for the attenuation of fire thermal radiation', *Transactions of the ASME*, vol. 123, no. 3, pp. 534-43.

Dombrovsky, LA, Dembele, S & Wen, JX 2016, 'A simplified model for the shielding of fire thermal radiation by water mists', *International Journal of Heat and Mass Transfer*, vol. 96, pp. 199-209.

Dorr, GJ, Hewitt, AJ, Adkins, SW, Hanan, J, Zhang, H & Noller, B 2013, 'A comparison of initial spray characteristics produced by agricultural nozzles', *Crop Protection*, vol. 53, pp. 109-17.

Dowdy, AJ, Mills, GA, Finkele, K & de Groot, W 2009, *Australian fire weather as represented by the mcarthur forest fire danger index and the canadian forest fire weather index*, Centre for Australian Weather and Climate Research, Melbourne, Australia, CAWR Technical Report No. 10.

Drysdale, D 2011, *An introduction to fire dynamics*, John Wiley & Sons, Chichester, UK.

Durbin, PA & Hunt, JCR 2006, 'On surface pressure fluctuations beneath turbulent flow round bluff bodies', *Journal of Fluid Mechanics*, vol. 100, no. 1, pp. 161-84.

Elghobashi, S 1994, 'On predicting particle-laden turbulent flows', *Applied scientific research*, vol. 52, no. 4, pp. 309-29.

Everest, D & Atreya, A 2003, 'Simultaneous measurements of drop size and velocity in large-scale sprinkler flows using laser-induced fluorescence and mie scattering', *Journal of flow visualization and image processing*, vol. 10, no. 3-4, pp. 163-81.

Faeth, GM, Hsiang, LP & Wu, PK 1995, 'Structure and breakup properties of sprays', *International Journal of Multiphase Flow*, vol. 21, pp. 99-127.

Fansler, TD & Parrish, SE 2015, 'Spray measurement technology: A review', *Measurement Science and Technology*, vol. 26, no. 1, p. 012002.

Fantini, E, Tognotti, L & Tonazzini, A 1990, 'Drop size distribution in sprays by image processing', *Computers & Chemical Engineering*, vol. 14, no. 11, pp. 1201-11.

Fdida, N & Blaisot, JB 2010, 'Drop size distribution measured by imaging: Determination of the measurement volume by the calibration of the point spread function', *Measurement Science and Technology*, vol. 21, no. 2, p. 025501.

Fdida, N, Vingert, L, Ristori, A & Le Sant, Y 2016, 'Droplet size and velocity measurements in a cryogenic jet flame of a rocket-type combustor using high-speed imaging', *Atomization and Sprays*, vol. 26, no. 5, pp. 411-38.

FEMA 2008, *Home builder's guide to construction in wildfire zones*, Technical fact sheet series - FEMA P-737, Federal Emergency Management Agency.

FPAA 2000, *External water spray systems to aid building protection from wildfire*, Report, Fire Protection Association Australia, Box Hill, Vic, Australia.

Franke, J & Hellsten 2011, 'The cost 732 best practice guideline for cfd simulation of flows in the urban environment: A summary', *International journal of environment and pollution*, vol. 44, no. 1/2/3/4, p. 419.

Franke, J, Hellsten, A, Schlünzen, H & Carissimo, B 2007, *Best practice guideline for the cfd simulation of flows in the urban environment*, COST, Brussels, Belgium.

Frohn, A & Roth, N 2000, *Dynamics of droplets*, Springer Science & Business Media, Verlag Berlin Heidelberg.

Garratt, JR 1994, 'The atmospheric boundary layer', *Earth-Science Reviews*, vol. 37, no. 1-2, pp. 89-134.

Glenn, GM, Bingol, G, Chiou, BS, Klamczynski, AP & Pan, Z 2012, 'Sodium bentonite-based coatings containing starch for protecting structures in wildfire emergency situations', *Fire Safety Journal*, vol. 51, pp. 85-92.

Godoy, WF & DesJardin, PE 2007, 'Efficient transmission calculations for polydisperse water sprays using spectral scaling', *Journal of Quantitative Spectroscopy and Radiative Transfer*, vol. 108, no. 3, pp. 440-53.

Gorokhovski, M & Herrmann, M 2008, 'Modeling primary atomization', *Annu. Rev. Fluid Mech.*, vol. 40, pp. 343-66.

Gosman, AD & loannides, E 1981, 'Aspects of computer simulation of liquid-fueled combustors', *Journal of Energy*, vol. 7, no. 6, pp. 482-90.

Graham, DI 1998, 'Improved eddy interaction models with random length and time scales', *International Journal of Multiphase Flow*, vol. 24, no. 2, pp. 335-45.

Graham, DI 2001, 'Spectral characteristics of eddy interaction models', *International Journal of Multiphase Flow*, vol. 27, no. 6, pp. 1065-77.

Grant, G, Brenton, J & Drysdale, D 2000, 'Fire suppression by water sprays', *Progress in Energy and Combustion Science*, vol. 26, no. 2, pp. 79-130.

GTVFD 2007, *Sprinkler protection systems - guidelines for gunflint trail fire district*, Gunflint Trail Fire Department, viewed March 2015 2015, <http://www.gunflint911.org/sprinkler_system_final.pdf>.

Guildenbecher, DR, López-Rivera, C & Sojka, PE 2011, 'Droplet deformation and breakup', in N Ashgriz (ed.), *Handbook of atomization and sprays: Theory and applications*, Springer US, Boston, MA, pp. 145-56.

Guler, H, Zhu, H, Ozkan, H, Derksen, R, Yu, Y & Krause, C 2007, 'Spray characteristics and drift reduction potential with air induction and conventional flat-fan nozzles', *Transactions of the ASABE*, vol. 50, no. 3, pp. 745-54.

Guler, H, Zhu, H, Ozkan, HE & Ling, P 2012, 'Characterization of hydraulic nozzles for droplet size and spray coverage', vol. 22, no. 8, pp. 627-45.

Gupta, JG & Agarwal, AK 2016, *Macroscopic and microscopic spray characteristics of diesel and karanja biodiesel blends*, SAE Technical Paper 2016-01-0869, Society of Automotive Engineers International.

Hakes, RSP, Caton, SE, Gorham, DJ & Gollner, MJ 2016, 'A review of pathways for building fire spread in the wildland urban interface part ii: Response of components and systems and mitigation strategies in the united states', *Fire Technology*, pp. 1-41.

Hay, KJ, Liu, Z-C & Hanratty, TJ 1998, 'A backlighted imaging technique for particle size measurements in two-phase flows', *Experiments in Fluids*, vol. 25, no. 3, pp. 226-32.

Haynes, K, Handmer, J, McAneney, J, Tibbits, A & Coates, L 2010, 'Australian bushfire fatalities 1900–2008: Exploring trends in relation to the 'prepare, stay and defend or leave early' policy', *Environmental Science & Policy*, vol. 13, no. 3, pp. 185-94.

Herráez, J & Belda, R 2006, 'Refractive indices, densities and excess molar volumes of monoalcohols + water', *Journal of Solution Chemistry*, vol. 35, no. 9, pp. 1315-28.

Högberg, A 2002, 'Microclimate load: Transformed weather observations for use in design of durable buildings', Department of Building Physics, Chalmers University of Technology.

Högström, U, Hunt, J & Smedman, A-S 2002, 'Theory and measurements for turbulence spectra and variances in the atmospheric neutral surface layer', *Boundary-Layer Meteorology*, vol. 103, no. 1, pp. 101-24.

Holmes, JD 2015, *Wind loading of structures*, 3 edn, Boca Raton: CRC press, Towbridge, Wiltshire.

Holterman, HJ, van de Zande, JC, Porskamp, HAJ & Huijsmans, JFM 1997, 'Modelling spray drift from boom sprayers', *Computers and Electronics in Agriculture*, vol. 19, no. 1, pp. 1-22.

Hsiang, LP & Faeth, GM 1992, 'Near-limit drop deformation and secondary breakup', *International Journal of Multiphase Flow*, vol. 18, no. 5, pp. 635-52.

Hsiang, LP & Faeth, GM 1995, 'Drop deformation and breakup due to shock wave and steady disturbances', *International Journal of Multiphase Flow*, vol. 21, no. 4, pp. 545-60.

Huang, SH & Li, QS 2010, 'Numerical simulations of wind-driven rain on building envelopes based on eulerian multiphase model', *Journal of Wind Engineering and Industrial Aerodynamics*, vol. 98, no. 12, pp. 843-57.

Husted, B 2007, 'Experimental measurements of water mist systems and implications for modelling in cfd', Doctoral Thesis thesis, Lund University.

Igual, SN, Marchitto, L, Merola, SS, Tornatore, C & Valentino, G 2015, 'Characterization of n-butanol and gasoline spray from a multihole injector using phase doppler anemometry', vol. 25, no. 12, pp. 1047-62.

IPCC 2014, *Climate change 2014: Impacts, adaptation, and vulnerability. Part b: Regional aspects*, Contribution of Working Group II to the Fifth Assessment Report of the Intergovernmental Panel on Climate Change.

Ishii, M & Zuber, N 1979, 'Drag coefficient and relative velocity in bubbly, droplet or particulate flows', *AIChE Journal*, vol. 25, no. 5, pp. 843-55.

ISO 2005, *Fire protection - automatic sprinkler system, requirements and test methods for water mist nozzles*, ISO 6182-9:2005, International Organisation for Standards.

Jaegle, F, Senoner, JM, García, M, Bismes, F, Lecourt, R, Cuenot, B & Poinsot, T 2011, 'Eulerian and lagrangian spray simulations of an aeronautical multipoint injector', *Proceedings of the Combustion Institute*, vol. 33, no. 2, pp. 2099-107.

Jain, M, Prakash, RS, Tomar, G & Ravikrishna, RV 2015, 'Secondary breakup of a drop at moderate weber numbers', *Proceedings of the Royal Society A: Mathematical, Physical and Engineering Science*, vol. 471, no. 2177.

Jain, S 1998, 'Three-dimensional simulation of turbulent particle dispersion applications', Doctoral thesis, Dept. of Chemical and Fuels Engineering, University of Utah.

Jiang, X, Siamas, GA, Jagus, K & Karayiannis, TG 2010, 'Physical modelling and advanced simulations of gas–liquid two-phase jet flows in atomization and sprays', *Progress in Energy and Combustion Science*, vol. 36, no. 2, pp. 131-67.

Jiang, Y, Alexander, D, Jenkins, H, Arthur, R & Chen, Q 2003, 'Natural ventilation in buildings: Measurement in a wind tunnel and numerical simulation with large-eddy simulation', *Journal of Wind Engineering and Industrial Aerodynamics*, vol. 91, no. 3, pp. 331-53.

Johnson, JF, Downing, T & Nelson, KC 2008, *External sprinkler systems and defensible space: Lessons learned from the ham lake fire and the gunflint trail*, A report prepared for the Firewise Program, Minnesota Department of Natural Resources, University of Minnesota, College of Food, Agricultural and Natural Resource Sciences.

Kallio, GA & Reeks, MW 1989, 'A numerical simulation of particle deposition in turbulent boundary layers', *International Journal of Multiphase Flow*, vol. 15, no. 3, pp. 433-46.

Kashdan, JT, Shrimpton, JS & Whybrew, A 2003, 'Two-phase flow characterization by automated digital image analysis. Part 1: Fundamental principles and calibration of the technique', *Particle & Particle Systems Characterization*, vol. 20, no. 6, pp. 387-97.

Katul, GG & Albertson, JD 1996, 'The `inactive' eddy motion and the large-scale turbulent pressure fluctuations in the dynamic', *Journal of the Atmospheric Sciences*, vol. 53, no. 17, p. 2512.

Kim, A & Lougheed, G 1990, 'The protection of glazing systems with dedicated sprinklers', *Journal of Fire Protection Engineering*, vol. 2, no. 2, pp. 49-59.

Kim, AK, Taber, B & Lougheed, G 1998, 'Sprinkler protection of exterior glazing', *Fire Technology*, vol. 34, no. 2, pp. 116-38.

Kim, KS & Kim, S-S 1994, 'Drop sizing and depth-of-field correction in tv imaging', *Atomization and Sprays*, vol. 4, no. 1, pp. 65-78.

Klinner, J & Willert, C 2012, 'Tomographic shadowgraphy for three-dimensional reconstruction of instantaneous spray distributions', *Experiments in Fluids*, vol. 53, no. 2, pp. 531-43.

Koh, KU, Kim, JY & Lee, SY 2001, 'Determination of in-focus criteria and depth of field in image processing of spray particles', *Atomization and Sprays*, vol. 11, no. 4, pp. 317-33.

Kohnen, B, Pieloth, D, Musemic, E & Walzel, P 2011, 'Characterization of full cone nozzles', *Atomization and Sprays*, vol. 21, no. 4, pp. 317-25.

Koo, J-Y & Martin, JK 1990, *Droplet sizes and velocities in a transient diesel fuel spray*, SAE Technical Paper 900397, Society of Automotive Engineers International.

Krawchuk, MA, Moritz, MA, Parisien, MA, Van Dorn, J & Hayhoe, K 2009, 'Global pyrogeography: The current and future distribution of wildfire', *PLoS ONE*, vol. 4, no. 4, p. e5102.

Kubilay, A, Derome, D, Blocken, B & Carmeliet, J 2013, 'Cfd simulation and validation of wind-driven rain on a building facade with an eulerian multiphase model', *Building and Environment*, vol. 61, no. 0, pp. 69-81.

Kubilay, A, Derome, D, Blocken, B & Carmeliet, J 2014, 'Numerical simulations of wind-driven rain on an array of low-rise cubic buildings and validation by field measurements', *Building and Environment*, vol. 81, pp. 283-95.

Kubilay, A, Derome, D, Blocken, B & Carmeliet, J 2015a, 'Numerical modeling of turbulent dispersion for wind-driven rain on building facades', *Environmental Fluid Mechanics*, vol. 15, no. 1, p. 109.

Kubilay, A, Derome, D, Blocken, B & Carmeliet, J 2015b, 'Wind-driven rain on two parallel wide buildings: Field measurements and cfd simulations', *Journal of Wind Engineering and Industrial Aerodynamics*, vol. 146, pp. 11-28.

Lateb, M, Masson, C, Stathopoulos, T & Bédard, C 2014, 'Simulation of near-field dispersion of pollutants using detached-eddy simulation', *Computers & Fluids*, vol. 100, pp. 308-20.

Launder, BE & Spalding, DB 1974, 'The numerical computation of turbulent flows', *Computer methods in applied mechanics and engineering*, vol. 3, no. 2, pp. 269-89.

Le Gal, P, Farrugia, N & Greenhalgh, DA 1999, 'Laser sheet dropsizing of dense sprays', *Optics & Laser Technology*, vol. 31, no. 1, pp. 75-83.

Lebrun, D, Touil, CE & Özkul, C 1996, 'Methods for the deconvolution of defocused-image pairs recorded separately on two ccd cameras: Application to particle sizing', *Applied Optics*, vol. 35, no. 32, pp. 6375-81.

Lecuona, A, Sosa, PA, Rodríguez, PA & Zequeira, RI 2000, 'Volumetric characterization of dispersed two-phase flows by digital image analysis', *Measurement Science and Technology*, vol. 11, no. 8, p. 1152.

Lee, SY & Kim, YD 2004, 'Sizing of spray particles using image processing technique', *KSME International Journal*, vol. 18, no. 6, pp. 879-94.

Legrand, M, Lecuona, A, Nogueira, J & Forte, R 2014, 'Single camera 3-d shadowgraphy system for droplet sizing', in *17th International Symposium on Applications of Laser Techniques to Fluid Mechanics*, Lisbon, Portugal.

Leonard, J, Blanchi, R & Bowditch, P 2004, *Bushfire impact from a house's perspective*, A background support document for ongoing work in the Bushfire CRC, CSIRO Manufacturing & Infrastructure Technology, Bushfire Cooperative Research Centre.

Leonard, J & McArthur, NA 1999, 'A history of research into building performance in australian bushfires', in *Proceedings of the Australian Bushfire Conference*, Charles Sturt University, Albury, pp. 219-25.

Li, W-W & Meroney, RN 1983, 'Gas dispersion near a cubical model building. Part i. Mean concentration measurements', *Journal of Wind Engineering and Industrial Aerodynamics*, vol. 12, no. 1, pp. 15-33.

Liang, G & Mudawar, I 2017, 'Review of drop impact on heated walls', *International Journal of Heat and Mass Transfer*, vol. 106, pp. 103-26.

Lin, S & Reitz, R 1998, 'Drop and spray formation from a liquid jet', *Annual Review of Fluid Mechanics*, vol. 30, no. 1, pp. 85-105.

Litchford, RJ & Jeng, S-M 1991, 'Efficient statistical transport model for turbulent particle dispersion in sprays', *AIAA Journal*, vol. 29, no. 9, pp. 1443-51.

Liu, J & Niu, J 2016, 'Cfd simulation of the wind environment around an isolated high-rise building: An evaluation of srans, les and des models', *Building and Environment*, vol. 96, pp. 91-106.

Loth, E 2000, 'Numerical approaches for motion of dispersed particles, droplets and bubbles', *Progress in Energy and Combustion Science*, vol. 26, no. 3, pp. 161-223.

Lucas, C, Hennessy, K, Mills, G & Bathols, J 2007, *Bushfire weather in southeast australia: Recent trends and projected climate change impacts*, Consultancy report prepared for The Climate Institute of Australia, Bushfire CRC, Bureau of Meteorology Research Centre.

Luke, RH & McArthur, AG 1978, *Bushfires in australia*, Australian Government Publishing Service for CSIRO.

Macindoe, L 2006, *Measuring ember attack on timber deck-joist connections using the mass loss cone calorimeter and methenamine as the ignition source*, Report to Bushfire CRC, CMIT-2006-190, CSIRO.

Macindoe, L & Leonard, JE 2009, *A preliminary test on sarking under corrugated steel roofing exposed to simulated ember attack*, Report to Bushfire CRC, CMSE-2009-640, CSIRO.

Macindoe, L, Mikaelsson, J & Leonard, J 2008, *Fire tests at the interface between timber decks and exterior doors*, Report to Bushfire CRC, CMMT-2008-168, CSIRO.

MacInnes, JM & Bracco, FV 1992, 'Stochastic particle dispersion modeling and the tracer-particle limit', *Physics of Fluids A: Fluid Dynamics*, vol. 4, no. 12, pp. 2809-24.

Malet, J & Parduba, Z 2016, 'Experimental characterization of vver-440 reactor containment type spray nozzle', *Atomization and Sprays*, vol. 26, no. 3, pp. 235-55.

Malot, H & Blaisot, J-B 2000, 'Droplet size distribution and sphericity measurements of low-density sprays through image analysis', *Particle & Particle Systems Characterization*, vol. 17, no. 4, pp. 146-58.

Manzello, SL 2014, 'Enabling the investigation of structure vulnerabilities to wind-driven firebrand showers in wildland-urban interface (wui) fires', *Fire Safety Science*, vol. 11, pp. 83-96.

Manzello, SL, Cleary, TG, Shields, JR & Yang, JC 2005, 'Urban-wildland fires: On the ignition of surfaces by embers', paper presented to Fourth joint meeting of the US Sections of the Combustion Institute, Philadelphia, PA.

Manzello, SL, Hayashi, Y, Yoneki, T & Yamamoto, Y 2010, 'Quantifying the vulnerabilities of ceramic tile roofing assemblies to ignition during a firebrand attack', *Fire Safety Journal*, vol. 45, no. 1, pp. 35-43.

Manzello, SL, Park, S-H & Cleary, TG 2009, 'Investigation on the ability of glowing firebrands deposited within crevices to ignite common building materials', *Fire Safety Journal*, vol. 44, no. 6, pp. 894-900.

Manzello, SL, Park, S-H, Suzuki, S, Shields, JR & Hayashi, Y 2011, 'Experimental investigation of structure vulnerabilities to firebrand showers', *Fire Safety Journal*, vol. 46, no. 8, pp. 568-78.

Manzello, SL & Suzuki, S 2012, *Exposing wood decking assemblies to continuous wind-driven firebrand showers*, Technical note 1778, National Institute of Standards and Technology, United States Department of Commerce.

Manzello, SL, Suzuki, S & Hayashi, Y 2012, 'Exposing siding treatments, walls fitted with eaves, and glazing assemblies to firebrand showers', *Fire Safety Journal*, vol. 50, no. 0, pp. 25-34.

Maranghides, A & Mell, W 2011, 'A case study of a community affected by the witch and guejito wildland fires', *Fire Technology*, vol. 47, no. 2, pp. 379-420.

Marklund, M & Engstrom, F 2010, 'Water spray characterization of a coaxial air-assisted swirling atomizer at sonic conditions', *Atomization and Sprays*, vol. 20, no. 11, pp. 955-63.

Mashayek, A & Ashgriz, N 2011, 'Dynamics of liquid droplets', in N Ashgriz (ed.), *Handbook of atomization and sprays: Theory and applications*, Springer US, Boston, MA, pp. 97-123.

Maughan, D, Krusel, N, Boura, J & Caling, T 1999, 'House safety zones: A theoretical model (draft)', *CFA Risk Management Report*.

Mawhinney, JR & Back, GG 2016, 'Water mist fire suppression systems', in MJ Hurley, DT Gottuk, JR Hall Jr, K Harada, ED Kuligowski, M Puchovsky, JL Torero, JM Watts Jr & CJ Wieczorek (eds), *Sfpe handbook of fire protection engineering*, Springer New York, New York, NY, pp. 1587-645.

McGrattan, KB, Hamins, A & Evans, DD 1998, 'Sprinklers, vent, and draft curtain interaction - modeling and experiment', in *National Fire Protection Research Foundation*, Quincy, MA, USA.

McRae, RD, Sharples, J, Wilkes, S & Walker, A 2013, 'An australian pyro-tornadogenesis event', *Natural Hazards*, vol. 65, no. 3, pp. 1801-11.

Meinders, ER, Hanjalic, K & Martinuzzi, RJ 1999, 'Experimental study of the local convection heat transfer from a wall-mounted cube in turbulent channel flow', *Journal of Heat Transfer*, vol. 121, no. 3, pp. 564-73.

Melbourne, W 1979, 'Turbulence effects on maximum surface pressures-a mechanism and possibility of reduction', in *Proceedings of the Fifth International Conference on Wind Engineering*, pp. 541-51.

Mell, WE, Manzello, SL, Maranghides, A, Butry, D & Rehm, RG 2010, 'The wildland–urban interface fire problem – current approaches and research needs', *International Journal of Wildland Fire*, vol. 19, no. 2, pp. 238-51.

Melling, A 1997, 'Tracer particles and seeding for particle image velocimetry', *Measurement Science and Technology*, vol. 8, no. 12, p. 1406.

Meng, H, Pan, G, Pu, Y & Woodward, SH 2004, 'Holographic particle image velocimetry: From film to digital recording', *Measurement Science and Technology*, vol. 15, no. 4, p. 673.

Meroney, RN 2006, 'Cfd prediction of cooling tower drift', *Journal of Wind Engineering and Industrial Aerodynamics*, vol. 94, no. 6, pp. 463-90.

Meroney, RN 2008, 'Protocol for cfd prediction of cooling-tower drift in an urban environment', *Journal of Wind Engineering and Industrial Aerodynamics*, vol. 96, no. 10–11, pp. 1789-804.

Meroney, RN 2009, 'Cfd prediction of airflow in buildings for natural ventilation', in *11th Americas Conference on*
Wind Engineering, San Juan, Puerto Rico.

Mitchell, JW 2006, 'Wind-enabled ember dousing', *Fire Safety Journal*, vol. 41, no. 6, pp. 444-58.

Mitroglou, N, Nouri, J, Gavaises, M & Arcoumanis, C 2006, 'Spray characteristics of a multi-hole injector for direct-injection gasoline engines', *International Journal of Engine Research*, vol. 7, no. 3, pp. 255-70.

Molle, B, Tomas, S, Hendawi, M & Granier, J 2012, 'Evaporation and wind drift losses during sprinkler irrigation influenced by droplet size distribution', *Irrigation and Drainage*, vol. 61, no. 2, pp. 240-50.

Montazeri, H, Blocken, B & Hensen, JLM 2015a, 'Cfd analysis of the impact of physical parameters on evaporative cooling by a mist spray system', *Applied Thermal Engineering*, vol. 75, no. 0, pp. 608-22.

Montazeri, H, Blocken, B & Hensen, JLM 2015b, 'Evaporative cooling by water spray systems: Cfd simulation, experimental validation and sensitivity analysis', *Building and Environment*, vol. 83, no. 0, pp. 129-41.

Moritz, MA, Batllori, E, Bradstock, RA, Gill, AM, Handmer, J, Hessburg, PF, Leonard, J, McCaffrey, S, Odion, DC & Schoennagel, T 2014, 'Learning to coexist with wildfire', *Nature*, vol. 515, no. 7525, pp. 58-66.

Morsi, S & Alexander, A 1972, 'An investigation of particle trajectories in two-phase flow systems', *Journal of Fluid Mechanics*, vol. 55, no. 02, pp. 193-208.

Mugele, R & Evans, H 1951, 'Droplet size distribution in sprays', *Industrial & Engineering Chemistry*, vol. 43, no. 6, pp. 1317-24.

Murakami, S 1993, 'Comparison of various turbulence models applied to a bluff body', *Journal of Wind Engineering and Industrial Aerodynamics*, vol. 46, pp. 21-36.

Murrell, JV, Crowhurst, D & Rock, P 1995, 'Experimental study of the thermal radiation attenuation of sprays from selected hydraulic nozzles', paper presented to Halon Options Technical Working Conference, Albuquerque, U.S.A.

Myers, T, Trouvé, A & Marshall, A 2018, 'Predicting sprinkler spray dispersion in firefoam', *Fire Safety Journal*, vol. 100, pp. 93-102.

NFPA 2010, *Standard on water mist fire protection systems*, NFPA 750, National Fire Protection Association, Quincy, MA, USA.

Nichols, D, Canderle, A, Knight, I & Leonard, J 2005, *Development of fire fighting vehicle crew protection systems*, Article for unnamed publication, CSIRO.

Nijdam, JJ, Guo, B, Fletcher, DF & Langrish, TAG 2006, 'Lagrangian and eulerian models for simulating turbulent dispersion and coalescence of droplets within a spray', *Applied Mathematical Modelling*, vol. 30, no. 11, pp. 1196-211.

Nouri, JM & Whitelaw, JH 2001, 'Spray characteristics of a gasoline direct injector injector with short durations of injection', *Experiments in Fluids*, vol. 31, no. 4, pp. 377-83.

Novozhilov, V, Harvie, DJE, Kent, JH, Apte, VB & Pearson, D 1997, 'A computational fluid dynamics study of wood fire extinguishment by water sprinkler', *Fire Safety Journal*, vol. 29, no. 4, pp. 259-82.

Nuyttens, D, Baetens, K, De Schampheleire, M & Sonck, B 2007, 'Effect of nozzle type, size and pressure on spray droplet characteristics', *Biosystems Engineering*, vol. 97, no. 3, pp. 333-45.

Nuyttens, D, De Schampheleire, M, Verboven, P, Brusselman, E & Dekeyser, D 2009, 'Droplet size and velocity characteristics of agricultural sprays', *Transactions of the ASABE*, vol. 52, no. 5, pp. 1471-80.

O'Grady, N & Novozhilov, V 2009, 'Large eddy simulation of sprinkler interaction with a fire ceiling jet', *Combustion Science and Technology*, vol. 181, no. 7, pp. 984-1006.

O'Rourke, PJ 1981, *Collective drop effects on vaporizing liquid sprays*, LA-9069-T, Los Alamos National Lab., NM, USA.

O'Rourke, PJ & Amsden, AA 1987, *The tab method for numerical calculation of spray droplet breakup*, SAE Technical Paper 872089, Society of Automotive Engineers International.

O'Neill, P, Nicolaides, D, Honnery, D & Soria, J 2004, 'Autocorrelation functions and the determination of integral length with reference to experimental and numerical data', in *15th Australasian Fluid Mechanics Conference*, vol. 1, pp. 1-4.

Ogata, K 1998, *System dynamics*, 4 edn, Pearson, Upper Saddle River, NJ, USA.

Oke, TR 1988, 'Street design and urban canopy layer climate', *Energy and Buildings*, vol. 11, no. 1, pp. 103-13.

Orme, M 1997, 'Experiments on droplet collisions, bounce, coalescence and disruption', *Progress in Energy and Combustion Science*, vol. 23, no. 1, pp. 65-79.

Paloposki, T 1994, 'Drop size distributions in liquid sprays', in *ICLASS 94 Sixth International Conference on Liquid Atomization and Spray Systems*, Rouen, France.

Parker, S, Foat, T & Preston, S 2008, 'Towards quantitative prediction of aerosol deposition from turbulent flows', *Journal of Aerosol Science*, vol. 39, no. 2, pp. 99-112.

Pathania, RS, Chakravarthy, SR & Mehta, PS 2016, 'Time-resolved characterization of low-pressure pulsed injector', *Atomization and Sprays*, vol. 26, no. 8, pp. 755-73.

Pavageau, M & Schatzmann, M 1999, 'Wind tunnel measurements of concentration fluctuations in an urban street canyon', *Atmospheric Environment*, vol. 33, no. 24, pp. 3961-71.

Paveglio, T, Carroll, MS & Jakes, PJ 2008, 'Alternatives to evacuation—protecting public safety during wildland fire', *Journal of Forestry*, vol. 106, no. 2, pp. 65-70.

Pellegrino, JL, Bryner, NP & Johnsson, EL 2013, *Wildland-urban interface fire research needs: Workshop summary report*, NIST Special Publication 1150, National Institute of Standards and Technology.

Penman, TD, Eriksen, C, Horsey, B, Green, A, Lemcke, D, Cooper, P & Bradstock, RA 2017, 'Retrofitting for wildfire resilience: What is the cost?', *International Journal of Disaster Risk Reduction*, vol. 21, pp. 1-10.

Pitcher, G, Wigley, G & Saffman, M 1990, 'Velocity and drop size measurements in fuel sprays in a direct injection diesel engine', *Particle & Particle Systems Characterization*, vol. 7, no. 1-4, pp. 160-8.

Potter, M & Leonard, J 2010, *Spray system design for ember attack - research findings and discussion paper*, Report no. D.06.10, CSIRO - Sustainable Ecosystems, Bushfire CRC.

Putorti, AD, Everest, D & Atreya, A 2004, 'Simultaneous measurements of drop size and velocity in large-scale sprinkler flows using particle tracking and laser-induced fluorescence', *Ann Arbor*, vol. 1001, pp. 48109-2125.

Ramponi, R & Blocken, B 2012a, 'Cfd simulation of cross-ventilation flow for different isolated building configurations: Validation with wind tunnel measurements and analysis of physical and numerical diffusion effects', *Journal of Wind Engineering and Industrial Aerodynamics*, vol. 104, pp. 408-18.

Ramponi, R & Blocken, B 2012b, 'Cfd simulation of cross-ventilation for a generic isolated building: Impact of computational parameters', *Building and Environment*, vol. 53, no. 0, pp. 34-48.

Ramsay, C 1985, 'How bushfires set houses alight - lessons from ash wednesday (otway ranges, australia)', *Ecos: CSIRO Environmental Research*, vol. 43, pp. 3-7.

Ramsay, GC, McArthur, NA & Dowling, V 1996, 'Building in a fire-prone environment: Research on building survival in two major bushfires', in *Procedings-Linnean Society of New South Wales*, vol. 116, pp. 133-42.

Ramsay, GC, McArthur, NA & Dowling, VP 1987, 'Preliminary results from an examination of house survival in the 16 february 1983 bushfires in australia', *Fire and Materials*, vol. 11, no. 1, pp. 49-51.

Ranz, W & Marshall, WR 1952, 'Evaporation from drops', *Chem. Eng. Prog*, vol. 48, no. 3, pp. 141-6.

Rasbash, D 1962, 'Heat transfer between water sprays and flames of freely burning fires', in *Proceedings of the Symposium on the Interaction of Fluids and Particles*, pp. 217-23.

Reischl, U 1979, 'Water fog stream heat radiation attenuation', *Fire Technology*, vol. 15, no. 4, pp. 262-70.

Reitz, RD 1987, 'Modeling atomization processes in high-pressure vaporizing sprays', *Atomisation and Spray Technology*, vol. 3, no. 4, pp. 309-37.

Reitz, RD & Bracco, F 1986, 'Mechanisms of breakup of round liquid jets', *Encyclopedia of fluid mechanics*, vol. 3, pp. 233-49.

Reitz, RD & Bracco, FV 1982, 'Mechanism of atomization of a liquid jet', *The Physics of Fluids*, vol. 25, no. 10, pp. 1730-42.

Ren, KF, Gouesbet, G, Géhan, G, Lebrun, D, Özkul, C & Kleitz, A 1996, 'On the measurements of particles by imaging methods: Theoretical and experimental aspects', *Particle & Particle Systems Characterization*, vol. 13, no. 2, pp. 156-64.

Ren, N, Baum, HR & Marshall, AW 2011, 'A comprehensive methodology for characterizing sprinkler sprays', *Proceedings of the Combustion Institute*, vol. 33, no. 2, pp. 2547-54.

Richards, PJ, Hoxey, RP, Connell, BD & Lander, DP 2007, 'Wind-tunnel modelling of the silsoe cube', *Journal of Wind Engineering and Industrial Aerodynamics*, vol. 95, no. 9, pp. 1384-99.

Richards, PJ, Hoxey, RP & Short, LJ 2001, 'Wind pressures on a 6 m cube', *Journal of Wind Engineering and Industrial Aerodynamics*, vol. 89, no. 14–15, pp. 1553-64.

Richards, PJ & Norris, SE 2011, 'Appropriate boundary conditions for computational wind engineering models revisited', *Journal of Wind Engineering and Industrial Aerodynamics*, vol. 99, no. 4, pp. 257-66.

Richardson, JK & Oleszkiewicz, I 1987, 'Fire tests on window assemblies protected by automatic sprinklers', *Fire Technology*, vol. 23, no. 2, pp. 115-32.

Ruger, M, Hohmann, S, Sommerfeld, M & Kohnen, G 2000, 'Euler/lagrange calculations of turbulent sprays: The effect of droplet collisions and coalescence', *Atomization and Sprays*, vol. 10, no. 1, p. 35.

Salvador, R, Bautista-Capetillo, C, Burguete, J, Zapata, N, Serreta, A & Playán, E 2009, 'A photographic method for drop characterization in agricultural sprinklers', *Irrigation Science*, vol. 27, no. 4, pp. 307-17.

Sanjosé, M, Senoner, JM, Jaegle, F, Cuenot, B, Moreau, S & Poinsot, T 2011, 'Fuel injection model for euler–euler and euler–lagrange large-eddy simulations of an evaporating spray inside an aeronautical combustor', *International Journal of Multiphase Flow*, vol. 37, no. 5, pp. 514-29.

Santangelo, PE 2010, 'Characterization of high-pressure water-mist sprays: Experimental analysis of droplet size and dispersion', *Experimental Thermal and Fluid Science*, vol. 34, no. 8, pp. 1353-66.

Shaw, R, Den Hartog, G & Neumann, H 1988, 'Influence of foliar density and thermal stability on profiles of reynolds stress and turbulence intensity in a deciduous forest', *Boundary-Layer Meteorology*, vol. 45, no. 4, pp. 391-409.

Sheppard, DT & Lueptow, RM 2005, 'Characterization of fire sprinkler sprays using particle image velocimetry', *Atomization and Sprays*, vol. 15, no. 3, pp. 341-62.

Shih, T-H, Liou, WW, Shabbir, A, Yang, Z & Zhu, J 1995, 'A new k-ϵ eddy viscosity model for high reynolds number turbulent flows', *Computers & Fluids*, vol. 24, no. 3, pp. 227-38.

Sidahmed, MM, Taher, MD & Brown, RB 2005, 'A virtual nozzle for simulation of spray generation and droplet transport', *Biosystems Engineering*, vol. 92, no. 3, pp. 295-307.

Standards Australia 1999, *As 4587-1999: Water mist fire protection systems*.

Standards Australia 2009, *Construction of buildings in bushfire-prone areas*, AS 3959-2009.

Standards Australia 2012, *Bushfire water spray systems*, AS 5414-2012.

Stathopoulos, T 2002, 'The numerical wind tunnel for industrial aerodynamics: Real or virtual in the new millennium?', *Wind and Structures*, vol. 5, no. 2, pp. 193-208.

Stone, HA 1994, 'Dynamics of drop deformation and breakup in viscous fluids', *Annual Review of Fluid Mechanics*, vol. 26, no. 1, pp. 65-102.

Stull, RB 1988, *An introduction to boundary layer meteorology*, vol. 13, Springer Science & Business Media.

Subramaniam, S 2013, 'Lagrangian–eulerian methods for multiphase flows', *Progress in Energy and Combustion Science*, vol. 39, no. 2–3, pp. 215-45.

Sullivan, A, Ellis, P & Knight, I 2003, 'A review of radiant heat flux models used in bushfire applications', *International Journal of Wildland Fire*, vol. 12, no. 1, pp. 101-10.

Sureshkumar, R, Kale, SR & Dhar, PL 2008a, 'Heat and mass transfer processes between a water spray and ambient air – i. Experimental data', *Applied Thermal Engineering*, vol. 28, no. 5, pp. 349-60.

Sureshkumar, R, Kale, SR & Dhar, PL 2008b, 'Heat and mass transfer processes between a water spray and ambient air – ii. Simulations', *Applied Thermal Engineering*, vol. 28, no. 5–6, pp. 361-71.

Syphard, AD, Massada, AB, Butsic, V & Keeley, JE 2013, 'Land use planning and wildfire: Development policies influence future probability of housing loss', *PLoS ONE*, vol. 8, no. 8, p. e71708.

Tanaka, H 1990, 'Similitude and modelling in wind tunnel testing of bridges', *Journal of Wind Engineering and Industrial Aerodynamics*, vol. 33, no. 1, pp. 283-300.

Taylor, GI 1938, 'The spectrum of turbulence', in *Proceedings of the Royal Society of London A: Mathematical, Physical and Engineering Sciences*, vol. 164, pp. 476-90.

Tharakan, TJ, Mukhopadhyay, A, Datta, A & Jog, MA 2013, 'Trends in comprehensive modeling of spray formation', *International Journal of Spray & Combustion Dynamics*, vol. 5, no. 2, pp. 123-80.

Tian, L & Ahmadi, G 2007, 'Particle deposition in turbulent duct flows—comparisons of different model predictions', *Journal of Aerosol Science*, vol. 38, no. 4, pp. 377-97.

Tieleman, HW 2003, 'Wind tunnel simulation of wind loading on low-rise structures: A review', *Journal of Wind Engineering and Industrial Aerodynamics*, vol. 91, no. 12, pp. 1627-49.

Tominaga, Y, Mochida, A, Yoshie, R, Kataoka, H, Nozu, T, Yoshikawa, M & Shirasawa, T 2008, 'Aij guidelines for practical applications of cfd to pedestrian wind environment around buildings', *Journal of Wind Engineering and Industrial Aerodynamics*, vol. 96, no. 10–11, pp. 1749-61.

Tominaga, Y & Stathopoulos, T 2009, 'Numerical simulation of dispersion around an isolated cubic building: Comparison of various types of k–ε models', *Atmospheric Environment*, vol. 43, no. 20, pp. 3200-10.

Tominaga, Y & Stathopoulos, T 2010, 'Numerical simulation of dispersion around an isolated cubic building: Model evaluation of rans and les', *Building and Environment*, vol. 45, no. 10, pp. 2231-9.

Tominaga, Y & Stathopoulos, T 2013, 'Cfd simulation of near-field pollutant dispersion in the urban environment: A review of current modeling techniques', *Atmospheric Environment*, vol. 79, no. 0, pp. 716-30.

Toparlar, Y, Blocken, B, Maiheu, B & van Heijst, GJF 2017, 'A review on the cfd analysis of urban microclimate', *Renewable and Sustainable Energy Reviews*.

Townsend, AA 1961, 'Equilibrium layers and wall turbulence', *Journal of Fluid Mechanics*, vol. 11, no. 1, pp. 97-120.

Tropea, C 2011, 'Optical particle characterization in flows', *Annual Review of Fluid Mechanics*, vol. 43, no. 1, pp. 399-426.

Turton, R & Levenspiel, O 1986, 'A short note on the drag correlation for spheres', *Powder Technology*, vol. 47, no. 1, pp. 83-6.

Urbas, J 2013, 'Effectiveness of pre-applied wetting agents in prevention of wildland urban interface fires', *Fire & Materials*, vol. 37, no. 8, pp. 563-80.

Usui, K & Matsuyama, K 2014, 'An experimental study on attenuation of radiation heat flux from flame through water droplets', in *Fire Safety Science - Proceedings of the Eleventh International Symposium*, Christchurch, New Zealand, pp. 1196-207.

van Hooff, T, Blocken, B & Tominaga, Y 2017, 'On the accuracy of cfd simulations of cross-ventilation flows for a generic isolated building: Comparison of rans, les and experiments', *Building and Environment*, vol. 114, pp. 148-65.

Vazquez, G, Alvarez, E & Navaza, JM 1995, 'Surface tension of alcohol water + water from 20 to 50 .Degree.C', *Journal of Chemical & Engineering Data*, vol. 40, no. 3, pp. 611-4.

Versteeg, H & Malalasekera, W 1995, *An introduction to computational fluid dynamics: The finite volume method*, 2 edn, Pearson, London, UK.

Viegas, D, Allgöwer, B, Koutsias, N & Eftichidis, G 2003, 'Fire spread and the wildland urban interface problem', in *International Workshop on Fires in the WUI, WARM Project*, Athens, Greece, pp. 93–103.

Vulgarakis Minov, S, Cointault, F, Vangeyte, J, Pieters, J & Nuyttens, D 2016, 'Spray droplet characterization from a single nozzle by high speed image analysis using an in-focus droplet criterion', *Sensors*, vol. 16, no. 2, p. 218.

Walklate, PJ 1992, 'A simulation study of pesticide drift from an air-assisted orchard sprayer', *Journal of Agricultural Engineering Research*, vol. 51, pp. 263-83.

Watson, K, Leonard, J, Bennetts, I, Kelly, M, Macindoe, L & Clayton, T 2010, 'Assessing the bushfire performance of low-rise steel structures using full scale bushfire flame front simulation', paper presented to 5th Civil Engineering Conference in the Asian Region and Australasian Structural Engineering Conference 2010, The, Sydney, N.S.W.

Weber, RO & Dold, JW 2006, 'Linking landscape fires and local meteorology - a short review', *JSME international journal. Series B, Fluids and thermal engineering*, vol. 49, no. 3, pp. 590-3.

Weiner, KL & Parkin, CS 1993, 'The use of computational fluid dynamic code for modelling spray from a mistblower', *Journal of Agricultural Engineering Research*, vol. 55, no. 4, pp. 313-24.

Widmann, J, Sheppard, D & Lueptow, R 2001, 'Non-intrusive measurements in fire sprinkler sprays', *Fire Technology*, vol. 37, no. 4, pp. 297-315.

Woo, MW, Daud, WRW, Mujumdar, AS, Wu, Z, Meor Talib, MZ & Tasirin, SM 2008, 'Cfd evaluation of droplet drying models in a spray dryer fitted with a rotary atomizer', *Drying Technology*, vol. 26, no. 10, pp. 1180-98.

Wotton, BM, Gould, JS, McCaw, WL, Cheney, NP & Taylor, SW 2012, 'Flame temperature and residence time of fires in dry eucalypt forest', *International Journal of Wildland Fire*, vol. 21, no. 3, pp. 270-81.

Yakhot, V, Orszag, S, Thangam, S, Gatski, T & Speziale, C 1992, 'Development of turbulence models for shear flows by a double expansion technique', *Physics of Fluids A: Fluid Dynamics*, vol. 4, no. 7, pp. 1510-20.

Yarin, AL 2006, 'Drop impact dynamics: Splashing, spreading, receding, bouncing…', *Annual Review of Fluid Mechanics*, vol. 38, no. 1, pp. 159-92.

Yoon, SH, Kim, DY, Kim, DK & Kim, BH 2011, 'Effect of nozzle geometry for swirl type twin-fluid water mist nozzle on the spray characteristic', *Journal of Mechanical Science and Technology*, vol. 25, no. 7, pp. 1761-6.

Yoon, SS, Kim, HY & Hewson, JC 2007, 'Effect of initial conditions of modeled pdfs on droplet characteristics for coalescing and evaporating turbulent water spray used in fire suppression applications', *Fire Safety Journal*, vol. 42, no. 5, pp. 393-406.

You, H 1986, 'Investigation of spray patterns of selected sprinklers with the fmrc drop size measuring system', *Fire Safety Science*, vol. 1, pp. 1165-76.

Yuan, L & Smith, AC 2015, 'Numerical modeling of water spray suppression of conveyor belt fires in a large-scale tunnel', *Process Safety and Environmental Protection*.

Zhou, X, D'Aniello, S & Yu, H-Z 2014, 'Spray measurements of an upright fire sprinkler', *Fire Technology*, vol. 50, no. 3, pp. 457-82.

Zhou, X, D'Aniello, SP & Yu, H-Z 2012, 'Spray characterization measurements of a pendent fire sprinkler', *Fire Safety Journal*, vol. 54, no. 0, pp. 36-48.